Title
Earth-Abundant Transition Metal Chemistry: Electrocatalytic Hydrogen Production and the Synthesis of High-spin Iron(IV)-oxo Complexes

Author
Bigi, Julian

Publication Date
2012

Peer reviewed|Thesis/dissertation

Earth-Abundant Transition Metal Chemistry: Electrocatalytic Hydrogen Production and the Synthesis of High-spin Iron(IV)-oxo Complexes

by

Julian Patrick Bigi

A dissertation submitted in partial satisfaction of the
requirements for the degree of
Doctor of Philosophy
in
Chemistry
in the
Graduate Division
of the
University of California, Berkeley

Committee in charge:
Professor Christopher J. Chang, Chair
Professor T. Don Tilley
Professor Wenjun Zhang

Fall 2012

Abstract

Earth-Abundant Transition Metal Chemistry: Electrocatalytic Hydrogen Production and the Synthesis of High-spin Iron(IV)-oxo Complexes

by

Julian Patrick Bigi

Doctor of Philosophy in Chemistry

University of California, Berkeley

Professor Christopher J. Chang, Chair

Herein is detailed the synthesis, characterization, and electrocatalytic activity for the reduction of protons for a series of polypyridyl complexes of cobalt and molybdenum. These complexes function as highly active and stable catalysts for the electrocatalytic reduction of protons in mixed organic/aqueous and aqueous media, respectively. In addition, the synthesis, detailed spectroscopic characterization and preliminary reactivity of two novel, thermally unstable $S = 2$ iron(IV)-oxo complexes of a tris(pyrrolide) ligand platform is described. These complexes add to the short but growing list of high-spin synthetic iron(IV)-oxo complexes. Lastly, preliminary investigations of iron complexes of alternative three-fold symmetric tris(pyridine) and tris(guanidine) ligands and their oxidative reactivity is included.

For my family

Acknowledgments

I am grateful to Chris Chang for the support, dedication and patience he has shown me during my Ph. D. He is always very accessible and obviously cares deeply about the happiness of his students both professionally and personally. Following my father's stroke, Chris was very supportive of my desire to be with my family and allowed me to be absent from lab for as long as I thought necessary. I will be forever grateful for that. He is also clearly very excited about research and being a professor at Berkeley and his overall relaxed attitude provides a calming presence in the face of the vicissitudes of synthetic chemistry.

I have also benefited greatly from the faculty in the College of Chemistry, especially Professors Don Tilley, Jeff Long, Dick Andersen, Bob Bergman, Ken Raymond, Michelle Chang and John Arnold who have helped mold me as a scientist from my first day in Berkeley. The atmosphere at Berkeley is both invigorating and mellow and to a large part because of the faculty. I am also very fortunate to have served as a graduate student instructor of inorganic chemistry under Dick Andersen. I thank Professors Don Tilley and Wenjun Zhang for reviewing my dissertation. Lynn Keithlin has been very helpful and has answered many questions about the process of getting through my Ph. D.

I am also grateful for the fantastic scientists I've met in the Chang lab and in Berkeley in general. I am particularly indebted to Dr. Han Sen Soo, Dr. Tamara Hanna, and Dr. W. Hill Harman for teaching me the techniques of synthetic chemistry and for discussing chemistry with me. I have also learned a great deal from Dr. Alex Lippert, Dr. Nick Piro, Dr. John Curley, Dr. Jonah Jurss, Dr. Ming Lee Tang, and Dr. Hemamala Karundasa and enjoyed their company. My interactions with the entire Long group have been rewarding and I'm lucky to have friends throughout the chemistry and chemical engineering departments, especially Dr. Geoffrey Feld, John Weinstein and Colin Cerretani and my friends from soccer, softball and climbing.

I thank Dr. Melissa Fardy and Dr. Yunjeong Hwang for their help with micro GC measurements, Professor David Britt, Dr. Troy Stich and Damon Robles for studying our iron(IV)-oxo complexes by EPR, Dr. Hemamala Karunadasa for help with electrochemical measurements, Dr. Junko Yano and Dr. Ben Lassalle for their EPR, XAS and EXAFS measurements and expertise, Dr. Tom Kent for help setting up and maintaining a Mössbauer instrument, Dr. Rita Nichiporuk for help with mass spectrometry, Dr. Antonio DiPasquale for help with Xray crystallography and Dr. Ho Yu Au-Yeung for help with a bioluminescence assay.

Table of Contents

Chapter 1
Electrocatalytic Reduction of Protons to Hydrogen by a Water-Compatible Cobalt Polypyridyl Platform

Introduction

Hydrogen derived from non-carbon sources has emerged as a potential fuel for sustainable energy cycles that minimize carbon dioxide emissions.[1,2] As such, the search for catalysts that can faciliate the reduction of protons to hydrogen using cheap and earth-abundant metals is an area of current interest.[3-15] However, despite recent advances in the field (especially with soluble Co complexes[16-28]), creating catalysts that generate hydrogen from protons at minimal overpotentials, possess high activity and stability, and operate in neutral aqueous media remains an outstanding challenge; as such, no single synthetic system possesses all of these desirable properties. In addition, recent work from the Savéant group has implicated Co-based nanoparticles as the active catalyst when a clathrochelate cobaloxime is sujected to acidic conditions.[24,29] In light of the work on the related, well-studied cobaloxime complexes for both electrocatlytic and photocatlytic hydrogen production,[17-21,25,30-32] the activity of Co nanomaterials highlights the necessity of studying multiple ligand platforms and their respective abilities to generate hetereogeneous catalysts under catalytic conditions. Because the major classes of hydrogen-producing small molecules reported to date include metal-sulfur clusters related to hydrogenase enzymes,[8-15,33-43] iron,[44] cobalt,[17-22,25,30-32,45-49] and nickel macrocycles,[10,47,50-52] and cobalt and nickel cyclopentadienyl and phosphine complexes,[53,54] we sought to explore alternative supporting ligand scaffolds to meet this goal. We reasoned that pyridine donors could stabilize reducing metal-based species with favorable aqueous compatibility. Inspired by the pentadentate PY5 platform used for biomimetic iron and manganese oxidation chemistry,[55-62] we sought to create tetradentate analogs that would support octahedral metal complexes with two fixed *cis* open coordination sites for reduction chemistry. With this background, we now present a new tetradentate polypyridine platform and the ability of its cobalt(II) derivative to reduce protons to hydrogen in acetonitrile solution. This catalyst can also operate in up to 50% aqueous media. Note that PY5 ligated to cobalt has recently been shown by our group to be a molecular catalyst for the production of dihydrogen from neutral water.[28] The molecularity of the catalysis was suggested by the ability to rationally tune the catalyst performance through ligand design. A different group has recently investigated related Co complexes for water oxidation activity.[63]

Results and Discussion

Synthesis of PY4 and its Co(II) and Zn(II) Complexes

Scheme 1.1 outlines the synthesis of 2-(bis(2-pyridyl)(methoxy)methyl-6-pyridylpyridine (PY4) based on these considerations. Lithiation of 2,6-dibromopyridine followed by reaction with 2,2'-dipyridylketone affords **1** in 50% yield. Methylation of **1** with iodomethane provides **2** in 52% yield, and subsequent Stille coupling with 2-trimethylstannylpyridine with catalytic $Pd(PPh_3)_4$ and CuI furnishes the final ligand PY4 (**3**) in 64% yield. Metal insertion with $CoCl_2$ followed by salt metathesis with $TlPF_6$ generates the cationic cobalt(II) PY4 complex **4**. The X-ray crystal structure of **4** confirms the expected octahedral geometry adopted at Co(II) for this compound (Fig. 1.1 left). Metalation with $ZnCl_2$ followed by $TlPF_6$ treatment delivers the corresponding Zn(II) PY4 congener **5** as a five-coordinate complex (Fig 1.1 right).

Electrocatalytic Dihydrogen Production with PY4Co(II)

Fig. 1.2 displays cyclic voltammogram (CV) data of **4** in acetonitrile solution with varying amounts of trifluoroacetic acid (TFA). In the absence of acid, the CV of **4** features a reversible reductive wave at -0.81 V vs SCE; we assign this wave to a metal-centered Co(II)/Co(I) reduction process as both the corresponding Zn(II) PY4 complex **5** and free PY4 ligand are electrochemically silent in this potential range. A quasi-reversible oxidative wave at +0.87 V vs SCE (ΔE_p = 430 mV) is likely due to the Co(III)/Co(II) couple (Fig. 1.3).

The addition of TFA triggers the appearance of a catalytic wave near the Co(II)/Co(I) couple of **4** that plateaus at higher acid concentrations (Fig. 1.2). Analysis of controlled-potential electrolysis samples confirms the production of hydrogen with a ca. 99% Faraday yield, suggesting that the observed current enhancements are due to electrocatalytic reduction of protons. To determine the order of the electrocatalysis in **4** and TFA, we performed a series of CV measurements under electrocatalytic conditions with a large excess of acid and at sufficiently negative potentials that electron transfer is fast. Under these conditions, for a reaction first order in catalyst and second order in acid, the plateau current (i_c) is related to the concentrations of catalyst and acid by the following expression:[64-69]

$$i_c = nFA[cat]\sqrt{Dk[H^+]^2}$$

Plotting the plateau current as a function of the concentration of **4** reveals that hydrogen generation is first-order in **4** (Fig. 1.4). An analogous plot of i_c as a function of [TFA] shows that the process is second-order in TFA (Fig. 1.5). With this information, according to the following equation, plotting i_c/i_p vs [TFA] (Fig. 1.6) should be linear for different scan rates (where i_p is the peak current in the absence of acid).[53,64-69]

$$\frac{i_c}{i_p} = \frac{n}{0.4463}\sqrt{\frac{RTk[H^+]^2}{Fv}}$$

The turnover frequency (TOF) calculated by plotting the slopes of these lines against $\nu^{-1/2}$ is ca. 40 mol H_2/(mol **4***hr) for [TFA] ~ 60 mM, a concentration of acid compatible with **4** (Fig. 1.7), with H_2 production occurring at an overpotential of ca. 400 mV.[9] Notably, the Zn(II) PY4 complex **5** does not catalyze hydrogen production under these conditions, implicating the need for a redox-active metal center for electrocatalysis (Fig. 1.8).

Observation of a Putative Co(I) Species by Spectroelectrochemistry

The observation that the electrocatalytic current for hydrogen production occurs near the Co(II)/Co(I) couple for **4** suggests that a reduced Co(I) species is involved in the catalytic cycle. We monitored spectral changes for this Co(II)/Co(I) reduction process by UV-visible absorption spectroelectrochemistry using an optically semi-transparent thin layer electrode (OSTTLE). As shown in Fig. 1.9, the reversible electrochemical reduction of **4** results in the appearance of two new features in the electronic absorption spectrum, a broad band at 550 nm with a shoulder near 600 nm and a weaker absorption centered at 900 nm. So far, we have been unable to obtain X-ray quality crystals of the reduced Co(I) species.

Water-compatible Electrocatalytic Dihydrogen Production

Finally, we sought to test whether electrocatalytic proton reduction mediated by **4** is compatible with aqueous conditions. The compound is sufficiently soluble to obtain reproducible electrochemical behavior in 1:1 water/acetonitrile solutions but is

not soluble in pure aqueous media at millimolar concentrations. The CV of **4** in 1:1 water/acetonitrile solution shows a reversible Co(II)/Co(I) reduction wave in the absence of acid (Fig. 1.10). The addition of TFA triggers an electrocatalytic current near the Co(II)/Co(I) couple consistent with hydrogen production, as observed for reactions in acetonitrile.

Concluding Remarks

In closing, we have presented a new polypyridyl platform and the ability of its octahedral cobalt(II) derivative to electrocatalytically reduce protons to hydrogen. The collective data suggest involvement of a Co(I) species and show that proton reduction is compatible in media containing up to 50% water. Ongoing and future work is geared toward additional mechanistic studies as well as exploiting the tunability of PY4 and related platforms to create catalysts with improved activity, reduced overpotentials, and compatibility with pure aqueous media.

Experimental Section

General Synthetic Details. Unless noted otherwise, all manipulations were carried out at room temperature under a dinitrogen atmosphere in a VAC glovebox or using high-vacuum Schlenk techniques. Methylene chloride, diethyl ether, tetrahydrofuran, and pentane were dried over activated 4 Å molecular sieves, passed through a column of activated alumina, and sparged with nitrogen prior to use. Acetonitrile, acetonitrile-d_3, propionitrile and butyronitrile were refluxed over CaH_2, distilled, and sparged with nitrogen. All other reagents and solvents were purchased from commercial sources and used without further purification.

Physical Methods. NMR spectra were recorded on Bruker spectrometers operating at 300 or 400 MHz as noted. Chemical shifts are reported in ppm relative to residual protiated solvent; coupling constants are reported in Hz. Magnetic susceptibility measurements were made using Evans' method: an NMR tube containing the paramagnetic compound in CD_3CN was fitted with an insert containing only CD_3CN. The paramagnetic shift of the CHD_2CN signal was used to calculate the room temperature solution magnetic moment.[70] Mass spectra were determined at the University of California, Berkeley Mass Spectrometry Facility. UV/Vis experiments were conducted on a Varian Cary 50 BIO UV-Visible Spectrophotometer. Non-aqueous electrochemical experiments were conducted under an inert atmosphere in 0.1 M Bu_4NPF_6 in CH_3CN. Cyclic voltammetry experiments were carried out using BASI's Epsilon potentiostat and C-3 cell stand. The working electrode was a glassy carbon disk (3.0 mm diameter) and the counter electrode was a platinum wire. A silver wire in a glass tube with a porous Vycor tip filled with 0.01 $AgNO_3$ in 0.1 M Bu_4NPF_6 in CH_3CN was used as a reference electrode. The scan rate for all cyclic voltammograms was 100 mV/sec. All potentials were referenced against Fc/Fc^+ as an internal standard and converted to SCE by adding 0.40 V to the measured potentials.[71] Electrochemical experiments conducted in 1:1 H_2O:CH_3CN were performed under a blanket of dinitrogen in 0.1 M KNO_3 and referenced with an aqueous Ag/AgCl electrode (BASI) and converted to SCE.

General Methods for X-ray Crystallography. Crystals were mounted on Kaptan loops in Paratone-N hydrocarbon oil. All data collection was performed on a Bruker (formerly

Siemens) SMART diffractometer/CCD area detector equipped with a low temperature apparatus. Data integration was performed using SAINT. Preliminary data analysis and absorption correction were performed using XPREP and SADABS.[72] Structure solution by direct methods and refinement were performed using the SHELX software package.[73-75] Hydrogen atoms were included in calculated positions, but not refined. In the case of chiral space groups, the correct enantiomer was determined by comparison of calculated and observed Friedel pairs.

2-(Bis(2-pyridyl)(hydroxy)methyl-6-bromopyridine (1). 2,6-Dibromopyridine (14.5 g, 61.4 mmol) was dissolved in 250 mL of ether and cooled to -78 ºC. 1.6 M *n*-Butyllithium in hexanes (42.2 mL, 67.6 mmol) was then added slowly over 25 minutes to produce a dark orange solution which was stirred an additional 20 minutes. Dipyridyl ketone (10.4 g, 56.6 mmol) was added as a 100 mL solution in THF over the course of 20 minutes to produce a dark brown mixture. After two hours of stirring at -78 ºC, the mixture was warmed to 0 ºC, acidified to pH 3.5 with 150 mL of 5% HCl, basified with 20 mL of saturated aqueous Na_2CO_3, and extracted into $CHCl_3$ (3 × 50 mL). The organics were combined, dried over Na_2SO_4, and removed under reduced pressure to afford a red oil. This oil was purified by passage through a plug of silica gel followed by hexanes and ether washes to provide **1** as an orange solid (9.68 g, 28.3 mmol, 50%). ^{1}H NMR (300 MHz, $CDCl_3$): δ 7.01 (br s, 1H), 7.20 (ddd, 6.0 Hz, 4.8 Hz, 2.4 Hz, 2H), 7.36 (dd, 8.0 Hz, 0.8 Hz, 1H), 7.53 (t, 7.6 Hz, 1H), 7.69 (m, 4H), 7.73 (dd, 7.6 Hz, 0.8 Hz, 1H), 8.53 (dt, 4.8 Hz, 1.2 Hz, 2H). ^{13}C NMR (75 MHz, $CDCl_3$): δ 81.1, 121.9, 122.7, 123.3, 126.9, 136.7, 138.9, 140.4, 148.0, 162.3, 164.7.

2-(Bis(2-pyridyl)(methoxy)methyl-6-bromopyridine (2). Compound **1** (4.50 g, 13.2 mmol) was dissolved in 100 mL THF to form an orange solution. Addition of NaH (1.58 g, 65.8 mmol) produced immediate bubbling and the formation of a peach mixture. Methyl iodide (9.33 g, 65.8 mmol) was then added slowly after which the reaction was heated to 40 ºC overnight. During this time the reaction became orange with precipitation of a colorless solid. The reaction was then acidified with 25 mL 5% HCl to a pH of 4 to produce a bright red solution. The solution was basified with 9 mL of saturated aqueous Na_2CO_3 to pH 9 with the precipitation of a white solid from the red solution. The mixture was extracted 3 × 30 mL with $CHCl_3$ and the organics were combined and dried over Na_2SO_4. Removal of solvent under reduced pressure followed by recrystallization from ether afforded **2** as a white solid (2.43 g, 6.83 mmol, 52%). ^{1}H NMR (400 MHz, $CDCl_3$): δ 3.28 (s, 3H), 7.17 (m, 2H), 7.33 (d, 8.0 Hz, 1H), 7.51 (t, 7.8 Hz, 1H), 7.68 (m, 5H), 8.57 (d, 4.8 Hz, 2H). ^{13}C NMR (75 MHz, $CDCl_3$): δ 53.06, 88.02, 122.24, 122.98, 124.14, 126.56, 136.09, 138.20, 140.49, 148.39, 160.81, 162.69.

2-(Bis(2-pyridyl)(methoxy)methyl-6-pyridylpyridine (PY4; 3). A 350-mL heavy-walled flask was charged with **2** (1.01 g, 2.84 mmol), 2-trimethylstannylpyridine[76] (687 mg, 2.87 mmol), $Pd(PPh_3)_4$ (35 mg, 0.030 mmol), CuI (12 mg, 0.063 mmol), and 60 mL of DMF. The reaction was heated to 100 ºC for 24 hr. The reaction was then cooled to room temperature and the DMF was removed under reduced pressure to give a dark brown oil. Silica gel chromatography (10% MeOH in CH_2Cl_2), followed by recrystallization from ether afforded **3** as a white solid (643 mg, 1.81 mmol, 64%). ^{1}H

NMR (300 MHz, $CDCl_3$): δ 3.34 (s, 3H), 7.18 (m, 3H), 7.70 (m, 7H), 8.08 (d, 8.1 Hz, 1H), 8.30 (d, 7.8 Hz, 1H), 8.61 (m, 3H). ^{13}C NMR (75 MHz, $CDCl_3$): δ 53.37, 88.78, 119.45, 121.42, 122.19, 123.69, 124.23, 124.62, 136.01, 136.94, 137.30, 148.48, 149.07, 154.56, 156.45, 160.88, 161.72. HRESIMS (MH^+) *m/z* calcd for $C_{22}H_{19}N_4O$ 355.1553, found 355.1557.

[(PY4)Co(NCCH$_3$)$_2$](PF$_6$)$_2$.THF (4). To a stirring, colorless slurry of PY4 (158 mg, 0.446 mmol) in CH_3CN was added $CoCl_2$ (57.9 mg, 0.446 mmol). Within five minutes, the reaction mixture turned grey colored. After two hours, $TlPF_6$ (312 mg, 0.892 mmol) was added with immediate precipitation of TlCl and the formation of a red solution. The reaction mixture was filtered through celite to remove TlCl and the volatiles were removed under reduced pressure. Red-orange crystals of **4**, suitable for X-ray diffraction, were isolated by recrystallization from CH_3CN/THF/pentane (247 mg, 0.288 mmol, 65%). Anal. Calc. for $C_{30}H_{32}CoF_{12}N_6O_2P_2$: C, 42.02; H, 3.76; N, 9.80. Found: C, 41.87; H, 3.56; N, 9.98%. ^1H NMR (300 MHz, CD_3CN): δ 5.60, 14.02, 18.31, 31.50, 39.12, 61.74, 62.57, 78.32, 83.83, 87.57. Magnetic susceptibility (CD_3CN): μ_{eff} = 4.3 μ_{BM}. HRESIMS (M^{2+}) *m/z* calcd for $C_{22}H_{18}CoN_4O$ 206.5401, found 206.5405.

[(PY4)Zn(NCCH$_3$)](PF$_6$)$_2$ (5). To a slurry of PY4 (154 mg, 0.435 mmol) in CH_3CN was added $ZnCl_2$ (59.1 mg, 0.434 mmol) to produce a turbid, colorless mixture. Following overnight stirring, $TlPF_6$ was added to the mixture with immediate TlCl precipitation. The resulting mixture was stirred for eight hours, filtered through celite to remove the TlCl, and concentrated under reduced pressure. Colorless crystals of **5**, suitable for X-ray diffraction, were obtained by recrystallization from CH_3CN layered beneath ether (157 mg, 0.209 mmol, 48%). Anal. Calc. for $C_{24}H_{21}F_{12}N_5OP_2Zn$: C, 38.39; H, 2.82; N, 9.33. Found: C, 38.20; H, 2.56; N, 9.16%. ^1H NMR (300 MHz, CD_3CN): δ 4.03 (s, 3H), 7.62 (m, 2H), 7.95 (t, 6.5 Hz, 1H), 8.19 (m, 5H), 8.33 (m, 3H), 8.50 (d, 8.1 Hz, 1H), 8.85 (d, 5.4 Hz, 2H), 9.15 (d, 4.8 Hz, 1H). ^{13}C NMR (75 MHz, CD_3CN): 56.64, 81.95, 120.21, 121.98, 122.28, 122.53, 124.05, 126.54, 140.82, 141.62, 142.31, 146.98, 147.35, 148.64, 154.85, 155.23. HRESIMS (M^{2+}) *m/z* calcd for $C_{22}H_{18}N_4OZn$ 209.0381, found 209.0385.

Controlled-Potential Electrolysis. A solution with a trifluoroacetic acid concentration of 65 mM in 100 mM Bu_4NPF_6 in CH_3CN was electrolyzed in the presence of **4** for 30 minutes at -1.0 V vs SCE in a custom-built, gas-tight electrochemical cell. Aliquots of the head-space gas were removed with a gas-tight syringe following electrolysis and the production of H_2 with a Faraday yield of 99% was confirmed by GC analysis with a thermal conductivity detector.

Spectroelectrochemistry. Electronic spectra were recorded using a Cary 5000 UV/Vis/NIR spectrophotometer interfaced to Varian WinUV software. The absorption spectra of the electrogenerated species were obtained *in situ*, by the use of a cryostatted Optically Semi-Transparent Thin-Layer Electrosynthetic (OSTLE) cell (path length 1.0 mm) mounted in the light-path of the spectrophotometer.

The OSTLE cell, which was secured in the beam of the spectrophotometer, was of quartz construction. A platinum gauze working electrode (70% transmittance) was located centrally in the optical beam in the lower section of the cell. To ensure electrolysis occurred only at the platinum gauze, the section of wire passing to the top of

the cell was sheathed by poly(tetrafluoroethylene) (PTFE) tubing. A platinum wire auxiliary electrode and Ag/Ag^+ reference electrode were positioned in the upper section of the cell and were separated from the solution by salt bridges containing electrolyte solution. A matching section of platinum gauze was placed in the reference beam.

All solutions were prepared under an N_2 atmosphere in a glovebox. Appropriate potentials were applied using a Bioanalytical Systems BAS 100A Electrochemical Analyzer. Both the current and potential were monitored during the electrolysis. By this method, the electrogenerated species were obtained *in situ*, and their absorption spectra recorded at regular intervals throughout the electrolysis. The attainment of a steady-state spectrum and the decay of the current to a constant minimum at a potential appropriately beyond $E_{1/2}$ (for the redox process in question) are indicative of the complete conversion of the starting material. The reversibility of the spectral data was confirmed by the regeneration of the starting spectrum following the attainment of the steady-state spectrum for the reduced species.

Proton Reduction: Kinetics Studies. Cyclic voltammetry was used to investigate the kinetics of the electrocatalysis. All kinetics studies were conducted in electrochemical cells with 5 mL solutions of 100 mM Bu_4NPF_6 in CH_3CN. The working electrode was a glassy carbon disk (3.0 mm diameter) and the counter electrode was a platinum wire. A silver wire in a glass tube with a porous Vycor tip filled with 0.1 M Bu_4NPF_6 in CH_3CN was used as a pseudo-reference electrode. Where the electrocatalytic current did not reach a plateau, the current at the top of the catalytic peak in the cyclic voltammogram was taken as equivalent to the plateau current.

Order with Respect to Catalyst. Trifluoroacetic acid was added to a solution of 100 mM Bu_4NPF_6 in CH_3CN in an electrochemistry cell to afford an acid concentration of 65 mM. Aliquots of a 22.6 mM stock solution of **4** were then added to the cell and cyclic voltammograms were taken. The order of the proton reduction in catalyst was determined by plotting the plateau current vs. catalyst concentration (Figure S2).

Order with Respect to Acid. Aliquots of neat trifluoroacetic acid were added to a 1.0 mM solution of **4** in 100 mM Bu_4NPF_6 and cyclic voltammograms were recorded. The order of the proton reduction electrocatalysis in acid was determined by plotting the plateau current vs the concentration of acid (Figure S3).

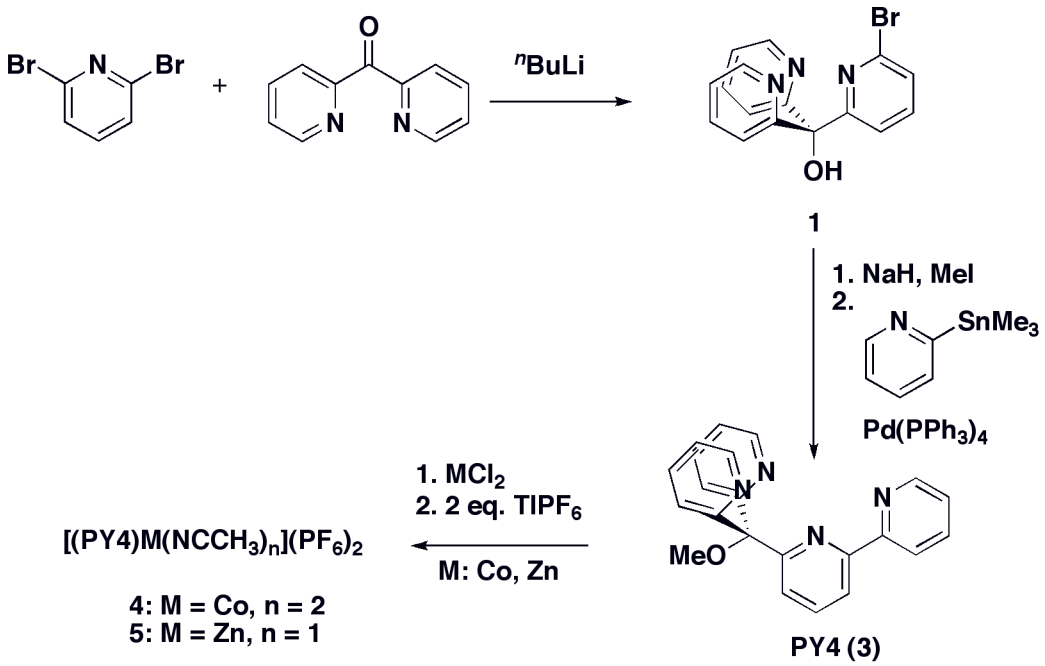

Scheme 1.1. Synthesis of PY4 and its Co(II) and Zn(II) complexes.

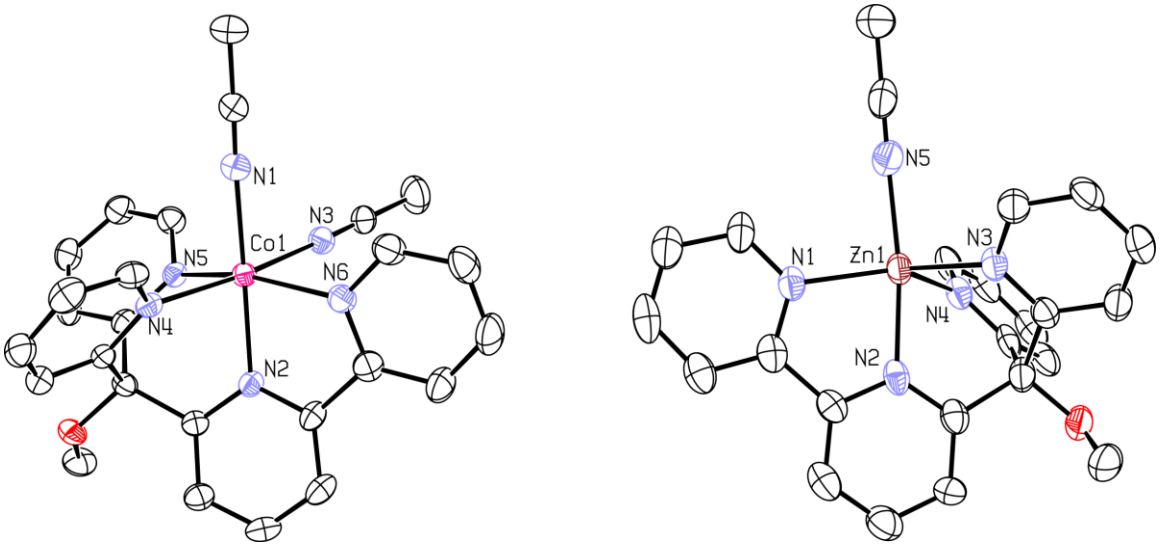

Figure 1.1. Solid-state structures of complexes **4** (left) and **5** (right). Anions, solvent molecules and hydrogen atoms are omitted for clarity; thermal ellipsoids are shown at 50% probability.

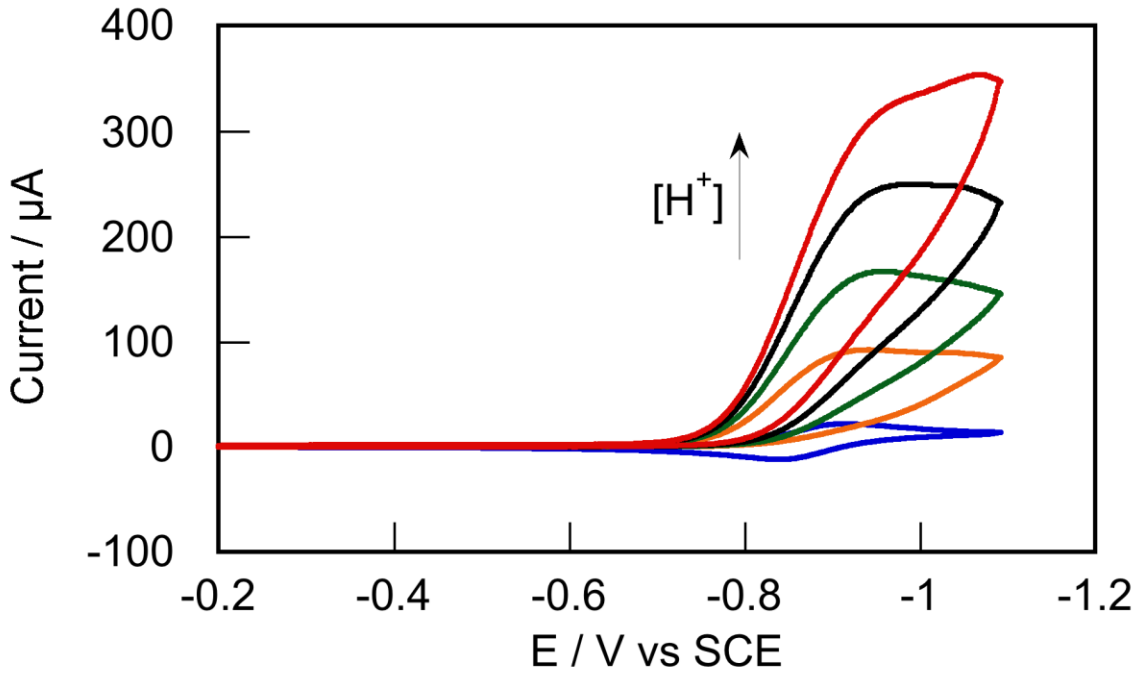

Figure 1.2. Cyclic voltammograms of complex **4** in 0.1 M Bu_4NPF_6 in acetonitrile in the presence of trifluoroacetic acid (TFA): (bottom-top) 1.0 mM **4** with no acid, 5.2 mM TFA, 10.4 mM TFA, 15.6 mM TFA, and 26.0 mM TFA. Scan rate: 100 mV/sec; glassy carbon electrode.

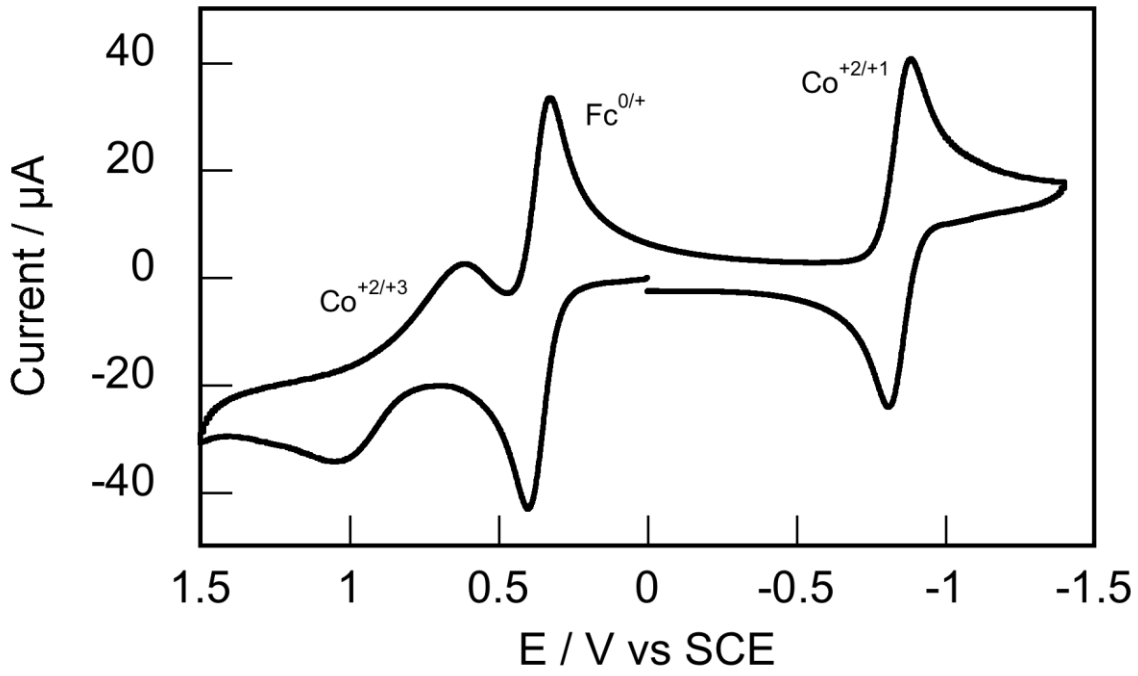

Figure 1.3. Cyclic voltammogram of complex **4** in 0.1 M Bu_4NPF_6 in acetonitrile with ferrocene as an internal standard. Scan rate: 100 mV/sec; glassy carbon electrode.

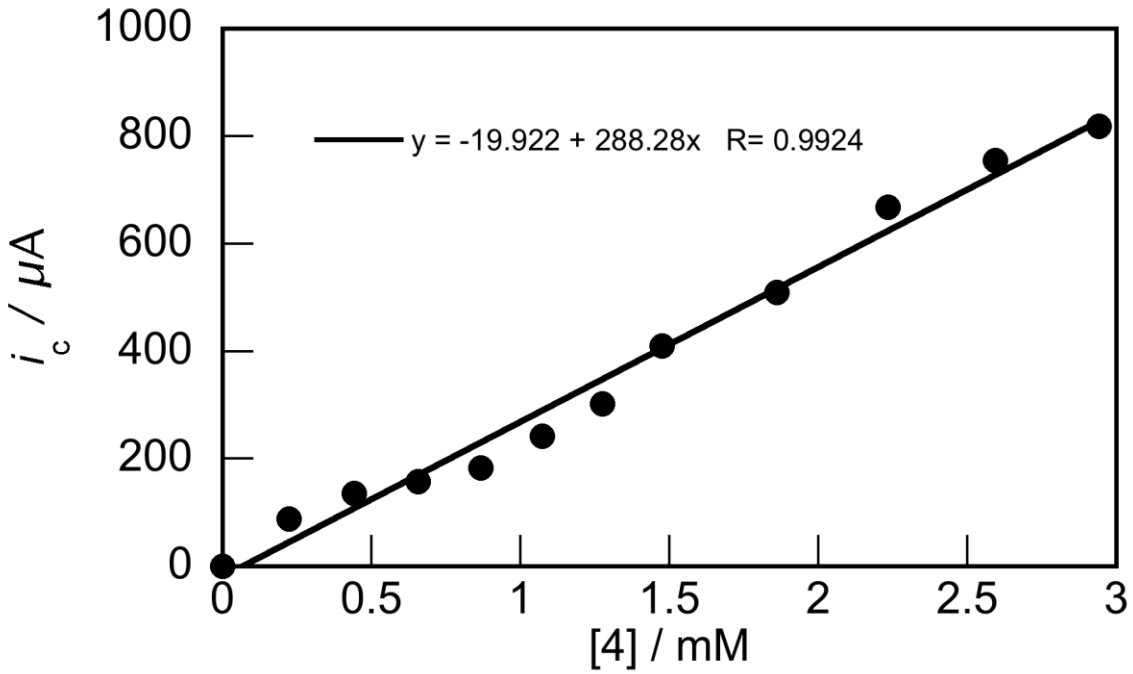

Figure 1.4. Electrocatalytic current for complex **4** in the presence of 65 mM TFA as a function of [**4**] in 0.1 Bu_4NPF_6 in acetonitrile. Scan rate: 100 mV/sec; glassy carbon working electrode.

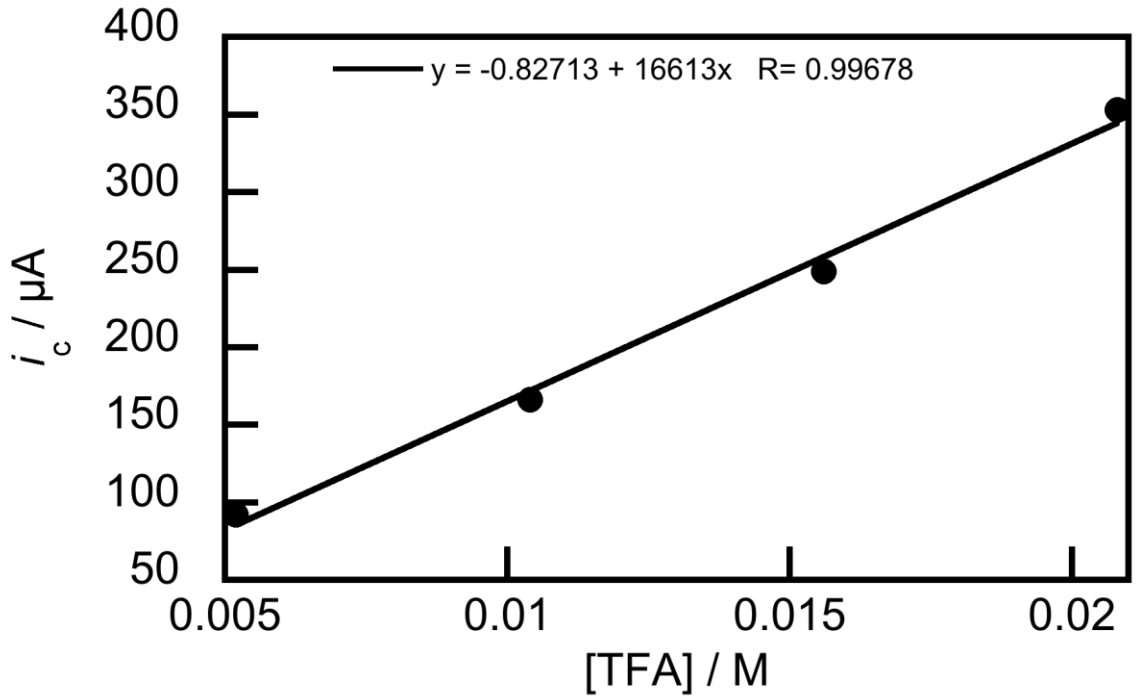

Figure 1.5. Electrocatalytic current for 1.0 mM of **4** as a function of [TFA] in 0.1 M Bu_4NPF_6 in acetonitrile. Scan rate: 100 mV/sec; glassy carbon electrode.

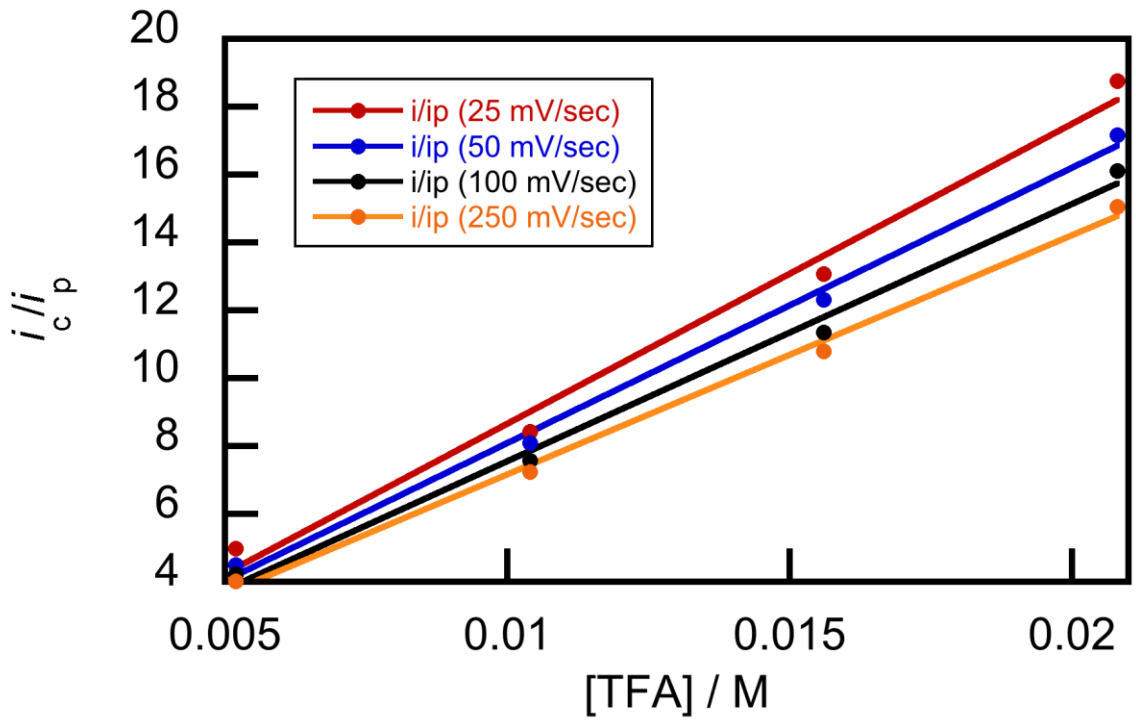

Figure 1.6. Plot of i_c/i_p as a function of [TFA] for 1.0 mM of **4** in 0.1 M Bu_4NPF_6 in acetonitrile; glassy carbon electrode. 250 mV/sec (orange), 0.705x+0.114; 100 mV/sec (black), 0.759x-0.0378; 50 mV/sec (blue), 0.812x-0.0303; 25 mV/sec (red), 0.883x-0.167.

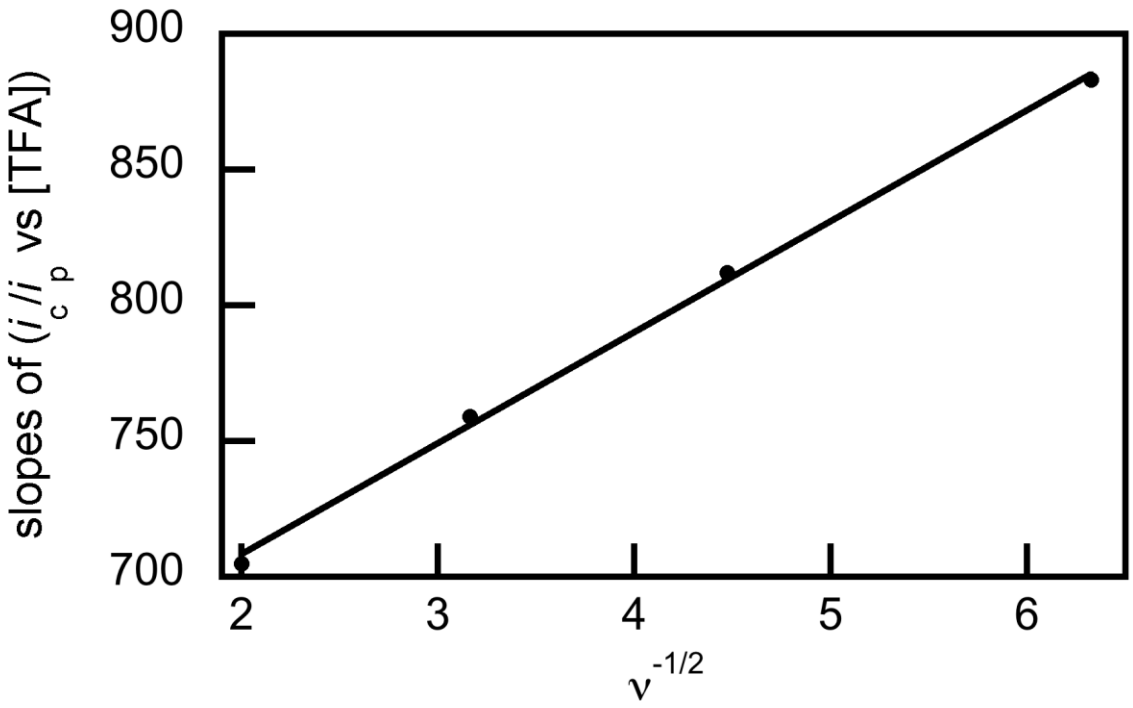

Figure 1.7. Plot of the slopes from Fig. 1.6 vs $\nu^{-1/2}$. The linear fit is 1.295x + 0.626, R = 0.9992. The rate constant for hydrogen production, *k*, can be calculated from the slope to be ca. 3 $M^{-2}s^{-1}$. For 60 mM TFA, this corresponds to a turnover frequency (TOF) of ca. 40 mol H_2/(mol **4***hr).

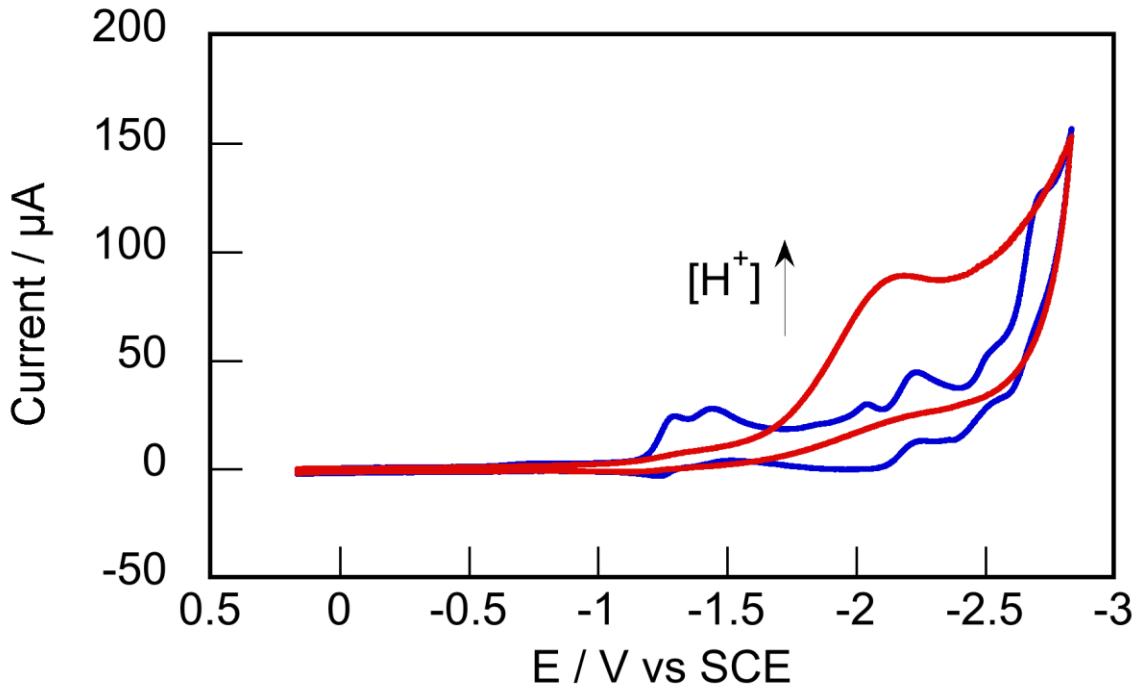

Figure 1.8. Cyclic voltammogram of complex **5** in 0.1 M Bu_4NPF_6 in acetonitrile in the presence of TFA: (bottom to top) 1.0 mM of **5** with no acid, 1.0 mM of **5** with 10 mM TFA. Scan rate: 100 mV/sec; glassy carbon electrode.

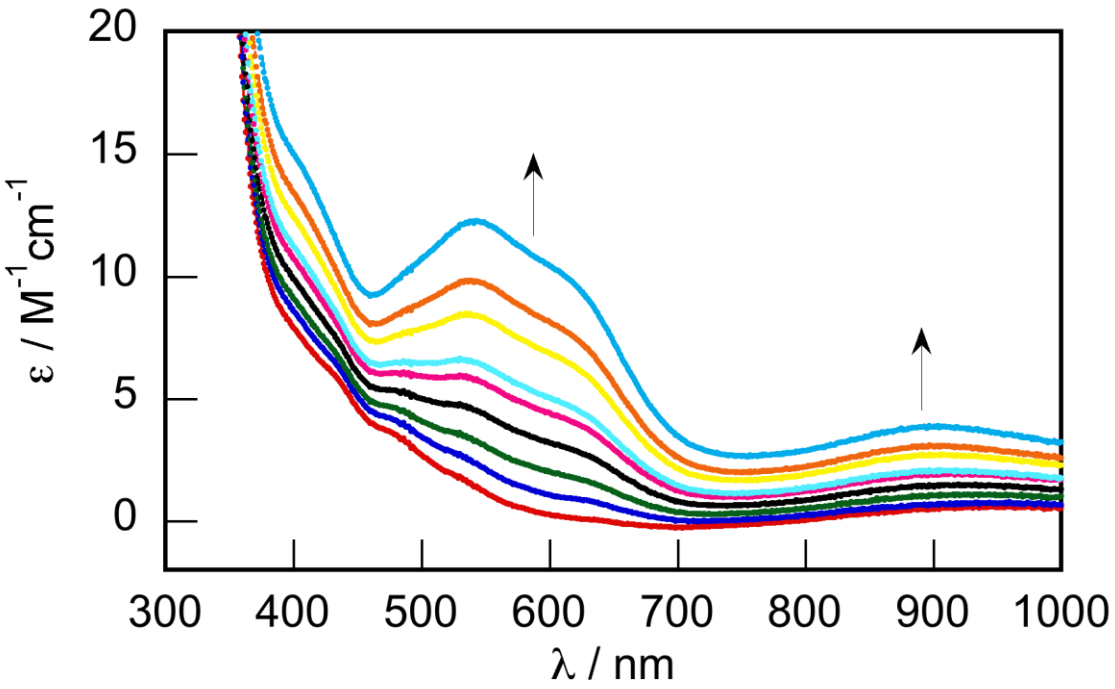

Figure 1.9. Electronic absorption spectrum of 23.5 mM of **4** in 0.1 Bu_4NPF_6 in acetonitrile upon electrochemical reduction at a platinum gauze electrode.

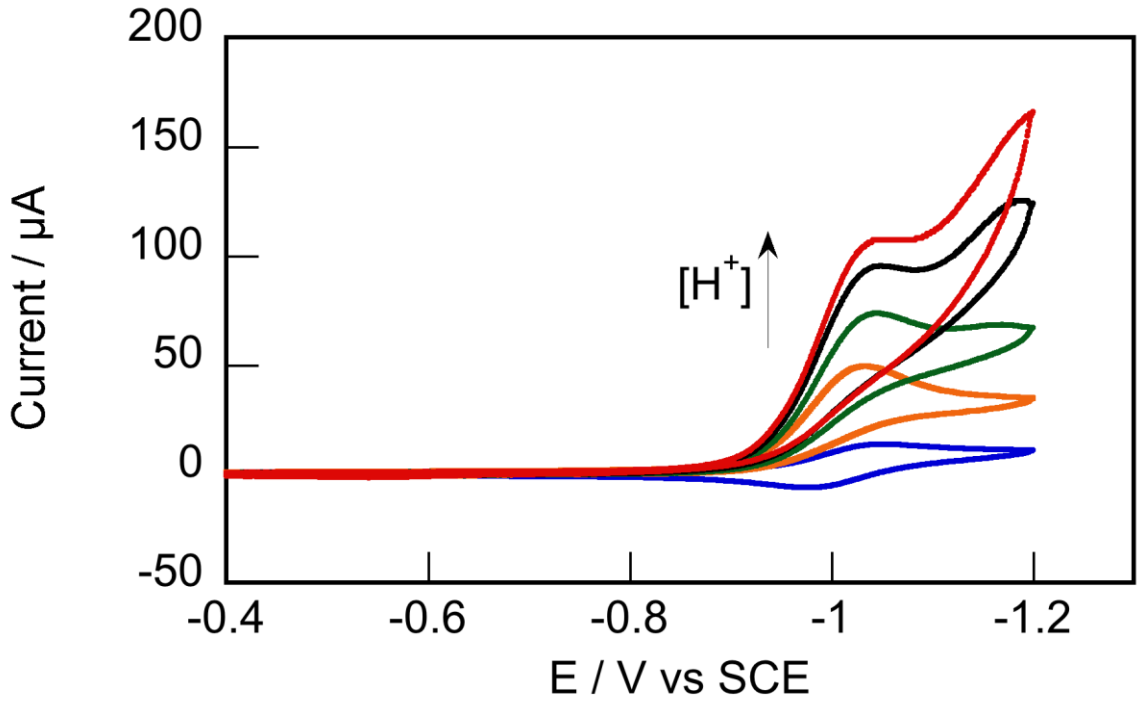

Figure 1.10. Cyclic voltammograms of complex **4** in 0.1 M KNO_3 in 1:1 water:acetonitrile in the presence of TFA: (bottom-top) 1.0 mM **4** with no acid, 1.3 mM TFA, 2.6 mM TFA, 3.9 mM TFA, and 5.2 mM TFA. Scan rate: 100 mV/sec; glassy carbon electrode.

Table 1.1. Crystallographic Details for **4**-**5**.

	4	**5**
Empirical Formula	$C_{30}H_{32}CoF_{12}N_6O_2P_2$	$C_{24}H_{21}F_{12}N_5OP_2Zn$
Formula Weight	857.49	750.77
T (K)	136	143
λ (Å)	0.71073	0.71073
Crystal System	Monoclinic	Monoclinic
Space Group	$P2_1/c$	$P2_1/n$
a (Å)	11.9665(12)	14.0273(77)
b (Å)	11.8487(12)	13.6709(75)
c (Å)	25.024(2)	16.2887(89)
α (º)	90	90
β (º)	90.723(2)	110.767(6)
γ (º)	90	90
V	3547.8(6)	2921(3)
Z	4	4
ρ_{calc} (g/cm^3)	1.605	1.707
μ (mm^{-1})	0.676	1.057
reflctns collected	19864	11717
T_{min}/T_{max}	0.91	0.81
data/restr/params	7232/0/480	4635/0/410
$2\theta_{max}$ (º)	52.8	48.9
R, R_w (%; I>2σ)	5.2, 13.3	6.4, 18.5
GOF	1.05	1.08
max shift/error	0.004	0.004

Table 1.2. Co electrocatalysts for proton reduction in aqueous media compared to the reported acetonitrile-based system. * = 2+/1+; # = 3+/2+; $ = 1+/0; E_{cpe} = potential of controlled potential electrolysis. HDME = hanging drop mercury electrode; GC = glassy carbon.

Complex	E^o (SCE)	E_{cpe} (SCE)	Medium	% H2 yield	Electrode	TOF	Reference
CoTMAP	-0.66*	-0.95	0.1 M TFA	>90	Hg pool	ca. 2hr-1	[48]
CoTMPyP	-0.75*	-0.95	0.1 M TFA	>90	Hg pool	ca. 2hr-1	"
CoTPyP		-0.95	0.1 M TFA	>90	Hg pool	ca. 2hr-1	"
$Co(C_5H_5CO_2H)_2]+$	-0.87#	-0.9	0.1 M KCl, phosphate buffer, pH 6.5	42	Hg pool	1.1hr-1	[77]
Co(sepulchrate)]3+	-0.54#	-0.7	0.1 M KCl, phthalate buffer, pH 4.0	55	Hg pool	0.85hr-1	"
Co(6,13-dimethyl-4,11-diene-N_4)]2+	ca -1.5*	-1.5	0.1 M KNO_3	90	Hg pool	9hr-1	[47]
Co(4,11-diene-N_4)]2+	ca -1.6*	-1.6	0.1 M KNO_3	93	Hg pool	7.8hr-1	"
Co(trans-diammac)]3+	-0.8#	-1.05	Phosphate pH 7		Hg pool/HDME	<1hr-1	[46]
Co(cis-diammac)]3+	-0.67#	-1.05	Phosphate pH 7		Hg pool/HDME	<1hr-1	"
$CpCo(P(OMe)_3)_2$	-0.32$	-1.15	pH 5	100	Hg pool	1.1hr-1	[54]
Cobis(triazacyclodecane)]3+	ca. -0.7#, -1.55*		Britton-Robinson buffer, pH 2.7-10.3		HDME		[78]
Co(dimethylglyoxime)	-0.55*	-0.72	Acetonitrile/TFA	ca 100	Carbon	20hr-1	[20]
CoPY4]2+	-0.9*, +0.87#	-1.0	Acetonitrile/TFA	99	Carbon	ca. 40hr-1	this work

References

(1) Lewis, N. S.; Nocera, D. G. *Proceedings of the National Academy of Sciences* **2006**, *103*, 15729-15735.
(2) Turner, J. A. *Science* **2004**, *305*, 972-974.
(3) Armstrong, F. A. *Current Opinion in Chemical Biology* **2004**, *8*, 133-140.
(4) Frey, M. *ChemBioChem* **2002**, *3*, 153-160.
(5) Garcin, E.; Vernede, X.; Hatchikian, E. C.; Volbeda, A.; Frey, M.; Fontecilla-Camps, J. C. *Structure* **1999**, *7*, 557-566.
(6) Peters, J. W.; Lanzilotta, W. N.; Lemon, B. J.; Seefeldt, L. C. *Science* **1998**, *282*, 1853-1858.
(7) Shima, S.; Pilak, O.; Vogt, S.; Schick, M.; Stagni, M. S.; Meyer-Klaucke, W.; Warkentin, E.; Thauer, R. K.; Ermler, U. *Science* **2008**, *321*, 572-575.
(8) Canaguier, S.; Artero, V.; Fontecave, M. *Dalton Transactions* **2008**, 315-325.
(9) Darensbourg, M. Y.; Lyon, E. J.; Zhao, X.; Georgakaki, I. P. *Proceedings of the National Academy of Sciences of the United States of America* **2003**, *100*, 3683-3688.
(10) DuBois, M. R.; DuBois, D. L. *Chemical Society Reviews* **2009**, *38*, 62-72.
(11) Esswein, A. J.; Nocera, D. G. *Chemical Reviews* **2007**, *107*, 4022-4047.
(12) Evans, D. J.; Pickett, C. J. *Chemical Society Reviews* **2003**, *32*, 268-275.
(13) Gloaguen, F.; Rauchfuss, T. B. *Chemical Society Reviews* **2009**, *38*, 100-108.
(14) Koelle, U. *New journal of chemistry(1987)* **1992**, *16*, 157-169.
(15) Sun, L.; Åkermark, B.; Ott, S. *Coordination Chemistry Reviews* **2005**, *249*, 1653-1663.
(16) Artero, V.; Chavarot-Kerlidou, M.; Fontecave, M. *Angewandte Chemie International Edition* **2011**, *50*, 7238-7266.
(17) Baffert, C.; Artero, V.; Fontecave, M. *Inorganic Chemistry* **2007**, *46*, 1817-1824.
(18) Dempsey, J. L.; Brunschwig, B. S.; Winkler, J. R.; Gray, H. B. *Accounts of Chemical Research* **2009**, *42*, 1995-2004.
(19) Hu, X.; Brunschwig, B. S.; Peters, J. C. *Journal of the American Chemical Society* **2007**, *129*, 8988-8998.
(20) Hu, X.; Cossairt, B. M.; Brunschwig, B. S.; Lewis, N. S.; Peters, J. C. *Chemical Communications* **2005**, *2005*, 4723-4725.
(21) Lazarides, T.; McCormick, T.; Du, P.; Luo, G.; Lindley, B.; Eisenberg, R. *Journal of the American Chemical Society* **2009**, *131*, 9192-9194.
(22) McCrory, C. C. L.; Uyeda, C.; Peters, J. C. *Journal of the American Chemical Society* **2012**, *134*, 3164-3170.
(23) McNamara, W. R.; Han, Z.; Alperin, P. J.; Brennessel, W. W.; Holland, P. L.; Eisenberg, R. *Journal of the American Chemical Society* **2011**, *133*, 15368-15371.
(24) Pantani, O.; Naskar, S.; Guillot, R.; Millet, P.; Anxolabéhère-Mallart, E.; Aukauloo, A. *Angewandte Chemie International Edition* **2008**, *47*, 9948-9950.
(25) Razavet, M.; Artero, V.; Fontecave, M. *Inorganic Chemistry* **2005**, *44*, 4786-4795.
(26) Singh, W. M.; Baine, T.; Kudo, S.; Tian, S.; Ma, X. A. N.; Zhou, H.; DeYonker, N. J.; Pham, T. C.; Bollinger, J. C.; Baker, D. L.; Yan, B.; Webster, C. E.; Zhao, X. *Angewandte Chemie International Edition*, n/a-n/a.
(27) Stubbert, B. D.; Peters, J. C.; Gray, H. B. *Journal of the American Chemical Society* **2011**, *133*, 18070-18073.

(28) Sun, Y.; Bigi, J. P.; Piro, N. A.; Tang, M. L.; Long, J. R.; Chang, C. J. *Journal of the American Chemical Society* **2011**, *133*, 9212-9215.
(29) Anxolabehere-Mallart, E.; Costentin, C.; Fournier, M.; Nowak, S.; Robert, M.; Saveant, J.-M. *Journal of the American Chemical Society* **2012**, *134*, 6104-6107.
(30) Aziz Fihri, V. A. M. R. C. B. W. L. M. F. *Angewandte Chemie International Edition* **2008**, *47*, 564-567.
(31) Connolly, P.; Espenson, J. H. *Inorganic Chemistry* **1986**, *25*, 2684-2688.
(32) Du, P.; Knowles, K.; Eisenberg, R. *Journal of the American Chemical Society* **2008**, *130*, 12576-12577.
(33) Appel, A. M.; DuBois, D. L.; Rakowski DuBois, M. *Journal of the American Chemical Society* **2005**, *127*, 12717-12726.
(34) Felton, G. A. N.; Vannucci, A. K.; Chen, J.; Lockett, L. T.; Okumura, N.; Petro, B. J.; Zakai, U. I.; Evans, D. H.; Glass, R. S.; Lichtenberger, D. L. *Journal of the American Chemical Society* **2007**, *129*, 12521-12530.
(35) Gloaguen, F.; Lawrence, J. D.; Rauchfuss, T. B. *Journal of the American Chemical Society* **2001**, *123*, 9476-9477.
(36) Keita, B.; Floquet, S.; Lemonnier, J.-F.; Cadot, E.; Kachmar, A.; Benard, M.; Rohmer, M.-M.; Nadjo, L. *The Journal of Physical Chemistry C* **2008**, *112*, 1109-1114.
(37) Li, P.; Wang, M.; Pan, J.; Chen, L.; Wang, N.; Sun, L. *Journal of Inorganic Biochemistry* **2008**, *102*, 952-959.
(38) Mejia-Rodriguez, R.; Chong, D.; Reibenspies, J. H.; Soriaga, M. P.; Darensbourg, M. Y. *Journal of the American Chemical Society* **2004**, *126*, 12004-12014.
(39) Sascha Ott, M. K., Bjorn Akermark, Licheng Sun, and Reiner Lomoth *Angewandte Chemie International Edition* **2004**, *43*, 1006-1009.
(40) Tard, C.; Liu, X.; Ibrahim, S. K.; Bruschi, M.; De Gioia, L.; Davies, S. C.; Yang, X.; Wang, L. S.; Sawers, G.; Pickett, C. J. *Nature* **2005**, *433*, 610-613.
(41) James, T. L.; Cai, L.; Muetterties, M. C.; Holm, R. H. *Inorganic Chemistry* **1996**, *35*, 4148-4161.
(42) Wright, R. J.; Lim, C.; Tilley, T. D. *Chemistry – A European Journal* **2009**, *15*, 8518-8525.
(43) Wright, R. J.; Zhang, W.; Yang, X.; Fasulo, M.; Tilley, T. D. *Dalton Transactions* **2012**, *41*, 73-82.
(44) Bhugun, I.; Lexa, D.; Saveant, J.-M. *Journal of the American Chemical Society* **1996**, *118*, 3982-3983.
(45) Bakac, A.; Brynildson, M. E.; Espenson, J. H. *Inorganic Chemistry* **1986**, *25*, 4108-4114.
(46) Bernhardt, P. V.; Jones, L. A. *Inorganic Chemistry* **1999**, *38*, 5086-5090.
(47) Fisher, B. J.; Eisenberg, R. *Journal of the American Chemical Society* **1980**, *102*, 7361-7363.
(48) Kellett, R. M.; Spiro, T. G. *Inorganic Chemistry* **1985**, *24*, 2373-2377.
(49) Kellett, R. M.; Spiro, T. G. *Inorganic Chemistry* **1985**, *24*, 2378-2382.
(50) Collin, J. P.; Jouaiti, A.; Sauvage, J. P. *Inorganic Chemistry* **1988**, *27*, 1986-1990.
(51) Oudart, Y.; Artero, V.; Pecaut, J.; Fontecave, M. *Inorganic Chemistry* **2006**, *45*, 4334-4336.

(52) Wilson, A. D.; Newell, R. H.; McNevin, M. J.; Muckerman, J. T.; Rakowski DuBois, M.; DuBois, D. L. *Journal of the American Chemical Society* **2006**, *128*, 358-366.
(53) Koelle, U.; Infelta, P. P.; Graetzel, M. *Inorganic Chemistry* **1988**, *27*, 879-883.
(54) Koelle, U.; Paul, S. *Inorganic Chemistry* **1986**, *25*, 2689-2694.
(55) Goldsmith, C. R.; Cole, A. P.; Stack, T. D. P. *Journal of the American Chemical Society* **2005**, *127*, 9904-9912.
(56) Goldsmith, C. R.; Jonas, R. T.; Cole, A. P.; Stack, T. D. P. *Inorganic Chemistry* **2002**, *41*, 4642-4652.
(57) Goldsmith, C. R.; Jonas, R. T.; Stack, T. D. P. *Journal of the American Chemical Society* **2002**, *124*, 83-96.
(58) Goldsmith, C. R.; Stack, T. D. P. *Inorganic Chemistry* **2006**, *45*, 6048-6055.
(59) Jonas, R. T.; Stack, T. D. P. *Journal of the American Chemical Society* **1997**, *119*, 8566-8567.
(60) Klein Gebbink, R. J. M.; Jonas, R. T.; Goldsmith, C. R.; Stack, T. D. P. *Inorganic Chemistry* **2002**, *41*, 4633-4641.
(61) Roelfes, G.; Vrajmasu, V.; Chen, K.; Ho, R. Y. N.; Rohde, J. U.; Zondervan, C.; la Crois, R. M.; Schudde, E. P.; Lutz, M.; Spek, A. L.; Hage, R.; Feringa, B. L.; Munck, E.; Que, L., Jr. *Inorganic Chemistry* **2003**, *42*, 2639-2653.
(62) Vries, M. E.; Crois, R. M. L.; Roelfes, G.; Kooijman, H.; Spek, A. L.; Hage, R.; Feringa, B. L. *Chemical Communications* **1997**, *1997*, 1549-1550.
(63) Wasylenko, D. J.; Palmer, R. D.; Schott, E.; Berlinguette, C. P. *Chemical Communications* **2012**, *48*, 2107-2109.
(64) Andrieux, C. P.; Blocman, C.; Dumas-Bouchiat, J. M.; M'Halla, F.; Sav√©ant, J. M. *Journal of Electroanalytical Chemistry and Interfacial Electrochemistry* **1980**, *113*, 19-40.
(65) Bard, A. J.; Faulkner, L. R. *Electrochemical Methods: Fundamentals and Applications, 2nd ed.*; John Wiley & Sons: New York, 2001.
(66) Delahay, P.; Stiehl, G. L. *Journal of the American Chemical Society* **1952**, *74*, 3500-3505.
(67) Nicholson, R. S.; Shain, I. *Analytical Chemistry* **1964**, *36*, 706-723.
(68) Saveant, J. M.; Vianello, E. *Electrochimica Acta* **1965**, *10*, 905-920.
(69) Saveant, J. M.; Vianello, E. *Electrochimica Acta* **1967**, *12*, 629-646.
(70) Evans, D. F. *Journal of the Chemical Society (Resumed)* **1959**, 2003-2005.
(71) Connelly, N. G.; Geiger, W. E. *Chemical Reviews* **1996**, *96*, 877-910.
(72) Sheldrick, G. M.; Bruker AXS Inc.: Madison, WI, 2005.
(73) Sheldrick, G. M. *Acta Crystallographica Section A* **1990**, *46*, 467-473.
(74) Sheldrick, G. M.; University of Gottingen: Gottingen, Germany, 1997.
(75) Sheldrick, G. M. *Acta Crystallographica Section A* **2008**, *64*, 112-122.
(76) Dorta, R.; Konstantinovski, L.; Shimon, Linda J. W.; Ben-David, Y.; Milstein, D. *European Journal of Inorganic Chemistry* **2003**, *2003*, 70-76.
(77) Houlding, V.; Geiger, T.; Kolle, U.; Gratzel, M. *Journal of the Chemical Society, Chemical Communications* **1982**, 681-683.
(78) Abdel-Hamid, R.; El-Sagher, H. M.; Abdel-Mawgoud, A. M.; Nafady, A. *Polyhedron* **1998**, *17*, 4535-4541.

Chapter 2
A High-Spin Iron(IV)-Oxo Complex Supported by a Trigonal Nonheme Pyrrolide Platform

Introduction

Iron centers supported by heme and non-heme ligands are potent oxidants in natural and synthetic systems.[1] In particular, non-heme iron(IV)-oxo intermediates are implicated in a diverse array of important biological oxidation processes, including hydroxylation, desaturation, ring-closing, and halogenation reaction pathways.[2-7] Interestingly, whereas iron(IV)-oxo species proposed as active oxidants in these aforementioned reactions possess high-spin, S = 2 ground states, the vast majority of synthetic iron(IV)-oxo complexes reside in intermediate-spin, S = 1 ground states.[8-30] Indeed, synthetic high-spin iron(IV)-oxo complexes remain rare and are limited to seminal contributions by Bakac, Que, and Borovik.[31-34] As such, the identification and characterization of new iron-oxo species, particularly with high-spin ground states, is of fundamental interest in elucidating underlying principles of their reactivity.

To meet this goal, we have initiated a program aimed at studying basic aspects of electronic structure, magnetism, and reactivity at synthetic iron centers[35-38], with recent efforts focusing on hybrid ligand architectures that combine features of both heme and non-heme systems.[35,37-43] We now report the generation, spectroscopic characterization, and reactivity of a new high-spin iron(IV)-oxo complex supported by a three-fold symmetric pyrrolide platform. A combination of mass spectrometry, UV-vis, FTIR, Mössbauer, XAS, and parallel-mode EPR measurements provides a coherent picture for this rare synthetic S = 2 ferryl system, and preliminary reactivity studies show that this species is capable of intermolecular C-H oxidation and oxygen-atom transfer chemistry.

Results and Discussion

Oxidation of [(tpa^{Mes})Fe]$^{-}$ Provides the Corresponding Fe^{III}-Alkoxide Complex

Previous work from our laboratory described N_2O activation and intra- and intermolecular C-H oxidation reactivity with iron complexes supported by three-fold symmetic tpa^{Ar} ligands (tpa^{Ar} = tris(5-arylpyrrol-2-ylmethyl)amine) and suggested the involvement of a putative iron(IV)-oxo species.[35] We sought to identify and characterize discrete ferryl intermediates in this platform and initial experiments centered on oxygen atom transfer reactions to the mesityl derivative [(tpa^{Mes})Fe^{II}]$^{-}$ (**1**). In contrast to the intermolecular oxidation reactivity observed in ethereal solvents with relatively weak C-H bonds (THF, DME, etc) to give the iron(III)-hydroxide complex [(tpa^{Mes})Fe^{III}(OH)]$^{-}$ (**2**) after oxygen transfer and subsequent hydrogen atom abstraction chemistry,[35] treatment of **1** with trimethylamine *N*-oxide in the more oxidatively robust solvent acetonitrile exclusively affords the iron(III)-alkoxide product [(tpa^{Mes2MesO})Fe^{III}]$^{-}$ (**3**) resulting from intramolecular benzylic C-H oxidation of one of the pendant mesityl arms (Scheme 2.1, Figure 2.1). We identified the iron(III)-alkoxide product by mass spectrometry and the Mössbauer spectrum of a frozen solution of the reaction mixture at 100 K displayed a single iron(III) product with δ = 0.32 mm/sec and ΔE_q = 0.88 mm/sec (Figure 2.2). No intermediates were observed in the conversion from **1** to **3** at a variety of different temperatures. Moreover, ^{1}H NMR and LC/MS analysis of the free tpa ligand isolated after demetalation confirmed ligand oxidation and desymmetrization (Figure 2.3).

Oxidation of [(tpa^{Mes})FeOH]$^{-}$ Also Provides the Fe^{III}-Alkoxide Product

Inspired by elegant work from Borovik showing that a hydrogen-bond stabilized iron(IV)-oxo species could be obtained by oxidation of an iron(III)-hydroxide

precursor,[34] we attempted to treat our iron(III)-hydroxide complex **2** with outer-sphere oxidants, as the cyclic voltammogram of this species shows an irreversible electrochemical oxidation process at reasonable potentials (Figure 2.4). However, even at temperatures as low as -60 ºC, reactions of **2** with oxidants like ferrocenium hexafluorophosphate produced the same iron(III) alkoxide **3** directly with no observable Fe(IV) intermediates (Figure 2.5, Scheme 2.1).

Oxidation of [(tpa^{Ph})Fe]$^{-}$ Yields the Corresponding Fe^{IV}-Oxo Complex

Undeterred, we turned our attention to the related phenyl derivative [(tpa^{Ph})Fe]$^{-}$ (**4**) to pursue high-valent ferryl species. We reasoned that the aryl C-H bonds on the pendant phenyl groups of this ligand would be comparatively less reactive than their benzylic C-H counterparts on tpa^{Mes} and thus enhance the stability of potential high-valent iron species prone to decomposition by C-H functionalization.[44] Indeed, upon oxidation of **4** with trimethylamine *N*-oxide in acetonitrile solution at -40 ºC, we observe the appearance of a new species **5** with a strong absorption band at 400 nm and a weaker absorption feature centered around 900 nm; the latter peak is reminiscent of the near-IR absorptions that are characteristic of synthetic iron(IV)-oxo complexes (Figure 2.6).[21] Importantly, the conversion of **4** to **5** proceeds with clean isosbestic behavior. The spectrum of **5** remains unchanged for hours when kept at -40 ºC and at concentrations near 0.5 mM. However, more concentrated solutions of **5** (ca. 10 mM) decompose with a half-life of approximately one hour, which to date has precluded isolation of solid samples of **5**. Nevertheless, identification of **5** as an iron(IV)-oxo complex comes from electrospray mass spectrometry on a cold acetonitrile solution of this species, where the most prominent signal in the spectrum has an *m/z* value of 551.151 that is consistent with the value expected for the iron(IV)-oxo complex [(tpa^{Ph})Fe(O)]$^{-}$ (predicted *m/z* = 551.153) (Figures 2.7 and 2.8). Moreover, within seconds, the most prominent signal shifts to an *m/z* value of 550.147, corresponding to the previously reported iron(III)-phenoxide complex [(tpa^{Ph2PhO})Fe^{III}]$^{-}$ (**6**) (predicted *m/z* = 550.146) produced from intramolecular aryl C-H oxidation (Figures 2.9 and 2.10, Scheme 2.1).

Spectroscopic Characterization of the Fe^{IV}-Oxo Complex: Identifying the Ferryl Chromophore and Fe(IV) Oxidation State

With the aforementioned result in hand, we proceeded to characterize this new iron(IV)-oxo complex using a variety of spectroscopic methods. Our findings from FTIR, Mössbauer, and XAS/EXAFS experiments are summarized as follows.

FTIR Spectroscopy. First, *in situ* react-IR spectroscopy of **5** generated from reaction of **4** with trimethylamine *N*-oxide in acetonitrile solution at -35 ºC showed a new band at 850 cm^{-1}, which shifted to 814 cm^{-1} upon ^{18}O labeling (Figure 2.11). We assign this band to an Fe=O vibration on the basis of agreement with the shift expected for a harmonic Fe-O oscillator model (38 cm^{-1}) and with the values reported for the related TMG_3tren and H_3buea ferryl systems.[32,34,45]

Mössbauer Spectroscopy. The Mössbauer spectrum of a frozen solution of 5 at 4.2 K showed a single iron-containing product with parameters consistent with iron(IV) with δ = 0.09 mm/sec and ΔE_q = 0.51 mm/sec (Figure 2.12). In particular, the near zero isomer shift is characteristic of an Fe(IV) oxidation state and is in close agreement with other ferryl species in the literature.[21,31,32,34]

XAS/EXAFS. The Fe K-edge X-ray absorption spectrum of a frozen acetonitrile solution of **5** shows an edge energy of 7122.0 eV (at F/I_0 = 0.5), which represents a shift

of 3.2 eV as compared to **4**, and is consistent with an oxidation of Fe(II) to Fe(IV) (Figure 2.13 left). The pre-edge region in **4** possesses two features at 7110.9 and 7112.5, with areas of 19.7 and 2.7 units, respectively (Figure 2.14 and Table 2.1). Such a pre-edge splitting has been observed previously in the case of iron complexes in C_{3v} geometries[46] and is explained by the non-centrosymmetric nature of the coordination environment as observed in **4**. Upon oxidation to **5**, the pre-edge region shows a strong main feature at 7112.3 eV, which is best fit with two components at 7112.3 and 7114.0 eV, with areas of 28.0 and 4.3 units, respectively (Figure 2.15 and Table 2.1). The presence of two peaks in this pre-edge is in agreement with the observations made by England *et al.* on a S = 2 Fe(IV)-oxo complex[32] and is theoretically explained by a splitting of the α and β d_z^2 orbitals.[47]

The first shell of the EXAFS Fourier transform of **4** was fit with four scatterers at 2.03 Å from the iron(II) center (Table 2.2), corresponding to an average of the equatorial and axial N ligands. The EXAFS of **5** could be fit with similar parameters, using four paths at 1.99 Å. However, the fit quality was significantly improved (as seen from the decrease in R factor and reduced χ^2 values) by adding a Fe-O path at 1.62 Å (Figure 2.13 right and Table 2.2). The contribution of this Fe-O vector is not seen as a separated peak in the Fourier transform due to its interaction with the four scatterers at 1.99 Å. The 1.62 Å scatterer observed in **5** is attributed to the oxygen of a newly formed Fe-O bond, the distance being in line with that of previously reported S = 2 Fe(IV)-oxo compounds.[32-34]

Parallel-Mode EPR Spectroscopy Reveals a High-Spin *S = 2* Fe^{IV}-Oxo Complex

With information on the iron-oxo chromophore and iron(IV) oxidation state in hand, we proceeded to examine the magnetic properties of this new ferryl species by EPR. Parallel-mode X-band EPR spectra of **5** acquired below 8 K possess almost no intensity (Figure 2.16). As the temperature increased, however, a broad derivative-shaped feature centered at g = 8.5 grows in, which is distinct from spectral features corresponding to either **4** or **6** (cf. Figures 2.16, 2.17, 2.18, and 2.19). Such behavior is consistent with **5** being a S = 2 system with a positive axial zero-field splitting constant D. The temperature-dependence of the intensity of this derivative feature is best fit using a value of D = +4.3 cm^{-1}. The field position of this resonance and the asymmetry of the corresponding lineshape are diagnostic of the central value and distribution of the rhombic zero-field splitting term E. All EPR spectral features and their corresponding temperature dependence are well-simulated using a S = 2 spin system with g = 2, D = +4.3 cm^{-1}, E/D = 0.098 and $\sigma_{E/D}$ = 0.02 (Figures 2.16 and 2.19). This value of D is very similar to that found for other high-spin Fe(IV) oxo species with trigonal bipyramidal ligand sets (D = 4.0 cm^{-1} for H_3buea;[34] 5.0 cm^{-1} for TMG_3tren;[32] and 10.0 cm^{-1} TauD-J)[48]. The spectral fit requires a rather large linewidth (8 mT) and distribution in E ($\sigma_{E/D}$, one standard deviation in the E/D ratio) compared to those determined for Fe(IV)O[H_3buea]$^-$.[34] This behavior reflects a distribution in the precise electronic-structure description of **5** that likely results from increased disorder of the phenyl groups on the tpa ligand relative to the urealato groups of [H_3buea]$^{3-}$ which can hydrogen bond to the ferryl-oxo.

To further confirm the electronic structure, spectra were calculated for an intermediate, S = 1, spin system. However, no single parameter set was found that correctly modeled both the line shape and field position of the observed resonance signal. Furthermore, to the best of our knowledge, there are no examples in the literature of $3d^4$

complexes with trigonal bipyramidal ligand field symmetry that have been characterized as $S = 1$ spin systems. A dramatic distortion in the trigonal ligand field would be required to produce this state, one that is not supported by the EXAFS data (*vide supra*). With the $S = 1$ formulation of **5** ruled out on this basis, and in concert with the combined data from a suite of other spectroscopic measurements we assign **5** as being a high-spin, $S = 2$ iron(IV)-oxo complex.

Preliminary Reactivity Studies Establish that the tpa-Supported Ferryl Can Participate in C-H Abstraction and Oxygen-Atom Transfer Chemistry

Finally, preliminary reactivity studies of high-spin ferryl **5** are consistent with the presence of a reactive yet sterically shielded iron-oxo unit, which is expected for this complex bearing a bulky ancillary ligand. For example, **5** fails to react with oxygen atom acceptors ranging from cyclooctene to thioanisole to triphenylphosphine. In contrast, **5** reacts rapidly upon mixing with the smaller phosphine PMe_2Ph to produce the phosphine oxide in 89 % yield (Figure 2.20). In addition, a 3.0 mM acetonitrile solution of **5** reacts rapidly with 1,4-cyclohexadiene (CHD) to produce benzene (90 % yield) with a second-order rate constant of 1.4 $M^{-1}s^{-1}$ at -30 ºC, showing that ferryl **5** is capable of intermolecular hydrogen atom transfer (HAT) chemistry (Figures 2.21 and 2.22). The steric demands on **5** preclude reactivity with other hydrogen atom donors such as 9,10-dihydroanthracene (DHA) or xanthene despite their weaker C-H bond strengths compared to CHD. As such, current efforts are aimed at reducing the steric crowding at the iron-oxo unit with the hope of increasing reactivity with external substrates.

Concluding Remarks

To close, we have presented the generation of a new high-spin iron(IV)-oxo complex, its characterization by a suite of spectroscopic methods, and its ability to participate in intra- and intermolecular C-H oxidation reactions as well as oxygen-atom transfer to a sterically undemanding phosphine. In particular, Mössbauer and XAS measurements establish the presence of an Fe(IV) center for $[(tpa^{Ph})Fe(O)]^-$, FTIR and UV-Vis studies identify the Fe-oxo chromophore, and parallel-mode EPR provides signatures indicative of a high-spin, $S = 2$ system. Taken together, this system adds to the small but growing number of high-spin ferryl complexes in non-heme environments. Ongoing work is geared toward further reactivity studies of high-spin ferryl species in this general manifold, and related group-transfer processes on iron and other first-row transition metals are also under investigation.

Experimental Section

General Synthetic Details. Unless otherwise noted, all synthetic manipulations were performed under an inert atmosphere of dinitrogen in a Vacuum Atmospheres glovebox or on a vacuum line using standard Schlenk technique. Solvents were dried on a Vacuum Atmospheres Solvent purification system and stored over 3 Å molecular sieves. Acetonitrile was further dried by filtering through a plug of basic alumina immediately prior to use. Molecular sieves, alumina, and celite were activated by heating at 200ºC under dynamic vacuum for at least 24 hours. Potassium hydride was purchased as a suspension in mineral oil, washed with pentane and used as a dry solid in the glovebox. 1,4-Cyclohexadiene was degassed with three freeze, pump, thaw cycles and dried over 3

Å molecular sieves. ^{18}O-labeled trimethylamine-*N*-oxide was prepared according to a literature procedure[49] using ^{18}O-labeled hydrogen peroxide (90 % $^{18}O_2$) purchased from Cambridge Isotope Laboratories (Andover, MA). All other reagents were purchased from Sigma-Aldrich and used as received. All glassware was dried by storage in an oven at 170 ºC for at least 12 hours before use. The iron complexes [(tpa^{Mes})Fe][K(dme)$_2$] (**1**), [(tpa^{Mes})FeOH][K(dme)] (**2**) and [(tpa^{Ph})Fe][Na(thf)] (**4**) were prepared according to literature procedures.[35]

Synthesis of [(tpa^{2MesMesO})Fe]K (3). An acetonitrile solution of trimethylamine-*N*-oxide (0.018 g, 0.24 mmol) was added to an acetonitrile solution of [(tpa^{Mes})Fe][K(dme)$_2$] (**1**) (0.047 g, 0.054 mmol) and stirred for three hours. Over the course of thirty minutes the colorless solution turned dark brown. The solvent was then removed *in vacuo* and the resulting brown solid residue was recrystallized by layering a concentrated THF solution of the product under ether to provide clumps of brown crystals of **3**. ESI MS ([**3**-K]$^-$): *m/z* calcd for $C_{42}H_{44}FeN_4O$ 676.2870, found at 676.2849. The oxidized ligand was separated from the metal and isolated by filtering an acetonitrile solution of **3** through a plug of silica and removing the solvent *in vacuo*. LC/MS ([H_3tpa^{2MesMesO}]$^-$): *m/z* calcd for $C_{42}H_{47}N_4O$ 623.38, found at 623.4. ^{1}H NMR spectrum (300 MHz, CD_3CN): δ 9.66 (s, 1H), 9.37 (s, 2H), 7.06 (s, 1H), 6.98 (s, 1H), 6.86 (s, 4H), 6.05 (s, 3H), 5.90 (s, 1H), 5.79 (s, 2H), 4.23 (s, 2H), 3.54 (s, 6H), 2.28 (s, 3H), 2.23 (s, 6H), 2.10 (s, 3H), 2.01 (s, 12H) (Figure 2.3).

Generation of [(tpa^{Ph})FeO]Na (5). An acetonitrile solution of trimethylamine-*N*-oxide (4 equivalents) was added to an acetonitrile solution of [(tpa^{Ph})Fe][Na(thf)] (**4**) at -40 ºC to produce a dark red/brown solution which could be monitored by UV/vis for the characteristic near IR band near 900 nm (ca. 1 – 10 mM). The solutions were immediately frozen at 77K for Mössbauer and XAS experiments (ca. 70 – 100 mM) and EPR samples were prepared similarly using a 1:1 mixture of toluene and acetonitrile as solvent (ca. 1 – 10 mM). Mass spectrometry experiments were performed on thawing acetonitrile solutions (*vide infra*). ESI MS ([**5**-Na]$^-$): *m/z* calcd for $C_{33}H_{27}FeN_4O$ 551.153, found at 551.151 (Figures 2.7 and 2.8).

General Physical Methods. Mass spectrometry measurements were performed on either an LTQ Orbitrap (Thermo Scientific, West Palm Beach, FL) or Waters Q-TOF Premier (Milford, MA) spectrometer at the QB3/Chemistry Mass Spectrometry Facility at UC Berkeley. Elemental analyses were performed on a Perkin Elmer 2400 Series II combustion analyzer (Waltham, MA) in the Microanalytical Laboratory in the College of Chemistry, University of California, Berkeley, California. Cyclic voltammetry experiments were conducted on a BASi Epsilon potentiostat (West Lafayette, IN) using a glassy carbon disc working electrode, a platinum wire auxiliary, and a platinum wire as a floating reference. Potentials were referenced using either ferrocene or cobaltocene as internal standards. *In situ* IR spectra were measured on a Mettler-Toledo ReactIR iC10 instrument (Columbus, OH). ^{1}H NMR spectra were recorded on Bruker spectrometers operating at 300 or 400 MHz as noted. Chemical shifts are reported in ppm and referenced to residual protiated solvent and coupling constants are reported in Hz. UV-vis spectra were acquired on a Varian Cary 50 BIO UV-Visible Spectrophotometer (Agilent Technologies, Santa Clara, CA) with a Unisoko cryostat attachment for temperature control (Unisoku Co, Osaka, Japan).

Mass Spectrometric Detection of 5. The thermally unstable iron(IV)-oxo complex **5** was analyzed using electrospray ionization in negative V mode on a Waters Q-TOF Premier spectrometer. Samples of **5** were generated at -35 ºC as ca. 1 mM acetonitrile solutions, frozen in liquid nitrogen, and introduced into the mass spectrometer as a thawing solution using a syringe pump. ESI source parameters were adjusted as follows: capillary voltage, 0.8 kV; sampling cone voltage, 19 V; source temperature, 60 ºC; desolvation temperature, 40 ºC.

Mössbauer Spectroscopy. Mössbauer spectra were recorded in constant acceleration mode as frozen acetonitrile solutions (ca. 80 – 100 mM) between room temperature and 4.2 K in a Janis Research Co. cryostat (Willmington, MA) and analyzed using the WMOSS software package (See Co, Medina MN). Isomer shifts are reported relative to α-iron (27 μm foil) at room temperature.

X-Ray Absorption Spectroscopy. X-ray data were collected at the Stanford Synchrotron Radiation Lightsource (SSRL) on beamline 7-3 at an electron energy of 3.0 GeV with an average current of 300 mA. The radiation was monochromatized by a Si(220) double-crystal monochromator. The intensity of the incident X-ray was monitored by an N_2-filled ion chamber (I0) in front of the sample. Solution samples were placed in 60 μL plastic sample holders, frozen with liquid nitrogen and collected at 20 K using a helium-cooled cryostat. Data were collected as fluorescence excitation spectra with a Ge 30 element detector (Canberra). Energy was calibrated by the first peak maximum of the first derivative of an iron foil (7111.20 eV). The standard was placed between two N_2-filled ionization chambers (I1 and I2) after the sample. The integrity of the sample upon measurement was assured by the XANES energy shift, and we did not observe any edge shift during the several scans under the current experimental condition.

XAS/EXAFS Data Reduction and Analysis. Pre-edge peaks of **4** and **5** were fit using the EDG_FIT program from the EXAFSPAK suite. (Drs. Graham George and Ingrid Pickering, SSRL) The parameters obtained from the fits are gathered in Table 2.1.

Data reduction of the EXAFS spectra was performed using EXAFSPAK. Pre-edge and post-edge backgrounds were subtracted from the XAS spectra, and the results were normalized with respect to edge height. Background removal in *k*-space was achieved through a five-domain cubic spline. Curve fitting was performed with Artemis and IFEFFIT software using *ab initio*-calculated phases and amplitudes from the program FEFF 8.2.[50,51] These *ab initio* phases and amplitudes were used in the EXAFS equation:

$$\chi(k) = S_0^2 \sum_j \frac{N_j}{kR_j^2} f_{eff_j}(\pi, k, R_j) e^{-2\sigma_j^2 k^2} e^{-2R_j/\lambda_j(k)} \sin(2kR_j + \phi_{ij}(k))$$

The neighboring atoms to the central atom(s) are divided into *j* shells, with all atoms with the same atomic number and distance from the central atom grouped into a single shell. Within each shell, the coordination number N_j denotes the number of neighboring atoms in shell *j* at a distance of R_j from the central atom. $f_{eff_j}(\pi, k, R_j)$ is the *ab initio* amplitude function for shell *j*, and the Debye-Waller term $e^{-2\sigma_j^2 k^2}$ accounts for damping due to static and thermal disorder in absorber-backscatterer distances. The mean free path term $e^{-2R_j/\lambda_j(k)}$ reflects losses due to inelastic scattering, where $\lambda_j(k)$ is the electron mean free path.

The oscillations in the EXAFS spectrum are reflected in the sinusoidal term, $sin(2kR_j + f_{ij}(k))$ where $f_{ij}(k)$ is the *ab initio* phase function for shell *j*. S_0^2 is an amplitude reduction factor due to shake-up/shake-off processes at the central atom(s). The EXAFS equation was used to fit the experimental data using *N*, *R*, and the EXAFS Debye-Waller factor (σ^2) as variable parameters. For the energy (eV) to wave vector (*k*, $Å^{-1}$) axis conversion, E_0 was defined as 7120 eV and the S_0^2 value was fixed to 0.78. EXAFS curve-fitting procedures and the estimation of the uncertainty in the parameters from the fits are described in detail as follows.

EXAFS Curve Fitting Procedure. The best fit parameters for the Fe EXAFS data are summarized in Table 2.2. As a goodness-of-fit index, we used the R-factor (the absolute difference between theory and data), which is defined as the sum of the squares of the differences between each experimental point and the fit normalized to the sum of the squares of the experimental points.[52] In all fits unless specified, N values were set while R and σ^2 values were left floating.

We first carried out a fit for **4**, using the parameters obtained from crystal structure. The EXAFS data are in good agreement with the XRD values. The Fe-N shell at 2.04 Å reflects an average of three equatorial (2.00 Å) and one axial (2.17 Å) N atoms. The Fe-C_1 shell at 2.91 Å reflects an average of the Fe to methylene carbon (2.92 Å) and Fe to pyrrolide proximal carbon (2.85 Å) distances. The Fe-C_2 shell at 3.20 Å reflects a Fe to pyrrolide distal carbon (3.29 Å) pathway with multiple scattering. The Fe-C_3 shell at 4.26 Å corresponds to the distance from Fe to the pyrrolide carbon 4.23 Å away from the Fe center. The 4.26 Å feature arising from the distal pyrrolide ring was absent in the EXAFS spectrum of the S=2 Fe(IV)-O compound reported by England *et al*.[32]

For **5**, the data was at first fit using the same parameters as **4** (Fit #1). A slight contraction of the Fe-N shell to 1.99 Å and the Fe-C_2 shell to 3.02 Å is observed, which is consistent with an oxidation of the iron center. However, by introducing a short Fe-O shell at 1.62 Å, the fit quality improved significantly, as is shown by the decrease of the R-factor and reduced χ^2 values (Fit #2). The Fe-O vector does not appear as a separate peak in the Fourier transform due to its interaction with the Fe-N shell.

EPR Spectroscopy. All continuous-wave parallel-mode ($B_0 \parallel B_1$) X-band (9.38 GHz) EPR spectroscopic characterization was performed at the CalEPR facility at UC Davis using a Bruker ECS 106 spectrometer (Billerica, MA) equipped with an Oxford Instruments ESR900 liquid helium cryostat and a Bruker TE_{102}/TE_{012} dual-mode cavity (ER4116DM). Temperature control was achieved using an Oxford ITC 403 temperature controller. Spectra were collected under slow passage and non-saturating conditions. For all presented data, a corresponding spectrum of the solvent (1:1 acetonitrile/toluene) was subtracted to remove signals from baseline artifacts and paramagnetic contaminants present in the cavity. All spectral simulations were carried out using the EasySpin[53] toolbox for MatLab R2010a (MathWorks, Inc., Natwick, MA).

Parallel-Mode EPR Experiments. At 3 K there is essentially no spectral intensity. Signals grow in with increasing temperature that are indicative of a high-spin ($S = 2$) species with a positive axial zero-field splitting constant *D* (Figure 2.16). At 40 K, a broad derivative-shaped feature is present at $g = 8.5$ and is assigned to the transition between the levels of the $m_S = \pm 2$ doublet (Figure 2.19). A best-fit analysis of the temperature dependence of the intensity of this derivative feature allows for the determination of the magnitude of *D*. Predicted intensities are computed in the following

manner. The energy levels for the system are calculated and then populated according to Boltzmann statistics for a particular temperature. The predicted spectrum is then computed as a function of these populations and doubly integrated to give the total spectral intensity. This is then compared to the experimentally determined spectral intensity. The resonant field position of the derivative feature allows for the determination of the central value in the distribution of *E/D*. All spectral features and their corresponding temperature dependence are well simulated using a $S = 2$ spin system with $g = 2$, $D = +4.3(\pm 0.1)$ cm^{-1}, $E/D = 0.098$ and $\sigma_{E/D} = 0.02$ The 40 K perpendicular-mode spectrum of this sample, shows an intense derivative-shaped feature at $g = 4.3$ that is assigned to the Fe(III)-phenoxy product (Figure 2.18). A small portion of this signal bleeds through to the parallel-mode spectrum due to small misalignments of the B_0 relative to B_1. Notably, the parallel-mode EPR signals described above are distinct from those of the Fe(II) starting complex ($S = 2$), which shows a strong negative feature at $g = 9.50$ (Figure 2.17).

Phosphine-Oxide Yield from the Reaction of 5 with Me_2PPh. The reaction of **5** with an excess of Me_2PPh was performed in an NMR tube and the yield of $Me_2P(O)Ph$ calculated by integration of the ^{31}P NMR resonances relative to PPh_3 as an internal standard. See Figure 2.20 for the spectrum.

Benzene Yield from the Reaction of 5 with 1,4-Cyclohexadiene (CHD). The reaction of **5** with an excess of CHD was performed in an NMR tube and the yield of benzene calculated by integration of the ^1H NMR resonances relative to 1,2,4,5-tetramethylbenzene as an internal standard. See Figure 2.22 for the spectrum.

Kinetics Studies of Reaction of 5 with 1,4-Cyclohexadiene (CHD). A 3.0 mM acetonitrile solution of **4** was prepared in a cuvet in an inert atmosphere glovebox and cooled to -30 ºC in the UV/vis spectrophotometer cryostat. An acetonitrile solution of trimethylamine-*N*-oxide was then added via syringe (four equivalents in ca 0.1 mL) and the formation of **5** was monitored at 900 nm. Once the absorbance of **5** at 900 nm reached a steady value, a pre-cooled (-30 ºC) acetonitrile solution of 10-100 equivalents of CHD was added via syringe and the decay of **5** was monitored at 900 nm holding the temperature at -30 ºC. The resulting decay curves were fit to a single exponential, allowing extraction of observed rate constants. The observed rate constants were then divided by two to account for the stoichiometry of the reaction and plotted against the concentration of CHD; the slope of the resulting line is the second-order rate constant (Figure 2.21).

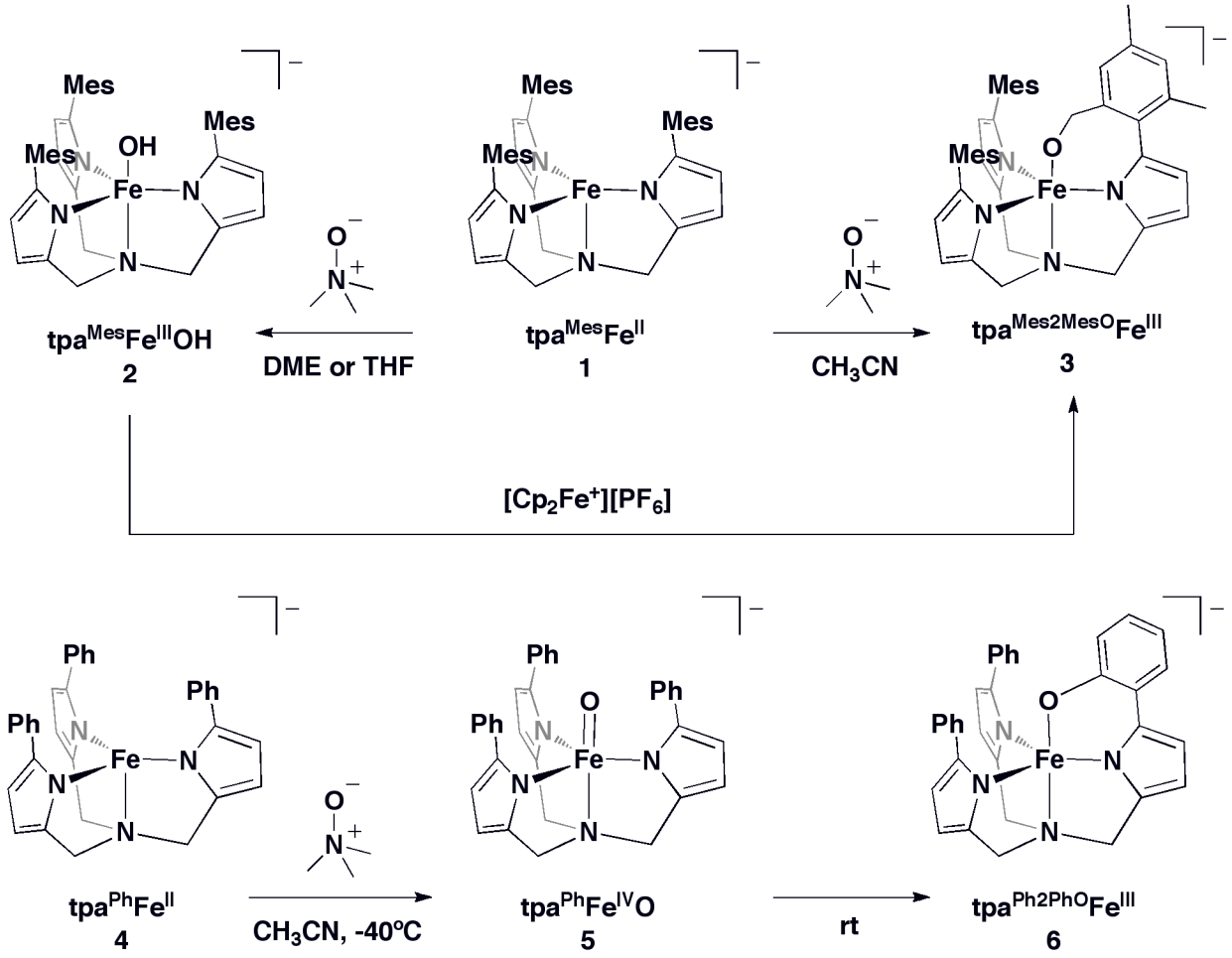

Scheme 2.2. Oxygen atom transfer reactivity and formation of an iron(IV)-oxo species supported by non-heme tpa^{R} ligands

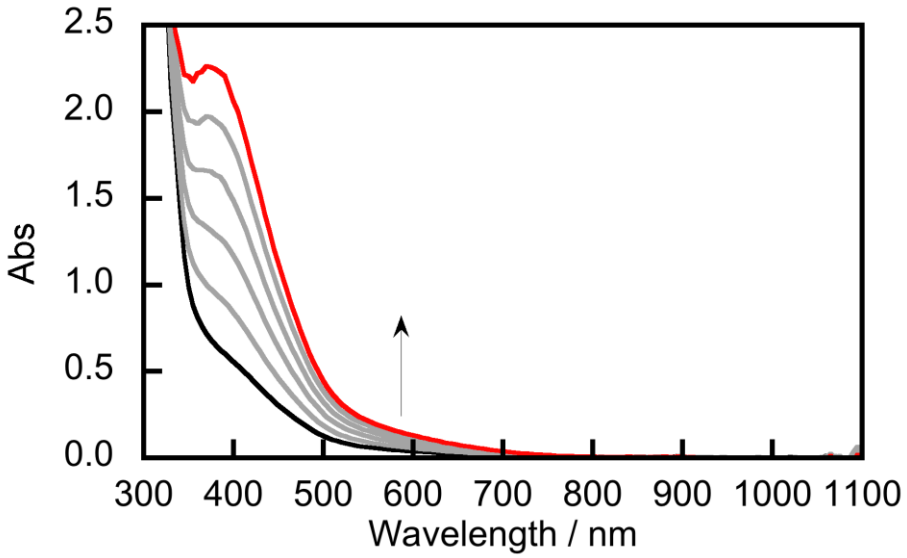

Figure 2.1. UV/vis spectrum of the oxidation of **1** by trimethylamine-*N*-oxide in acetonitrile at -40 ºC

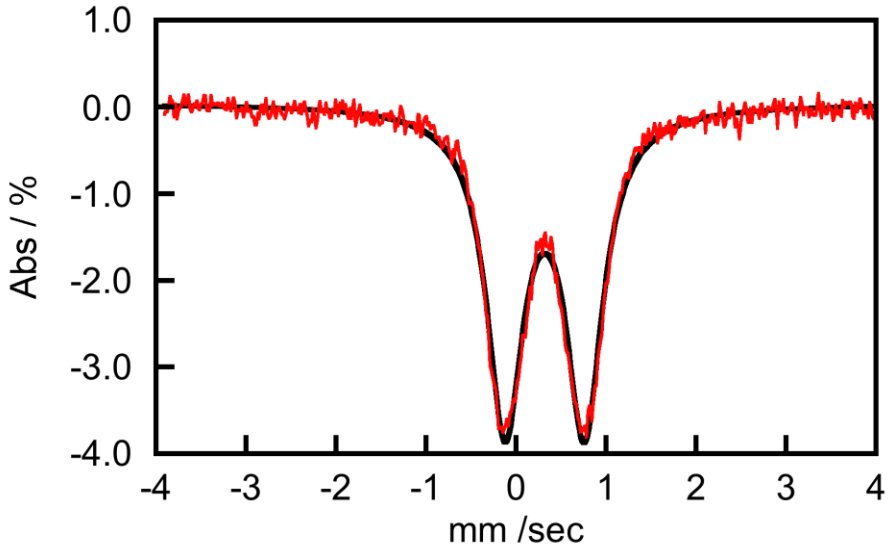

Figure 2.2. 100 K Mössbauer spectrum of the oxidation of **1** with trimethylamine-*N*-oxide at -40 ºC in acetonitrile as a frozen solution (ca. 100 mM). A least squares fit to the data provided the following parameters: ™ = 0.32 mm/sec, $\otimes E_q$ = 0.88 mm/sec.

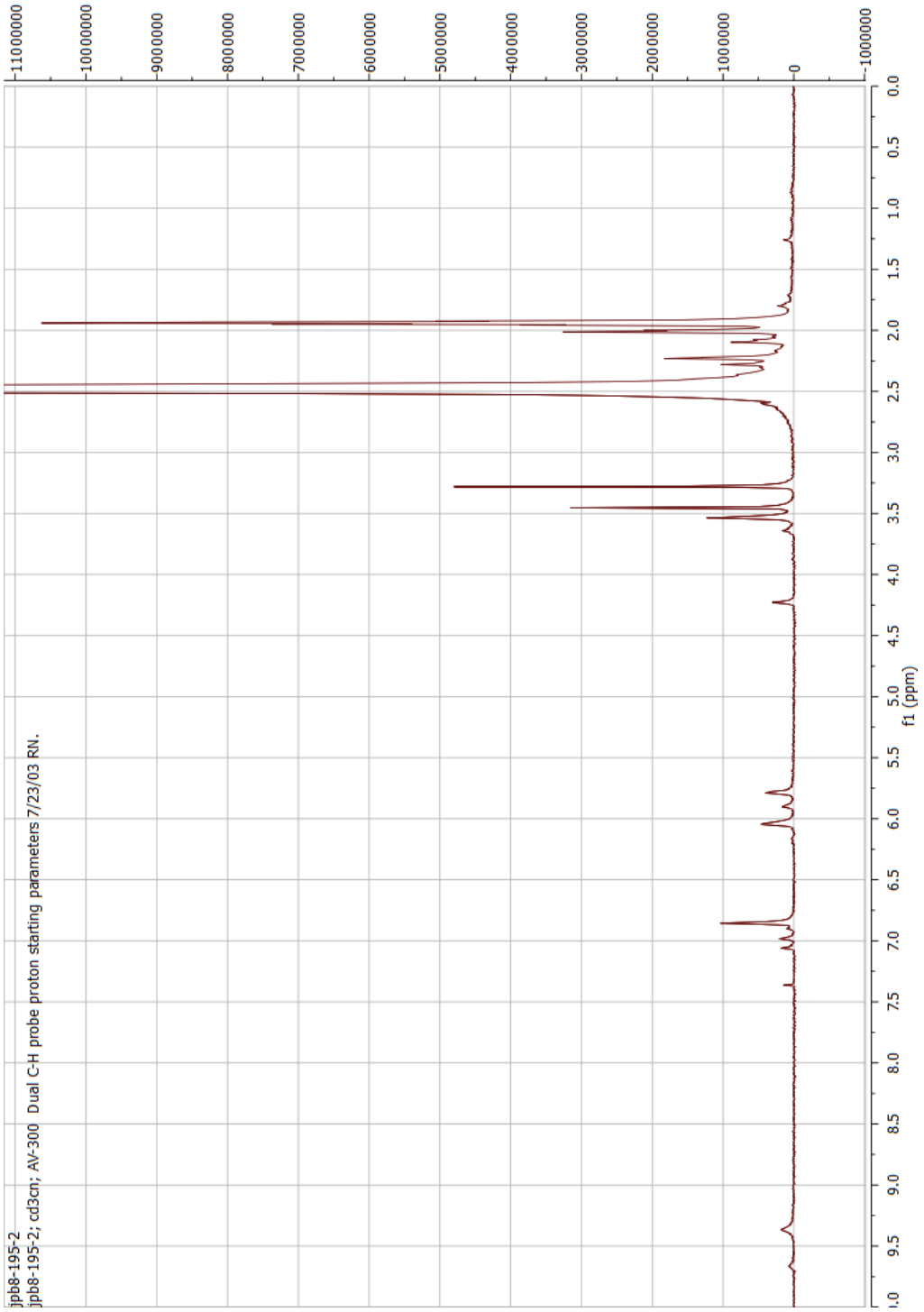

Figure 2.3. ^{1}H NMR spectrum for ligand product after demetallation of **3**. See experimental section for chemical shifts.

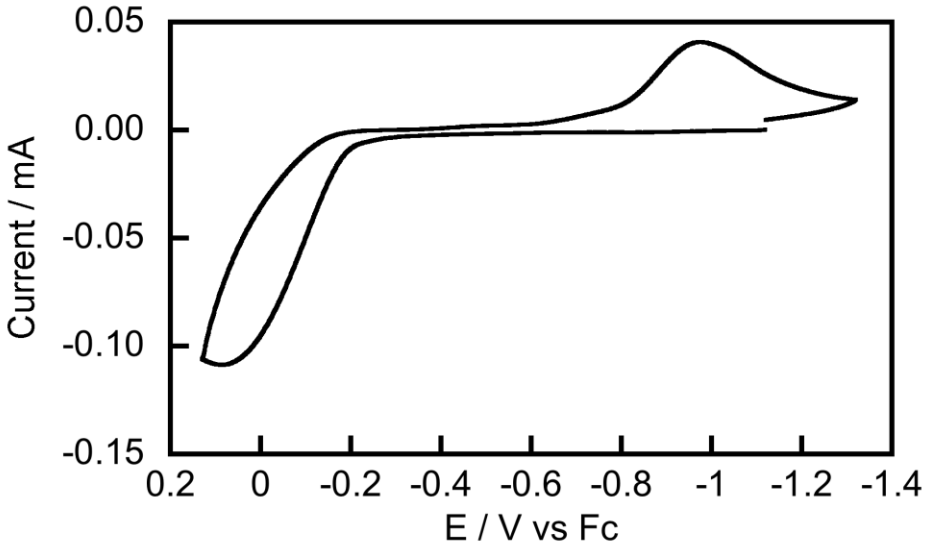

Figure 2.4. Cyclic voltammogram of **2** in 0.1 M $^{n}Bu_4NPF_6$ in acetonitrile. Working electrode: glassy carbon. Scan rate: 100 mV/sec.

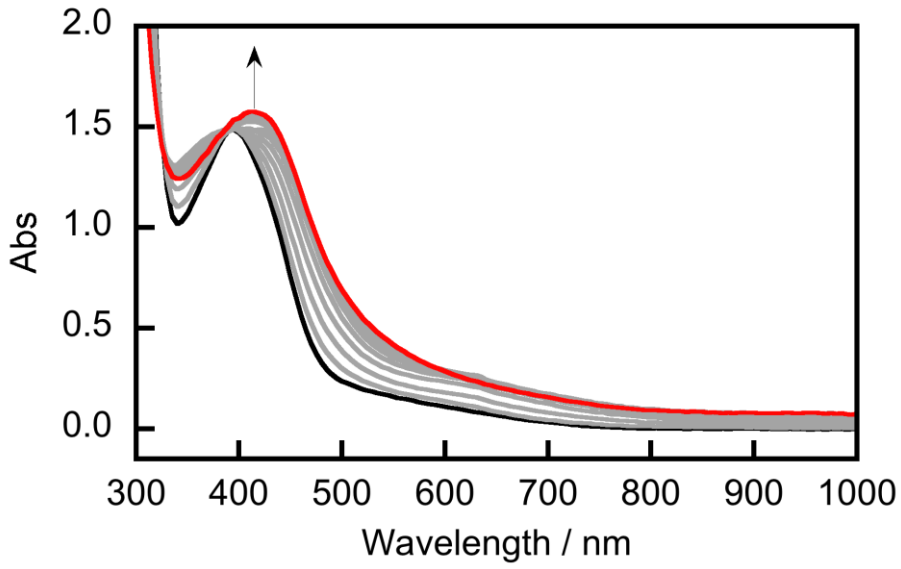

Figure 2.5. UV/vis spectrum of the oxidation of **2** with ferrocenium hexafluorophosphate in methylene chloride at -60ºC.

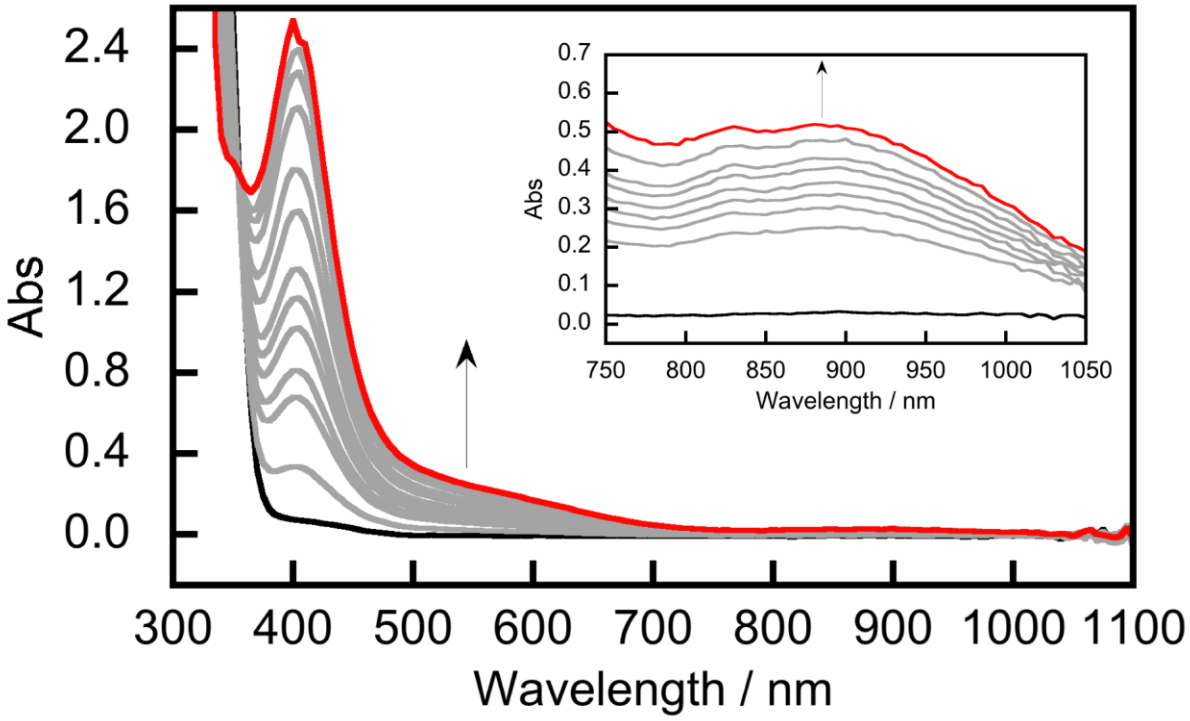

Figure 2.6. UV/vis spectra monitoring the oxidation of a 0.40 mM solution of **4** in acetonitrile with trimethylamine-*N*-oxide at -40 ºC to produce iron(IV)-oxo complex **5**. Inset: growth of near-IR band for an analogous experiment run at a higher concentration of **4** (8.0 mM).

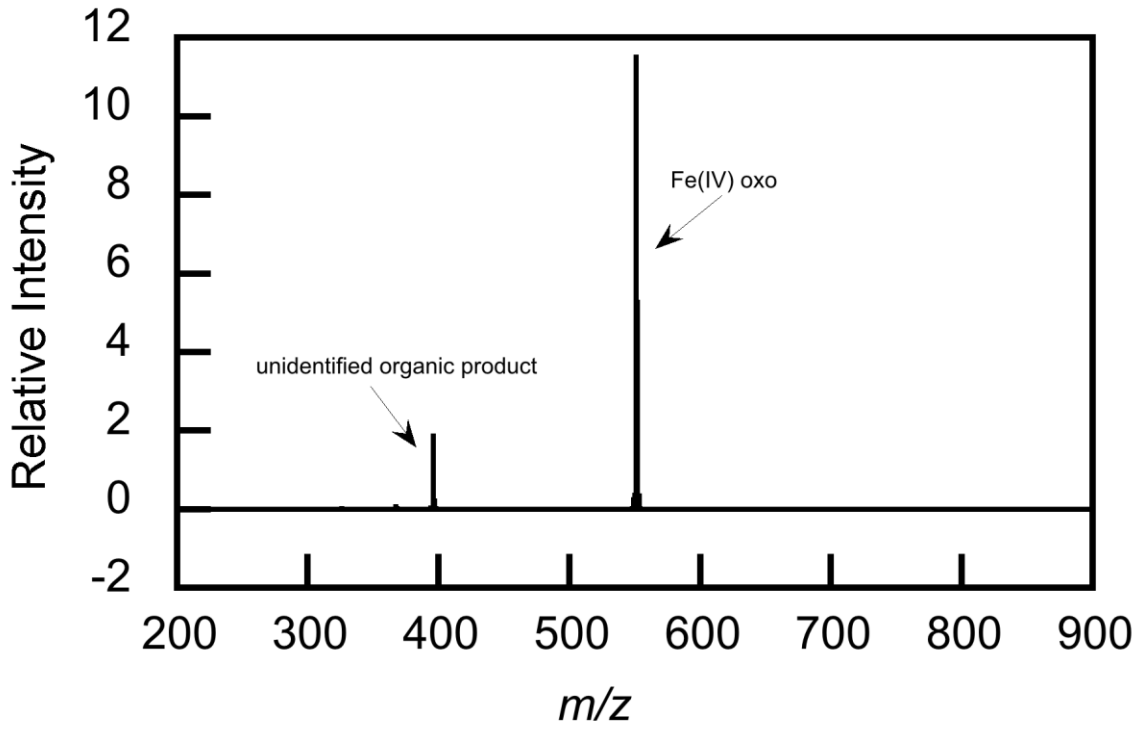

Figure 2.7. Full electrospray ionization mass spectrum of **5** (see Figure 2.8 below for simulation of signal corresponding to **5**).

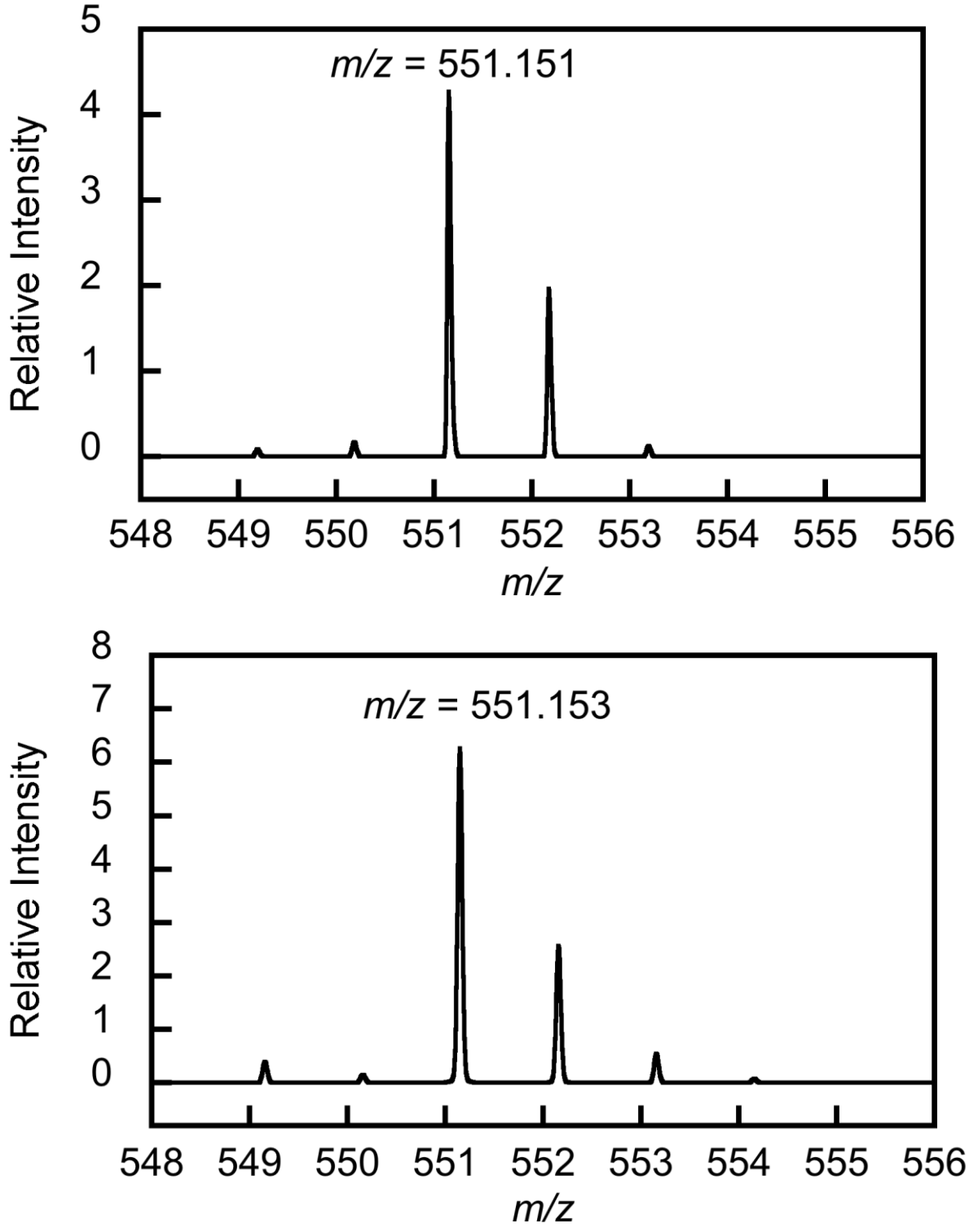

Figure 3.8. The electrospray ionization mass spectrum of **5**, showing the experimentally observed (top) and theoretical (bottom) isotopic distribution pattern for $[(tpa^{Ph})FeO]^-$.

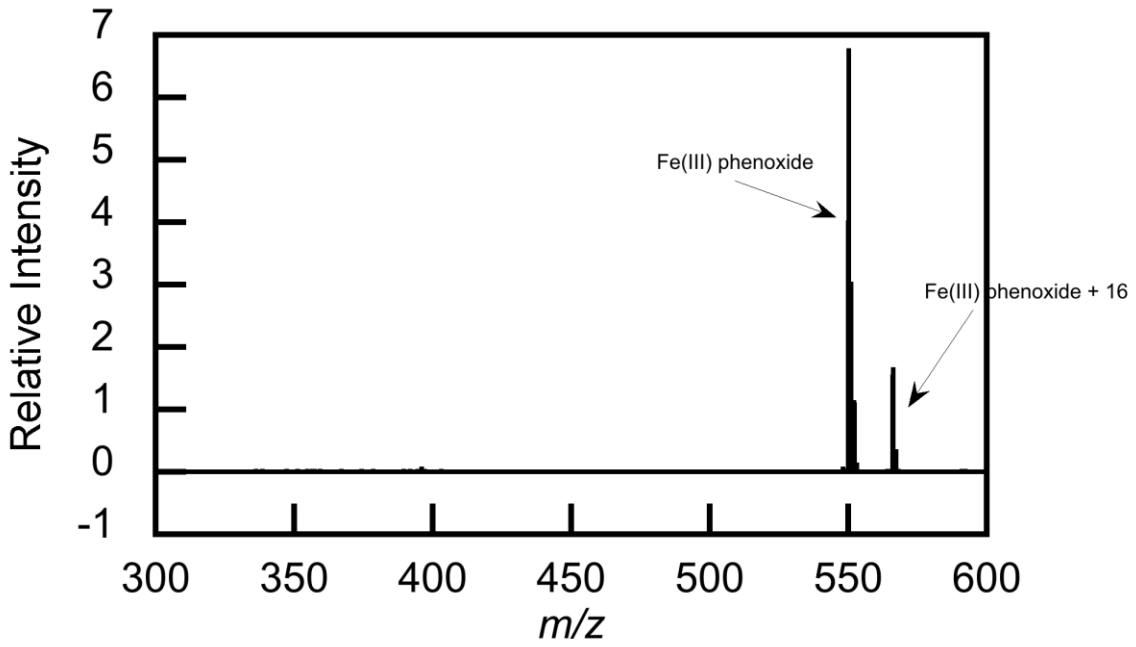

Figure 2.9. Full electrospray ionization mass spectrum of the decomposition product of **5** (see Figure 2.10 below for simulation of the signal corresponding to the iron(III) phenoxide **6**).

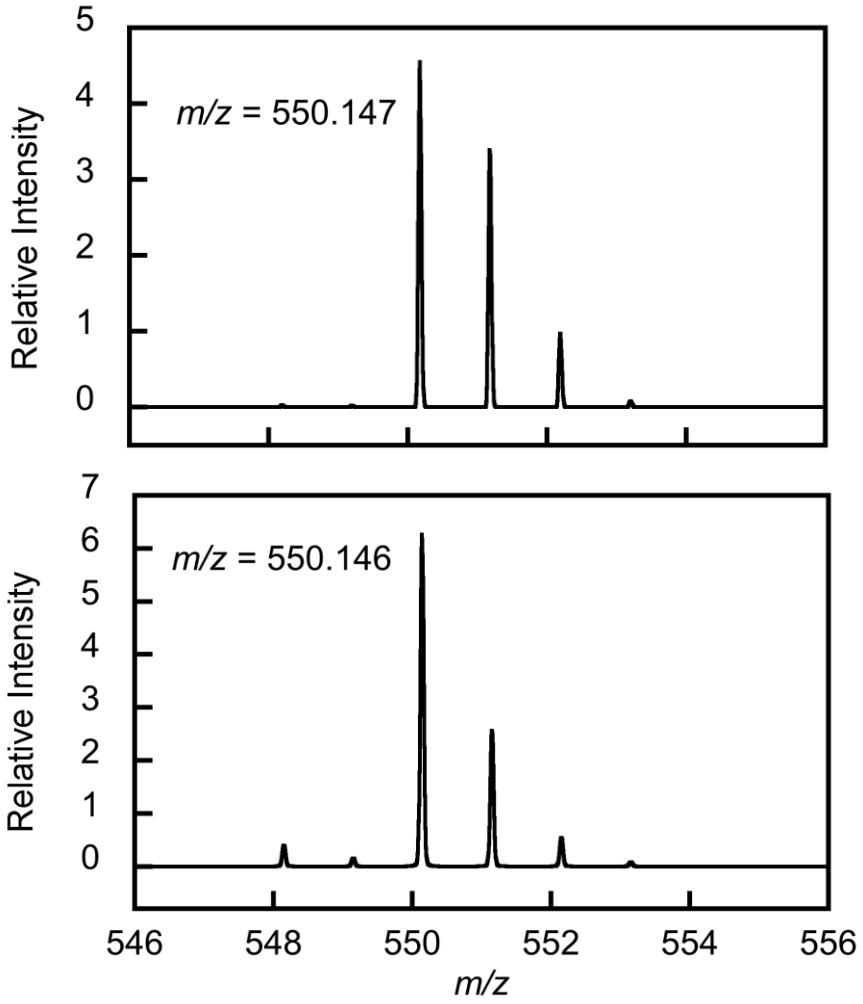

Figure 2.10. The electrospray ionization mass spectrum of the decomposition product of **5** (taken seconds after the spectrum in Figures 2 and S6), showing the experimentally observed (top) and theoretical (bottom) isotopic distribution pattern for $[(tpa^{2PhPhO})Fe]^-$.

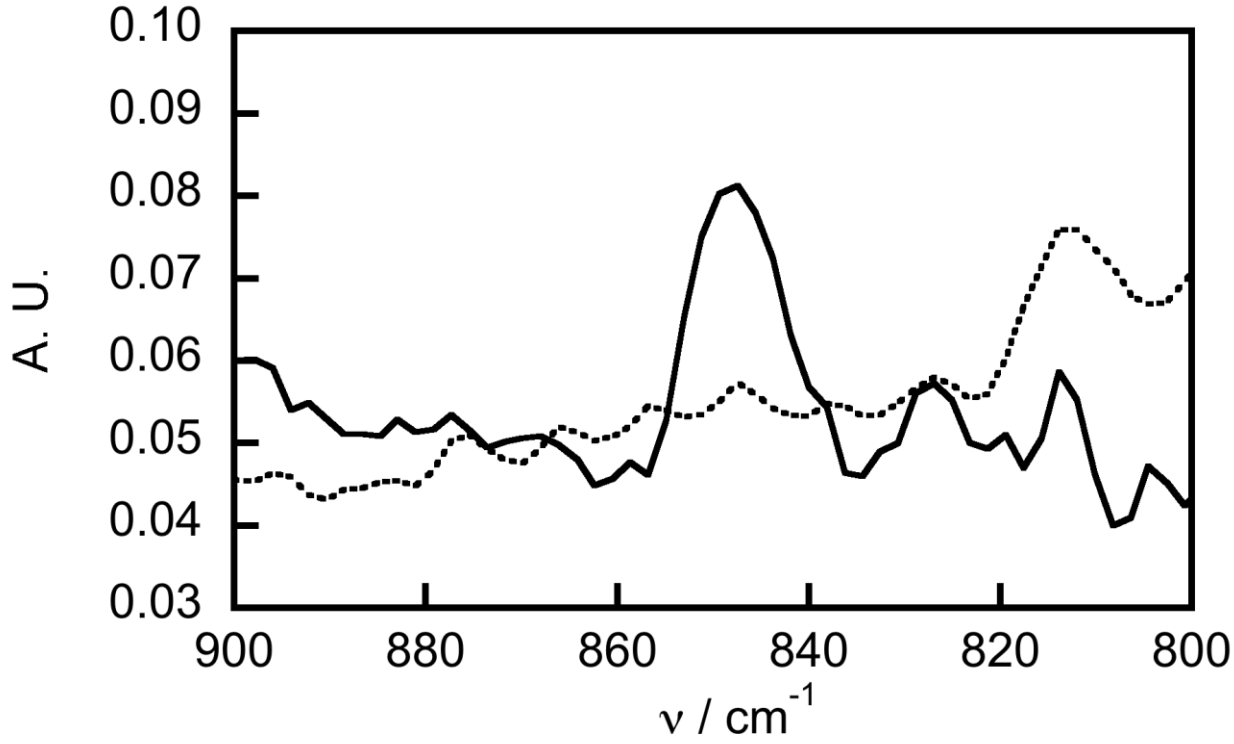

Figure 2.11. IR spectrum of **5** generated *in situ* by trimethylamine-*N*-oxide oxidation of **4** in acetonitrile at -35ºC (^{16}O: solid line; ^{18}O: dotted line).

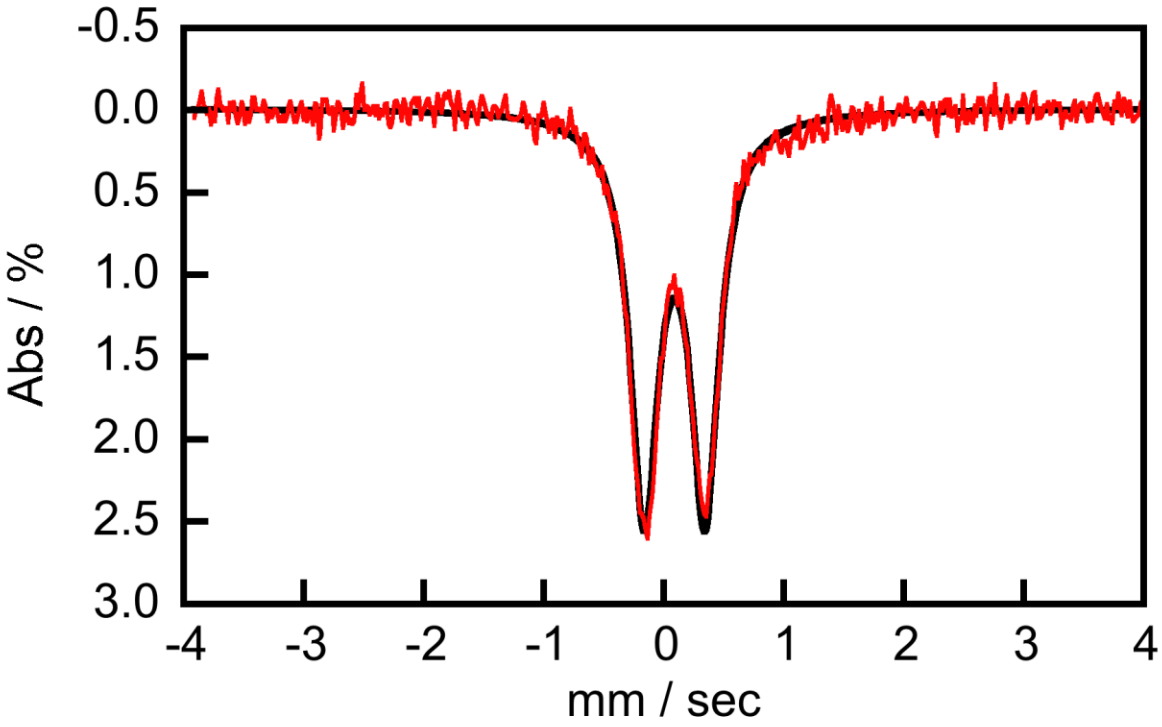

Figure 2.12. Mössbauer spectrum of a 85 mM frozen solution of **5** in acetonitrile acquired at 4.2 K. A least squares fit to the data (solid black line) provided the following parameters: δ = 0.09 mm/sec, ΔE_q = 0.51 mm/sec.

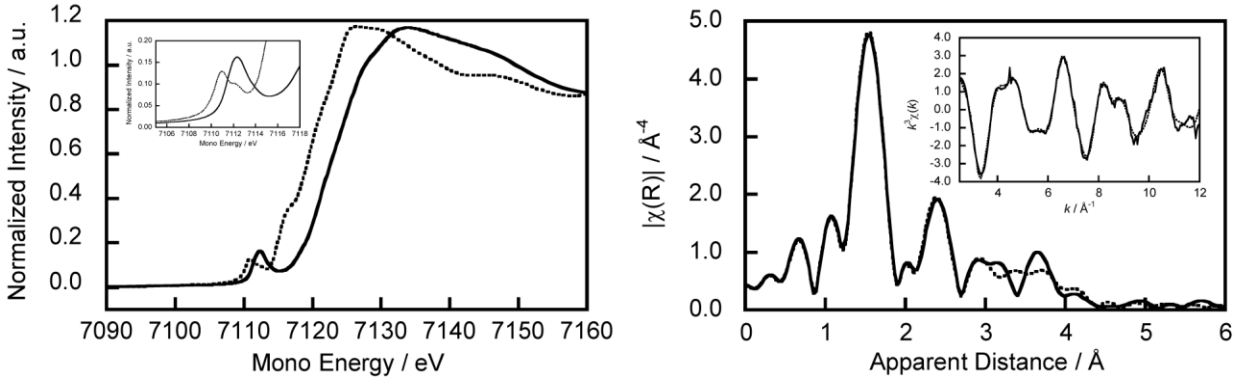

Figure 2.13. Left: Fe K-edge XANES and pre-edge (inset) of **4** (dotted trace) and **5** (solid trace). Right: EXAFS Fourier transform and k^3-weighted oscillations (inset) of **5** (solid trace) and the best fit (dotted trace).

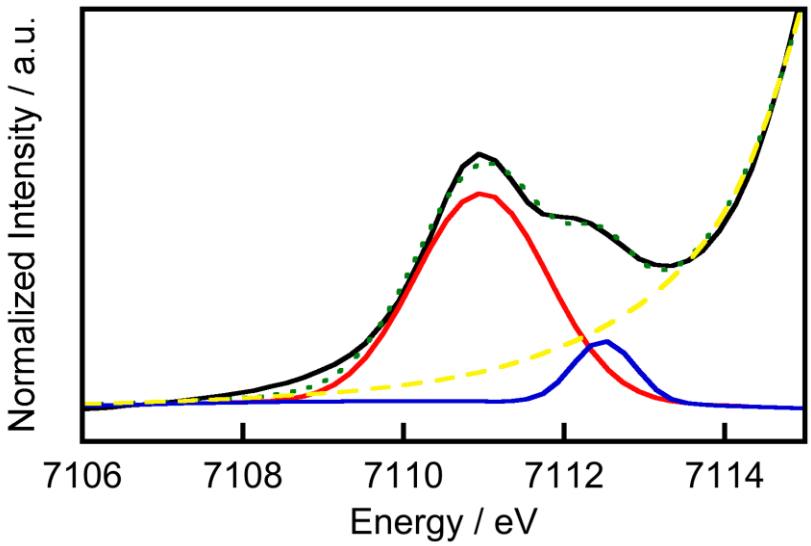

Figure 2.14. Pre-edge fittings of **4**. Experimental data: solid black line, fit: green dotted line, solid red line: peak 1, solid blue line: peak 2, yellow dashed line: background.

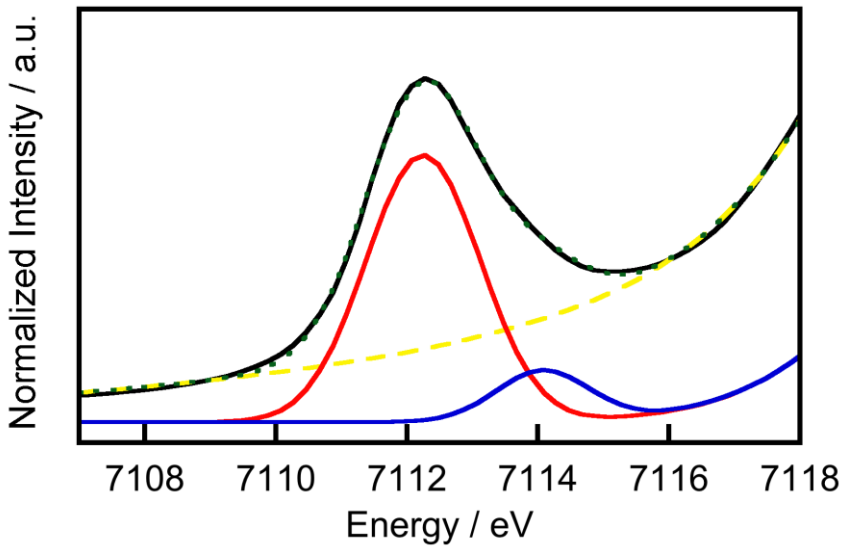

Figure 2.15. Pre-edge fittings of **5**. Experimental data: solid black line, fit: green dotted line, solid red line: peak 1, solid blue line: peak 2, yellow dashed line: background.

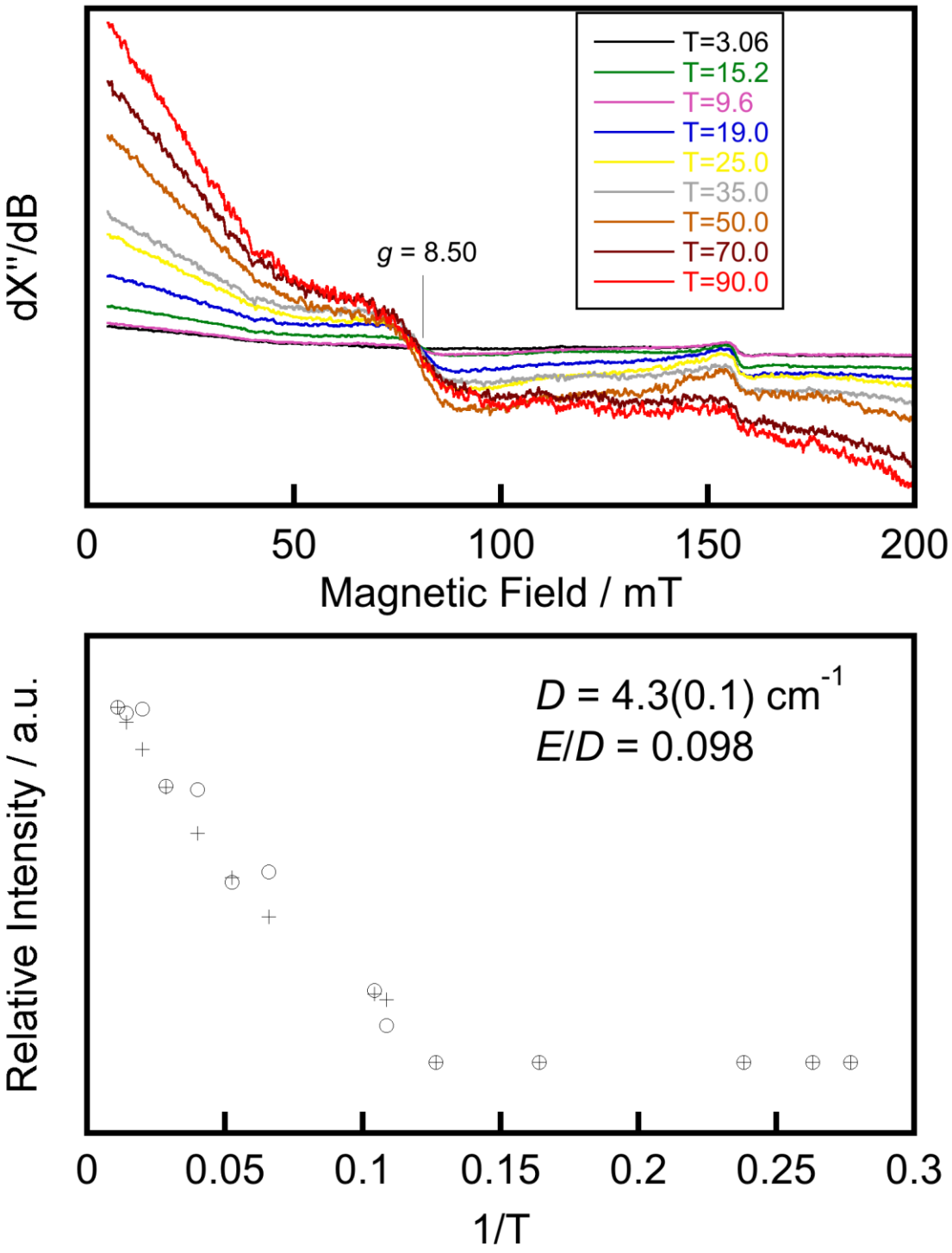

Figure 2.16. Temperature dependence of parallel-mode EPR spectrum of 5 from 3 – 90 K (top). Relative intensity of g = 8.50 feature versus 1/T for experimental (o) and calculated (+) spectra (bottom). Best fit analysis provides a value for the axial zero-field splitting paramater, D, of 4.3 cm^{-1}.

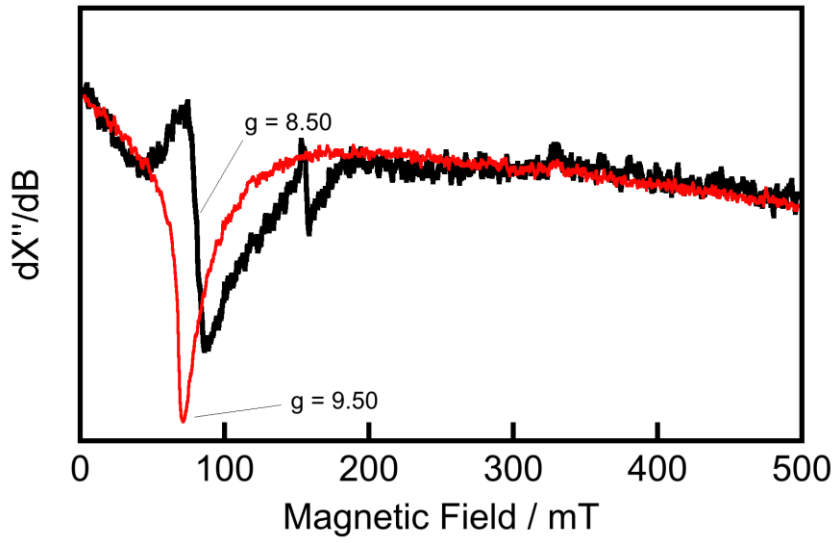

Figure 2.17. Parallel-mode X-band EPR spectra of **4** (red) and **5** (black) in 1:1 acetonitrile/toluene. Spectra recorded at 10 K with excitation frequency of 9.38 GHz at 2.02 mW.

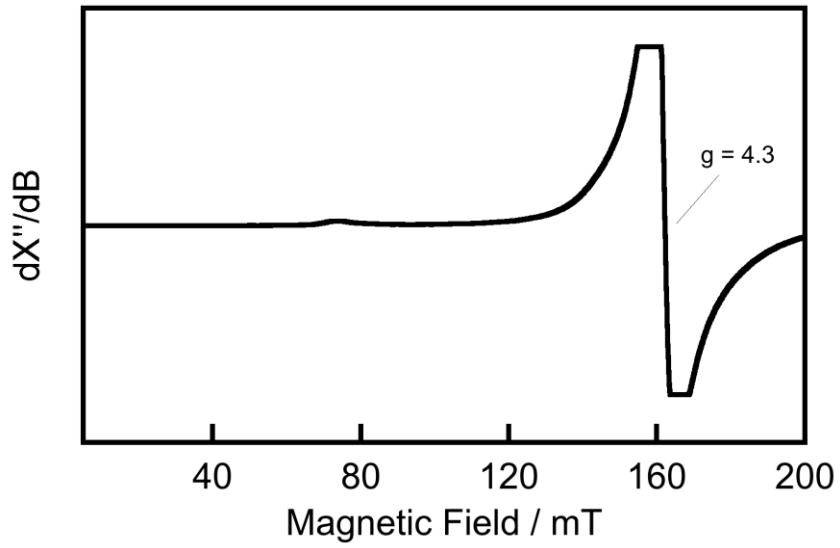

Figure 2.18. Perpendicular-mode X-band EPR spectrum of the iron(III) phenoxide product **6** from the decomposition of **5** in 1:1 acetonitrile/toluene showing a strong derivative feature at g = 4.3. (Note: Signal goes off scale). Spectra recorded at 10 K with excitation frequency of 9.69 GHz at 2.02 mW.

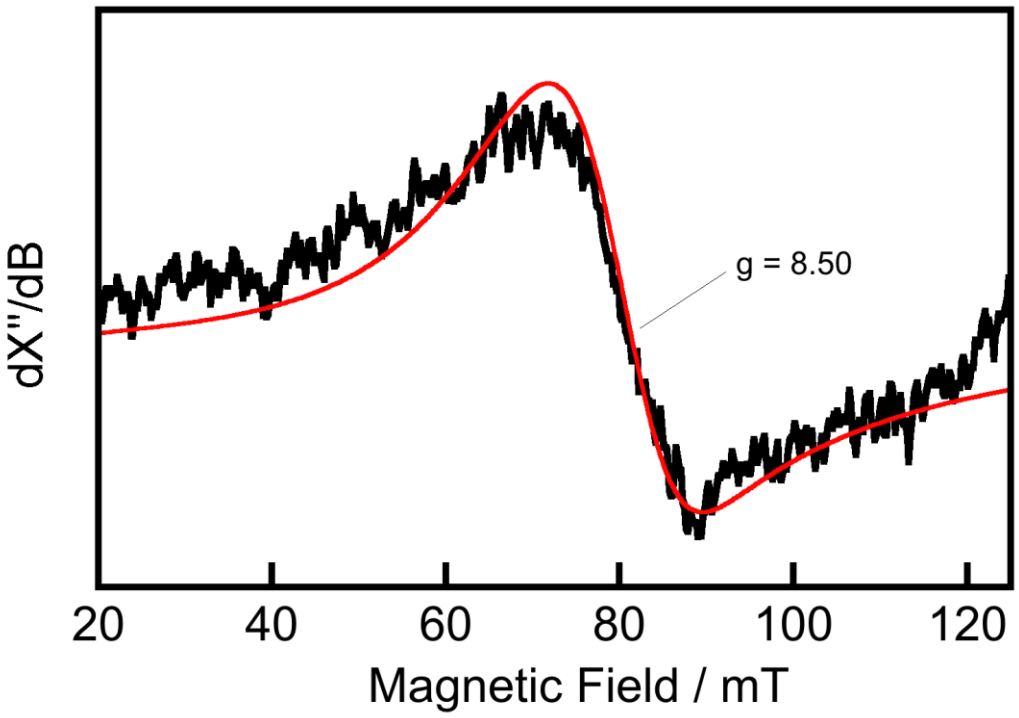

Figure 2.19. Parallel-mode X-band (9.38 GHz) EPR spectrum of **5** (black) and simulation (red) in 1:1 acetonitrile/toluene. Spectrometer conditions: temperature 40 K, incident power 2.02 mW, modulation amplitude 0.8 mT. Simulation parameters: D = +4.32 cm^{-1}, E/D = 0.098, $\sigma_{E/D}$ = 0.02, and a line broadening of 8 mT.

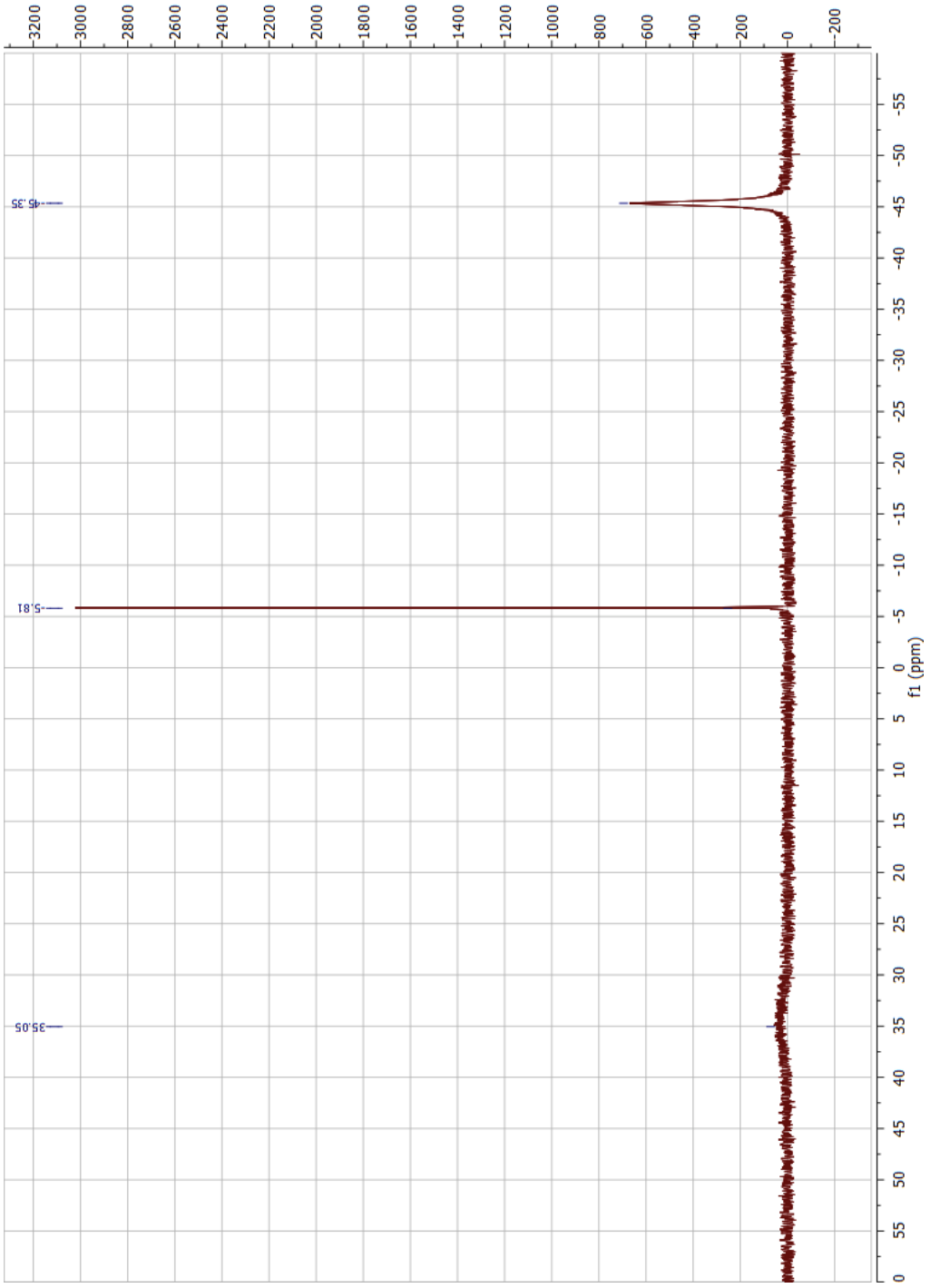

Figure 2.20. ^{31}P NMR of the reaction of **5** with PMe_2Ph. PPh_3 is present as an internal standard.

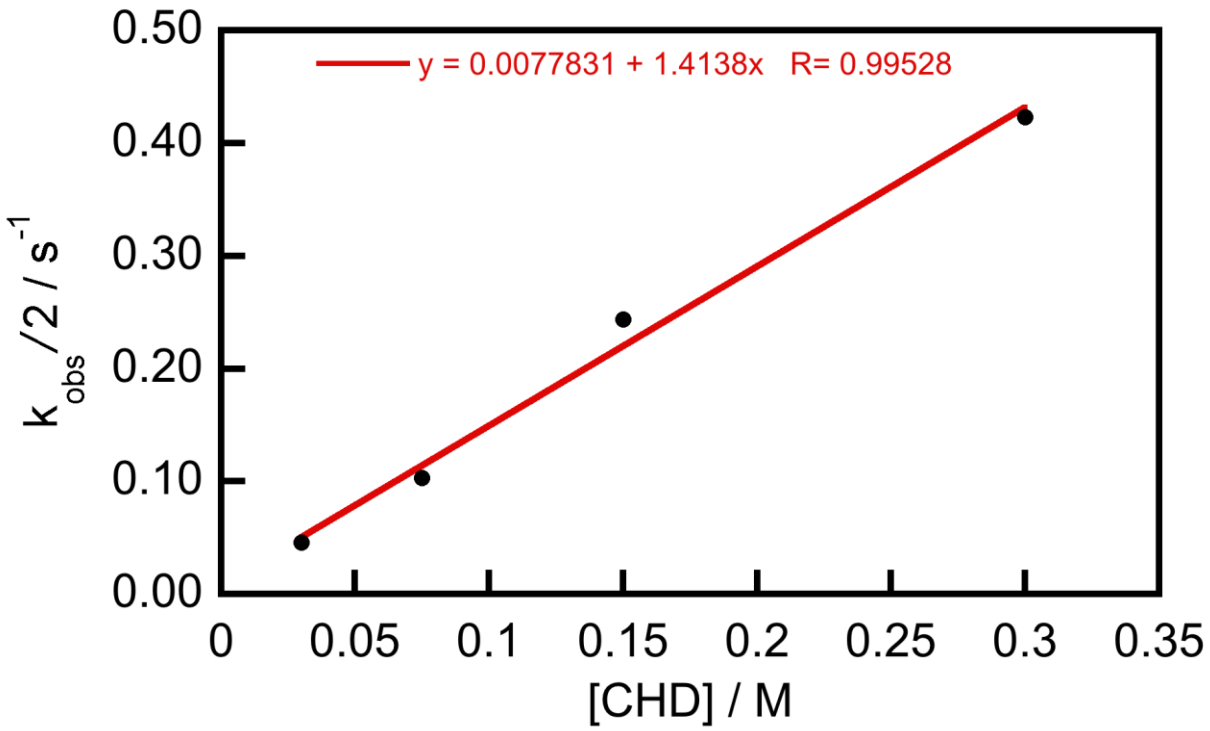

Figure 2.21. Plot of $k_{obs}/2$ vs [CHD] for the reaction of **5** with CHD at -30 ºC. The second-order rate constant is obtained from the slope to be 1.4 $M^{-1}s^{-1}$.

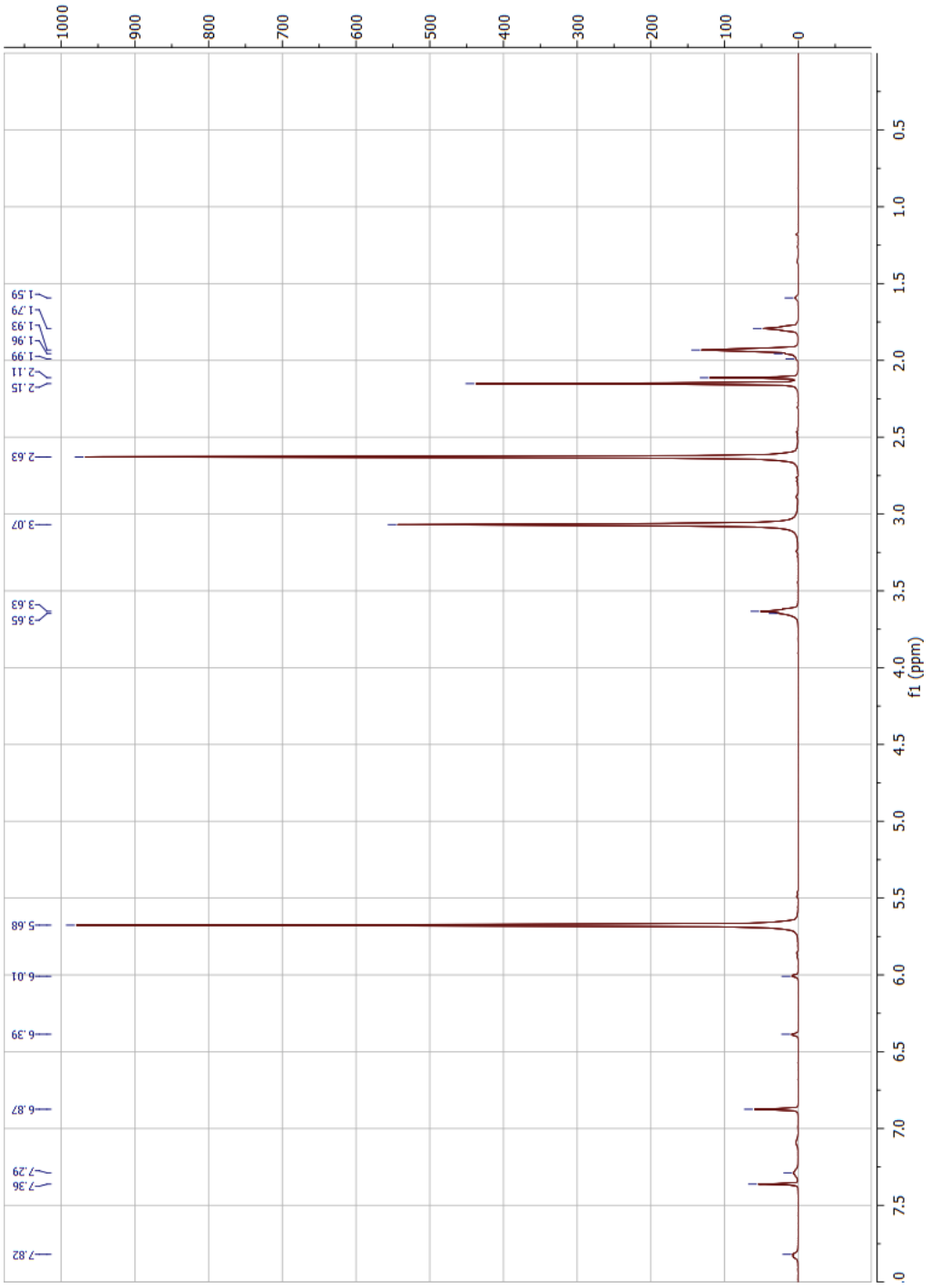

Figure 2.22. ^{1}H NMR of the reaction of **5** with 1,4-cyclohexadiene. 1,2,4,5-tetramethylbenzene is present as an internal standard.

Table 2.1. Observed edge values (measured at $F/I_0 = 0.5$) and pre-edge energies and areas derived from fittings for **4** and **5**.

Compound	**E_{edge} (eV)**	**$E_{pre\text{-}edge}$ (eV)**	**Area**
4	7118.8	7110.9	19.72
		7112.5	2.75
5	7122.0	7112.3	28.05
		7114.1	4.38

Table 2.2. 4 and **5** EXAFS fitting parameters. The amplitude reduction factor S_0^2 was set to 0.78. All fits were performed in the R-space.[b]

					R / Å		
Sample	**Fit #**	**Shell**	**N[a]**	**XRD**	**EXAFS**	**σ^2 / Å**	**R / %**
Fe(II) (**4**)	1	Fe-N	**4**	~2.0	2.04 (0.011)	0.005 (0.001)	2.6
	(98)	Fe-C_1	**6**	~2.9	2.91 (0.028)	0.009 (0.004)	
		Fe-C_2	**12**	~3.2	3.20 (0.026)	0.012 (0.007)	
		Fe-C_3	**6**	4.23	4.26 (0.043)	0.005 (0.005)	
						Reduced χ^2=	324.9
						E_0 (eV)=	1.68 (1.3)
Fe(IV)-O (**5**)	1	Fe-N	**4**		1.99 (0.011)	0.008 (0.001)	1.7
	(84)	Fe-C_1	**6**		2.90 (0.019)	0.006 (0.002)	
		Fe-C_2	**12**		3.02 (0.029)	0.018 (0.006)	
		Fe-C_3	**6**		4.28 (0.041)	0.007 (0.005)	
						Reduced χ^2=	342.0
						E_0 (eV)=	8.37 (1.3)
	2	Fe-O	**1**		1.62 (0.011)	0.007 (0.002)	0.5
	(83)	Fe-N	**4**		1.99 (0.008)	0.008 (0.001)	
		Fe-C_1	**6**		2.92 (0.014)	0.006 (0.001)	
		Fe-C_2	**12**		3.05 (0.022)	0.019 (0.004)	
		Fe-C_3	**6**		4.31 (0.035)	0.007 (0.003)	
						Reduced χ^2=	165.3
						E_0 (eV)=	10.33 (1.3)

[a] Numbers in bold were set.
[b] Numbers in parentheses indicate uncertainties.

References

(1) Groves, J. T. *J. Inorg. Biochem.* **2006**, *100*, 434-447.
(2) Feig, A. L.; Lippard, S. J. *Chem. Rev.* **1994**, *94*, 759-805.
(3) Que, L.; Ho, R. Y. N. *Chem. Rev.* **1996**, *96*, 2607-2624.
(4) Baik, M.-H.; Newcomb, M.; Friesner, R. A.; Lippard, S. J. *Chem. Rev.* **2003**, *103*, 2385-2420.
(5) Costas, M.; Mehn, M. P.; Jensen, M. P.; Que, L. *Chem. Rev.* **2004**, *104*, 939-986.
(6) Vaillancourt, F. H.; Yeh, E.; Vosburg, D. A.; Garneau-Tsodikova, S.; Walsh, C. T. *Chem. Rev.* **2006**, *106*, 3364-3378.
(7) Krebs, C.; Galonic Fujimori, D.; Walsh, C. T.; Bollinger, J. M. *Acc. Chem. Res.* **2007**, *40*, 484-492.
(8) Que, L.; Dong, Y. *Acc. Chem. Res.* **1996**, *29*, 190-196.
(9) Grapperhaus, C. A.; Mienert, B.; Bill, E.; Weyhermueller, T.; Wieghardt, K. *Inorg. Chem.* **2000**, *39*, 5306-5317.
(10) MacBeth, C. E.; Golombek, A. P.; Young, V. G.; Yang, C.; Kuczera, K.; Hendrich, M. P.; Borovik, A. S. *Science* **2000**, *289*, 938-941.
(11) Lim, M. H.; Rohde, J.-U.; Stubna, A.; Bukowski, M. R.; Costas, M.; Ho, R. Y. N.; Münck, E.; Nam, W.; Que, L. *Proc. Natl. Acad. Sci. U.S.A.* **2003**, *100*, 3665-3670.
(12) Rohde, J.-U.; In, J.-H.; Lim, M. H.; Brennessel, W. W.; Bukowski, M. R.; Stubna, A.; Münck, E.; Nam, W.; Que, L. *Science* **2003**, *299*, 1037-1039.
(13) Klinker, E. J.; Kaizer, J.; Brennessel, W. W.; Woodrum, N. L.; Cramer, C. J.; Que, L. *Angew. Chem., Int. Ed.* **2005**, *44*, 3690-3694.
(14) Martinho, M.; Banse, F.; Bartoli, J.-F.; Mattioli, T. A.; Battioni, P.; Horner, O.; Bourcier, S.; Girerd, J.-J. *Inorg. Chem.* **2005**, *44*, 9592-9596.
(15) Bautz, J.; Bukowski, M. R.; Kerscher, M.; Stubna, A.; Comba, P.; Lienke, A.; Münck, E.; Que, L. *Angew. Chem., Int. Ed.* **2006**, *45*, 5681-5684.
(16) Goldsmith, C. R.; Stack, T. D. P. *Inorg. Chem.* **2006**, *45*, 6048-6055.
(17) Tiago de Oliveira, F.; Chanda, A.; Banerjee, D.; Shan, X.; Mondal, S.; Que, L.; Bominaar, E. L.; Münck, E.; Collins, T. J. *Science* **2007**, *315*, 835-838.
(18) Ekkati, A. R.; Kodanko, J. J. *J. Am. Chem. Soc.* **2007**, *129*, 12390-12391.
(19) Korendovych, I. V.; Kryatov, S. V.; Rybak-Akimova, E. V. *Acc. Chem. Res.* **2007**, *40*, 510-521.
(20) Nam, W. *Acc. Chem. Res.* **2007**, *40*, 522-531.
(21) Que, L. *Acc. Chem. Res.* **2007**, *40*, 493-500.
(22) Chanda, A.; Shan, X.; Chakrabarti, M.; Ellis, W. C.; Popescu, D. L.; Tiago de Oliveira, F.; Wang, D.; Que, L.; Collins, T. J.; Münck, E.; Bominaar, E. L. *Inorg. Chem.* **2008**, *47*, 3669-3678.
(23) Ray, K.; England, J.; Fiedler, A. T.; Martinho, M.; Münck, E.; Que, L. *Angew. Chem., Int. Ed.* **2008**, *47*, 8068-8071.
(24) Thibon, A.; England, J.; Martinho, M.; Young, V. G.; Frisch, J. R.; Guillot, R.; Girerd, J.-J.; Münck, E.; Que, L.; Banse, F. *Angew. Chem., Int. Ed.* **2008**, *47*, 7064-7067.
(25) Abouelatta, A. I.; Campanali, A. A.; Ekkati, A. R.; Shamoun, M.; Kalapugama, S.; Kodanko, J. J. *Inorg. Chem.* **2009**, *48*, 7729-7739.

(26) McGown, A. J.; Kerber, W. D.; Fujii, H.; Goldberg, D. P. *J. Am. Chem. Soc.* **2009**, *131*, 8040-8048.
(27) Mukherjee, A.; Martinho, M.; Bominaar, E. L.; Münck, E.; Que, L. *Angew. Chem., Int. Ed.* **2009**, *48*, 1780-1783.
(28) Kotani, H.; Suenobu, T.; Lee, Y.-M.; Nam, W.; Fukuzumi, S. *J. Am. Chem. Soc.* **2011**, *133*, 3249-3251.
(29) Morimoto, Y.; Kotani, H.; Park, J.; Lee, Y.-M.; Nam, W.; Fukuzumi, S. *J. Am. Chem. Soc.* **2011**, *133*, 403-405.
(30) Seo, M. S.; Kim, N. H.; Cho, K.-B.; So, J. E.; Park, S. K.; Clemancey, M.; Garcia-Serres, R.; Latour, J.-M.; Shaik, S.; Nam, W. *Chem. Sci.* **2011**, *2*, 1039-1045.
(31) Pestovsky, O.; Stoian, S.; Bominaar, E. L.; Shan, X.; Münck, E.; Que, L.; Bakac, A. *Angew. Chem., Int. Ed.* **2005**, *44*, 6871-6874.
(32) England, J.; Martinho, M.; Farquhar, E. R.; Frisch, J. R.; Bominaar, E. L.; Münck, E.; Que, L. *Angew. Chem., Int. Ed.* **2009**, *48*, 3622-3626.
(33) England, J.; Guo, Y.; Farquhar, E. R.; Young Jr, V. G.; Münck, E.; Que Jr, L. *J. Am. Chem. Soc.* **2010**, *132*, 8635-8644.
(34) Lacy, D. C.; Gupta, R.; Stone, K. L.; Greaves, J.; Ziller, J. W.; Hendrich, M. P.; Borovik, A. S. *J. Am. Chem. Soc.* **2010**, *132*, 12188-12190.
(35) Harman, W. H.; Chang, C. J. *J. Am. Chem. Soc.* **2007**, *129*, 15128-15129.
(36) Soo, H. S.; Komor, A. C.; Iavarone, A. T.; Chang, C. J. *Inorg. Chem.* **2009**, *48*, 10024-10035.
(37) Freedman, D. E.; Harman, W. H.; Harris, T. D.; Long, G. J.; Chang, C. J.; Long, J. R. *J. Am. Chem. Soc.* **2010**, *132*, 1224-1225.
(38) Harman, W. H.; Harris, T. D.; Freedman, D. E.; Fong, H.; Chang, A.; Rinehart, J. D.; Ozarowski, A.; Sougrati, M. T.; Grandjean, F.; Long, G. J.; Long, J. R.; Chang, C. J. *J. Am. Chem. Soc.* **2010**, *132*, 18115-18126.
(39) Shi, Y.; Cao, C.; Odom, A. L. *Inorg. Chem.* **2004**, *43*, 275-281.
(40) King, E. R.; Betley, T. A. *Inorg. Chem.* **2009**, *48*, 2361-2363.
(41) Sazama, G. T.; Betley, T. A. *Inorg. Chem.* **2010**, *49*, 2512-2524.
(42) King, E. R.; Hennessy, E. T.; Betley, T. A. *J. Am. Chem. Soc.* **2011**, *133*, 4917-4923.
(43) Piro, N. A.; Lichterman, M. F.; Harman, W. H.; Chang, C. J. *J. Am. Chem. Soc.* **2011**, *133*, 2108-2111.
(44) Two examples of high-valent iron oxidants stabilized by ligands with phenyl groups: (a) Lange, S. J.; Miyake, H.; Que Jr, L. *J. Am. Chem. Soc.* **1999**, *121*, 6330-6331; (b) Mukherjee, A.; Martinho, M.; Bominaar, E. L; Münck, E.; Que Jr, L. *Angew. Chem., Int. Ed.* **2009**, *48*, 1780-1783.
(45) The first example of using Resonance Raman to identify the Fe=O stretching frequency in synthetic iron(IV)-oxo complexes: Sastri, C. V.; Park, M. J.; Ohta, T.; Jackson, T. A.; Stubna, A.; Seo, M. S.; Lee, J.; Kim, J.; Kitagawa, T.; Münck, E.; Que Jr, L.; Nam, W. *J. Am. Chem. Soc.* **2005**, *127*, 12494-12495.
(46) Westre, T. E.; Kennepohl, P.; DeWitt, J. G.; Hedman, B.; Hodgson, K. O.; Solomon, E. I. *J. Am. Chem. Soc.* **1997**, *119*, 6297-6314.
(47) Berry, J. F.; DeBeer George, S.; Neese, F. *Phys. Chem. Chem. Phys.* **2008**, *10*, 4361-4374.

(48) Krebs, C.; Price, J. C.; Baldwin, J.; Saleh, L.; Green, M. T.; Bollinger, J. M. *Inorg. Chem.* **2005**, *44*, 742-757.
(49) Hickinbottom, W. J. *Reactions of Organic Compounds*, Longmans, Green and Co.: New York, 1957, p. 420.
(50) Newville, M. *Synchrotron Rad.* **2001**, *8*, 322-324.
(51) Rehr, J. J.; Albers, R. C. *Rev. Mod. Phys.* **2000**, *72*, 621-654.
(52) Newville, M.; Ravel, B.; Haskel, D.; Rehr, J. J.; Stern, E. A.; Yacoby, Y. *Physica B* **1995**, *208*, 154.
(53) Stoll, S.; Schweiger, A. *J. Magn. Reson.* **2006**, *178*, 42-55.

Chapter 3
Synthetic Tuning of the PY5MoO Catalyst Applied to Electrocatalytic H_2 Production

Introduction

Hydrogen has recently been widely proposed as a carbon-neutral fuel alternative to carbon-based fossil fuels.[1-3] The most common sources of hydrogen, however, are steam reformation and the gasification of coal, both of which generate carbon dioxide that must be sequestered or reduced (with H_2 or its equivalents) to maintain carbon neutrality.[1,3] In contrast, the photocatalytic production of dihydrogen from water is a carbon-neutral process and one fostering a great deal of attention in academic chemistry in the context of artificial photosynthesis.[2] Much research has been conducted in the area of homogeneous catalysis for the photocatalytic[4,5] and electrocatalytic[6-11] production of dihydrogen but most of the current catalytic systems suffer from one or more of the following disadvantages: (i) large overpotentials; (ii) low turn-over numbers and/or frequencies; and/or (iii) the requirement of organic solvents, acids, or other organic additives. Our group has focused our work on earth-abundant metal electrocatalysts that catalyze the production of hydrogen in the presence of water.

Recently, our group reported new molecular catalysts of polypyridyl ligands for the production of dihydrogen in the presence of water.[12-17] In particular, a molybdenum(IV)-oxo complex of the $PY5Me_2$ ligand ($[(PY5Me_2)MoO]^{2+}$, **1**) that operates in neutral, buffered water (or seawater) was discovered that possesses both high activity and stability.[13] With an eye toward photocatalytic hydrogen product, which would benefit from a lower overpotential for catalysis than **1** to be compatible with common photosensitizers, we prepared a variety of derivatives of **1** and tested them under electrocatalytic conditions.

Results and Discussion

Synthesis of 1st Generation Derivatives of PY5 and a New Synthetic Approach for Molybdenum Insertion

We first explored derivatives of the PY5 platform incorporating electron-withdrawing groups at the methine position of $PY5H_2$. The strategy, outlined in Scheme 3.1, involves oxidation of both methine positions with a halogenating reagent. In this way, $PY5F_2$ (**2**), $PY5Cl_2$ (**3**) and $PY5Br_2$ (**4**) are synthesized in 60 %, 77 %, and 21 % yields, respectively. However, attempts to install the molybdenum metal in the ligands using $MoI_2(CO)_3(CH_3CN)_2$[18] in refluxing toluene, as previously described for **1**,[13] fail due to ligand decomposition, pointing toward the necessity for milder metallation conditions.

To this end, molybdenum(III)- and molybdenum(IV)-chloride salts are substituted for $MoI_2(CO)_3(CH_3CN)_2$ and stirred with ligands **2**-**4** at room temperature in acetonitrile in the presence of halide abstractors such as silver triflate (AgOTf). Although **3** and **4** react directly with the halide abstractor, the molybdenum(III)-chloride complex of **2** ($[(PY5F_2)MoCl](OTf)_2$, **5**) is successfully prepared from $MoCl_4(DME)$[19] with two equivalents of AgOTf as a green crystalline compound (Scheme 3.2). The molecular structure of **5** determined by Xray crystallography is shown in Figure 3.1. Note the large ellipsoid for the Cl group, which is likely due to the presence of trace Mo(IV)-oxo.[20] The green Mo(IV)-oxo is also detected by ESI MS in samples of **5** and arises from the $MoCl_4(DME)$ starting material. Subsequent syntheses of PY5MoCl compounds use the $MoCl_4(CH_3CN)_2$[21] starting material, which avoids this problem (*vide infra*).

Since **5** likely has the least negative reduction potentials of the series, we next sought to prepare the molybdenum(IV)-oxo complex for electrocatalytic studies. To this end, reaction of **5** with water provides one diamagnetic product as judged by ^{1}H NMR, consistent with the tetragonal Mo(IV)-oxo complex $[(PY5F_2)MoO](OTf)_2$ (**6**). This assignment is confirmed by Xray crystallography and the molecular structure of **6** is shown in Figure 3.2. The CV of **6** in acetonitrile is shown in Figure 3.3 and reveals a rich electrochemistry for **6** similar to that for **1**:[13] multiple quasi-reversible reductions and a single irreversible oxidation.

More importantly, in neutral water (buffered with phosphate) **6** serves as an electrocatalyst for the production of dihydrogen (Figure 3.4). Significantly, the first two reductive waves preceding the catalytic wave are shifted anodically for **6** relative to **1**, as would be expected for the more electron poor complex **6** (Figure 3.4, inset). Unfortunately, the fluoro groups have little impact on the onset potential of the *electrocatalytic* wave (Figure 3.4, inset). Reasoning that the fluoro groups are somewhat removed from the Mo center, we next turned to the synthesis of more robust PY5 derivatives with electron-withdrawing groups on the pyridine rings themselves. Derivatization at the pyridine rings is expected to exert a more significant influence on the metal center via inductive effects and through the π system of the pyridine rings.

Synthesis of 2nd Generation Derivatives of PY5 and Their Mo-oxo Complexes

As shown in Scheme 3.3, four new ligand derivatives were prepared, differing by the appended group and its location. First, two derivatives with *meta* chloro-substitution, $^{Cl2}PY5Me_2$ (**7**) and $^{Cl2}PY5H_2$ (**8**), are synthesized from 2,6-difluoro-3,5-dichloropyridine prepared following a literature preparation from 2,4,6-trifluoro-3,5-dichloropyridine by reduction with diisobutylaluminum hydride. $^{Ph}PY5Me_2$ (**9**) and $^{CF3}PY5Me_2$ (**10**) are synthesized from the corresponding 2,6-dichloropyridine using refluxing dioxane as the solvent instead of THF (the higher boiling point of dioxane is necessary for complete reaction of the 1,2-dipyridylethane groups with the 2,6-dichloropyridine). Note that **10** has recently been utilized in Co-catalyzed hydrogen production by our group.[14]

Synthesis of the metal precursors to the desired molybdenum(IV)-oxo complexes – $[(^{Cl2}PY5H_2)MoCl](OTf)_2$ (**11**), $[(^{Ph}PY5Me_2)MoCl](OTf)_2$ (**12**), and $[(^{CF3}PY5Me_2)MoCl](OTf)_2$ (**13**) – is accomplished for **8**-**10** using $MoCl_4(DME)$ or $MoCl_4(CH_3CN)_2$ and two equivalents of AgOTf in analogy to the synthesis of the fluoro compound **5**. The molecular structures of **11** and **13** are shown in Figures 3.5 and 3.6. No crystalline material is obtained from **7** under these conditions. One reason for this might be steric clash between the cloro and methyl groups of **7** (Scheme 3.4). In addition, the molybdenum(III)-iodide compounds $[(^{Ph}PY5Me_2)MoI]I_2$ (**14**) and $[(^{CF3}PY5Me_2)MoI]I_2$ (**15**) could be prepared from $MoI_2(CO)_3(CH_3CN)_2$ in refluxing toluene with no evidence of ligand decomposition. **11**-**13** are easily converted to the target molybdenum(IV)-oxo complexes (**16**-**18**, respectively; see Figure 3.7 for the molecular structure of **16** and Figure 3.8 for the di(iodo) precursor to **18**) by reaction with water in refluxing mixtures of water and acetonitrile, although **13** somewhat sluggishly (likely) as a result of the highly electron-withdrawing trifluoromethyl group. The iodo salts **14** and **15** react more rapidly with water to form $[(^{Ph}PY5Me_2)MoO]I_2$ and $[(^{CF3}PY5Me_2)MoO]I_2$ and were used for convenience in electrochemical studies (*vide infra*) after conversion to **17** and **18**, respectively, by reaction with AgOTf (iodide is electrochemically active and complicates

the interpretation of CVs of the molybdenum complexes[13]). The two synthetic routes to **17** are summarized in Scheme 3.5 along with the molecular structures of **14** and **17**.

Electrochemical Characterization

Acetonitrile

The electrochemical behavior of the new Mo(IV)-oxo complexes was first explored in acetonitrile where characterization is uncomplicated by electrocatalytic hydrogen production. These molybdenum(IV)-oxo complexes tend to have one quasireversible oxidation and two quasireversible reductions with further irreversible anodic and cathodic events at more extreme potentials. The cyclic voltammograms (CVs) of **16**-**18** are shown in Figures 3.9-3.11.

In acetonitrile, the most dramatic effect of the substituent on the redox potential of the Mo(IV)-oxo complexes is on the reduction potentials: as expected, the electron-withdrawing groups (Cl and CF_3) make the complexes easier to reduce, relative to **1** (Table 3.1). In contrast, the Ph group has little effect on the redox properties relative to **1** (Table 3.1). This trend is conveniently displayed, for the *para*-substituted PY5 derivatives, in the Hammett plot shown in Figure 3.12 ($^{NMe2}PY5Me_2$, reported elsewhere, is included)[14]. Notably, the effect of the substituents is nearly identical for both the first and second reductions. In contrast, the oxidation of the Mo(IV)-oxo complexes shows a weaker trend, with the elecron-withdrawing groups making the Mo(IV)-oxo complexes more difficult to oxidize (Table 3.1).

Water

The new Mo(IV)-oxo complexes were next investigated under electrocatalytic conditions in pH 7, PO_4^{2-} buffered water at a controlled growth mercury electrode (CGME). The CVs of **16**-**18** under these conditions are shown in Figures 3.13-3.15. In general two features precede the catalytic current. The appearance of the CVs is quite variable, depending on both the complex and the scan rate. For instance, at a scan rate of 5120 mV/sec, **16** and **18** appear to adsorb to the electrode following the first reduction, while **17** appears to involve a species freely diffusing in solution.

In Figure 3.16, the CVs under electrocatalytic conditions are displayed for **1**, **17**, **18** as well as $[(^{NMe2}PY5Me_2)MoO]^{2+}$ showing just the first sweep for clarity. In contrast to the electrochemistry in acetonitrile, the aqueous electrochemistry reveals no obvious trend between the *para*-substituent and the reduction potentials. In addition, the onset of the catalytic wave appears to be independent of the ligand as was seen for **6**. Further investigation is necessary to understand the absence of a substituent effect on the electrocatalytic wave.

Concluding Remarks

The syntheses of a new series of PY5 derivatives and several of their Mo(IV)-oxo complexes are described. Except for fluorination, halogenation at the methine position of $PY5H_2$ is insufficiently robust for the synthetic conditions necessary for preparing molybdenum complexes and inspired a mild metal insertion procedure using Mo(IV)-chloride salts and AgOTf. In contrast, derivatization on a pyridine ring provides more robust PY5 platforms that are capable of stabilizing new Mo(IV)-oxo complexes which could be prepared from either the Mo(II) or Mo(IV) starting materials. In acetonitrile, the electrochemical behavior of the Mo(IV)-oxo complexes displays the expected trend, with electron withdrawing groups shifting the formal Mo(IV)/Mo(III) and Mo(III)/Mo(II)

redox couples to more cathodic potentials. The Mo(IV)/Mo(V) oxidation potential displays the expected, opposite trend, although the trend is weaker than for the reduction potentials. In aqueous media, however, the redox potentials reveal no obvious trend and, more surprisingly, the onset of the electrocatalytic wave appears insensitive to the ligand substitution. In the future, Mo(IV)-complexes of distinct axial ligation (e.g., imido, nitrido, sulfido) will be investigated with the goal of synthetic tuning of the onset of electrocatalytic hydrogen production.[17]

Experimental Section

General Synthetic Details. All synthetic manipulations were performed under an inert atmosphere of dinitrogen in a Vacuum Atmospheres glovebox or on a Schlenk line using standard Schlenk techniques. Solvents were dried on a Vacuum Atmospheres solvent purification system and stored over 3 Å molecular sieves. Molecular sieves, alumina, and celite were activated by heating at 200 ºC under dynamic vacuum for at least 24 hours and glassware was heated at 170 ºC overnight in an oven prior to use. $MoI_2(CO)_3(CH_3CN)_2$,[18] $MoCl_4(CH_3CN)_2$,[21] $MoCl_4$(DME),[19] 1,1-dipyridylmethane,[22] $PY5H_2$,[22] 2,6-difluoro-3,5-dichloropyridine[23], and 4-phenyl-2,6-dichloropyridine[24] were synthesized following published procedures. 2,6-difluoro-3,5-dichloropyridine was further purified by sublimation.[25] 1,1-dipyridylethane was prepared analogously to 1,1-dipyridylmethane using 2-ethylpyridine in place of 2-picoline taking care to separate the excess 2-ethylpyridine during the distillation of 1,1-dipyridylethane. $MoCl_5$ was purchased from Strem Chemicals Inc. 2-fluoropyridine and 2,6-difluoropyridine were purchased from Oakwood Products. All other reagents were purchased from Sigma-Aldrich and used as received.

Synthesis of $PY5F_2$ (2). A round bottom flask was charged with $PY5H_2$ (667.7 mg, 1.61 mmol) and selectfluor (1.14 g, 3.22 mmol) in acetonitrile and heated to 80 ºC overnight under dinitrogen. Upon cooling, the mixture was concentrated *in vacuo* and extracted into dichloromethane. The organic layer was then washed 2 × with water, 2 × with saturated aqueous $NaHCO_3$ and rinsed 1 × with brine. The organics were dried over Na_2SO_4, filtered and concentrated under vacuum to a yellow/brown oil which was triturated with diethyl ether to provide **2** as an off-white solid (433.5 mg, 0.96 mmol, 60 %). ^{1}H NMR (400 MHz, $CDCl_3$): δ 8.54 (d, 4.0 Hz, 4H), 7.83 (t, 7.8 Hz, 1H), 7.64 (d, 8.0 Hz, 2H), 7.53 (td, 8.0 Hz, 1.6 Hz, 4H), 7.30 (d, 8.4 Hz, 4H), 7.17 (m, 4H). ^{19}F NMR (376 MHz, $CDCl_3$): δ -145.74.

Synthesis of $PY5Cl_2$ (3). A mixture of $PY5H_2$ (1.08 g, 2.6 mmol) and NCS (1.12 g, 8.4 mmol) was heated to reflux in CCl_4 (sparged with N_2 prior to heating) under N_2 for two hours. The reaction was complete as judged by TLC (Al_2O_3, 1 % MeOH in dichloromethane). After cooling the mixture was transferred to a separatory funnel using dichloromethane and washed 3 × with 5 % aqueous Na_2CO_3. The organics were separated, dried over Na_2SO_4 and concentrated under vacuum to a yellow oily foam. The reaction mixture was purified by flash chromatography on basic alumina eluting with 1 % MeOH in dichloromethane to yield **3** as an off-white solid (972.4 mg, 2.0 mmol, 77 %). ^{1}H NMR (400 MHz, $CDCl_3$): δ 8.49 (d, 4.0 Hz, 4H), 7.77 (m, 3H), 7.44 (td, 1.6 Hz, 7.8 Hz, 4H), 7.10 (m, 4H), 7.00 (d, 8.4 Hz, 4H).

Synthesis of $PY5Br_2$ (4). $PY5H_2$ (2.018 g, 4.86 mmol) and NBS (3.36 g, 18.9 mmol) were heated to reflux overnight in CCl_4 (sparged with N_2 prior to heating) under

N_2. Upon cooling, the reaction mixture was transferred to a separatory funnel with dichloromethane and washed 4 × with ca. 50 mL 5 % aqueous Na_2CO_3. The organics were dried with Na_2SO_4, filtered, and concentrated under vacuum to yield a brown solid. The solid was purified on basic alumina eluting with a gradient of 0.5 % - 2 % MeOH in dichloromethane to afford **4** (575 mg, 1.00 mmol, 21 %). ^{1}H NMR ($CDCl_3$): δ 8.51 (dq, 0.9 Hz, 4.8 Hz, 4H), 7.74 (m, 3H), 7.43 (td, 1.8 Hz, 7.8 Hz, 4H), 7.05 (m, 8). ESI MS: *m/z* calculated for $C_{27}H_{20}N_5Br_2$: 572.0085, found 572.0078.

Synthesis of [(PY5F$_2$)MoCl](OTf)$_2$ (5). To a stirring slurry of **2** (109.5 mg, 0.243 mmol) in acetonitrile was added solid $MoCl_4$(DME) (79.5 mg, 0.243 mmol). The dark orange solution was stirred with the formation of yellow precipitate occurring within minutes. After eight hours of stirring at room temperature, AgOTf (124.9 mg, 0.486 mmol) was added with the immediate formation of AgCl. This mixture was then stirred overnight and filtered through celite to remove AgCl. The green filtrate was concentrated *in vacuo*, extracted into acetonitrile, and filtered to provide a green solid which was collected and recrystallized from acetonitrile/ether to yield dark green, Xray quality crystals of **5** (100.5 mg, 0.114 mmol, 43 %). CHN calculated for **5**$(CH_3CN)_2$: C: 41.15, H: 2.62, N: 10.18; found C: 41.19, H: 2.29, N: 10.13. ESI MS: *m/z* calculated for $C_{28}H_{19}O_3N_5ClF_5MoS$ (**5**-OTf): 732.9866, found 732.9887.

Synthesis of [(PY5F$_2$)MoO](OTf)$_2$ (6). 5 was dissolved in water and stirred in a 20 mL vial open to air overnight. The green solution was then concentrated *in vacuo* and recrystallized from CH_3CN/ether to provide dark green, Xray quality crystals of **6**. ^{1}H NMR (400 MHz, CD_3CN): δ 9.34 (d, 5.6 Hz, 4H), 8.38 (m, 5H), 8.28 (td, 1.4 Hz, 7.9 Hz, 4H), 8.12 (dd, 2.8 Hz, 8.0 Hz, 2H), 7.85 (td, 1.6 Hz, 6.6Hz, 4H). ^{19}F NMR (376 MHz, CD_3CN): δ -78.37, -173.25. CHN calculated for **6**$(CH_3CN)_2$: C: 42.00, H: 2.67, N: 10.39, S: 6.80; found C: 41.78, H: 2.66, N: 10.70, S: 6.97. ESI MS: *m/z* calculated for $C_{28}H_{19}O_4N_5F_5MoS$ (**6**-OTf): 714.0126, found 714.0147.

Synthesis of ^{Cl2}PY5Me$_2$ (7). A stirring THF solution of 1,1-dipyridylethane (680 mg, 3.7 mmol) was cooled under N_2 to -78 ºC followed by the addition of 1.6 M ^{n}BuLi (2.4 mL, 3.8 mmol) dropwise via syringe. The dark red/orange solution was stirred at -78 ºC for ca. two hours at which point 2,6-difluoro-3,5-dichloropyridine (340 mg, 1.85 mmol) was added as a solid. The mixture was allowed to warm to room temperature and stirred for an additional 7 hours. The reaction was then quenched with 20 mL H_2O, the organics were separated, and the aqueous layer extracted 3 × further with ether. The organics were combined, dried with sodium sulfate and concentrated to a yellow oil that solidified with standing in air. The solid thus obtained was rinsed with copious ether to yield **7** as a colorless solid (386.1 mg, 0.753 mmol, 41 %). ^{1}H NMR (400 MHz, $CDCl_3$): δ 8.51 (s, 4H), 7.78 (s, 1H), 7.62 (s, 4H), 7.28 (d, 6.8 Hz, 4H), 7.08 (s, 4H), 2.13 (s, 6H).

Synthesis of ^{Cl2}PY5H$_2$ (8). A stirring THF solution of 1,1-dipyridylmethane (2.5 g, 14.7 mmol) was cooled under N_2 to -78 ºC followed by the addition of 1.6 M ^{n}BuLi (9.2 mL, 14.7 mmol) dropwise via syringe. After stirring at -78 ºC for one hour, 2,6-difluoro-3,5-dichloropyridine (679 mg, 3.69 mmol) was added as a solid and the reaction allowed to warm to room temperature. After stirring for 7 hours at room temperature, the reaction was quenched with 20 mL water. The THF layer was separated, the aqueous layer further extracted 2 × with ether and 1 × with dichloromethane. The organic portions were combined, dried over sodium sulfate, and concentrated *in vacuo* to a red/orange oil that crystallized upon standing in air. The excess 1,1-dipyridylmethane was then removed

via multiple ether washings to yield **8** as a pale yellow solid (566.4 mg, 11.7 mmol, 32 %). ^{1}H NMR (400 MHz, $CDCl_3$): δ 8.5 (d, 4H), 7.72 (s, 1H), 7.43 (t, 6.8 Hz, 4H), 7.10 (m, 4H), 6.89 (d, 4H), 6.36 (s, 2H).

Synthesis of ^{Ph}PY5Me$_2$ (9). To a stirring 1,4-dioxane solution of 1,1-dipyridylethane (235.7 mg, 1.28 mmol) was added 1.6 M ^{n}BuLi (0.9 mL, 1.44 mmol) dropwise via syringe at 10 ºC under N_2. The dark red/orange solution was stirred for 20 minutes after which 4-phenyl-2,6-dichloropyridine (103 mg, 0.46 mmol) was added as a solid. The mixture was then heated to reflux under N_2 overnight. Following cooling to room temperature, the reaction was quenched with 15 mL H_2O, extracted into ether and dried over sodium sulfate. The oil that resulted was then purified on basic alumina eluting with 30 % EtOAc in hexanes to provide **9** as a colorless oil that solidified over time in air (204 mg, 0.39 mmol, 85 %). ^{1}H NMR (400 MHz, $CDCl_3$): δ 8.53 (d, 4.8 Hz, 4H), 7.48 (dd, 1.6 Hz, 10.2 Hz, 2H), 7.4 (m, 7H), 7.3 (s, 2H), 7.05 (m, 4H), 6.87 (d, 8 Hz, 4H), 2.26 (s, 6H). ^{13}C NMR (100 MHz, $CDCl_3$): δ 166.12, 164.63, 149.16, 148.38, 139.25, 135.48, 128.77, 128.53, 127.22, 124.05, 120.92, 118.22, 60.08, 26.73.

Synthesis of ^{CF3}PY5Me$_2$ (10). To a stirring 1,4-dioxane solution of 1,1-dipyridylethane (1.212 g, 6.58 mmol) at room temperature ^{n}BuLi (4.11 mL, 6.58 mmol) was added dropwise via syringe under N_2. The dark red/orange solution was stirred at room temperature for 10 minutes followed by syringe addition of 4-trifluoromethyl-2,6-dichloropyridine (270 µL, 1.88 mmol). The reation was then heated to reflux overnight under N_2. Upon cooling, the reaction was quenched with 15 mL H_2O and then extracted into ether. The organics were combined, dried over sodium sulfate and concentratd *in vacuo* to an oil that solidified on standing to provide **10** as a colorless solid after rinsing with copious ether (849.6 mg, 1.66 mmol, 88 %). ^{1}H NMR (400 MHz, $CDCl_3$): δ 8.51 (dd, 1.2 Hz, 4.8 Hz, 4H), 7.43 (td, 2.0 Hz, 7.6 Hz, 4H), 7.29 (s, 2H), 7.07 (m, 4H), 6.85 (d, 8.4 Hz, 4H), 2.21 (s, 6H). ^{19}F NMR (376 MHz, $CDCl_3$): δ -63.47.

Synthesis of [(^{Cl2}PY5H$_2$)MoCl](OTf)$_2$ (11). To a stirring acetonitrile solution of **8** (92.5 mg, 0.191 mmol) was added solid $MoCl_4$(DME) (62.6 mg, 0.191 mmol). After three hours, the reaction mixture was dark brown with a yellow precipitate present. Solid AgOTf (98.2 mg, 0.382 mmol) was then added, turning the color of the reaction mixture green, and the mixture was stirred overnight. The precipitated AgCl was removed by filtration through celite and the brown filtrate concentrated under vacuum. The brown residue was extracted into CH_3CN and filtered to recover a green solid. This green solid was subsequently recrystallized from CH_3CN/ether to provide **11** as green crystals, which were suitable for Xray diffraction analysis.

Synthesis of [(^{Ph}PY5Me$_2$)MoCl](OTf)$_2$ (12). $MoCl_4(CH_3CN)_2$ (28.9 mg, 0.090 mmol) was added to a stirring acetonitrile slurry of **9** (47.0 mg, 0.090 mmol) to form a dark red/orange solution within 15 minutes. After stirring for 5 hours AgOTf was added with the immediate precipitation of AgCl. The reaction was stirred overnight, filtered through celite to remove AgCl, concentrated *in vacuo* and crystallized from CH_3CN/ether to provide **12** as orange crystals. ^{1}H NMR (400 MHz, CD_3CN): δ 73.18, 61.39, 36.05, 14.55, -7.48, -8.74, -9.54, -65 (b), -75.18.

Synthesis of [(^{CF3}PY5Me$_2$)MoCl](OTf)$_2$ (13). To an acetonitrile slurry of **10** (204.7 mg, 0.40 mmol) was added solid $MoCl_4(CH_3CN)_2$ (128 mg, 0.40 mmol) with stirring to form an orange mixture. The mixture was stirred at room temperature for ca. 8 hours and then reacted with AgOTf (206 mg, 0.80 mmol) to form a lighter orange

mixture with immediate AgCl precipitation. This mixture was stirred overnight, filtered through celite to remove AgCl, and concentrated to a dark oil which was recrystallized from propionitrile/ether by vapor diffusion to provide **13** as yellow crystals. These crystals were washed with a small amount of cold propionitrile and ether and dried under vacuum. A second crop of **13** was obtained from the combined mother liquor and washings by concentration under vacuum followed by rinsing with copious THF and a small amount of cold propionitrile (195.1 mg, 0.207 mmol, 52 %). ^{1}H NMR (400 MHz, CD_3CN): δ 75.42, 63.00, 35.62, -8.05, -65 (b), -75.00. CHN calculated for **13**: C: 40.8, H: 2.6, N: 7.4; found C: 40.86, H: 2.23, N: 7.33.

Synthesis of [(^{Ph}PY5Me$_2$)MoI]I$_2$ (14). A mixture of **9** (111.1 mg, 0.214 mmol) and $MoI_2(CO)_3(CH_3CN)_2$ (166 mg, 0.321 mmol) was heated in toluene to reflux under N_2 for three days. Upon cooling, the reaction flask was partially evacuated, sealed, and transferred into the glovebox. Brown solid was collected by filtration and washed with copious toluene. The solid was then extracted into CH_3CN with stirring over three days, filtered, and recrystallized from CH_3CN/ether by vapor diffusion. The orange crystals, suitable for Xray diffraction studies, were rinsed with ether and dried under vacuum to provide **14** as an orange powder. ^{1}H NMR (400 MHz, CD_3CN): δ 67.27, 60.69, 36.25, 13.50, -7.34, -8.68, -9.10, -55.5, -72.83. CHN calculated for **14**(Et_2O): C: 43.76, H: 3.67, N: 6.54; found C: 43.48, H: 3.22, N: 6.61.

Synthesis of [(^{CF3}PY5Me$_2$)MoI]I$_2$ (15). A mixture of **10** (103.9 mg, 0.203 mmol) and $MoI_2(CO)_3(CH_3CN)_2$ (156.7 mg, 0.303 mmol) in toluene was heated to reflux under N_2 for 3 days. After cooling, the flask was partially evacuated, sealed and transferred to the glovebox. A brown solid was collected via filtration and rinsed with copious toluene. The solid was then extracted into CH_3CN, filtered through celite and recrystallized by diffusion of ether into the CH_3CN solution. The dark orange/brown crystals thus obtained were rinsed with ether and dried to afford **15**. ^{1}H NMR (400 MHz, CD_3CN): δ (major product) 68.37, 62.60, 35.88, -7.95, -55.8, -72; (minor product) 116.1, 63.8, 60.5, 36.30, -7.38.

Synthesis of [(^{Cl2}PY5H$_2$)MoO](OTf)$_2$ (16). An aqueous solution of **11** was heated to 90 ºC in air for three days. The reaction progress was monitored by direct injection into an LC/MS and was considered complete when the Mo(III)-chloride **11** was no longer detected by MS. The green solution so obtained was concentrated under vacuum and recrystallized from CH_3CN/ether to provide green crystals of **16**. ^{1}H NMR (400 MHz, CD_3CN): δ 9.30 (d, 5.6 Hz, 4H), 8.35 (s, 1H), 8.19 (m, 8H), 7.78 (m, 4H), 7.20 (s, 2H). ^{19}F NMR (376 MHz, CD_3CN): δ -78.53.

Synthesis of [(^{Ph}PY5Me$_2$)MoO](OTf)$_2$ (17). 12 was heated to reflux under N_2 in a 3:1 CH_3CN:H_2O mixture for 3 days. The reaction mixture was then cooled to room temperature, concentrated *in vacuo*, and recrystallized from CH_3CN/ether by vapor diffusion to provide green, Xray quality crystals of **17**. ^{1}H NMR (400 MHz, CD_3CN): δ 9.41 (d, 4.8 Hz, 4H), 8.31 (d, 8.4 Hz, 4H), 8.17 (t, 7.9 Hz, 4H), 8.14 (s, 2H), 7.81 (m, 2H), 7.74 (t, 6.6 Hz, 4H), 7.57 (m, 3H), 2.96 (s, 6H). IR (neat; Mo=O): 963 cm^{-1}. This compound could also be prepared from **14** by reaction with degassed water for 2-3 days at room temperature under N_2 in a 3:1 CH_3CN:H_2O mixture followed by salt metathesis with two equivalents AgOTf and recrystallization from CH_3CN/ether.

Synthesis of [(^{CF3}PY5Me$_2$)MoO](OTf)$_2$ (18). A 3:1 CH_3CN:H_2O solution of **13** was heated to reflux under N_2 for 3 days. Upon cooling, the solvent was removed on a

rotary evaporator and the green residue was purified by crystallization from CH_3CN/ether by vapor diffusion. The dark green crystals were rinsed with THF, ether and then dried to provide **18** as a green solid. Xray quality crystals could be obtained from $CH_3CN/^iPr_2O$ by vapor diffusion. ^1H NMR (400 MHz, CD_3CN): δ 9.39 (d, 4.4 Hz, 4H), 8.3 (d, 8.0 Hz, 4H), 8.18 (m, 6H), 7.77 (t, 6.6 Hz, 4H), 2.92 (s, 6H). ^{19}F NMR (376 MHz, CD_3CN): δ -64.77, -78.20. IR (neat; Mo=O): 968 cm^{-1}. This compound could also be prepared from **15** by reaction with degassed water for 2-3 days at room temperature under N_2 in a 3:1 $CH_3CN:H_2O$ mixture followed by salt metathesis with two equivalents AgOTf and recrystallization from $CH_3CN/^iPr_2O$.

General Physical Methods. Mass spectrometry measurements were performed on either an LTQ Orbitrap (Thermo Scientific, West Palm Beach, FL) or Waters Q-TOF Premier (Milford, MA) spectrometer at the QB3/Chemistry Mass Spectrometry Facility at UC Berkeley. Elemental analyses were performed on a Perkin Elmer 2400 Series II combustion analyzer (Waltham, MA) in the Microanalytical Laboratory in the College of Chemistry, University of California, Berkeley, California. Non-aqueous cyclic voltammetry experiments were conducted on a BASi Epsilon potentiostat (West Lafayette, IN) using a glassy carbon disc working electrode, a platinum wire auxiliary, and a platinum wire as a floating reference. Potentials were referenced using either ferrocene or cobaltocene as internal standards. Aqueous CV experiments were performed with a BASi controlled growth mercury elecrode and referenced against a Ag/AgCl reference electrode. IR spectra were measured on a Bruker ALPHA FT-IR with a Platinum ATF accessory. ^1H, ^{13}C, and ^{19}F NMR spectra were recorded on Bruker spectrometers. Chemical shifts are reported in ppm and referenced to residual protiated solvent (for ^1H and ^{13}C) or $CFCl_3$ (for ^{19}F) and coupling constants are reported in Hz. UV-vis spectra were acquired on a Varian Cary 50 BIO UV-Visible Spectrophotometer (Agilent Technologies, Santa Clara, CA) with a Unisoko cryostat attachment for temperature control (Unisoku Co, Osaka, Japan).

Xray Crystallography. See Tables 3.2-3.5 for crystal data for **5**, **6**, **11**, **13**, **14**, and **16** - **18**. Xray crystallographic data was collected using fine-focused Mo-Kα radiation on a Bruker 3-circle Smart-Apex or Siemens Smart 1000 diffractometer with an Apex 1 or Smart 1000 CCD detector, respectively. Samples on Smart-Apex were cooled to 100 K using an Oxford Cryostream 700 low temperature device (or to ca 130 K on the Smart 1000 using a home-built device). Structures were solved using either direct methods or the Patterson method in conjunction with standard difference Fourier techniques and refined by full-matrix least-squares procedures.[26] A semi-empirical absorption correction (SADABS) was applied to the diffraction data for all structures. All non-hydrogen atoms were refined anisotropically, and hydrogen atoms were treated as idealized contributions and refined isotropically. All software used for diffraction data processing and crystal-structure solution and refinement are contained in the APEX2 program suite (Bruker AXS, Madison, WI).[27]

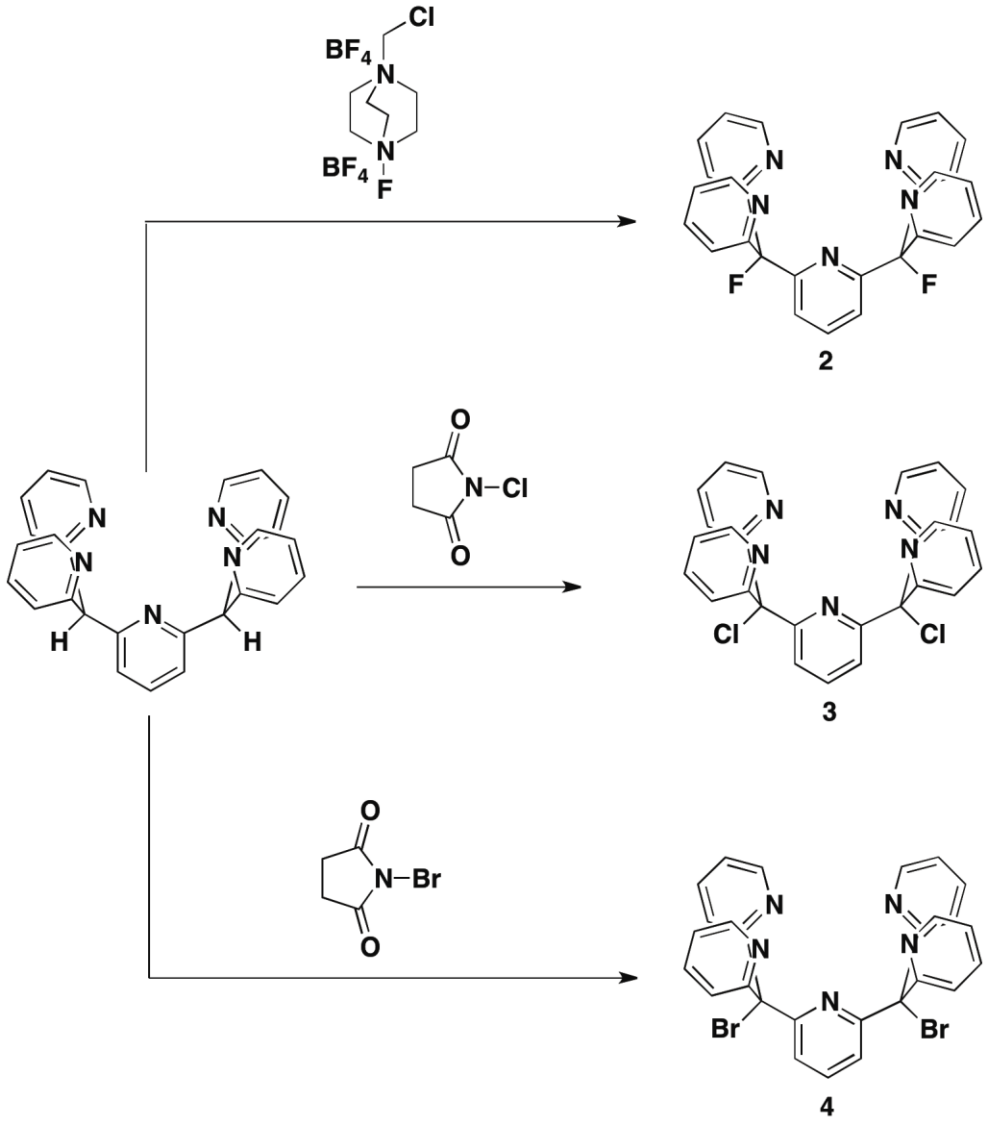

Scheme 3.4. Synthesis of the halogenated PY5 derivatives **2-4**.

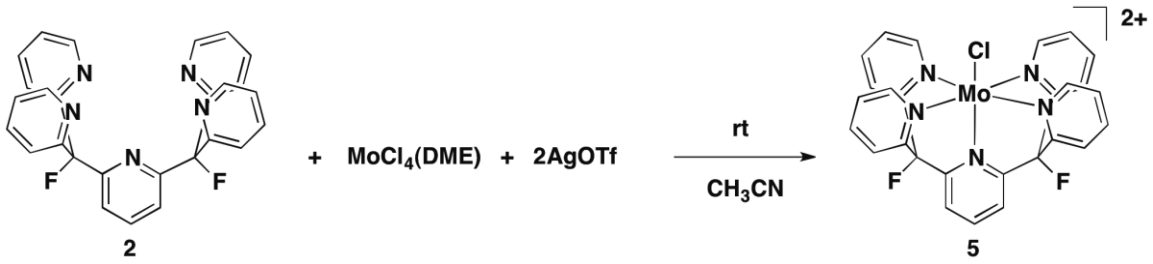

Scheme 3.5. Room temperature synthesis of **5**.

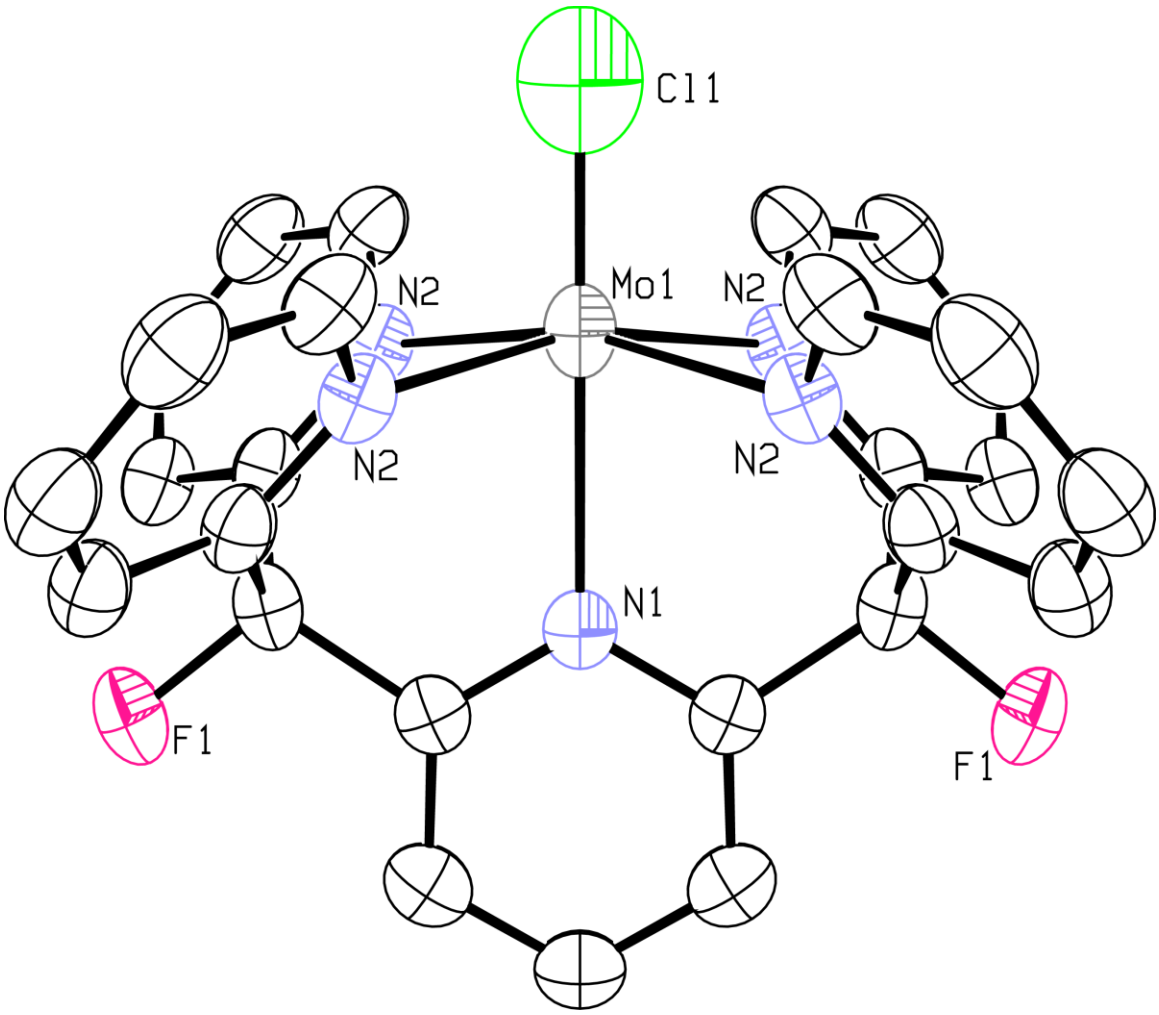

Figure 6.1. The molecular structure of the dication of **5** as determined by Xray diffraction. Hydrogen atoms, triflate counterions, and solvents of crystallization are removed for clarity. Thermal ellipsoids are shown at 50 % probability.

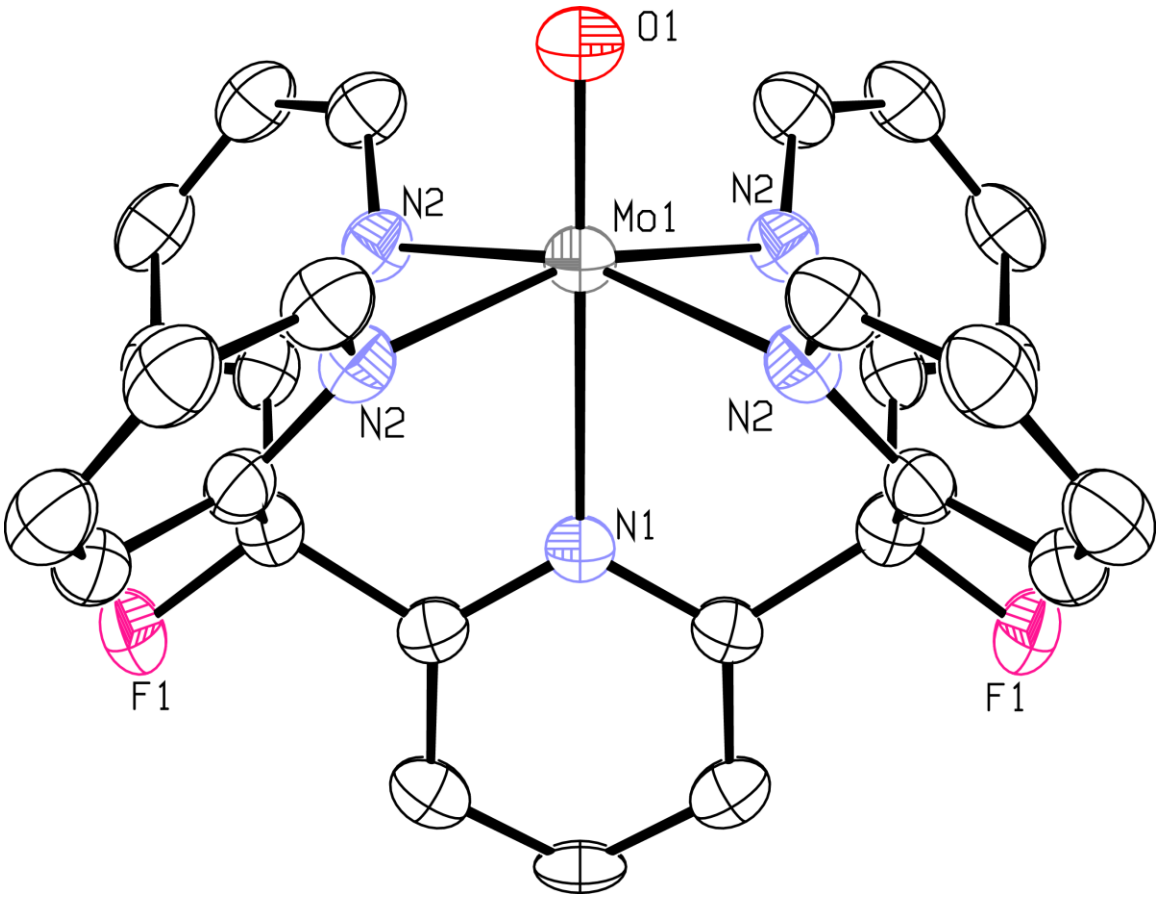

Figure 3.2. The molecular structure of the dication of **6** as determined by Xray diffraction. Hydrogen atoms, triflate counterions, and solvents of crystallization are removed for clarity. Thermal ellipsoids are shown at 50 % probability.

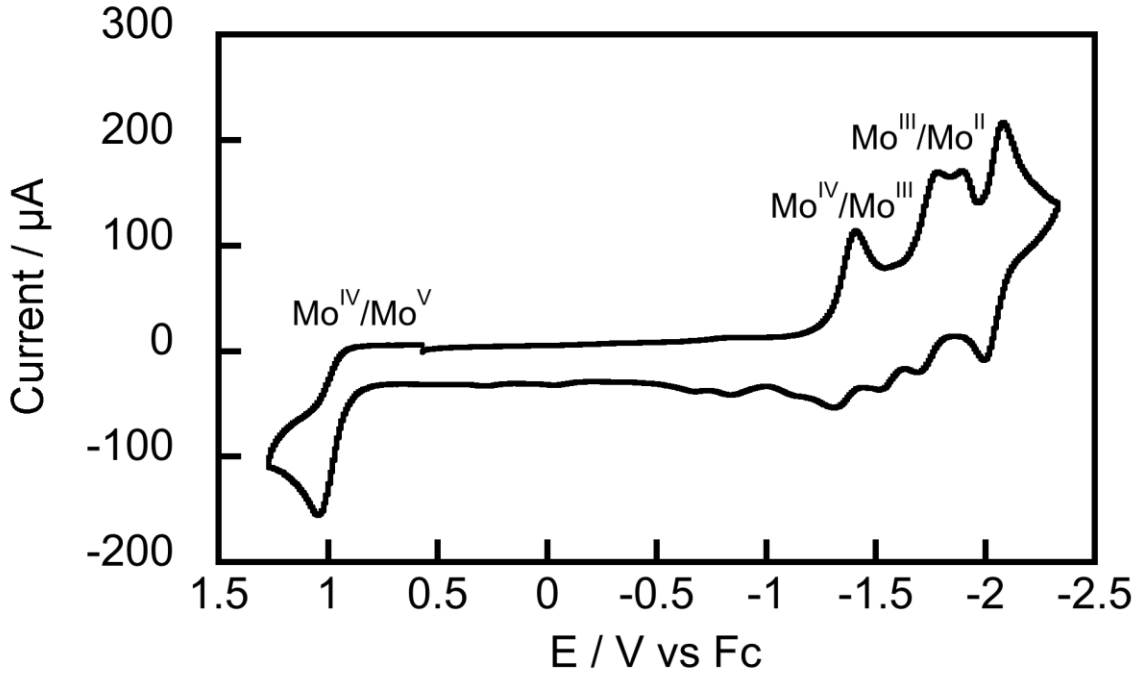

Figure 3.3. Cyclic voltammogram of **6** recorded in 0.1 M $^{n}Bu_4NPF_6$ in acetonitrile. Scan rate: 1000 mV/sec; working electrode: glassy carbon.

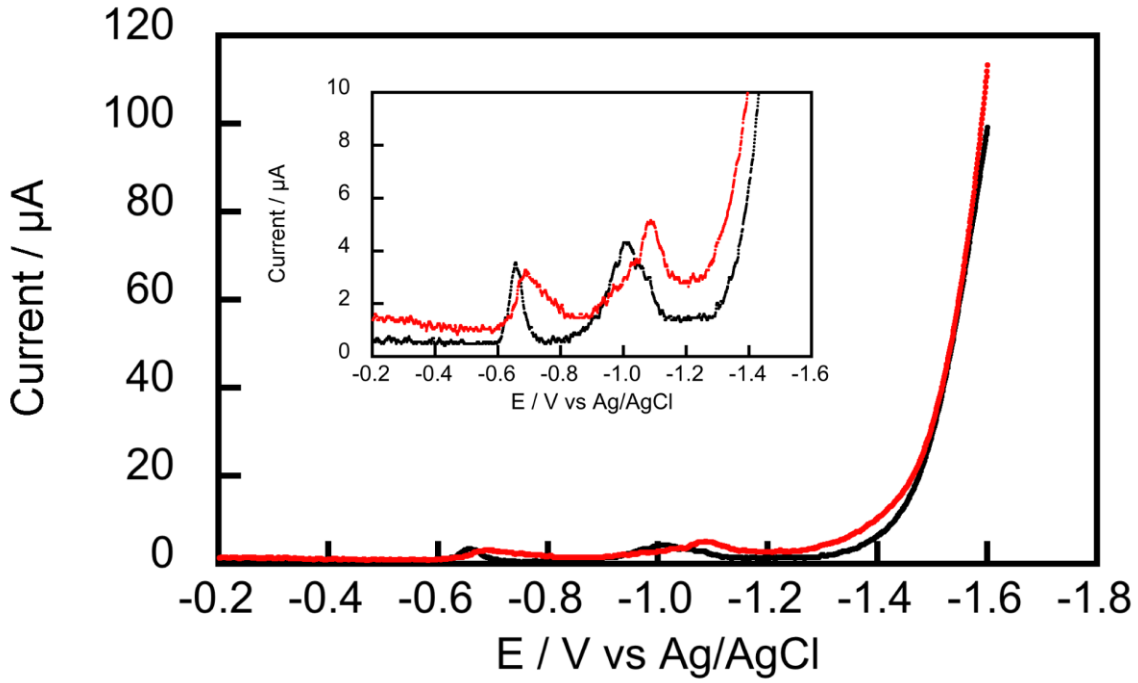

Figure 3.7. The initial sweep of the cyclic voltammograms of **6** (black trace) and **1** (red trace) recorded in phosphate-buffered neutral water. Inset: close-up of the reductive events preceeding catalysis. Scan rate: 700 mV/sec; working electrode: controlled growth mercury electrode; drop size: 8.

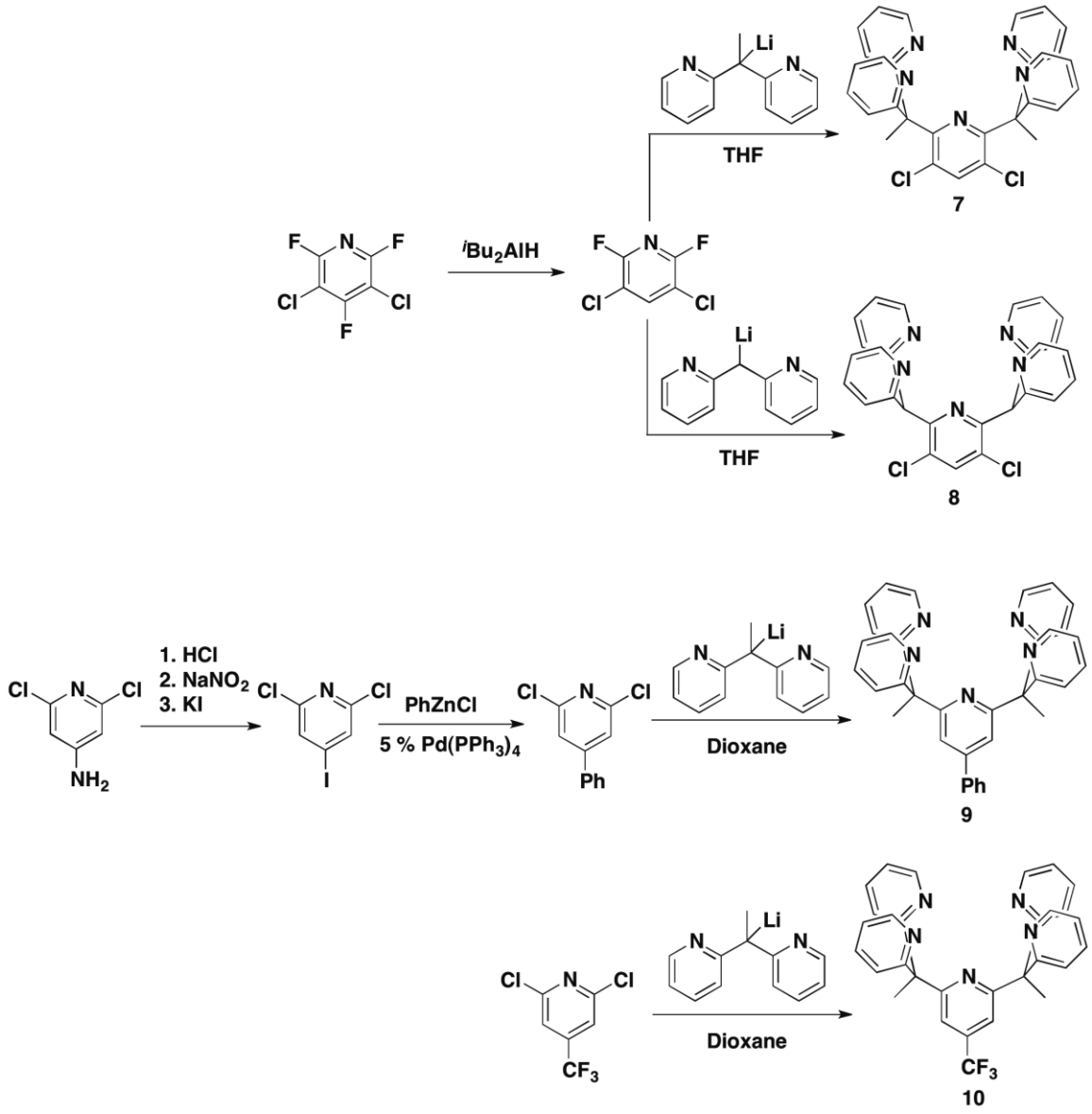

Scheme 3.3. Synthesis of the PY5 derivatives **7**-**10**.

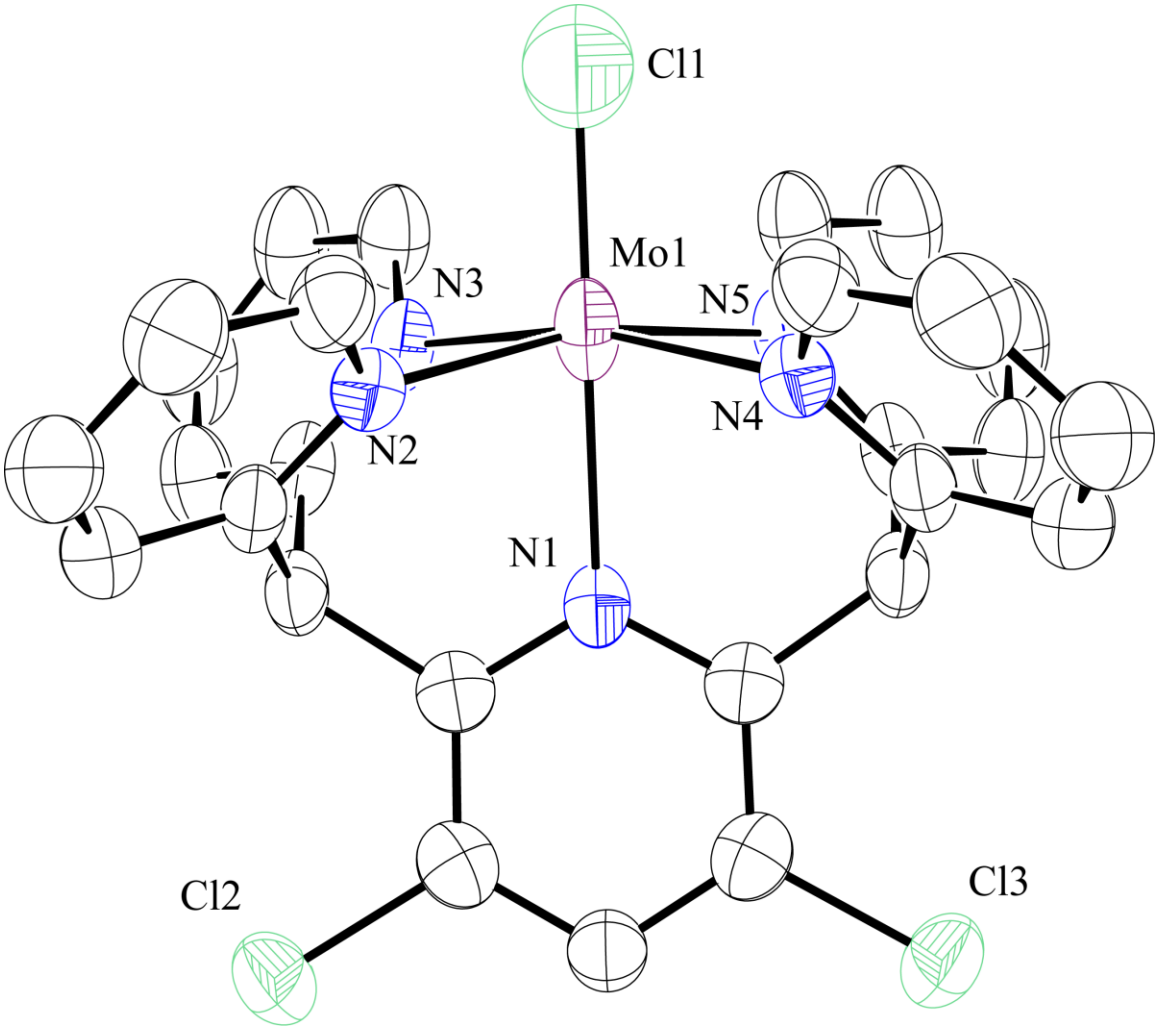

Figure 3.5. Molecular structure of the dicationic portion of **11** as determined by Xray diffraction. Ellipsoids are shown at 50 % probability. Hydrogen atoms, triflate counterions and solvents of crystallization are not shown for clarity.

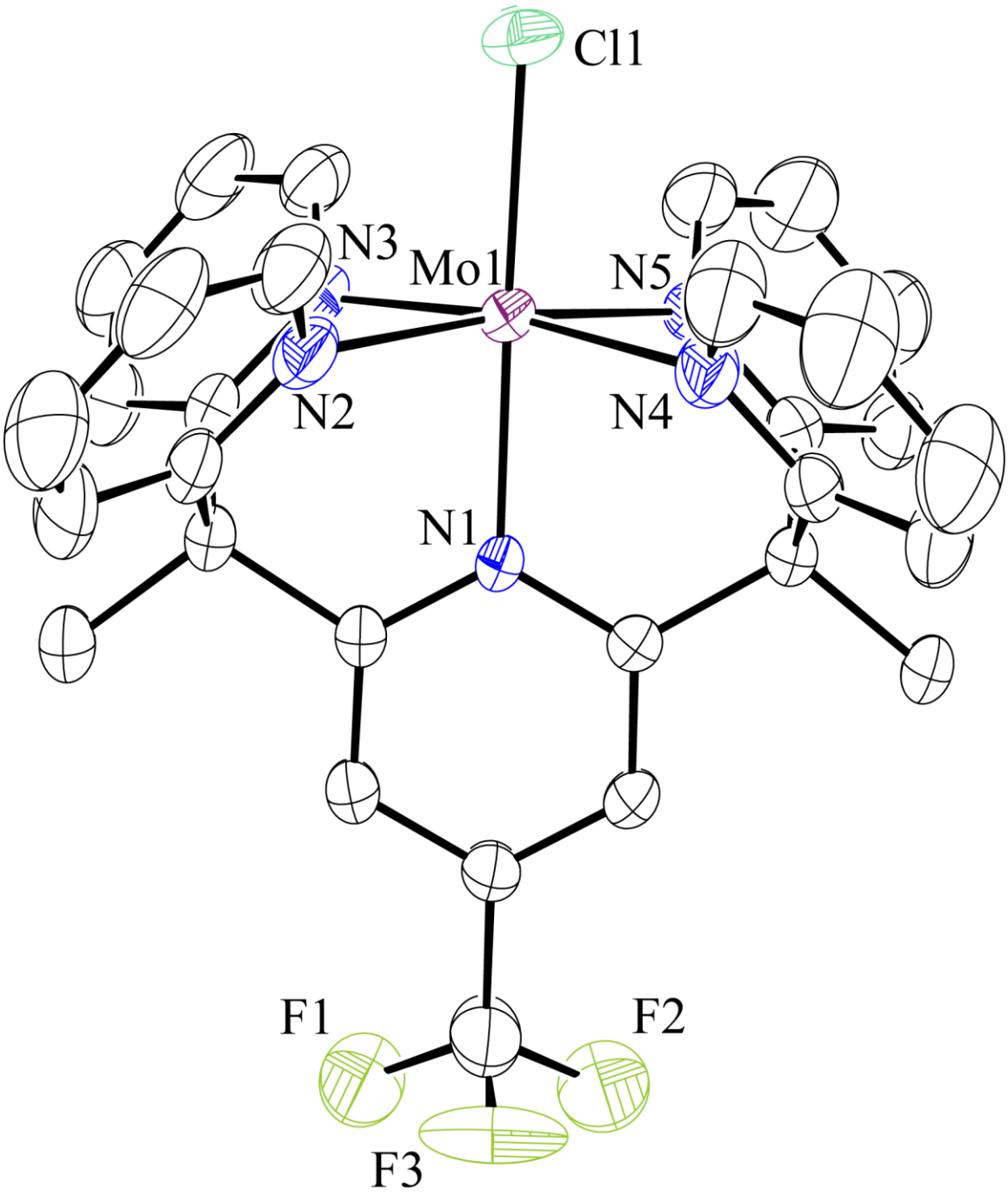

Figure 3.6. Molecular structure of the dicationic portion of **13** as determined by Xray diffraction. Ellipsoids are shown at 50 % probability. Hydrogen atoms, triflate counterions and solvents of crystallization are not shown for clarity.

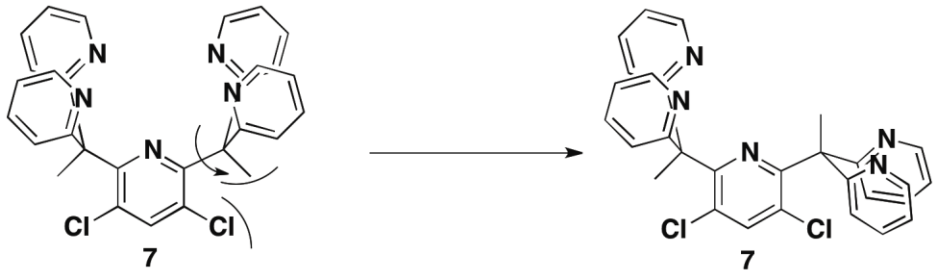

Scheme 3.4. Possible steric clash within **7** makes synthesis of molybdenum complex difficult.

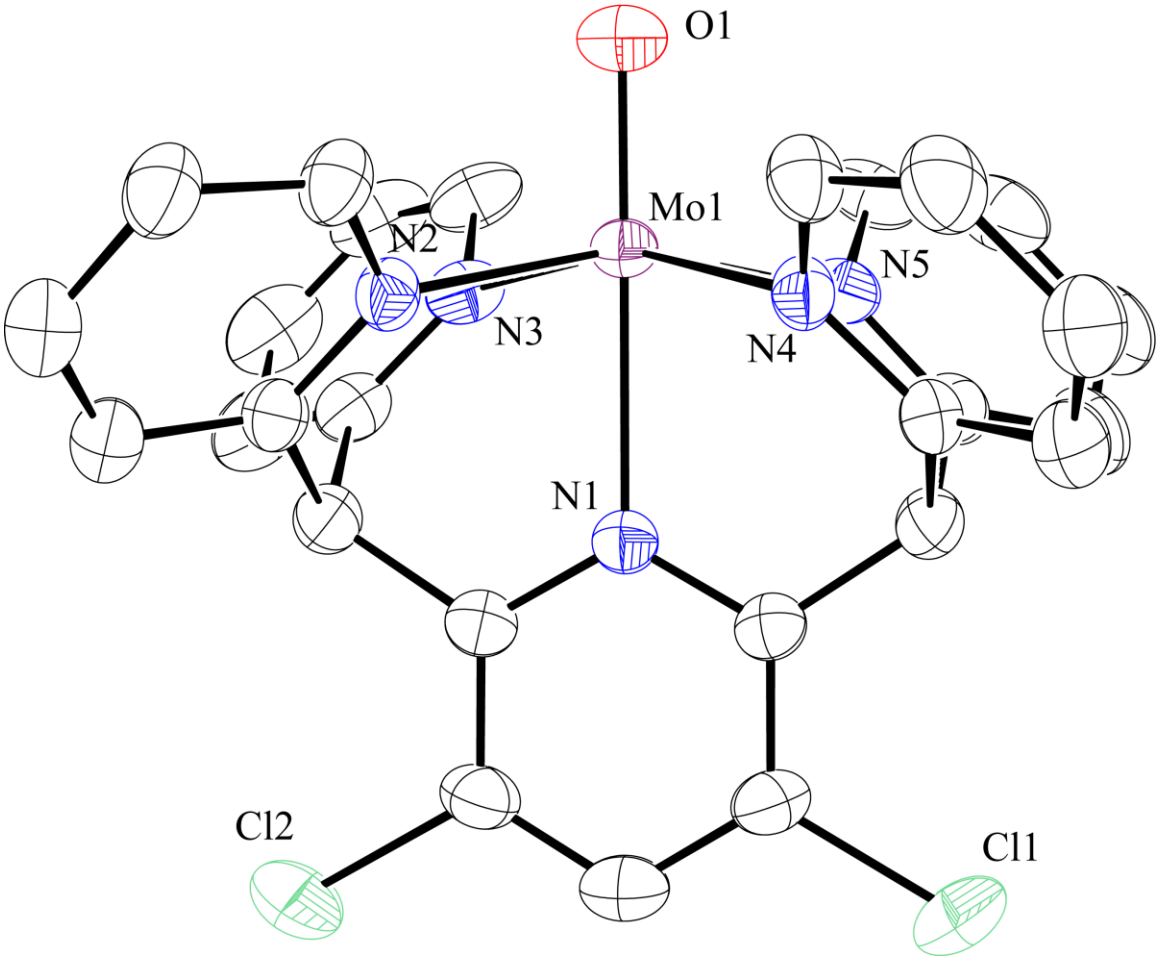

Figure 3.7. Molecular structure of the dicationic portion of **16** as determined by Xray diffraction. Ellipsoids are shown at 50 % probability. Hydrogen atoms, triflate counterions and solvents of crystallization are not shown for clarity.

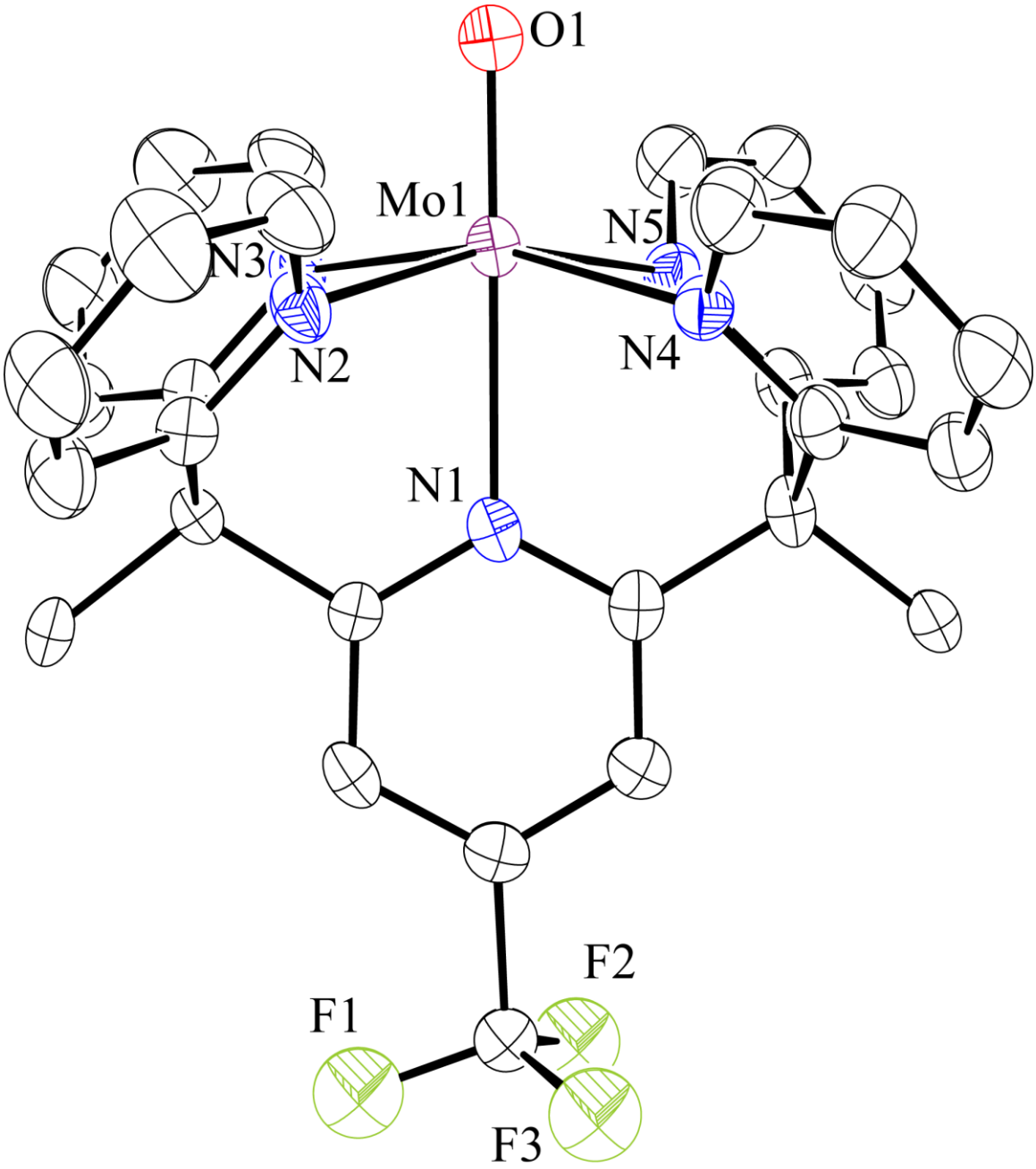

Figure 3.8. Molecular structure of the dicationic portion of the di(iodo) precursor of **18** as determined by Xray diffraction. Ellipsoids are shown at 50 % probability. Hydrogen atoms, iodide counterions and solvents of crystallization are not shown for clarity.

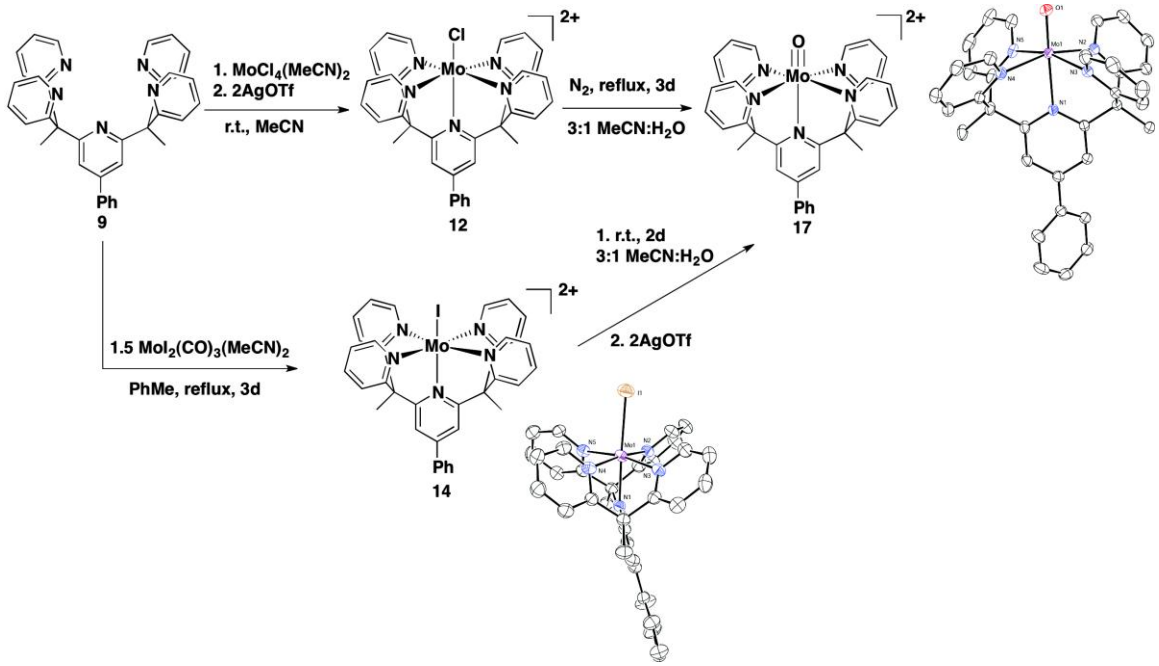

Scheme 3.5. Synthesis of **17** by two routes and the molecular structures of **14** and **17** as determined by Xray crystallography (hydrogen atoms and counterions omitted for clarity; 50 % ellipsoids).

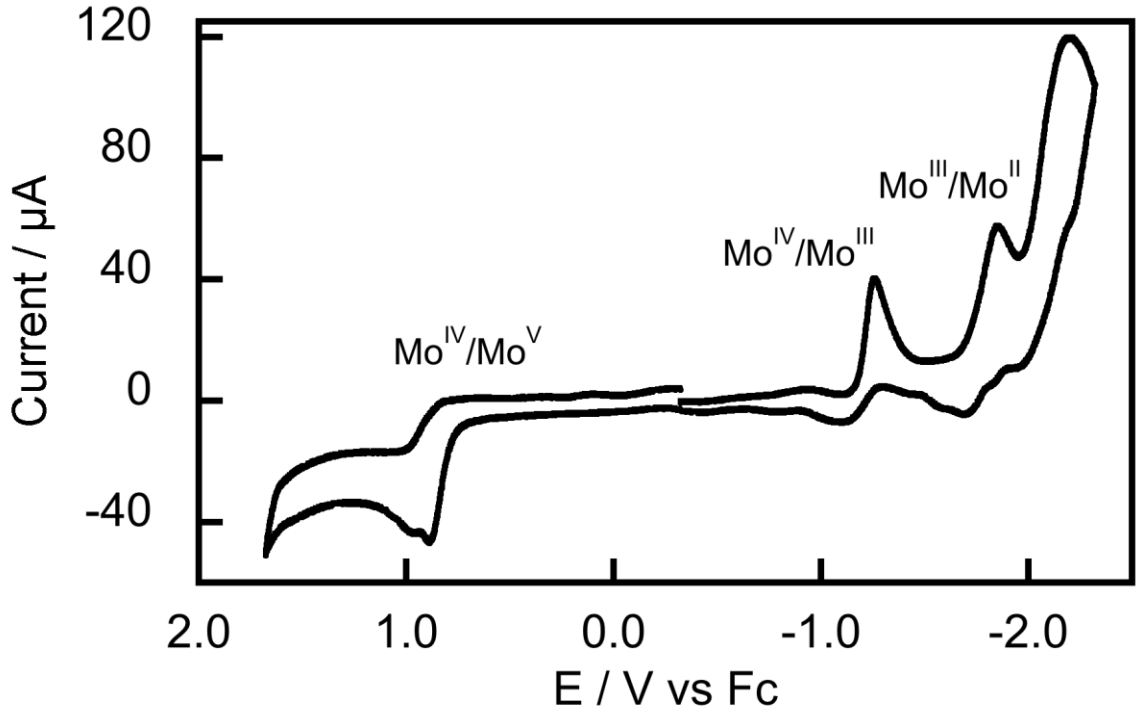

Figure 3.9. Cyclic voltammogram of **16** recorded in 0.1 M $^{n}Bu_4NPF_6$ in acetonitrile. Scan rate: 100 mV/sec; working electrode: glassy carbon.

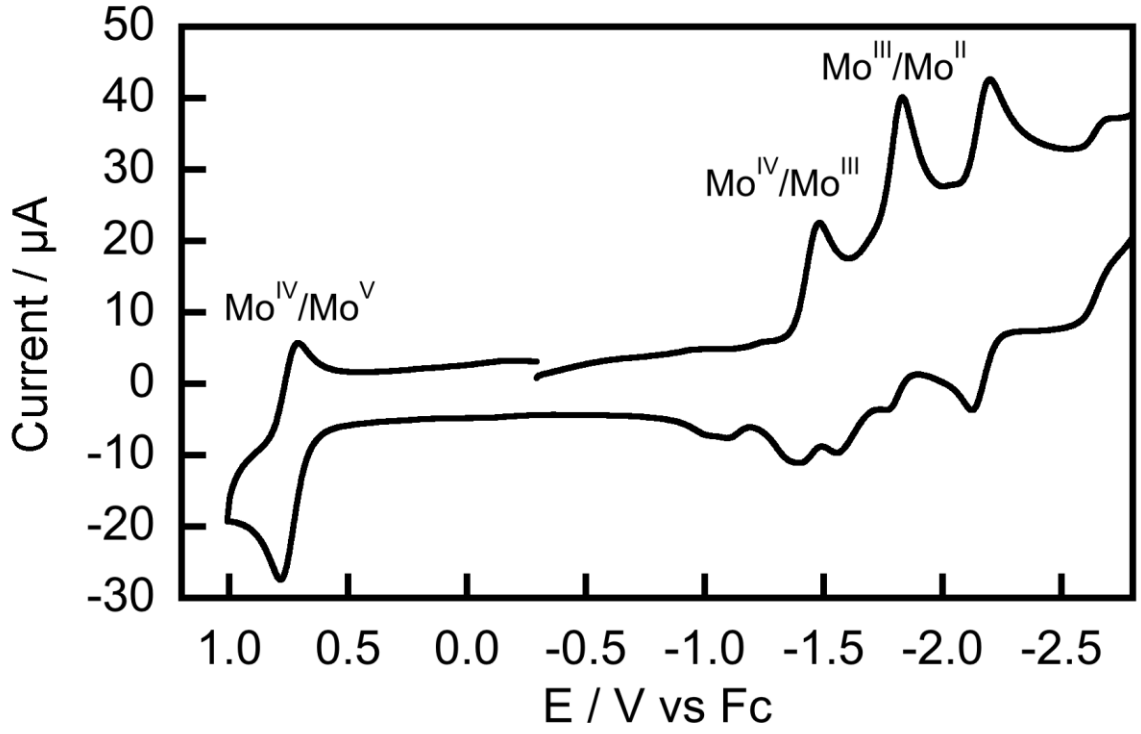

Figure 3.10. Cyclic voltammogram of **17** recorded in 0.1 M $^{n}Bu_4NPF_6$ in acetonitrile. Scan rate: 100 mV/sec; working electrode: glassy carbon.

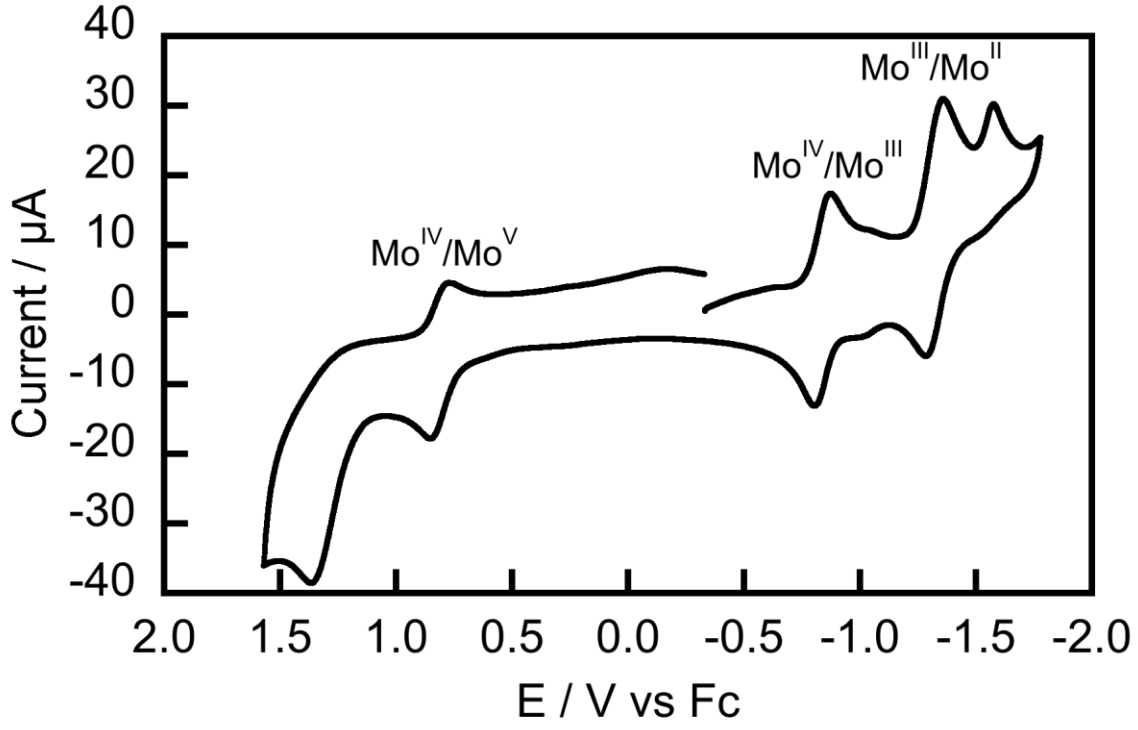

Figure 3.11. Cyclic voltammogram of **18** recorded in 0.1 M $^{n}Bu_4NPF_6$ in acetonitrile. Scan rate: 100 mV/sec; working electrode: glassy carbon.

Table 3.1. Redox potentials for new PY5MoO derivatives.

E (V) vs Fc/Fc^+	**$PyNMe_2$**	**$Py5Me_2$**	**PyPh**	**$PyCF_3$**
Mo(V)/Mo(IV)	0.66	0.754	0.75	0.8
Mo(IV)/Mo(III)	-1.637	-1.489	-1.44	-0.84
Mo(III)/Mo(II)	-2.107	-1.882	-1.80	-1.32

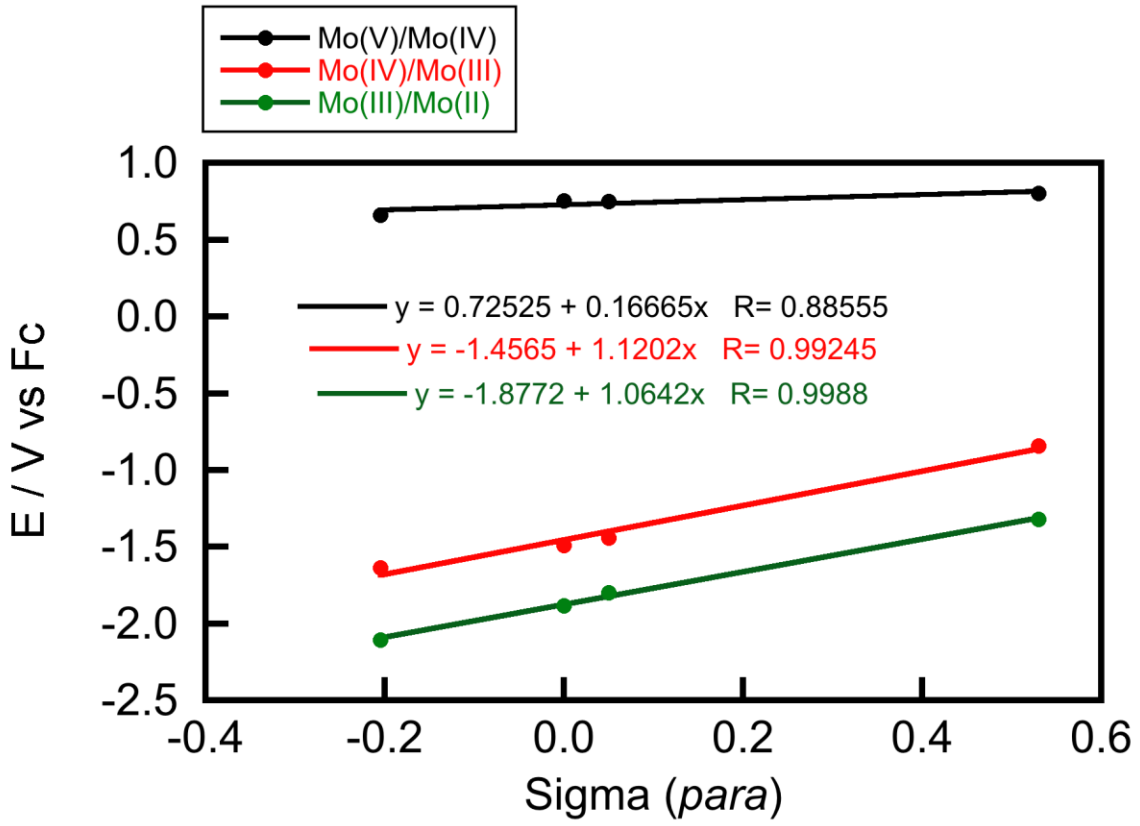

Figure 3.12. Hammett plot showing the effect of the *para*-substituent on the redox potentials of $[(^{R}PY5Me_2)MoO]^{2+}$ derivatives.

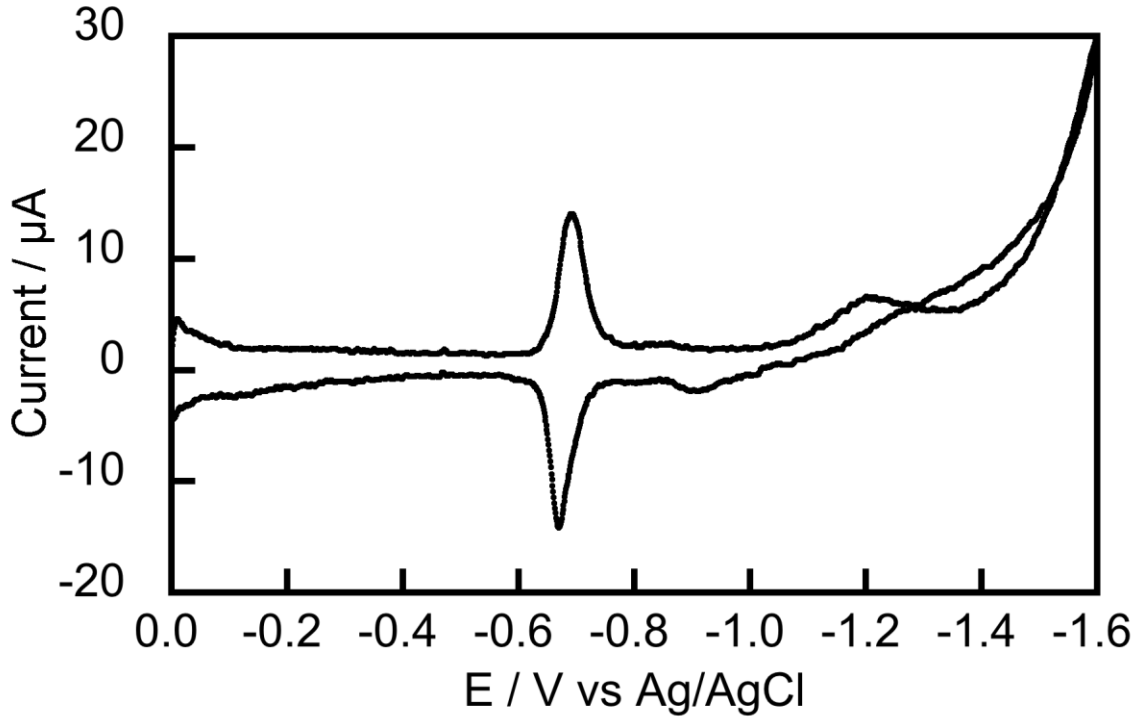

Figure 3.13. Cyclic voltammogram of **16** recorded in phosphate-buffered neutral water. Scan rate: 5120 mV/sec; working electrode: controlled growth mercury electrode; drop size: 8.

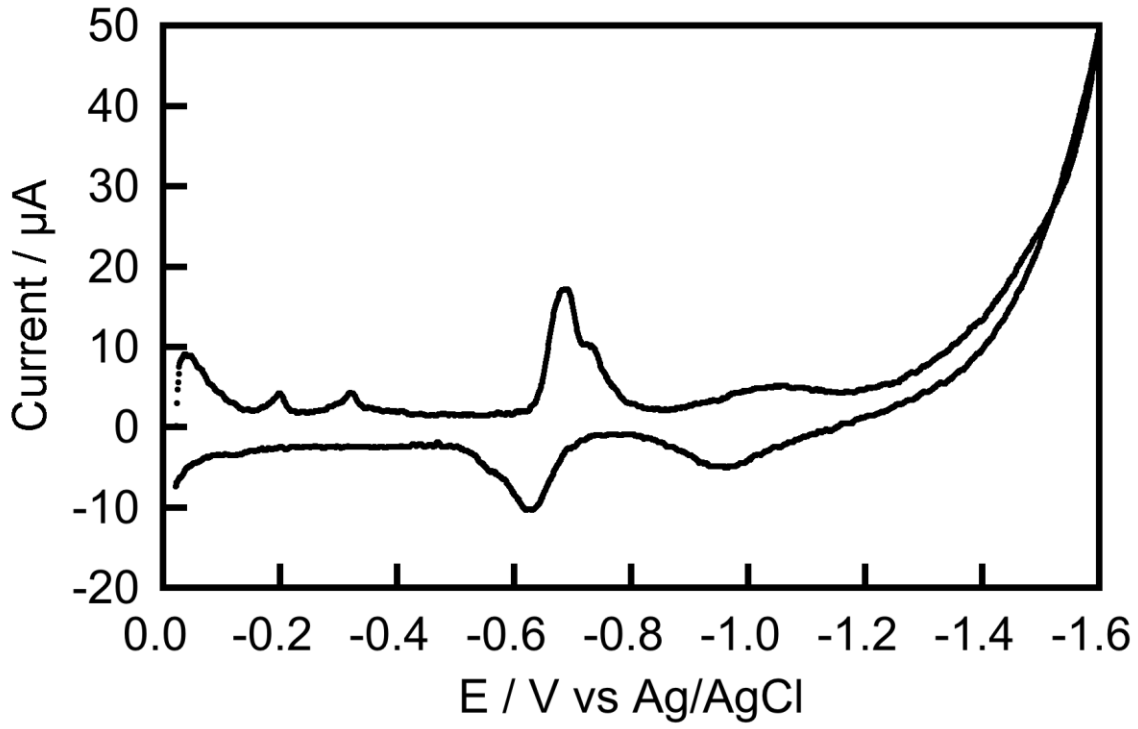

Figure 3.14. Cyclic voltammogram of **17** recorded in phosphate-buffered neutral water. Scan rate: 5120 mV/sec; working electrode: controlled growth mercury electrode; drop size: 8.

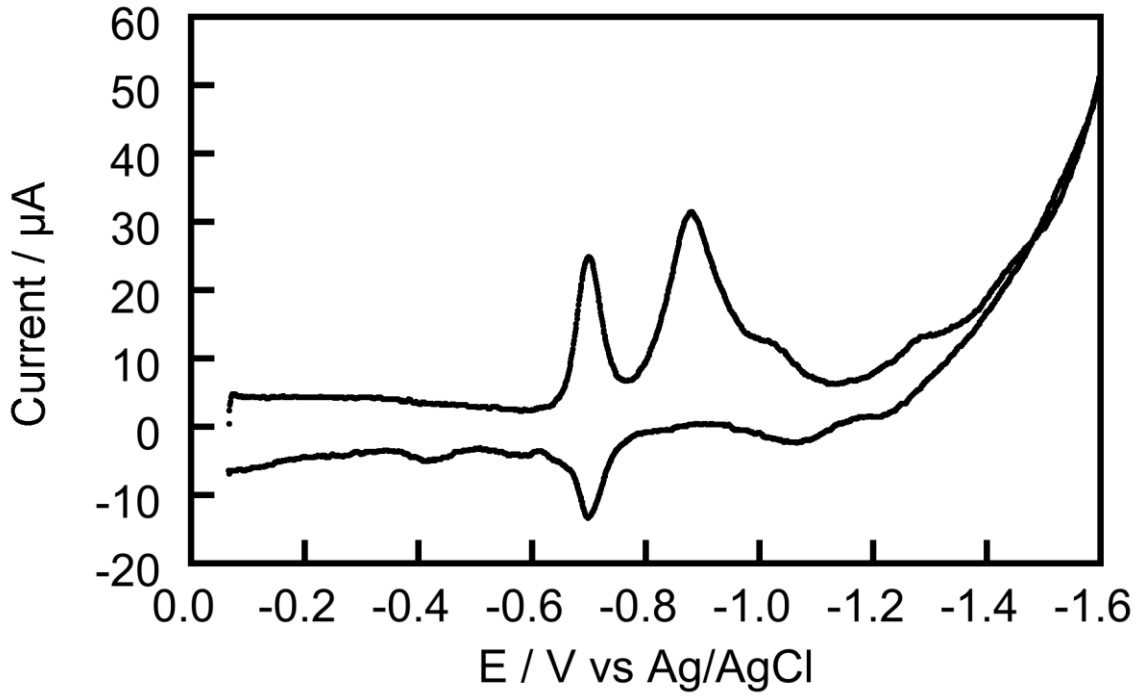

Figure 3.15. Cyclic voltammogram of **18** recorded in phosphate-buffered neutral water. Scan rate: 5120 mV/sec; working electrode: controlled growth mercury electrode; drop size: 8.

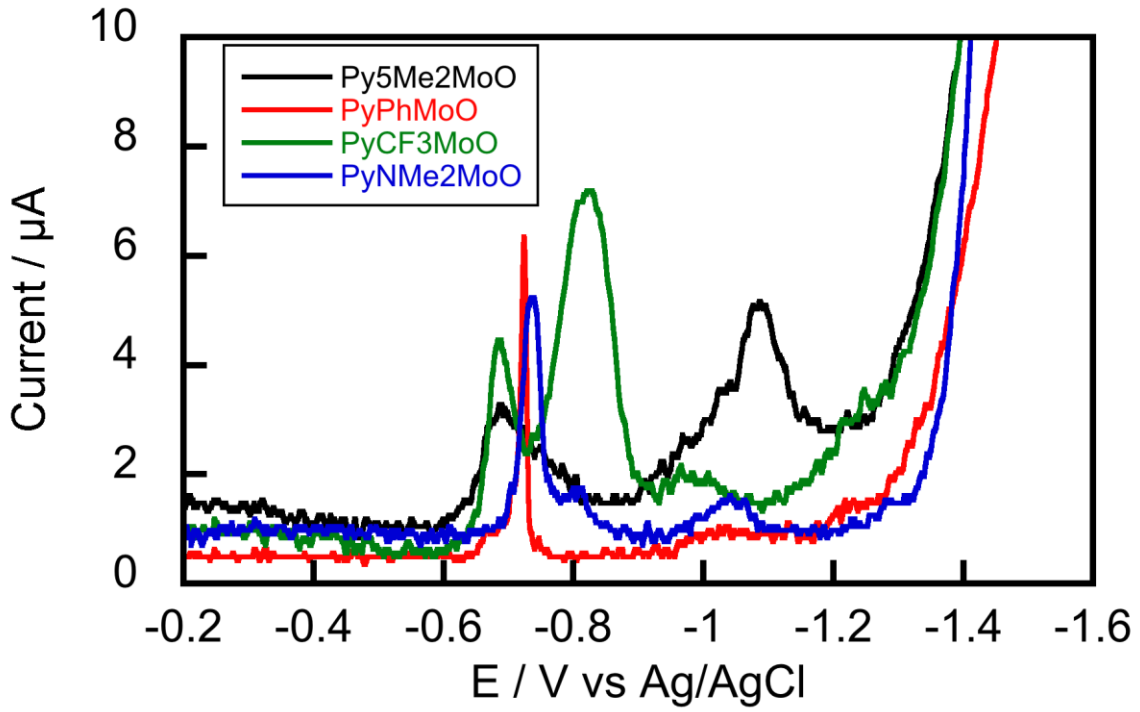

Figure 3.16. Initial sweep of the CVs under electrocatalytic conditions for **1**, **17**, **18**, and $[(^{NMe2}PY5)MoO]^{2+}$. Scan rate: 700 mV/sec; working electrode: controlled mercury growth electrode; drop size: 8.

Table 3.2. Crystallographic Details for **5** and **6**.		
	5	**6**
Empirical Formula	$C_{31}H_{24}ClF_8MoN_6O_6S_2$	$C_{29}H_{21}F_8MoN_5O_7S_2$
Formula Weight	924.07	863.57
T (K)	145	133
λ (Å)	0.71073	0.71073
Crystal System	Cubic	Cubic
Space Group	*Im-3*	*Im-3*
a (Å)	23.0200(17)	22.9445(19)
b (Å)	23.0200(17)	22.9445(19)
c (Å)	23.0200(17)	22.9445(19)
α (º)	90.00	90.00
β (º)	90.00	90.00
γ (º)	90.00	90.00
V	12198.8(16)	12079.1(17)
Z	16	16
ρ_{calc} (g/cm^3)	2.013	1.899
μ (mm^{-1})	0.766	0.682
reflctns collected	73716	115634
T_{min}/T_{max}	0.89	0.87
data/restr/params	2009/19/180	1996/19/175
$2\theta_{max}$ (º)	50.6	50.6
R, R_w (%; I>4σ)	6.6, 22.1	7.7, 25.5
GOF	1.041	0.912
mean shift/error	0.007	0.018

Table 3.3. Crystallographic Details for **11** and **13**.		
	11	**13**
Empirical Formula	$C_{29}H_{19}Cl_3F_6MoN_5O_6S_2$	$C_{34}H_{27}ClF_9MoN_6O_6S_2$
Formula Weight	913.90	982.13
T (K)	178	139
λ (Å)	0.71073	0.71073
Crystal System	Tetragonal	Orthorhombic
Space Group	*I4/m*	*Pnma*
a (Å)	24.429(5)	18.3389(11)
b (Å)	24.429(5)	22.9450(14)
c (Å)	13.344(3)	9.9864(6)
α (º)	90.00	90.00
β (º)	90.00	90.00
γ (º)	90.00	90.00
V	7964(3)	4202.1(4)
Z	8	4
ρ_{calc} (g/cm^3)	1.525	1.552
μ (mm^{-1})	0.708	0.564
reflctns collected	50530	81401
T_{min}/T_{max}	0.88	0.88
data/restr/params	3809/0/293	3955/19/396
$2\theta_{max}$ (º)	50.6	50.7
R, R_w (%; I>4σ)	8.2, 25.4	4.3, 15.3
GOF	1.868	0.646
mean shift/error	0.179	0.001

Table 3.4. Crystallographic Details for **16** and **18(I_2 salt)**.		
	16	**18(I_2 salt)**
Empirical Formula	$C_{29}H_{19}Cl_2F_6MoN_5O_7S_2$	$C_{30}H_{24}F_3I_2MoN_5O$
Formula Weight	894.45	877.28
T (K)	143	127
λ (Å)	0.71073	0.71073
Crystal System	Orthorhombic	Monoclinic
Space Group	*Pnma*	*P2(1)/m*
a (Å)	21.361(3)	9.5358(6)
b (Å)	13.2054(15)	20.3562(13)
c (Å)	13.6109(16)	9.8948(7)
α (º)	90.00	90.00
β (º)	90.00	111.9640(10)
γ (º)	90.00	90.00
V	3839.4(8)	1781.3(2)
Z	4	2
ρ_{calc} (g/cm^3)	1.547	1.636
μ (mm^{-1})	0.667	2.145
reflctns collected	19552	24028
T_{min}/T_{max}	0.8	0.85
data/restr/params	3675/0/296	3363/0/264
$2\theta_{max}$ (º)	50.8	50.7
R, R_w (%; I>4σ)	5.7, 16.9	4.3, 13.7
GOF	1.010	0.929
mean shift/error	0.016	0.113

Table 3.5. Crystallographic Details for **14** and **17**.		
	14	**17**
Empirical Formula	$C_{35}H_{30}I_3MoN_5O$	$C_{37}H_{29}F_6MoN_5O_7S_2$
Formula Weight	1013.28	929.71
T (K)	146	
λ (Å)	0.71073	0.71073
Crystal System	Monoclinic	Monoclinic
Space Group	*P2(1)/c*	*P2(1)/c*
a (Å)	29.491(3)	15.5448(9)
b (Å)	16.7542(18)	13.3512(7)
c (Å)	16.7170(18)	17.7620(10)
α (º)	90.00	90.00
β (º)	110.256(2)	98.2530(10)
γ (º)	90.00	90.00
V	7749.0(14)	3648.2(4)
Z	8	4
ρ_{calc} (g/cm^3)	1.737	1.693
μ (mm^{-1})	2.761	0.564
reflctns collected	80684	59838
T_{min}/T_{max}	0.73	0.86
data/restr/params	7102/0/449	6683/225/596
$2\theta_{max}$ (º)	50.8	50.7
R, R_w (%; I>4σ)	12.7, 36.7	3.0, 9.0
GOF	2.583	0.998
mean shift/error	0.181	0.008

References

(1) Turner, J. A. *Science* **2004**, *305*, 972-974.

(2) Lewis, N. S.; Nocera, D. G. *Proceedings of the National Academy of Sciences* **2006**, *103*, 15729-15735.

(3) Ott, S. *Science* **2011**, *333*, 1714-1715.

(4) Esswein, A. J.; Nocera, D. G. *Chemical Reviews* **2007**, *107*, 4022-4047.

(5) Sun, L.; Åkermark, B.; Ott, S. *Coordination Chemistry Reviews* **2005**, *249*, 1653-1663.

(6) Dempsey, J. L.; Brunschwig, B. S.; Winkler, J. R.; Gray, H. B. *Accounts of Chemical Research* **2009**, *42*, 1995-2004.

(7) DuBois, M. R.; DuBois, D. L. *Chemical Society Reviews* **2009**, *38*, 62-72.

(8) Evans, D. J.; Pickett, C. J. *Chemical Society Reviews* **2003**, *32*, 268-275.

(9) Frey, M. *ChemBioChem* **2002**, *3*, 153-160.

(10) Gloaguen, F.; Rauchfuss, T. B. *Chemical Society Reviews* **2009**, *38*, 100-108.

(11) Koelle, U. *New journal of chemistry(1987)* **1992**, *16*, 157-169.

(12) Bigi, J. P.; Hanna, T. E.; Harman, W. H.; Chang, A.; Chang, C. J. *Chemical Communications* **2010**, *46*, 958-960.

(13) Karunadasa, H. I.; Chang, C. J.; Long, J. R. *Nature* **2010**, *464*, 1329-1333.

(14) Sun, Y.; Bigi, J. P.; Piro, N. A.; Tang, M. L.; Long, J. R.; Chang, C. J. *Journal of the American Chemical Society* **2011**, *133*, 9212-9215.

(15) Sundstrom, E. J.; Yang, X.; Thoi, V. S.; Karunadasa, H. I.; Chang, C. J.; Long, J. R.; Head-Gordon, M. *Journal of the American Chemical Society* **2012**, *134*, 5233-5242.

(16) Thoi, V. S.; Karunadasa, H. I.; Surendranath, Y.; Long, J. R.; Chang, C. J. *Energy & Environmental Science* **2012**.

(17) Karunadasa, H. I.; Montalvo, E.; Sun, Y.; Majda, M.; Long, J. R.; Chang, C. J. *Science* **2012**, *335*, 698-702.

(18) Baker, P. K.; Fraser, S. G.; Keys, E. M. *Journal of Organometallic Chemistry* **1986**, *309*, 319-321.

(19) Gilbert, T. M.; Landes, A. M.; Rogers, R. D. *Inorganic Chemistry* **1992**, *31*, 3438-3444.

(20) Parkin, G. *Accounts of Chemical Research* **1992**, *25*, 455-460.

(21) Dilworth, J. R.; Richards, R. L.; Chen, G. J. J.; McDonald, J. W. In *Inorganic Syntheses*; John Wiley & Sons, Inc.: 1980, p 119-127.

(22) Dyker, G.; Muth, O. *European Journal of Organic Chemistry* **2004**, *2004*, 4319-4322.

(23) Chambers, R. D.; Hall, C. W.; Hutchinson, J.; Millar, R. W. *Journal of the Chemical Society, Perkin Transactions 1* **1998**, 1705-1714.

(24) Mello, J. V.; Finney, N. S. *Organic Letters* **2001**, *3*, 4263-4265.

(25) Finger, G. C.; Starr, L. D.; Dickerson, D. R.; Gutowsky, H. S.; Hamer, J. *The Journal of Organic Chemistry* **1963**, *28*, 1666-1668.

(26) Sheldrick, G. M. *Acta Crystallographica Section A* **1990**, *46*, 467-473.

(27) Sheldrick, G. M. *Acta Crystallographica Section A* **2008**, *64*, 112-122.

Chapter 4
Stabilization of an Iron(IV)-oxo Complex by Ligand Deuteration

Introduction

Our group recently reported the synthesis, characterization and preliminary reactivity of a novel, S = 2 iron(IV)-oxo complex of the tris(pyrrolide) ligand platform tpa^{Ph}, $[(tpa^{Ph})FeO]^-$ (**1**), at low temperature in acetonitrile to add to the short, but growing list of synthetic, high-spin iron(IV)-oxo complexes.[1-5] Synthetic, high-spin iron(IV)-oxo complexes are of interest due to their rarity, high predicted reactivity relative to the more common intermediate spin (S = 1) analogs[6-8] as well as in the context of non-heme iron enzymes, for which S = 2 iron(IV)-oxo intermediates have been characterized in a few cases.[9] Upon warming in the absence of an external substrate **1** decomposed to the iron(III)-phenoxide product **2**, a reaction with precedent in the literature for iron-based oxidants.[10-14] In that same work, we described the observation that for the related iron complex $[(tpa^{Mes})Fe^{II}]^-$ (**3**), an iron(IV)-oxo complex was not observed, although the observed iron(III)-alkoxide product (**4**) implied the presence of a transient iron(IV)-oxo intermediate apparently capable of intramolecular CH activation of the ligand. This observation built on previous work from our group with **3** in ethereal solvents wherein the same putative iron(IV)-oxo intermediate effected intermolecular CH activation of the solvent to yield the iron(III)-hydroxide complex **5**.[10] Intrigued by the diverse reactivity of **3** in different solvents, we sought to explore the oxidation of **3** (and a deuterated analog **10**, *vide infra*) in non-coordinating solvents (Scheme 4.1).

Results and Discussion

Oxidation of $[(tpa^{Mes})Fe^{II}]^-$ in DME with Trimethylamine-*N*-oxide

As described previously,[10] the oxidation of **3** in ethereal solvents using pyridine-*N*-oxide yields the ironIII)-hydroxide complex **5**. Since **3** does not react with pyridine-*N*-oxide in CH_3CN,[1] we first investigated the oxidation of **3** with trimethylamine-*N*-oxide (tmao) for comparison with the reactions with tmao described below. Not surprisingly, the oxidation of **3** with tmao in DME provides **5**, the same product as the pyridine-*N*-oxide reaction, albeit in lower yield.[10]

The Isolation of a C-C Coupled Dimer following Oxidation of $[(tpa^{Mes})Fe^{II}]^-$ in Toluene

We next performed the oxidation of **3** with tmao in toluene. Surprisingly, crystallization of the solution provides a yet unseen oxidation product, the C-C coupled iron(III) dimer **6**, likely the result of radical coupling of benzylic radicals formed from H-atom abstraction by an iron(IV)-oxo intermediate (Scheme 4.1). The molecular structure of **6**, as determined by Xray crystallography, is shown in Figure 4.1. At this stage, it is unclear why the stability of the benzylic radical (with respect to radical rebound) is heightened in toluene relative to acetonitrile, wherein the product is the iron(III)-alkoxide **4**.

Ligand Deuteration leads to Observation of an Iron(IV)-oxo Complex

In light of the isolation of **4** and **6** from benzylic CH oxidation we turned to ligand deuteration to stabilize the implied metal-oxo intermediate, reasoning that the observed benzylic oxidations likely proceed via rate-determining H-atom abstraction. This strategy was recently employed successfully by Que and coworkers in their isolation of the first S = 2 iron(IV)-oxo complex sufficiently stable for Xray crystallographic studies.[2] The deuterated ligand $H_3tpa^{Mes\text{-}d}$ is synthesized in three steps from d_{12}-1,3,5-trimethylbenzene following literature procedures for the protio analog.[10,15] First, d_{12}-1,3,5-trimethylbenzene

is brominated with NBS in acetone to yield d_{11}-mesitylbromide (**7**) in near quantitative yield[15], followed by Pd-catalyzed cross coupling with sodium pyrrole to provide the aryl pyrrole (**8**)[16]. A triple Mannich reaction then affords the deuterated ligand $H_3tpa^{Mes\text{-}d}$ (**9**) in 87 % yield.[10]

Oxidation of the deuterated analog of **3**, $[(tpa^{Mes\text{-}d})Fe^{II}]^-$, **10**, in acetonitrile at -40 ºC with tmao provides a new species with a UV/vis absorbance near 400 nm that forms with an isosbestic point at 320 nm (Figure 4.2). However, the lack of a discernible near-IR band is inconsistent with the presence of an iron(IV)-oxo complex. In contrast, tmao oxidation of **10** in 1,2-difluorobenzene affords a new species, **11**, with a UV/vis spectrum with a strong band near 400 nm and a weak near-IR band around 850 nm, suggesting the presence of an iron(IV)-oxo complex (Figure 4.3). Note that the oxidation of **3** does not produce the near-IR band, suggesting ligand deuteration is necessary for the observation of **11**. ESI MS (*m/z* calcd for $C_{42}H_{12}D_{33}FeN_4O$ 710.50, found at 710.53) and Mössbauer spectroscopy (δ: 0.06 mm/sec; ΔE_q: 0.14 mm/sec) confirm the presence of an iron(IV)-oxo complex analogous to **1**, $[(tpa^{Mes\text{-}d})FeO]^-$ (Figures 4.4 and 4.5). The interesting solvent dependence of the observation of **11** is likely the result of reversible acetonitrile coordination to **10**, which prevents the build up of sufficient quantities of **11** necessary for spectroscopic observation. This coordination didn't hamper observation of **1** in acetonitrile, as its precursor $[(tpa^{Ph})Fe^{II})]^-$ doesn't bind acetonitrile.

Reactivity of $[(tpa^{Mes\text{-}d})FeO]^-$ and Comparison to $[(tpa^{Ph})FeO]^-$

A brief survey of the reactivity of **11** is consistent with its assignment as an iron(IV)-oxo complex capable of both CH oxidation and O-atom transfer. Firstly, similar to the $[(tpa^{Ph})FeO]^-$ analog **1**, **11** reacts with 1,4-cyclohexadiene and dimethylphenylphosphine to provide benzene and the phosphine oxide, respectively. Secondly, **11** reacts with 9,10-dihydroanthracene to yield anthracene and a small amount of anthraquinone. This suggests both that **11** is less sterically shielded than **1** (which doesn't react with 9,10-dihydroanthracene) and capable of hydroxylation of weak aliphatic CH bonds, a reactivity unavailable to **1**. Future studies will focus on characterizing the electronic structure of **11** by parallel-mode EPR and XAS/EXAFS to compare with that previously determined for **1**.

Concluding Remarks

In conclusion, we have furthered our understanding of the oxidative behavior of the tris(pyrrolide) iron complex $[(tpa^{Mes})Fe^{II}]^-$ (**3**). In toluene the oxidation of **3** with tmao provides a novel C-C coupled dimer that is the result of coupling of two benzylic radicals formed from H-atom abstraction by an unobserved iron(IV)-oxo intermediate. In contrast, oxidation of the deuterated analog of **3** ($[(tpa^{Mes\text{-}d})Fe^{II}]^-$, **10**) with tmao in 1,2-difluorobenzene yields a novel iron(IV)-oxo complex, **11**. As was observed by Que and coworkers, ligand deuteration is integral to the stabilization of **11**, likely because of rate-determining H-atom abstraction being the primary means of decomposition.[2]

Experimental Section

General Synthetic Details. Unless otherwise noted, all synthetic manipulations were performed under an inert atmosphere of dinitrogen in a Vacuum Atmospheres glovebox or on a vacuum line using standard Schlenk technique. Solvents were dried on a Vacuum Atmospheres solvent purification system and stored over 3 Å molecular sieves.

Molecular sieves, alumina, and celite were activated by heating at 200ºC under dynamic vacuum for at least 24 hours. All glassware was dried in an oven at 170 ºC for at least 12 hours before use. Potassium hydride was purchased as a suspension in mineral oil, washed with pentane and used as a dry solid in the glovebox. 1,4-Cyclohexadiene was degassed with three freeze, pump, thaw cycles and dried over 3 Å molecular sieves. d_{12}-mesitylene was purchased from Cambridge Isotope Laboratories (Andover, MA). The iron complexes [(tpa^{Mes})Fe^{II}][K(dme)$_2$] (**8**) and [(tpa$^{Mes\text{-}d}$)Fe^{II}][K(dme)$_2$] (**10**) were prepared according to a literature procedure.[10] All other reagents were purchased from Sigma-Aldrich and used as received.

Synthesis of [(tpa^{Mes})FeOH][K(DME)] (5) using TMAO. To a stirring DME solution of **3** (74 mg, 0.084 mmol) was added tmao (13 mg, 0.17 mmol) to form a dark brown solution immediately. The reaction was stirred for one hour at room temperature, filtered through celite and concentrated *in vacuo*. The brown residue was recrystallized from DME layered beneath pentane at -35 º to provide dark brown crystals of **5** (11.9 mg, 0.015 mmol, 18 %). Negative-mode ESI MS [**5**–K]$^-$: *m/z* calcd for $C_{42}H_{46}FeN_4O$ 678.3027, found at 678.3021.

Synthesis of [HOFe(tpa$^{Mes\text{-}Mes}$tpa)FeOH][K(tmao)]$_2$(thf)$_2$ (6). To a stirring toluene solution of **3** (39.9 mg, 0.045 mmol) was added tmao (15 mg, 0.20 mmol). The solution became dark brown immediately. After 15 min the reaction mixture was filtered to yield a brown solid which was collected and recrystallized by layering a concentrated THF solution of the solid underneath diethyl ether. The brown crystals of **6** so obtained were suitable for Xray crystallography. See Table 4.1 for the crystallographic details for **6**. Negative-mode ESI MS [**6**–K(tmao)$_2$(thf)$_2$]$^-$: *m/z* calcd for $C_{84}H_{90}Fe_2N_8O_2K$ 1393.553, found at 1393.549.

Synthesis of d_{11}-mesitylbromide (7). **7** was prepared by modification of a literature preparation[15] substituting d_{12}-mesitylene for mesitylene. To a 20 mL scintillation vial was added d_{12}-mesitylene (526.6 mg, 3.99 mmol), NBS (1.99 g, 11.2 mmol), and 8 mL acetone. 1M aqueous hydrochloric acid (120 µL) was then added with stirring to form a yellow solution (excess NBS didn't dissolve). After stirring for 30 min, the acetone was removed *in vacuo* and 20 mL of hexanes were added. The mixture was then cooled to 0 ºC, filtered to remove the succinimide and the filtrate concentrated *in vacuo* to afford **7** as a colorless liquid (823.3 mg, 3.92 mmol, 98 %). ^{2}H NMR ($CHCl_3$, 61 MHz): δ 6.95 (s, 2D, Ar*D*), 2.35 (s, 6D, *o*-CD_3), 2.22 (s, 3D, *p*-CD_3).

Synthesis of 2-(d_{11}-mesityl)-1*H*-pyrrole (8). A modification of a literature preparation was followed for the synthesis of **8** substituting d_{11}-mesitylbromide for mesitylbromide.[16] In an inert atmosphere glovebox, a pressure flask was charged with sodium pyrrole and THF. Anhydrous zinc chloride was then added slowly with stirring (**caution: this reaction is very exothermic**). After stirring for five minutes, Pd_2dba_3, 2-(di-*tert*-butylphosphino)biphenyl, and d_{11}-mesitylbromide were then added. The flask was sealed and heated to 100 ºC for 2 days. Following cooling to room temperature, water and ether were added and the black mixture filtered through celite. The filter cake was rinsed with ether, and the filtrate transferred to a separatory funnel. The organic layer was then collected and the aqueous layer extracted twice with ether. The combined organics were dried over Na_2SO_4 and concentrated to a black liquid. This crude material was purified by filtering through a plug of silica gel (20 % ethyl acetate in hexanes) and recrystallized from hexanes at -20 ºC to yield **8**. ^{2}H NMR ($CHCl_3$, 61 MHz): δ 2.30 (s,

3D, *p*-CD_3), 2.11 (s, 6D, *o*-C*D*$_3$). ^{1}H NMR ($CDCl_3$, 400 MHz): δ 7.90 (s, 1H, N*H*), 6.85 (s, 1H), 6.31 (s, 1H), 6.05 (s, 1H).

Synthesis of Tris((5-*d*$_{11}$-mesityl-1H-pyrrol-2-yl)methylamine, $H_3tpa^{Mes\text{-}d}$ (9). **9** was synthesized by modification of a literature procedure.[10] To a 3 mL aqueous solution of ammonium chloride (70 mg, 1.31 mmol) was added aqueous formaldehyde (37 wt %, 317.8 mg, 3.92 mmol) followed by a solution of **8** (769 mg, 3.92 mmol) in 11 mL absolute ethanol. The mixture was then stirred for 3 days under N_2 after which it was filtered, washed with a small portion of cold ethanol and air-dried. The solid was then transferred in dichloromethane to a separatory funnel, neutralized with 20 % aqueous NaOH and extracted twice further into dichloromethane. The organic portions were combined, dried over Na_2SO_4, and concentrated *in vacuo* to a pale pink foamy solid (727 mg, 1.13 mmol, 87 %). ^{2}H NMR ($CHCl_3$, 61 MHz): δ 2.29 (s, 9D, *p*-CD_3), 2.11 (s, 18D, *o*-C*D*$_3$). ^{1}H NMR ($CDCl_3$, 400 MHz): δ 8.03 (s, 3H, N*H*), 6.12 (s, 3H), 5.95 (s, 3H), 3.63 (s, 6H).

Generation of [($tpa^{Mes\text{-}d}$)FeO]K (11). A 1,2-difluorobenzene solution of trimethylamine-*N*-oxide (4 equivalents) was added to a 1,2-difluorobenzene solution of [($tpa^{Mes\text{-}d}$)Fe^{II}][K(dme)$_2$] (**10**) at -35 ºC to produce a brown solution which could be monitored by UV/vis for the characteristic near IR band near 850 nm. A similarly prepared solution was frozen at 77K for analysis by Mössbauer (ca. 100 mM). Mass spectrometry experiments were performed on thawing 1,2-difluorobenzene solutions. ESI MS ([**11**-K]$^-$): *m/z* calcd for $C_{42}H_{12}D_{33}FeN_4O$ 710.50, found at 710.53.

General Physical Methods. Mass spectrometry measurements were performed on either an LTQ Orbitrap (Thermo Scientific, West Palm Beach, FL) or Waters Q-TOF Premier (Milford, MA) spectrometer at the QB3/Chemistry Mass Spectrometry Facility at UC Berkeley. The thermally unstable iron(IV)-oxo complex **11** was analyzed using electrospray ionization in negative V mode on a Waters Q-TOF Premier spectrometer. Samples of **11** were generated at -35 ºC as ca. 1 mM 1,2-difluorobenzene solutions, frozen in liquid nitrogen, and introduced into the mass spectrometer as a thawing solution using a syringe pump. ESI source parameters were adjusted as follows: capillary voltage, 0.8 kV; sampling cone voltage, 19 V; source temperature, 60 ºC; desolvation temperature, 40 ºC. ^{1}H NMR spectra were recorded on Bruker spectrometers operating at 300 or 400 MHz as noted. Chemical shifts are reported in ppm and referenced to residual protiated solvent and coupling constants are reported in Hz. UV-vis spectra were acquired on a Varian Cary 50 BIO UV-Visible Spectrophotometer (Agilent Technologies, Santa Clara, CA) with a Unisoko cryostat attachment for temperature control (Unisoku Co, Osaka, Japan). Mössbauer spectra were recorded in constant acceleration mode using a triangular velocity waveform as frozen acetonitrile or 1,2-difluorobenzene solutions (ca. 80 – 100 mM) between room temperature and 4.2 K in a Janis Research Co. cryostat (Willmington, MA) and analyzed using the WMOSS software package (SEE Co, Medina MN). Isomer shifts are reported relative to α-iron (27 μm foil) at room temperature.

General Methods for Xray Crystallography. Xray crystallographic data was collected using fine-focused Mo-Kα radiation on a Bruker 3-circle Smart-Apex diffractometer with an Apex 1-CCD detector. Samples were cooled to 100K using an Oxford Cryostream 700 low temperature device. Structures were solved using either direct methods or the Patterson method in conjunction with standard difference Fourier techniques and refined

by full-matrix least-squares procedures.[17] A semi-empirical absorption correction (SADABS) was applied to the diffraction data for all structures. All non-hydrogen atoms were refined anisotropically, and hydrogen atoms were treated as idealized contributions and refined isotropically. All software used for diffraction data processing and crystal-structure solution and refinement are contained in the APEX2 program suite (Bruker AXS, Madison, WI).[18]

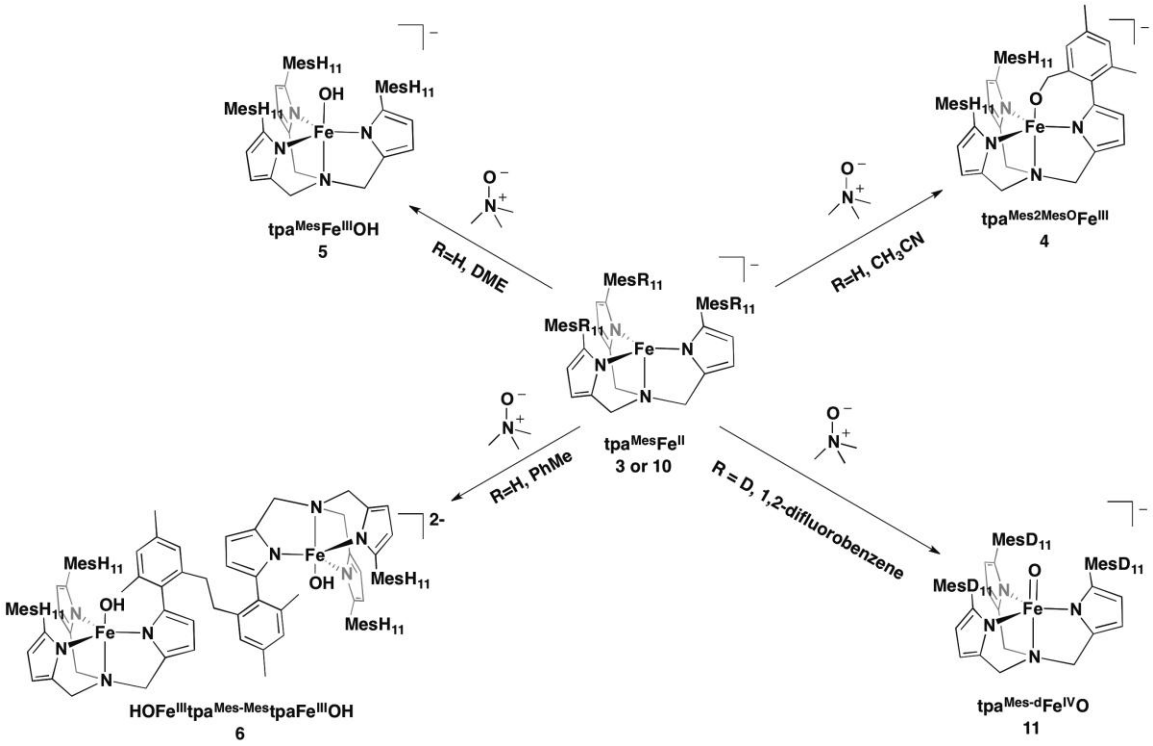

Scheme 4.1. Solvent dependence of the oxidation of $[(tpa^{Mes})Fe^{II}]^-$ (**3** or **10**) to provide four distinct products.

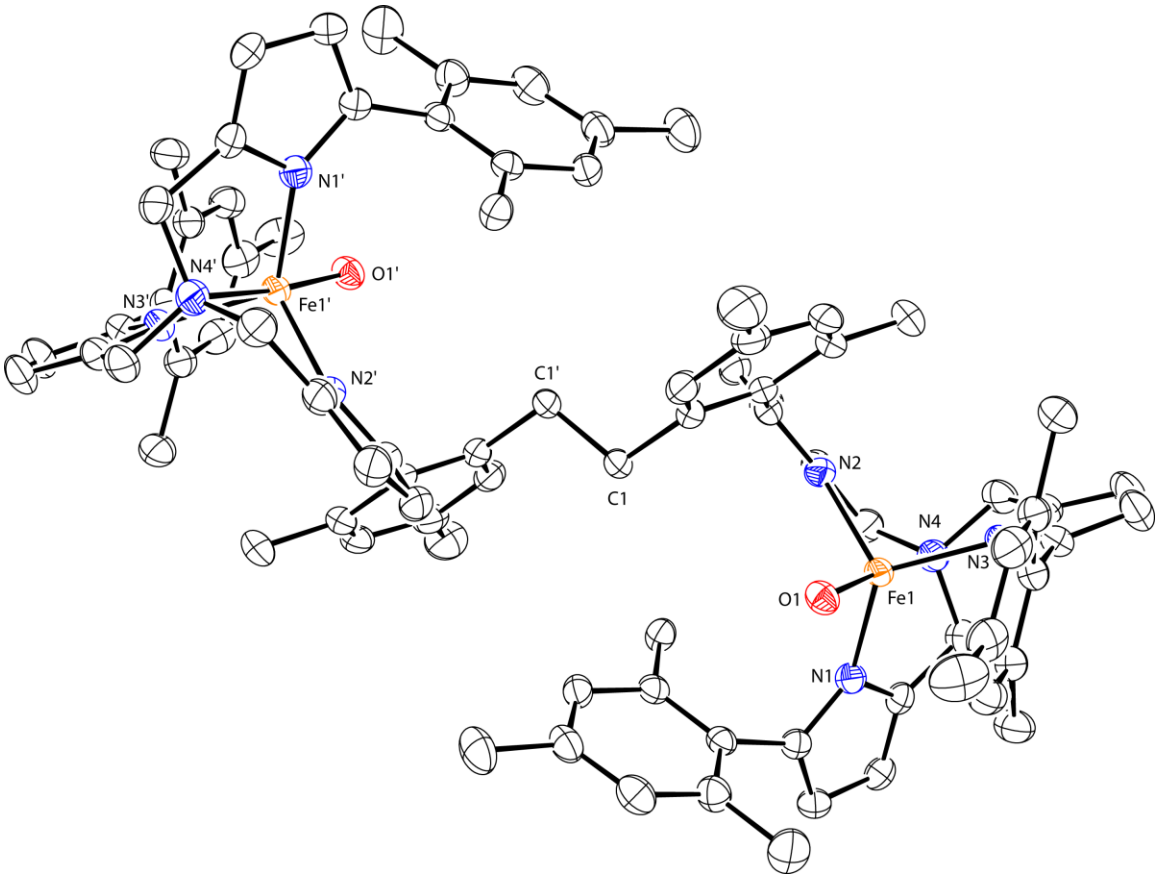

Figure 4.1. Molecular structure of **6** as determined by Xray crystallography. Ellipsoids are displayed at 50% probability and hydrogen atoms, potassium ions, and thf and tmao molecules are not shown for clarity.

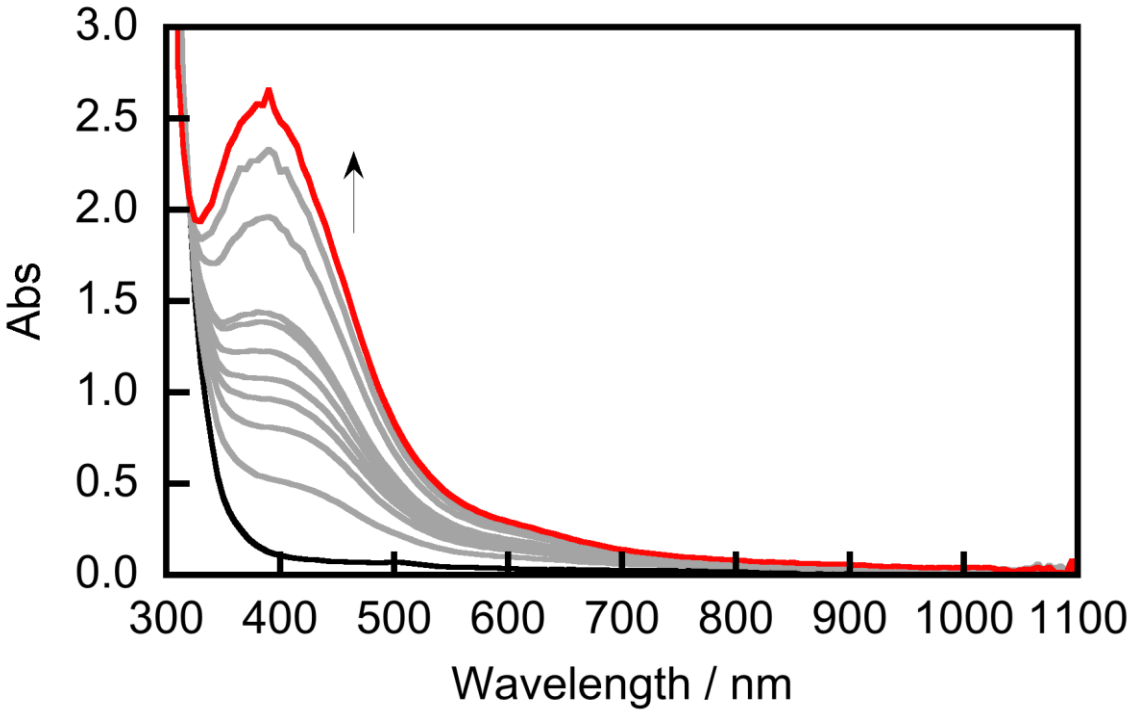

Figure 4.2. Reaction of $[(tpa^{Mes\text{-}d})Fe^{II}]^-$, **10**, with trimethylamine-*N*-oxide at -40 ºC in acetonitrile.

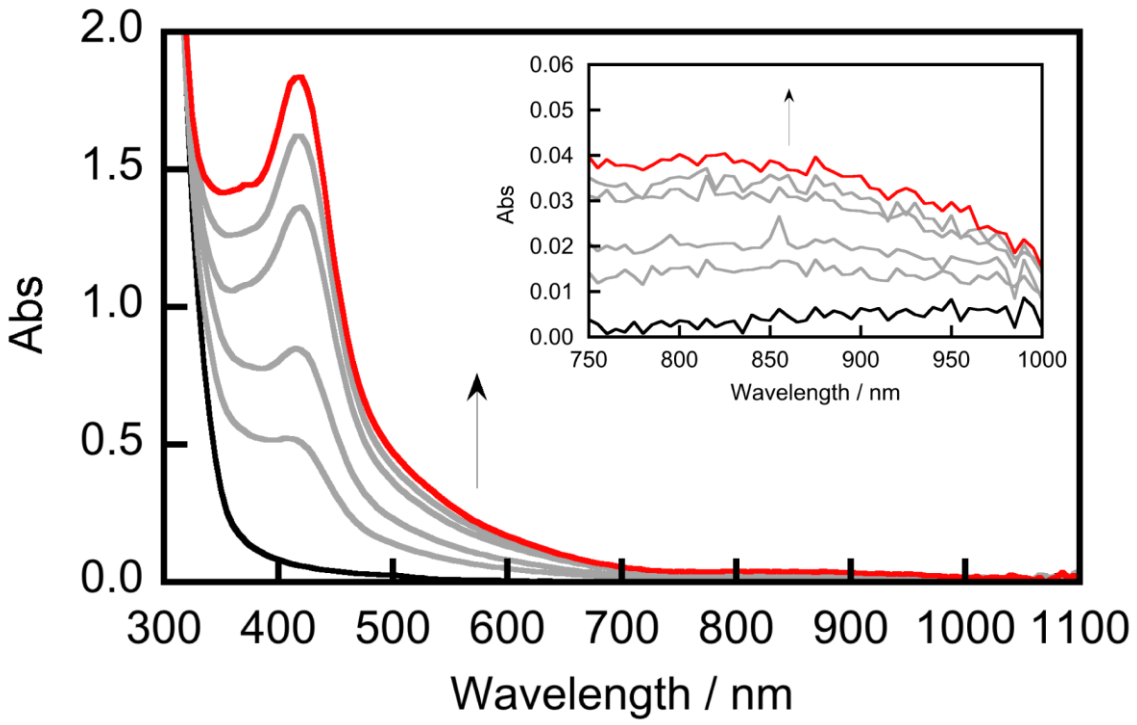

Figure 4.3. Reaction of $[(tpa^{Mes\text{-}d})Fe^{II}]^-$, **10**, with trimethylamine-*N*-oxide at -35 ºC in 1,2-difluorobenzene. Inset: growth of weak near-IR band of **11**.

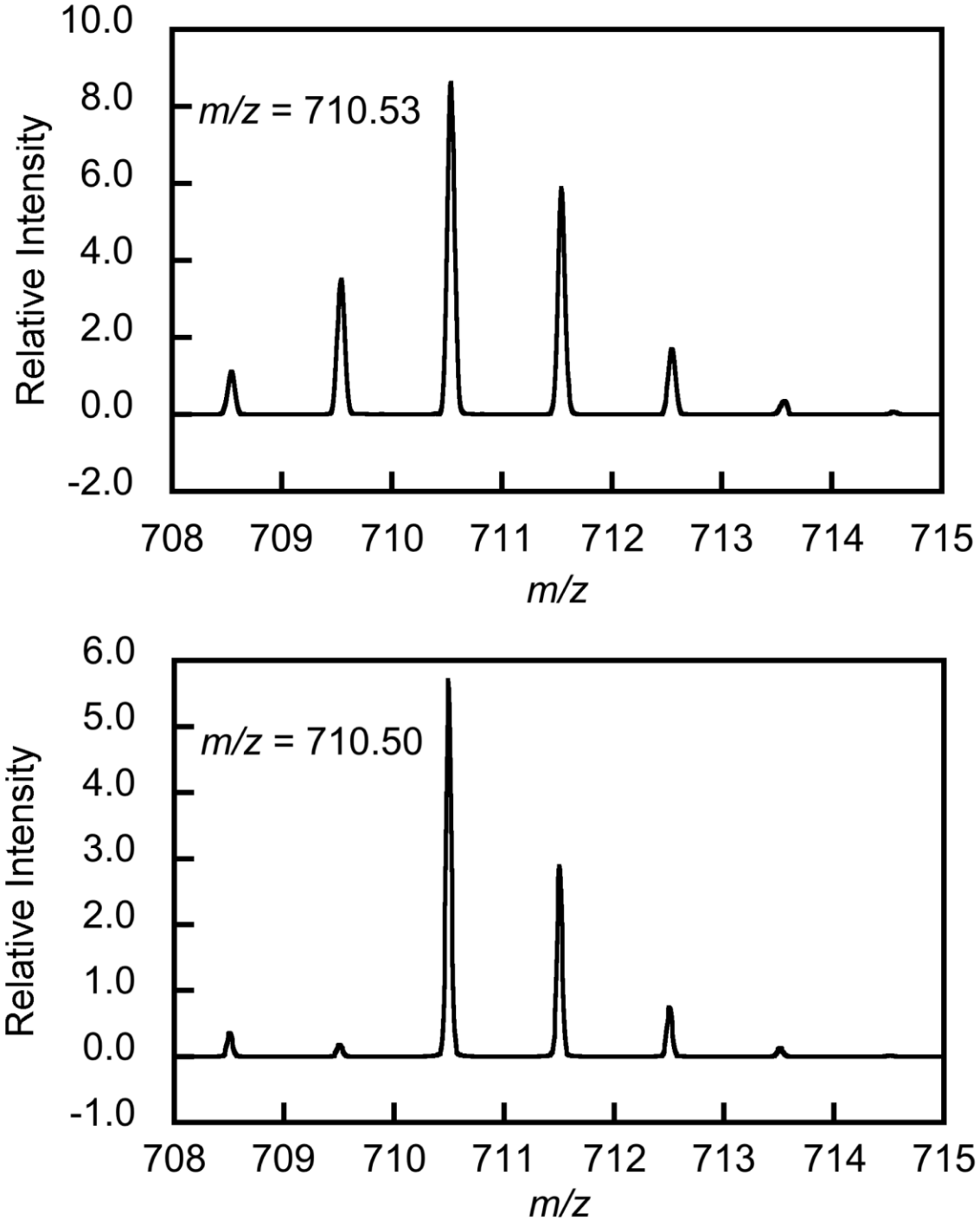

Figure 4.4. Electrospray ionization mass spectrum of **11** showing the experimentally observed spectrum (top) and the theoretical spectrum (bottom) for $[(tpa^{Mes\text{-}d})FeO]^-$.

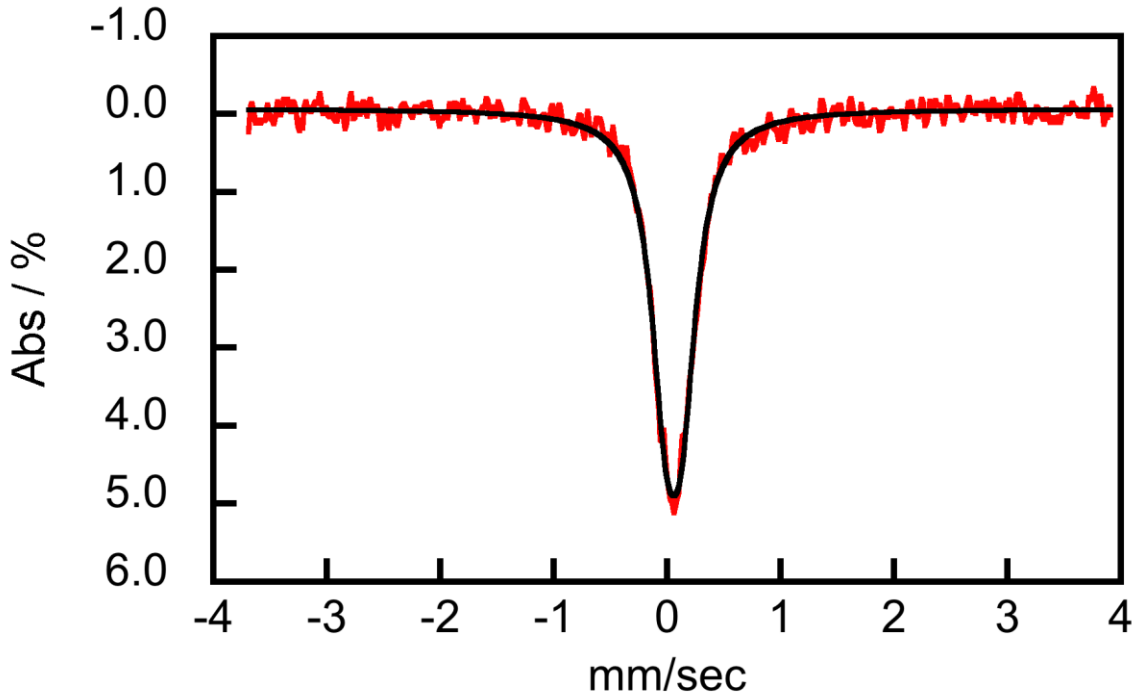

Figure 4.5. Mössbauer spectrum of a ca 100 mM frozen solution of **11** in 1,2-difluorobenzene acquired at 4.2 K. A least squares fit to the data (solid black line) provided the following parameters: δ = 0.06 mm/sec, ΔE_q = 0.14 mm/sec.

Table 4.1. Crystallographic Details for **6**.

	6
Empirical Formula	$C_{98}H_{124}Fe_2K_2N_{10}O_6$
Formula Weight	1727.98
T (K)	100
λ (Å)	0.71073
Crystal System	Orthorhombic
Space Group	*Pbca*
a (Å)	12.6917(7)
b (Å)	22.8121(13)
c (Å)	32.2635(18)
α (º)	90
β (º)	90
γ (º)	90
V	9341.07
Z	4
ρ_{calc} (g/cm^3)	1.229
μ (mm^{-1})	0.46
reflctns collected	114661
T_{min}/T_{max}	0.92
data/restr/params	8561/0/538
$2\theta_{max}$ (º)	50.7
R, R_w (%; I>4σ)	5.7, 17.5
GOF	0.995
mean shift/error	0.001

References

(1) Bigi, J. P.; Harman, W. H.; Lassalle-Kaiser, B.; Robles, D. M.; Stich, T. A.; Yano, J.; Britt, R. D.; Chang, C. J. *Journal of the American Chemical Society* **2012**, *134*, 1536-1542.

(2) England, J.; Guo, Y.; Farquhar, E. R.; Young Jr, V. G.; Münck, E.; Que Jr, L. *Journal of the American Chemical Society* **2010**, *132*, 8635-8644.

(3) England, J.; Guo, Y.; Van Heuvelen, K. M.; Cranswick, M. A.; Rohde, G. T.; Bominaar, E. L.; Münck, E.; Que, L. *Journal of the American Chemical Society* **2011**, *133*, 11880-11883.

(4) England, J.; Martinho, M.; Farquhar, E. R.; Frisch, J. R.; Bominaar, E. L.; Münck, E.; Que, L. *Angewandte Chemie International Edition* **2009**, *48*, 3622-3626.

(5) Lacy, D. C.; Gupta, R.; Stone, K. L.; Greaves, J.; Ziller, J. W.; Hendrich, M. P.; Borovik, A. S. *Journal of the American Chemical Society* **2010**, *132*, 12188-12190.

(6) Bernasconi, L.; Louwerse, M. J.; Baerends, E. J. *European Journal of Inorganic Chemistry* **2007**, *2007*, 3023-3033.

(7) Decker, A.; Rohde, J.-U.; Klinker, E. J.; Wong, S. D.; Que, L.; Solomon, E. I. *Journal of the American Chemical Society* **2007**, *129*, 15983-15996.

(8) Hirao, H.; Kumar, D.; Que, L.; Shaik, S. *Journal of the American Chemical Society* **2006**, *128*, 8590-8606.

(9) Krebs, C.; Galonic Fujimori, D.; Walsh, C. T.; Bollinger, J. M. *Accounts of Chemical Research* **2007**, *40*, 484-492.

(10) Harman, W. H.; Chang, C. J. *Journal of the American Chemical Society* **2007**, *129*, 15128-15129.

(11) Jensen, M. P.; Lange, S. J.; Mehn, M. P.; Que, E. L.; Que, L. *Journal of the American Chemical Society* **2003**, *125*, 2113-2128.

(12) Mukherjee, A.; Martinho, M.; Bominaar, E. L.; Münck, E.; Que, L. *Angewandte Chemie International Edition* **2009**, *48*, 1780-1783.

(13) Jensen, M. P.; Mehn, M. P.; Que, L. *Angewandte Chemie International Edition* **2003**, *42*, 4357-4360.

(14) Yamashita, M.; Furutachi, H.; Tosha, T.; Fujinami, S.; Saito, W.; Maeda, Y.; Takahashi, K.; Tanaka, K.; Kitagawa, T.; Suzuki, M. *Journal of the American Chemical Society* **2007**, *129*, 2-3.

(15) Andersh, B.; Murphy, D. L.; Olson, R. J. *Synthetic Communications* **2000**, *30*, 2091-2098.

(16) Rieth, R. D.; Mankad, N. P.; Calimano, E.; Sadighi, J. P. *Organic Letters* **2004**, *6*, 3981-3983.

(17) Sheldrick, G. *Acta Crystallographica Section A* **1990**, *46*, 467-473.

(18) Sheldrick, G. *Acta Crystallographica Section A* 2008, *64*, 112-122.

Appendix A
Unexpected Reactivity Under Oxidative Conditions of a Fluorinated Tris(Pyrrolide) Iron Complex

Introduction

Our group recently described the synthesis, spectroscopic characterization and preliminary reactivity of a novel, $S = 2$ iron(IV)-oxo complex of the tris(pyrrolide) ligand platform tpa^{Ph}, $[(tpa^{Ph})FeO]^-$ (**1**), one of just a few such complexes reported in the literature (Scheme A.1).[1-5] Upon warming, in the absence of an external substrate, **1** decomposed via intramolecular *ortho*-hydroxylation of an aryl C-H bond to the iron(III)-phenoxide product **2**, a reaction with precedent in the literature for iron-based oxidants.[6-10] In light of the sterically limited reactivity of **1**, and its intramolecular decomposition to **2**, we sought to prepare a new iron(IV)-oxo complex with a ligand derivative protected from *ortho* hydroxylation by fluorination. It is noteworthy that ancillary ligands with aryl chloride groups blocking intramolecular *ortho* oxidation have recently been discovered in the context of copper catalyzed C-H amination.[11,12]

Results and Discussion

Ligand Fluorination Leads to Unexpected Reactivity

The fluorinated tris(pyrrolide) iron complex $[(tpa^{DFP})Fe^{II}]^-$ (**3**) was previously synthesized in the context of slow magnetic relaxation studies.[13] The 2,6-difluoro substitution was expected to decrease the likelihood of intramolecular *ortho*-hydroxylation as seen for **1** and increase external reactivity via steric interactions of the 2,6-difluorophenyl groups which serve to increase access to the metal (or metal-oxo) unit. Toward this end, oxidation of **3** in acetonitrile at -40 ºC with trimethylamine-*N*-oxide (tmao) yields a new species with a prominent shoulder at 400 nm and a weak band at 850 nm in the UV/vis spectrum (Figure A.1). The latter absorption band is reminiscent of the near-IR band of synthetic iron(IV)-oxo complexes, including the complex of tpa^{Ph} recently reported by our group.[1-5,14,15] However, further characterization by electrospray ionization mass spectrometry (ESI MS), EPR and Mössbauer (Figure A.2) at low temperature indicates the products of the reaction to be two unexpected iron(III) complexes, the iron(III)-phenoxide **4** and the iron(III)-fluoride **5** (Scheme A.2). Interestingly, reaction with O_2 (1 atm.) yields the same products as judged by ESI MS. Unfortunately, crystallization of the mixture did not produce single crystals, so an Xray crystal structure could not be obtained for **4** or **5**. Although the prospect of C-F activation by a transient iron(IV)-oxo intermediate is intriguing, in light of the paucity of evidence (and of precedent), we suspect the reaction to proceed via nucleophilic substitution by tmao on **3**. The lack of reactivity of **3** with N_2O, which wouldn't be sufficiently nucleophilic to displace the fluoride from **3**, is consistent with this hypothesis. Note that $[(tpa^{Mes})Fe^{II}]^-$ reacts rapidly with N_2O.[6] Regardless of the mechanism of the reaction, tpa^{DFP} does not seem to be a promising platform for iron-oxo chemistry.

Concluding Remarks

In conclusion, oxidation of a fluorinated complex **3** with tmao leads to an interesting fluoride substitution reaction of the ligand to provide an iron(III) phenoxide **4** and an iron(III) fluoride complex (**5**). Despite a diagnostic near-IR band in the UV/vis spectrum at low temperature, no iron(IV)-oxo complex is observed at low temperature by parallel-mode EPR or Mössbauer. This suggests the interesting transformation does not proceed via a high-valent iron(IV)-oxo oxidant.

Experimental Section

General Synthetic Details. Unless otherwise noted, all synthetic manipulations were performed under an inert atmosphere of dinitrogen in a Vacuum Atmospheres glovebox or on a vacuum line using standard Schlenk technique. Solvents were dried on a Vacuum Atmospheres Solvent purification system and stored over 3 Å molecular sieves. Molecular sieves, alumina, and celite were activated by heating at 200ºC under dynamic vacuum for at least 24 hours. All glassware was dried in an oven at 170 ºC for at least 12 hours before use. Potassium hydride was purchased as a suspension in mineral oil, washed with pentane and used as a dry solid in the glovebox. The iron complex $[(tpa^{DFP})Fe^{II}][K(dme)_2]$ (**5**)[13] was prepared according to a literature procedure. All other reagents were purchased from Sigma-Aldrich and used as received.

Oxidation of $[(tpa^{DFP})Fe^{II}]^-$ with TMAO. An acetonitrile solution of tmao (0.8 mg, 0.011 mmol) was added to a stirring aceonitrile solution of **3** (2.2 mg, 0.0026 mmol) at room temperature with the color of the solution turning dark brown immediately. The solution was then frozen and injected as a thawing solution into a mass spectrometer or frozen for Mössbauer analysis. The negative-mode ESI MS had two prominent peaks corresponding to **4** and **5**. [**4**-K]$^-$: *m/z* calcd for $C_{33}H_{21}FeF_5N_4O$ 640.099, found at 640.098. [**5**-K]$^-$: *m/z* calcd for $C_{33}H_{21}FeF_7N_4$ 662.100, found at 662.106. The 143 K Mössbauer spectrum was fit to two symmetric quadrupole doublets (ca 1:1 ratio) with parameters consistent with high-spin Fe(III): #1: δ = 0.26 mm/sec, ΔE_q = 1.09 mm/sec; component #2: δ = 0.491 mm/sec, ΔE_q = 1.03 mm/sec.

Oxidation of $[(tpa^{DFP})Fe^{II}]^-$ with O_2. An acetonitrile solution of **3** was stirred in a 25 mL Schlenk tube under N_2. Dioxygen (1 atm.) was then bubbled into the solution turning the solution a dark brown. The solution was concentrated under vacuum to a brown oil and analyzed by ESI MS. The negative-mode mass spectrum revealed the same mass peaks assigned to the anionic portions of **4** and **5** (*vide supra*).

General Physical Methods. Mass spectrometry measurements were performed on either an LTQ Orbitrap (Thermo Scientific, West Palm Beach, FL) or Waters Q-TOF Premier (Milford, MA) spectrometer at the QB3/Chemistry Mass Spectrometry Facility at UC Berkeley. ^{1}H NMR spectra were recorded on Bruker spectrometers operating at 300 or 400 MHz as noted. Chemical shifts are reported in ppm and referenced to residual protiated solvent and coupling constants are reported in Hz. UV-vis spectra were acquired on a Varian Cary 50 BIO UV-Visible Spectrophotometer (Agilent Technologies, Santa Clara, CA) with a Unisoko cryostat attachment for temperature control (Unisoku Co, Osaka, Japan). Mössbauer spectra were recorded in constant acceleration mode using a triangular velocity waveform as frozen acetonitrile or 1,2-difluorobenzene solutions (ca. 80 – 100 mM) between room temperature and 4.2 K in a Janis Research Co. cryostat (Willmington, MA) and analyzed using the WMOSS software package (SEE Co, Medina MN). Isomer shifts are reported relative to α-iron (27 μm foil) at room temperature.

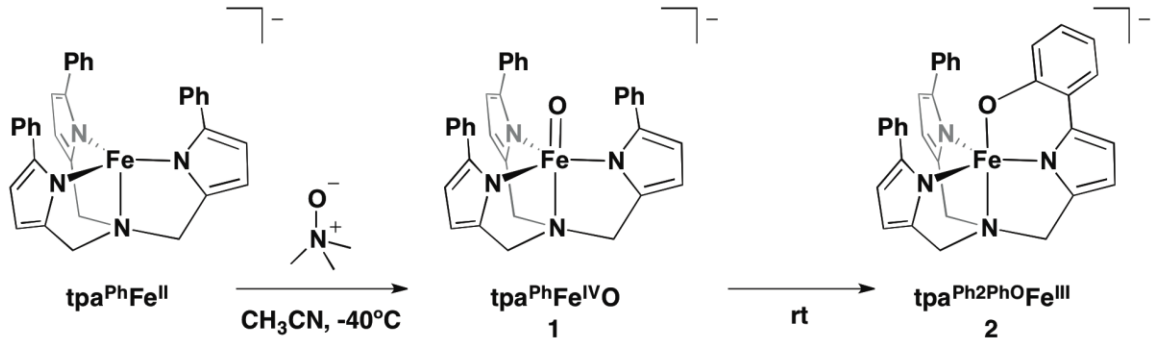

Scheme A.1. The previously reported synthesis and intramolecular aryl CH oxidation mediated by the *S* = 2 iron(IV)-oxo complex **1**.

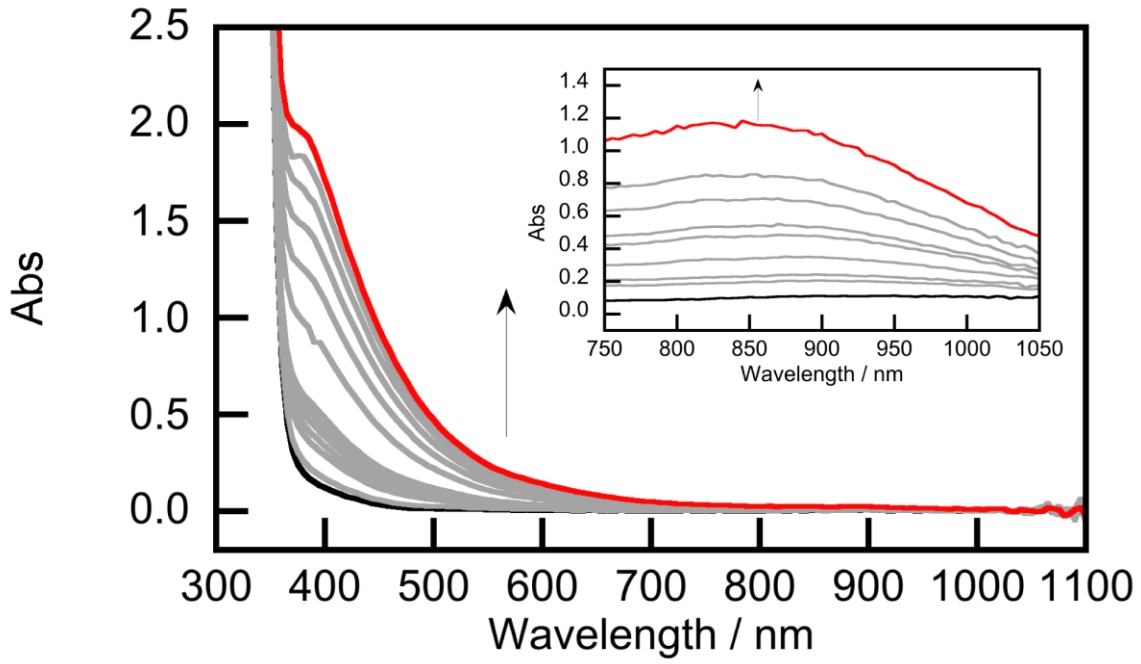

Figure A.1. UV/vis spectrum of the oxidation of **3** by trimethylamine-*N*-oxide in acetonitrile at -40 ºC. Inset: growth of weak near-IR band for an analogous experiment conducted at a higher concentration of **3** (ca. 7 mM).

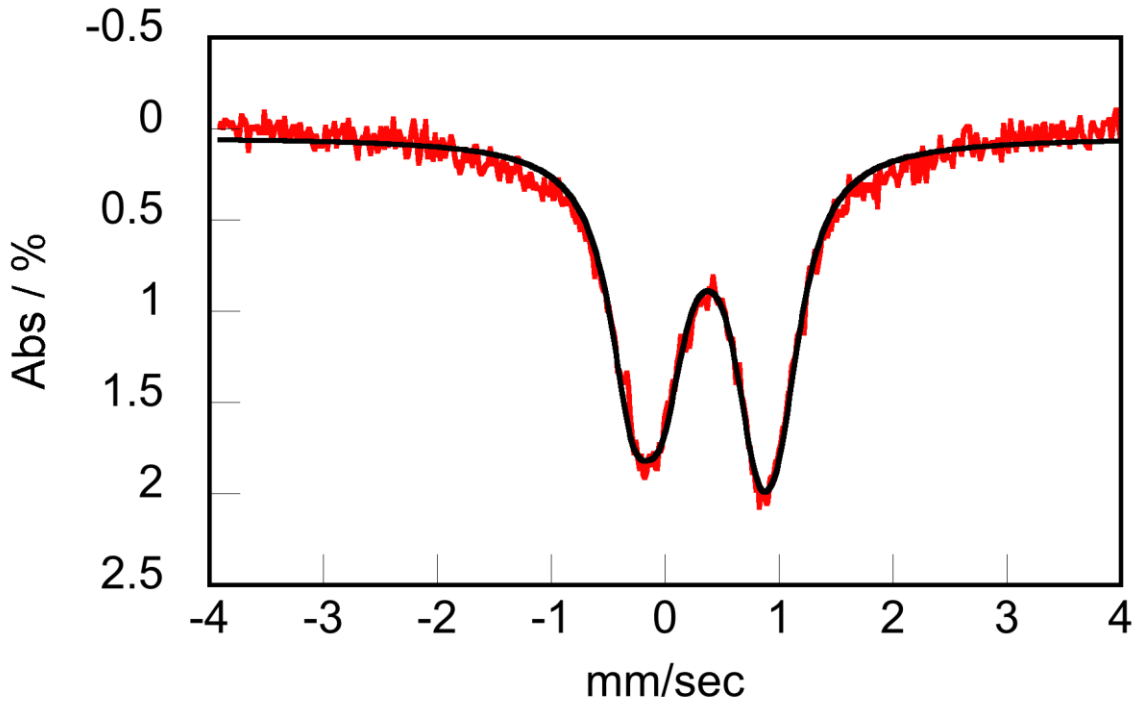

Figure A.2. Mössbauer spectrum of a 140 mM frozen solution of **4** and **5** in acetonitrile acquired at 143 K. A least squares fit for a pair of quadrupole doublets in an approximately 1:1 ratio (solid black line) provided the following parameters: component #1: δ = 0.26 mm/sec, ΔE_q = 1.09 mm/sec; component #2: δ = 0.491 mm/sec, ΔE_q = 1.03 mm/sec.

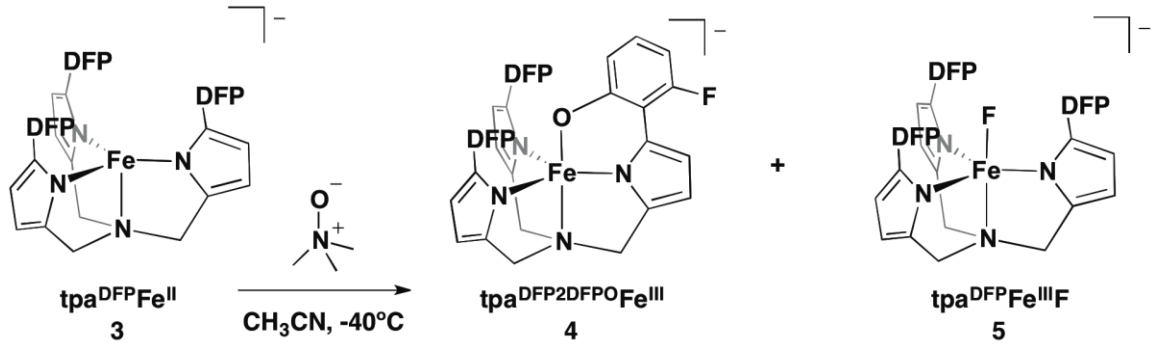

Scheme A.2. Reaction of trimethylamine-*N*-oxide with **3** at -40 ºC in acetonitrile provides the two iron(III) products **4** and **5**.

References

(1) Bigi, J. P.; Harman, W. H.; Lassalle-Kaiser, B.; Robles, D. M.; Stich, T. A.; Yano, J.; Britt, R. D.; Chang, C. J. *Journal of the American Chemical Society* **2012**, *134*, 1536-1542.

(2) England, J.; Guo, Y.; Farquhar, E. R.; Young Jr, V. G.; Münck, E.; Que Jr, L. *Journal of the American Chemical Society* **2010**, *132*, 8635-8644.

(3) England, J.; Guo, Y.; Van Heuvelen, K. M.; Cranswick, M. A.; Rohde, G. T.; Bominaar, E. L.; Münck, E.; Que, L. *Journal of the American Chemical Society* **2011**, *133*, 11880-11883.

(4) England, J.; Martinho, M.; Farquhar, E. R.; Frisch, J. R.; Bominaar, E. L.; Münck, E.; Que, L. *Angewandte Chemie International Edition* **2009**, *48*, 3622-3626.

(5) Lacy, D. C.; Gupta, R.; Stone, K. L.; Greaves, J.; Ziller, J. W.; Hendrich, M. P.; Borovik, A. S. *Journal of the American Chemical Society* **2010**, *132*, 12188-12190.

(6) Harman, W. H.; Chang, C. J. *Journal of the American Chemical Society* **2007**, *129*, 15128-15129.

(7) Jensen, M. P.; Lange, S. J.; Mehn, M. P.; Que, E. L.; Que, L. *Journal of the American Chemical Society* **2003**, *125*, 2113-2128.

(8) Mukherjee, A.; Martinho, M.; Bominaar, E. L.; Münck, E.; Que, L. *Angewandte Chemie International Edition* **2009**, *48*, 1780-1783.

(9) Jensen, M. P.; Mehn, M. P.; Que, L. *Angewandte Chemie International Edition* **2003**, *42*, 4357-4360.

(10) Yamashita, M.; Furutachi, H.; Tosha, T.; Fujinami, S.; Saito, W.; Maeda, Y.; Takahashi, K.; Tanaka, K.; Kitagawa, T.; Suzuki, M. *Journal of the American Chemical Society* **2007**, *129*, 2-3.

(11) Badiei, Y. M.; Dinescu, A.; Dai, X.; Palomino, R. M.; Heinemann, F. W.; Cundari, T. R.; Warren, T. H. *Angewandte Chemie International Edition* **2008**, *47*, 9961-9964.

(12) Wiese, S.; Badiei, Y. M.; Gephart, R. T.; Mossin, S.; Varonka, M. S.; Melzer, M. M.; Meyer, K.; Cundari, T. R.; Warren, T. H. *Angewandte Chemie International Edition* **2010**, *49*, 8850-8855.

(13) Harman, W. H.; Harris, T. D.; Freedman, D. E.; Fong, H.; Chang, A.; Rinehart, J. D.; Ozarowski, A.; Sougrati, M. T.; Grandjean, F.; Long, G. J.; Long, J. R.; Chang, C. J. *Journal of the American Chemical Society* **2010**, *132*, 18115-18126.

(14) Que, L. *Accounts of Chemical Research* **2007**, *40*, 493-500.

(15) Seo, M. S.; Kim, N. H.; Cho, K.-B.; So, J. E.; Park, S. K.; Clemancey, M.; Garcia-Serres, R.; Latour, J.-M.; Shaik, S.; Nam, W. *Chemical Science* **2011**, *2*, 1039-1045.

Appendix B
Oxygen Activation by a Pseudo-tetrahedral Fe(II) Complex of a Tripodal Guanidine-based Ligand

Introduction

The activation of dioxygen by non-heme iron metalloenzymes is an elegant way of generating a potent oxidant using an environmentally-benign and ubiquitous terminal oxidant.[1-5] In synthetic chemistry, oxygen activation by iron complexes is also well-established, although catalytic systems capable of difficult oxidations are still rare. Moreover, generating synthetic, high-valent iron-oxo complexes[6,7] – often the metal-based oxidant in enzymatic oxidations – from dioxygen is still a synthetic challenge with pioneering work conducted in the labs of Nam[8], Borovik[9] and Que[10,11].

Our group recently started a program in non-heme iron-oxygen chemistry that has explored the impact of the secondary coordination sphere on oxygen activation[12] as well as the synthesis and reactivity of iron(IV)-oxo complexes of rare (S = 2) ground electronic structures[13,14]. The current work sought to generate an iron(IV)-oxo complex of a novel coordination geometry – namely, pseudotetrahedral – inspired by the work of Peters[15], Meyer[16], and Smith[17] on related nitrido chemistry of pseudotetrahedral iron. We hypothesized that a pseudotetrahedral iron(IV)-oxo complex would allow access to a novel electronic manifold (either S = 2 or S = 0) with potentially exciting reactivity consequences (Scheme B.1).

To stabilize the related iron(IV)-nitrido complexes prepared by Peters, Meyer, and Smith required strong field phosphine or carbene based ligand architectures with bulky groups to prevent (or slow) dimerization pathways.[15-17] Unfortunately, these ligands are susceptible to oxidation[18], which has likely precluded their being used for the analogous iron-oxo chemistry.[19] We decided to investigate tripodal guanidine ligands, which should be stable to oxidation and of sufficient ligand field strength to stabilize high-valent metal-oxo complexes likely in diamagnetic ground states analogous to the aforementioned iron(IV)-nitrido complexes. Moreover, the related TMG_3tren ligand has been used to aid the isolation of both the first crystallographically-characterized S = 2, trigonal bipyramidal iron(IV)-oxo complex[20,21] as well as a rare example of an end-on copper superoxide complex[22-24].

Results and Discussion

Synthesis of the Fe(II) Complexes of Guanidine Ligand 1

The synthesis of the previously-reported guanidine ligand **1** is shown in Scheme B.2.[25] 1,1,1-trihydroxymethylethane is condensed with phenyl sulfonyl chloride in neat pyridine to provide the phenyl sulfone tripod.[26] Sodium azide is then reacted with the sulfone to yield the unstable azide, which is reduced with $LiAlH_4$ in refluxing THF to provide the amine as the hydrochloride salt.[26] This salt is reacted with the cloro-amidinium salt of N,N'-tetramethylurea[27] in refluxing acetonitrile to form the tripodal guanidine ligand.[25]

The coordination chemistry of **1** was previously explored with $MnCl_2$ and $ZnCl_2$.[25] Consistent with that report, we isolate the $FeCl_2$ complex of **1** as a tetrahedral complex **2** from reaction of **1** with $FeCl_2$ with two guanidine arms of the bound to Fe and one guanidine arm unbound (Scheme B.3). In contrast, reaction of **1** with $FeCl_2$ followed by addition of trimethylsilyl triflate or of **1** with $Fe(OTf)_2$ directly yields the desired pseudotetrahedral complexes **3** and **4**, respectively, after crystallization (Scheme B.3). The azide complex **5** is prepared from **3** by simple salt metathesis with sodium azide

(Scheme B.3). Figure B.1 shows the structures of **2**-**5** as determined by X-ray crystallography.

To assess the donor-strength of **1** relative to other ligands we prepared the carbonyl complex [**1**Mn(CO)$_3$]OTf (**6**) by reaction of **1** with [MnBr(CO)$_3$(^{t}BuCN)]$_2$ followed by AgOTf or trimethylsilyltriflate in analogy to work published by Smith (Scheme B.3).[28] As recorded in Table B.1, the two infrared active C=O stretches, of A_1 and E symmetry, predicted for a C_{3v} complex are observed at 2007 and 1906 cm^{-1}, respectively. Interesting, these stretching frequencies suggest **1** is a more strongly-donating ligand than the *anionic* ligands Tp* and Cp*,[29] though not as strongly-donating as the tris(carbene)borato ligand studied by Smith in the context of iron-nitrido chemistry (Table B.1).[28]

Reactivity of [1Fe(OTf)]OTf with O-atom Transfer Reagents Provides a CH Oxidation Product Suggestive of an Iron(IV)-oxo Complex

Satisfied that **1** is sufficiently basic to stabilize highly oxidized metal centers, we next explored the oxidation chemistry of the ferrous complex [**1**Fe(OTf)]OTf (**4**). **4** reacts with the O-atom transfer reagents iodosobenzene, 2-*tert*-butylsulfonyliodosobenzene (PhIO*), and pyridine-*N*-oxide in acetonitrile solution to yield an orange (400 nm) solution immediately. Interestingly, **4** also reacts rapidly with O_2, although the reaction is more complicated than that with the former O-atom transfer reagents (*vide infra*). ESI-MS of the solution from reaction of **4** with PhIO* displays an iron-containing signal at an *m*/*z* of 631.3 (*m/z* calcd for $C_{21}H_{44}F_3FeN_9O_4S$: 631.3) consistent with the Fe(III)-alkoxide **7**, likely resulting from intramolecular C-H hydroxylation of a methyl group of a nearby guanidine by the target iron(IV)-oxo complex, a reaction analogous to that seen for the *S* = 2 iron(IV)-oxo complex of TMG$_3$tren reported by Que and coworkers (Scheme B.4).[21] The Mössbauer spectrum of this solution at 5K provides an isomer shift of 0.35 mm/sec and a quadrupole splitting of 1.46 mm/sec, consistent with the assignment of **7** as a high-spin Fe(III) complex. For comparison, the analogous iron(III)-alkoxide derived from decomposition of [(TMG$_3$tren)FeO]$^{2+}$ has the following Mössbauer parameters: δ: 0.34 mm/sec, ΔE_q: 2.00 mm/sec further validating the assignment of **7** as an alkoxide complex derived from intramolecular CH oxidation of a guanidine methyl group.[21] Unfortunately, attempts to observe the putative iron(IV)-oxo intermediate at low temperature prior to decomposition to **7** have been unsuccessful.

Reaction of [1Fe(OTf)]OTf with O_2 Yields a Thermally Unstable Intermediate

As noted above **4** also reacts with O_2. As shown in Figure B.2, however, this reaction follows a course different from that of the reaction with PhIO*, generating a new species **8** with an absorbance at 550 nm that decays over the course of one hour at -40 ºC in acetonitrile. As judged by ESI MS, the product of the reaction is again **7**, suggesting the 550 nm intermediate could be the putative iron(IV)-oxo. However, **8** doesn't react with 9,10-dihydroanthracene at -40 ºC, as would be expected for an iron(IV)-oxo complex. Moreover, deuteration of the guanidine methyl groups of **1** has little impact on the stability of **8**-d_{36}, suggesting the intermediate is not decomposing via rate-determining H-atom abstraction.[20] This too would be expected if **8** were an iron(IV)-oxo complex.

Spectroscopic Characterization of 8

Spectroscopy was next explored to determine the identity of intermediate **8**. The *in situ* IR spectrum of an acetonitrile solution of **4** exposed to O_2 shows a strong band at 810 cm^{-1}. Although this is consistent with other Fe=O stretching frequencies (e.g.,

Borovik's high-spin iron(IV)-oxo complex has an Fe=O stretch at 798 cm^{-1})[30], there is no change when the reaction is performed using $^{18}O_2$, suggesting the 810 cm^{-1} stretch does not involve an oxygen atom. Monitoring the *in situ* IR spectrum of an acetonitrile solution of **4** in the presence of 1 atm of O_2 at -35 ºC produces no obvious intermediate; instead, the product simply appears more slowly than at room temperature. Either **8** is not generated under these conditions (ca. 50 - 100 times more concentrated than UV/vis or MS experiments) or **8** does not have any obvious IR-active stretches.

In contrast, the Raman spectrum of an acetonitrile solution of **4** exposed to O_2 shows an isotope-sensitive band at 850 cm^{-1} that shifts to 815 cm^{-1} when $^{18}O_2$ is used (Figure B.3). These data are remarkably similar to that reported for Que's high-spin iron(IV)-oxo complex (Fe=^{16}O 843 cm^{-1}, Fe=^{18}O 810 cm^{-1}).[21] However, there also appear weaker, isotope-sensitive bands near 1000 cm^{-1} and 600 cm^{-1}, which could be due, respectively, to the stretching of a superoxide O-O bond and a Fe-O single bond of a dioxygen adduct.

The reaction of **4** with O_2 was also explored by EPR. Although a putative $S = 0$ or $S = 2$ iron(IV)-oxo would be EPR inactive, iron(III) species, including **7**, would be observable. After seconds, the EPR signal is a mixture of two signals, one axial with a g value of 2 and one isotropic with a g value of 4.3 (Figure B.4). After ca 1.5 hr, however, the EPR signal is dominated by the isotropic signal near g of 4.3. The identity of the $g \sim 2$ signal, which could arise from the intermediate **8**, is unfortunately obscure as both high-spin and low-spin iron(III) ions may possess g values of 2. The isotropic $g \sim 4.3$ signal is either 'junk' iron (i.e., decomposition to insoluble high-spin iron(III)) or due to a high-spin iron(III) complex with a large rhombic distortion (E/D). If the latter, **7** is a likely candidate for the source of the 4.3 signal due to the structural (and electronic) distortion resulting from oxidation of one methyl group on one of the guanidine arms of **1**.

Concluding Remarks

In conclusion the oxidation chemistry of iron complexes of the tripodal guanidine ligand **1** was explored. Although the characterization of **7** suggests the potential for **1** to stabilize a pseudotetrahderal iron(IV)-oxo complex, no direct evidence of such an intermediate was obtained. Furthermore, the interesting dioxygen reactivity of **4** is promising, but requires further investigation in order to determine the reaction pathway and products. In addition, the photolysis of the azide complex **5** should be explored toward the synthesis of an iron(IV)-nitrido complex of similar structure but potentially distinct reactivity than those previously described.[15-17]

Experimental Section

General Synthetic Details. All synthetic manipulations were performed under an inert nitrogen atmosphere in a Vacuum atmospheres glovebox or on a Schlenk line using standard Schlenk technique. Solvents were dried on a Vacuum Atmospheres solvent purification system and stored over 3 Å molecular sieves. Acetonitrile was further dried by filtering through a plug of basic alumina immediately prior to use (intermediate **8** was not observed if this secondary drying of acetonitrile wasn't performed). Molecular sieves, alumina, and celite were activated by heating at 200ºC under dynamic vacuum for at least 24 hours. $^{18}O_2$ was purchased from Cambridge Isotope Laboratories (Andover, MA). All other reagents were purchased from Sigma-Aldrich and used as received. $Fe(OTf)_2$ was

purchased from Strem and used as received. All glassware was dried by storage in an oven at 170 ºC for at least 12 hours before use. **1** was prepared according to a literature preparation.[25-27] $[MnBr(CO)_3(^tBuCN)]_2$ was prepared by following a literature method.[28]

Synthesis of 1FeCl$_2$ (2). To a stirring THF solution of **1** (100.9 mg, 0.245 mmol) was added $FeCl_2$ (30.5 mg, 0.241 mmol). The mixture was stirred for several hours and then filtered through celite to remove some brown solid. The filtrate was concentrated *in vacuo* to a colorless foamy solid, triturated with ether and pentane and recrystallized from DME layered beneath pentane to provide crystals suitable for Xray crystallography. The large colorless crystals were rinsed with pentane and dried to provide **2** as a white powder (94.3 mg, 0.175 mmol, 73 %).

Synthesis of [1FeCl]OTf (3). $FeCl_2$ (43.0 mg, 0.339 mmol) was added to a stirring THF solution of **1** (139.7 mg, 0.339 mmol) and stirred overnight. Trimethylsilyl triflate (75.4 mg, 0.339 mmol) was then added followed by stirring for 1.5 hr. The reaction mixture was then concentrated under vacuum to give a foamy solid, which was crystallized from THF/ether to afford Xray quality crystals of **3**.

Synthesis of [1FeOTf]OTf (4). To a stirring DME solution of **1** (66.9 mg, 0.163 mmol) was added $Fe(OTf)_2$ (56.4 mg, 0.159 mmol). The cloudy mixture was stirred overnight and filtered through celite to provide a colorless filtrate that was concentrated under vacuum to an oil. Crystallization of the oil from THF layered beneath ether provided colorless crystals suitable for Xray crystallography. The crystals were separated from the mother liquor, rinsed with ether and dried to afford **3** as a white powder (103.6 mg, 0.135 mmol, 85 %).

Synthesis of [1FeN$_3$]OTf (5). To a stirring slurry of **3** (63 mg, 0.097 mmol) in THF was added sodium azide (8.4 mg, 0.13 mmol). The mixture was stirred overnight, filtered through celite and concentrated *in vacuo* to a colorless oil. Crystals suitable for Xray crystallography were obtained from concentrated DME solutions of the oil layered beneath ether. The crystals were removed from the mother liquor, rinsed with ether and dried to yield **5** as a white powder (34.8 mg, 0.053 mmol, 55 %).

Synthesis of [1Mn(CO)$_3$]OTf (6). To a THF slurry of **1** (48.8 mg, 0.119 mmol) was added $[MnBr(CO)_3(^tBuCN)]_2$ (35.8 mg, 0.059 mmol) with stirring. After stirring overnight, silver triflate (30.3 mg, 0.118 mmol) was added to the yellow/orange mixture with immediate precipitation of a white solid. The mixture was then stirred overnight to ensure complete precipitation of AgBr followed by filtering through celite. The yellow filtrate thus obtained was concentrated under vacuum to a foamy yellow solid of **6**. IR (neat): 1998 cm^{-1} and 1897 cm^{-1}; IR (methylene chloride solution): 2007 cm^{-1} and 1906 cm^{-1}.

General Physical Methods. Mass spectrometry measurements were performed on either an LTQ Orbitrap (Thermo Scientific, West Palm Beach, FL) or Waters Q-TOF Premier (Milford, MA) spectrometer at the QB3/Chemistry Mass Spectrometry Facility at UC Berkeley. Elemental analyses were performed on a Perkin Elmer 2400 Series II combustion analyzer (Waltham, MA) in the Microanalytical Laboratory in the College of Chemistry, University of California, Berkeley, California. *In situ* IR spectra were measured on a Mettler-Toledo ReactIR iC10 instrument (Columbus, OH). IR spectra of **6** were measured on a Bruker ALPHA FT-IR with a Platinum ATF accessory. ^{1}H NMR spectra were recorded on Bruker spectrometers operating at 300 or 400 MHz as noted. Chemical shifts are reported in ppm and referenced to residual protiated solvent and

coupling constants are reported in Hz. UV-vis spectra were acquired on a Varian Cary 50 BIO UV-Visible Spectrophotometer (Agilent Technologies, Santa Clara, CA) with a Unisoko cryostat attachment for temperature control (Unisoku Co, Osaka, Japan). EPR, Raman.

Xray Crystallography. See Table B.2. for Xray data for **2-5**. Xray crystallographic data was collected using fine-focused Mo-Kα radiation on a Bruker 3-circle Smart-Apex or Siemens Smart 1000 diffractometer with an Apex 1 or Smart 1000 CCD detector, respectively. Samples on Smart-Apex were cooled to 100 K using an Oxford Cryostream 700 low temperature device (or to ca 130 K on the Smart 1000 using a home-built device). Structures were solved using either direct methods or the Patterson method in conjunction with standard difference Fourier techniques and refined by full-matrix least-squares procedures.[31] A semi-empirical absorption correction (SADABS) was applied to the diffraction data for all structures. All non-hydrogen atoms were refined anisotropically, and hydrogen atoms were treated as idealized contributions and refined isotropically. All software used for diffraction data processing and crystal-structure solution and refinement are contained in the APEX2 program suite (Bruker AXS, Madison, WI).[32]

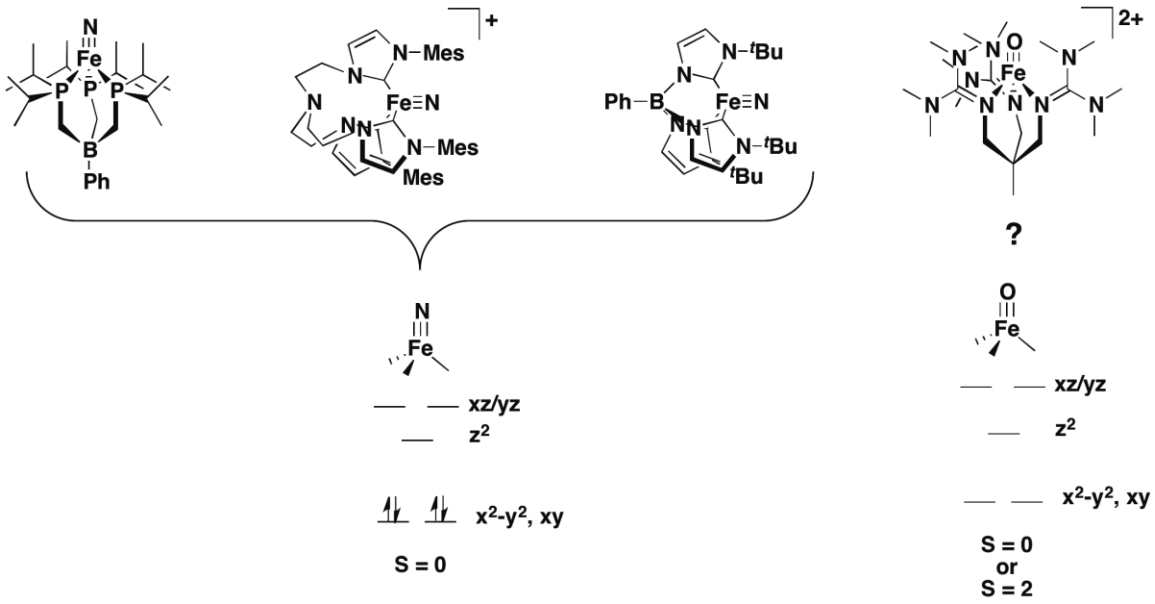

Scheme B.8. Previous work on pseudotetrahedral high-valent iron(IV) nitrides suggested the pseudotetrahedral iron(IV)-oxo target.

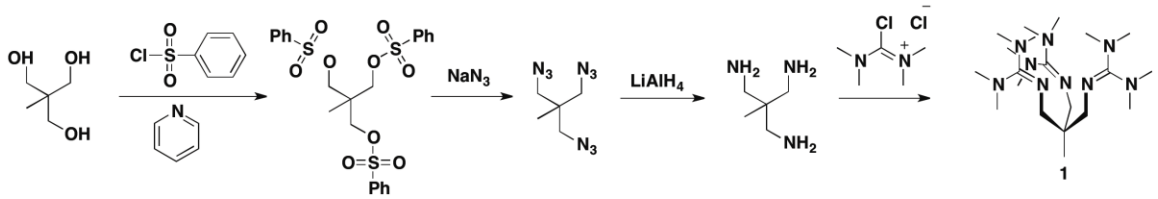

Scheme B.9. Synthesis of the previously reported tripodal tris(guanidine) ligand **1**.

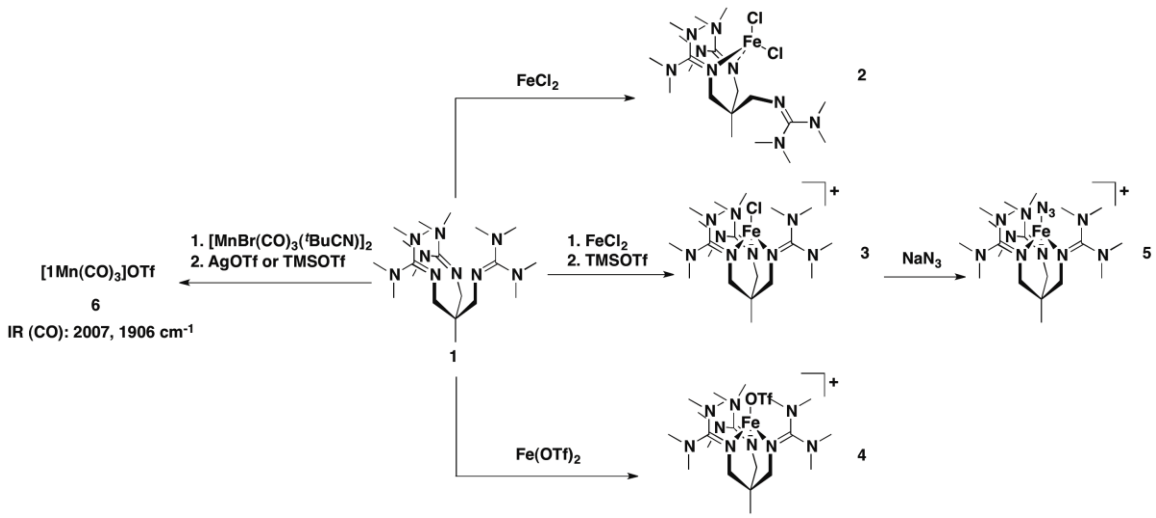

Scheme B.3. Synthesis of iron complexes **2-5** and manganese complex **6**.

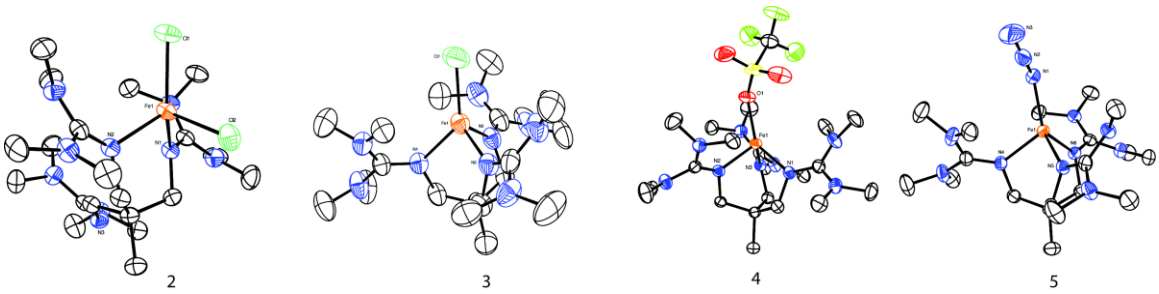

Figure B.1. Molecular structures of **2-5** as determined by Xray crystallography. Hydrogen atoms, counterions (except for **2**, which is a neutral species), and solvents of crystallization are removed for clarity.

$LMn(CO)_3$	***A_1*/cm^{-1}**	***E*/cm^{-1}**	**Reference**
Tp^*	2032	1927	29
Cp^*	2017	1929	29
1	2007	1906	*this work*
$PhB(MeIm)_3^-$	1990	1889	28

Table B.1. Comparison of the carbonyl stretching frequencies for a series of $Mn(CO)_3$ complexes of tripodal, tridentate (considering Cp^* to be tridentate) ligands. Note that the *neutral* ligand **1** is more donating than both Tp^* and Cp^*, two anionic ligands.

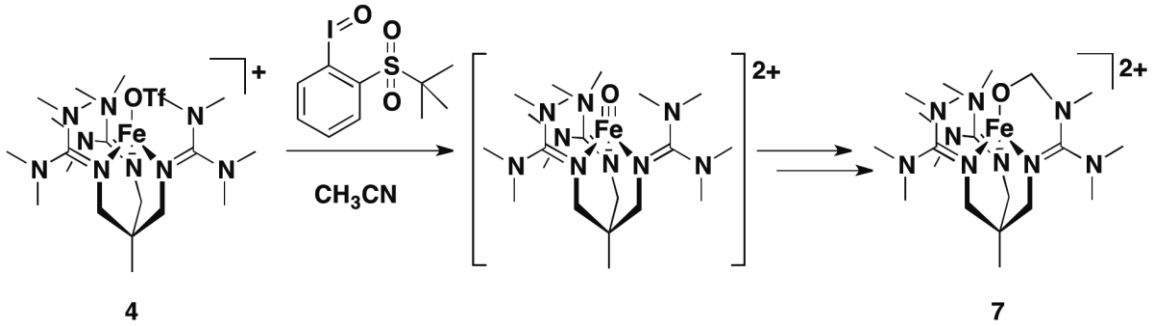

Scheme B.4. Reaction of **4** with PhIO* provides the iron(III)-alkoxide **7**, likely via an iron(IV)-oxo intermediate.

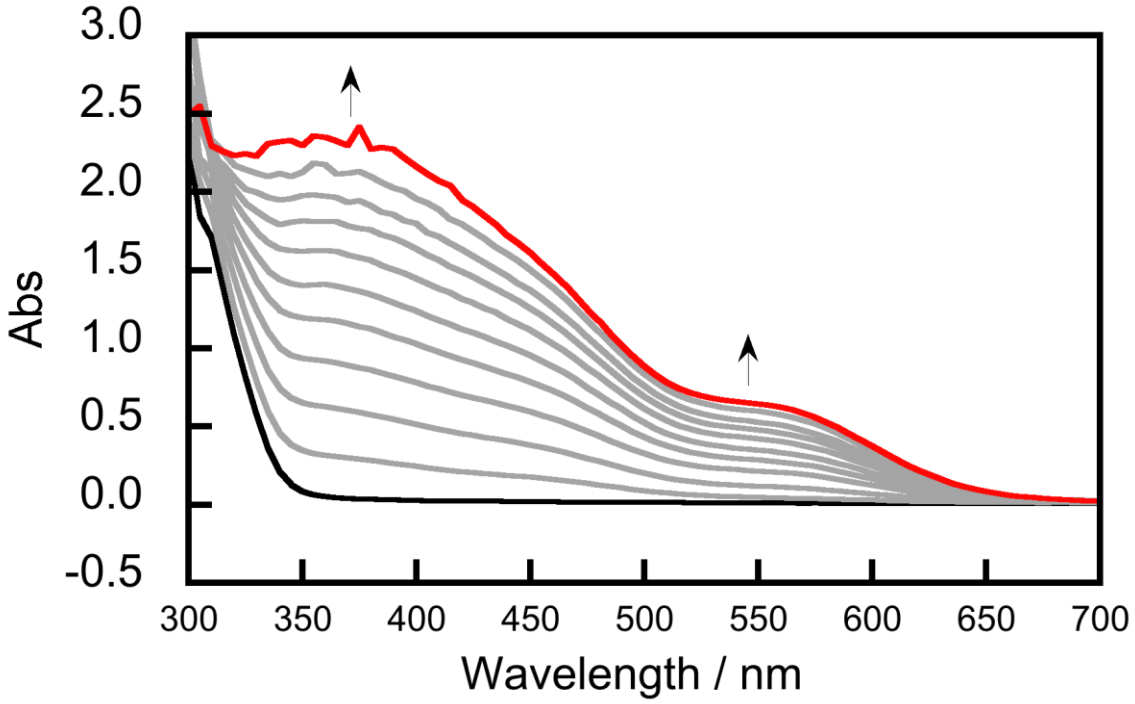

Figure B.2. The reaction of **4** with 1 atm O_2 at -40 ºC in acetonitrile generates a species with an absorbance at 550 nm that decays over the course of one hour.

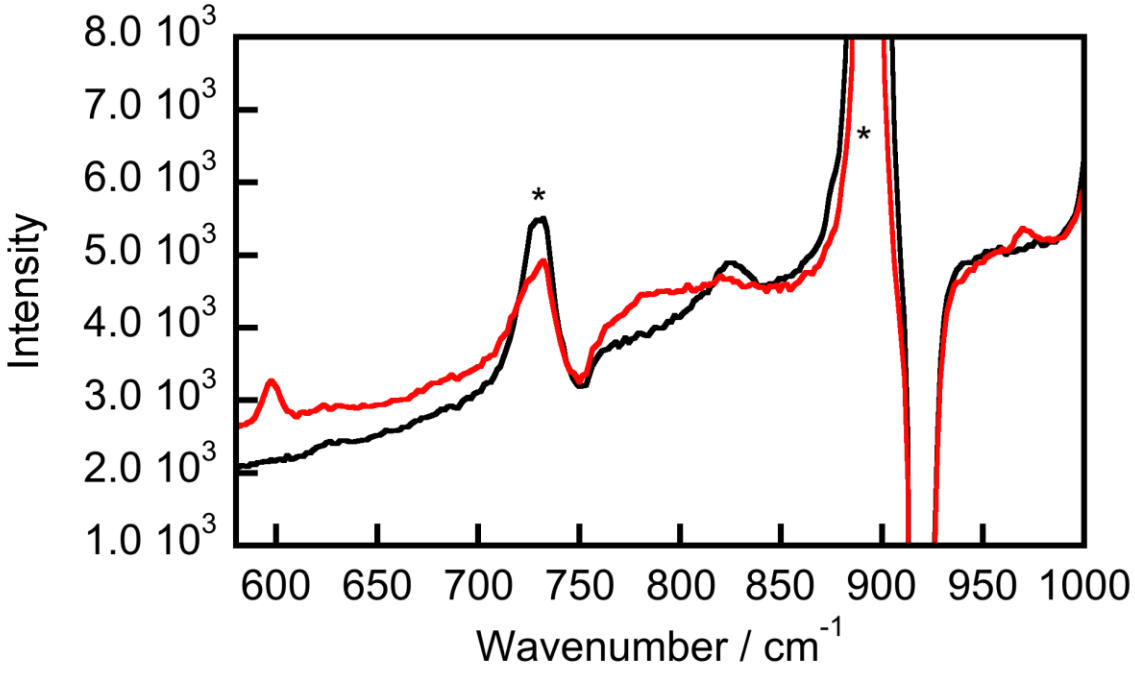

Figure B.3. Raman spectra for the reaction of **4** with $^{16}O_2$ (black) and $^{18}O_2$ (red) in acetonitrile. Peaks due to solvent are labeled *.

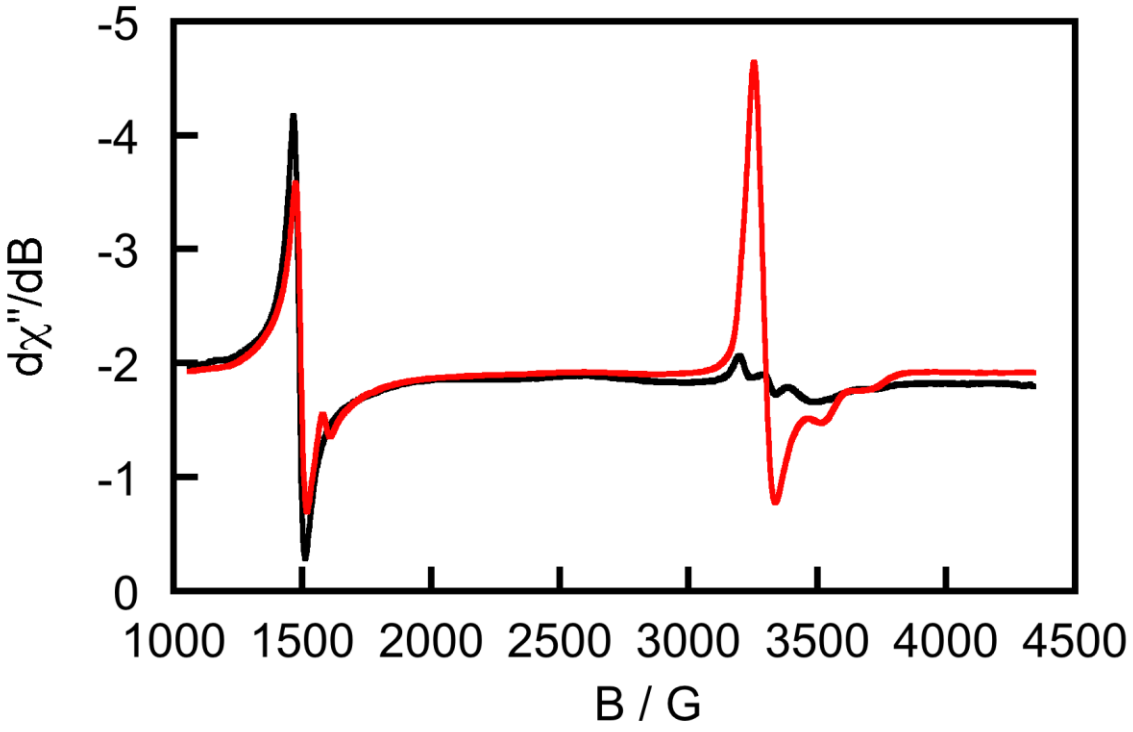

Figure B.4. EPR spectra at 11K for the reaction of **4** with O_2 after seconds (red) and after 1.5 hr (black).

Table B.2. Crystallographic Details for **2-5**.				
	2	**3**	**4**	**5**
Empirical Formula	$C_{20}H_{45}FeN_9Cl_2$	$C_{21}H_{45}ClF_3FeN_9O_3S$	$C_{22}H_{45}F_6FeN_9O_6S_2$	$C_{21}H_{45}F_3FeN_{12}O_3S$
Formula Weight	535.88	652.02	765.64	658.60
T (K)	103	138	148	119
λ (Å)	0.71073	0.71073	0.71073	0.71073
Crystal System	Triclinic	Triclinic	Monoclinic	Triclinic
Space Group	*P-1*	*P-1*	*P2(1)/c*	*P-1*
a (Å)	8.5050(8)	8.910(3)	13.2464(5)	8.630(2)
b (Å)	12.6965(13)	13.669(5)	12.6268(4)	13.487(3)
c (Å)	13.9377(14)	14.132(5)	20.8705(7)	13.950(3)
α (º)	73.9540(10)	81.673(5)	90.00	81.893(3)
β (º)	79.555(2)	85.609(5)	90.8790(10)	86.659(3)
γ (º)	83.7270(10)	71.062(5)	90.00	73.197(3)
V	1419.7(2)	1610.1(10)	3490.4(2)	1538.4(6)
Z	2	4	4	2
ρ_{calc} (g/cm^3)	1.254	2.690	1.457	1.422
μ (mm^{-1})	0.744	1.341	0.632	0.621
reflctns collected	28611	23874	22444	27736
T_{min}/T_{max}	0.91	0.93	0.89	0.94
data/restr/params	5185/0/289	5269/102/389	6374/129/488	5268/0/370
$2\theta_{max}$ (º)	50.8	48.8	50.7	49.7
R, R_w (%; I>4σ)	3.4, 9.1	5.4, 16.7	6.4, 18.9	3.8, 11.3
GOF	1.033	1.064	1.225	1.007
mean shift/error	0.002	0.083	0.023	0.000

References

(1) Korendovych, I. V.; Kryatov, S. V.; Rybak-Akimova, E. V. *Accounts of Chemical Research* **2007**, *40*, 510-521.

(2) Kovaleva, E. G.; Neibergall, M. B.; Chakrabarty, S.; Lipscomb, J. D. *Accounts of Chemical Research* **2007**, *40*, 475-483.

(3) Murray, L. J.; Lippard, S. J. *Accounts of Chemical Research* **2007**, *40*, 466-474.

(4) Nam, W. *Accounts of Chemical Research* **2007**, *40*, 465-465.

(5) Krebs, C.; Galonic Fujimori, D.; Walsh, C. T.; Bollinger, J. M. *Accounts of Chemical Research* **2007**, *40*, 484-492.

(6) Nam, W. *Accounts of Chemical Research* **2007**, *40*, 522-531.

(7) Que, L. *Accounts of Chemical Research* **2007**, *40*, 493-500.

(8) Kim, S. O.; Sastri, C. V.; Seo, M. S.; Kim, J.; Nam, W. *Journal of the American Chemical Society* **2005**, *127*, 4178-4179.

(9) MacBeth, C. E.; Golombek, A. P.; Young, V. G.; Yang, C.; Kuczera, K.; Hendrich, M. P.; Borovik, A. S. *Science* **2000**, *289*, 938-941.

(10) Mukherjee, A.; Martinho, M.; Bominaar, E. L.; Münck, E.; Que, L. *Angewandte Chemie International Edition* **2009**, *48*, 1780-1783.

(11) Thibon, A.; England, J.; Martinho, M.; Young, V. G.; Frisch, J. R.; Guillot, R.; Girerd, J.-J.; Münck, E.; Que, L.; Banse, F. *Angewandte Chemie International Edition* **2008**, *47*, 7064-7067.

(12) Soo, H. S.; Komor, A. C.; Iavarone, A. T.; Chang, C. J. *Inorganic Chemistry* **2009**, *48*, 10024-10035.

(13) Bigi, J. P.; Harman, W. H.; Lassalle-Kaiser, B.; Robles, D. M.; Stich, T. A.; Yano, J.; Britt, R. D.; Chang, C. J. *Journal of the American Chemical Society* **2012**, *134*, 1536-1542.

(14) Harman, W. H.; Chang, C. J. *Journal of the American Chemical Society* **2007**, *129*, 15128-15129.

(15) Betley, T. A.; Peters, J. C. *Journal of the American Chemical Society* **2004**, *126*, 6252-6254.

(16) Vogel, C.; Heinemann, F. W.; Sutter, J.; Anthon, C.; Meyer, K. *Angewandte Chemie International Edition* **2008**, *47*, 2681-2684.

(17) Scepaniak, J. J.; Fulton, M. D.; Bontchev, R. P.; Duesler, E. N.; Kirk, M. L.; Smith, J. M. *Journal of the American Chemical Society* **2008**, *130*, 10515-10517.

(18) Hu, X.; Meyer, K. *Journal of the American Chemical Society* **2004**, *126*, 16322-16323.

(19) Smith, J. M.; Mayberry, D. E.; Margarit, C. G.; Sutter, J.; Wang, H.; Meyer, K.; Bontchev, R. P. *Journal of the American Chemical Society* **2012**, *134*, 6516-6519.

(20) England, J.; Guo, Y.; Farquhar, E. R.; Young Jr, V. G.; Münck, E.; Que Jr, L. *Journal of the American Chemical Society* **2010**, *132*, 8635-8644.

(21) England, J.; Martinho, M.; Farquhar, E. R.; Frisch, J. R.; Bominaar, E. L.; Münck, E.; Que, L. *Angewandte Chemie* **2009**, *121*, 3676-3680.

(22) Maiti, D.; Lee, D.-H.; Gaoutchenova, K.; Würtele, C.; Holthausen, M. C.; Narducci Sarjeant, A. A.; Sundermeyer, J.; Schindler, S.; Karlin, K. D. *Angewandte Chemie International Edition* **2008**, *47*, 82-85.

(23) Schatz, M.; Raab, V.; Foxon, S. P.; Brehm, G.; Schneider, S.; Reiher, M.; Holthausen, M. C.; Sundermeyer, J.; Schindler, S. *Angewandte Chemie International Edition* **2004**, *43*, 4360-4363.

(24) Würtele, C.; Gaoutchenova, E.; Harms, K.; Holthausen, M. C.; Sundermeyer, J.; Schindler, S. *Angewandte Chemie International Edition* **2006**, *45*, 3867-3869.

(25) Wittmann, H.; Schorm, A.; Sundermeyer, J. *Zeitschrift für anorganische und allgemeine Chemie* **2000**, *626*, 1583-1590.

(26) Fleischer, E. B.; Gebala, A. E.; Levey, A.; Tasker, P. A. *The Journal of Organic Chemistry* **1971**, *36*, 3042-3044.

(27) Peters, A.; Kaifer, E.; Himmel, H.-J. *European Journal of Organic Chemistry* **2008**, *2008*, 5907-5914.

(28) Forshaw, A. P.; Bontchev, R. P.; Smith, J. M. *Inorganic Chemistry* **2007**, *46*, 3792-3794.

(29) Tellers, D. M.; Skoog, S. J.; Bergman, R. G.; Gunnoe, T. B.; Harman, W. D. *Organometallics* **2000**, *19*, 2428-2432.

(30) Lacy, D. C.; Gupta, R.; Stone, K. L.; Greaves, J.; Ziller, J. W.; Hendrich, M. P.; Borovik, A. S. *Journal of the American Chemical Society* **2010**, *132*, 12188-12190.

(31) Sheldrick, G. *Acta Crystallographica Section A* **1990**, *46*, 467-473.

(32) Sheldrick, G. *Acta Crystallographica Section A* **2008**, *64*, 112-122.

Appendix C
Iron(II) Complexes of Bulky Tris(pyridyl)methylamine Ligands: Aryl CH Hydroxylation by a Putative Iron(IV)-oxo Complex

Introduction

Previous work from our group has focused on rare[1-6] S = 2 iron(IV)-oxo complexes of bulky, trianionic, tris(pyrrolyl)methylamine (tpa) ligands.[1,7] A natural extension of this work would be to study the ability of the neutral, tris(pyridyl)methylamine (TPA) scaffold to stabilize similar S = 2 iron(IV)-oxo complexes. Although the parent TPA has been shown to stabilize iron(IV)-oxo complexes, these are intermediate spin, as the tetradentate TPA ligand isn't sufficiently bulky to prevent formation of octahedral iron complexes (which are almost without exception intermediate spin).[8-10] This appendix describes our synthesis of bulky TPA derivatives that form trigonal bipyramidal complexes of iron(II). The oxidation of one of these leads to aryl CH hydroxylation, a reaction that implies the presence of an iron(IV)-oxo complex.[1,7,11-14] At this stage, the electronic structure of the putative iron(IV)-oxo complex is unknown.

Results and Discussion

Synthesis of the Bulky TPA Derivatives and their Iron(II) Complexes

We focused our efforts on the neutral analogs of the previously studied tpa^{Mes} and tpa^{Ph}, TPA^{3Mes} and TPA^{3Ph}. TPA^{3Ph} is a known ligand which has been studied on Cu(I)[15] and we prepared TPA^{3Mes} in an analogous fashion substituting an alkylation in the last step for the published reductive amination (which fails for the bulkier mesityl ligand) (Scheme C.1). 2,6-dibromopyridine is lithiated with ^{n}BuLi and reacted with DMF to afford 2-bromo-6-formylpyridine (**1**).[16] A Suzuki coupling with mesityl boronic acid provides 2-formyl-6-mesitylpyridine (**2**),[17] which is reduced to the alcohol (**3**) with $NaBH_4$ in refluxing methanol.[17] **3** can be chlorinated with $SOCl_2$[15] or brominated with $POBr_3$[17] to provide **4** and **5**, respectively, either of which can be converted to the amine (**6**) in two steps using potassium phthalimide followed by deprotection with hydrochloric acid.[15] TPA^{3Mes} (**7**) is prepared by alkylating **6** with two equivalents of **4** or **5** in acetonitrile in the presence of excess NaI and excess Cs_2CO_3.

The iron(II) complexes $[(TPA^{3Mes})FeCl](PF_6)$ (**8**) and $[(TPA^{3Mes})Fe(NCCH_3)](PF_6)_2$ (**9**) are then easily prepared by stirring **7** with $FeCl_2$ in acetonitrile followed by salt metathesis with either one or two equivalents of $TlPF_6$, respectively. Both complexes are trigonal bipyramidal iron(II) complexes as judged by Xray diffraction analysis (Figures C.1 and C.2 and Table C.1). Solution ^{1}H NMR spectra are consistent with the trigonal bipyramidal structure also being adopted in acetonitrile solution: both **8** and **9** exhibit ten paramagnetically shifted and broadened ^{1}H NMR signals, consistent with approximate C_3 symmetry in solution. Room-temperature solution magnetic moments of **8** and **9** are 4.95 and 5.13 μ_{BM}, respectively, in good agreement with the spin-only value of 4.90 μ_{BM} predicted for a high-spin, S = 2 ground state.[18]

TPA^{3Ph} was synthesized in an analogous manner to TPA^{3Mes} (Scheme C.2). First, **1** is coupled with phenylboronic acid under Pd catalysis to form 2-formyl-6-phenylpyridine (**10**).[15] Second, reduction of **10** to the alcohol **11**, followed by chlorination of **11** with $SOCl_2$ yields 2-chloromethyl-6-phenylpyridine (**12**).[15] Third, the amine **13** is formed from S_N2 substitution with potassium phthalimide followed by acidic hydrolysis and reacted with two equivalents **12** in the presence of excess NaI and Cs_2CO_3 to afford TPA^{3Ph} (**14**). The iron(II) complex of TPA^{3Ph}, $[(TPA^{3Ph})Fe(NCCH_3)](OTf)_2$

(**15**) is prepared using $Fe(OTf)_2(CH_3CN)_2$ in acetonitrile. The molecular structure of **15**, a trigonal bipyramid similar to **9**, is shown in Figure C.3 (crystal data shown in Table C.2). The ^{1}H NMR spectrum of **15** in acetonitrile consists of 7 paramagnetically shifted and broadened peaks, which is consistent with approximate C_{3v} symmetry on the NMR timescale. The integrations are also consistent with a C_{3v} structure. Note that the solid-state structure appears to possess C_3 symmetry, which likely epimerizes rapidly in solution. Interestingly, and in contrast, the larger mesityl groups of **8** and **9** appear to prevent this rapid epimerization, as judged by ^{1}H NMR (*vide supra*).

Oxidation of the New Iron Complexes

The dicationic complexes **9** and **15** were then subjected to O-atom transfer conditions with the goal of generating transiently stable iron(IV)-oxo species. Although **9** reacts rapidly with O-atom transfer reagents including iodosylbenzene and *m*-CPBA, no crystalline products have been isolated and ^{1}H NMR suggests demetallation. Appearance of free ligand in the ^{1}H NMR is accompanied by the formation of orange precipitate, which is likely rust. **9** thus doesn't appear to be a robust candidate for iron(IV)-oxo chemistry.

In contrast, **15** reacts rapidly with iodosylbenzene to provide the *ortho* CH-hydroxylation product **16** in good yield (Scheme C.3). **16** was identified by ESI MS and its structure determined by Xray diffraction analysis (Figure C.4 and Table C.2). Although no transient intermediates are observed by UV/vis at low temperature, **16** implies the presence of a potent oxidant capable of aryl CH oxidation, likely an iron(IV)-oxo complex as described previously for related non-heme iron complexes.[1,7,11-14] Significantly, **16** contains a bound triflate anion and is six-coordinate, in contrast to the five-coordinate **15**. Whether the triflate binds to **15** prior to, or after, oxo formation is not known at this time and would have implications on the electronic structure of the putative iron(IV)-oxo: i.e., a six-coordinate iron(IV)-oxo would likely be intermediate spin,[10] while a five-coordinate iron(IV)-oxo would likely be high spin (Scheme C.3).[1-6]

Concluding Remarks

In conclusion, two bulky polpyridyl ligands based on TPA were prepared, namely TPA^{3Mes} and TPA^{3Ph}. The iron(II) complexes were synthesized and their ability to mediate oxidative chemistry was investigated. In particular, $[(TPA^{3Ph})Fe(NCCH_3)]^{2+}$ (**15**) reacts with iodosylbenzene to produce an *ortho* CH-hydroxylation product **16** which implies the transient existence of an iron(IV)-oxo complex. Unfortunately, the lack of spectroscopic observation of the proposed iron(IV)-oxo intermediate precludes the investigation of its electronic structure at this time.

Experimental Section

General Methods. Unless noted otherwise, all manipulations were carried out at room temperature under a dinitrogen atmosphere in a VAC Atmospheres Co. glovebox or using high-vacuum Schlenk techniques. Methylene chloride, diethyl ether, tetrahydrofuran, and pentane were dried over activated 4 Å molecular sieves, passed through a column of activated alumina, and sparged with nitrogen prior to use. Acetonitrile, acetonitrile-d_3, and butyronitrile were refluxed over CaH_2, distilled, and sparged with nitrogen. All other reagents and solvents were purchased from commercial

sources and used without further purification. UV/Vis experiments were conducted on a VARIAN CARY 50 BIO UV-Visible Spectrophotometer. Infrared spectra were recorded as nujol mulls on KBr plates on a Mattson Genesis Series FTIR spectrometer. NMR spectra were recorded on Bruker spectrometers operating at 300 or 400 MHz as noted. Chemical shifts are reported in ppm relative to residual protiated solvent; coupling constants are reported in Hz. Mass spectra and elemental analyses were determined at the University of California, Berkeley Mass Spectrometry and Microanalytical facility.

Synthesis of 2-bromo-6-formylpyridine (1). This compound was prepared by modification of a literature procedure[16] using 10.0 g (42.2 mmol) of 2,6-dibromopyridine to afford 6.17 g (33.2 mmol, 78%) of **1**.

Synthesis of 2-formyl-6-mesitylpyridine (2). This compound was prepared by modification of a literature procedure[17] using 3.03 g (16.3 mmol) of 2-formyl-6-bromopyridine to provide 3.01 g (13.4 mmol, 82%) of **2**.

Synthesis of 2-hydroxymethyl-6-mesitylpyridine (3). This compound was prepared by modification of a literature procedure[17] using 3.12 g (13.8 mmol) of 2-formyl-6-mesitylpyridine to deliver 2.73 g (12.0 mmol, 86%) of **3**.

Synthesis of 2-bromomethyl-6-mesitylpyridine (4). This compound was prepared by modification of a literature procedure[17] using an excess of $POBr_3$ instead of PBr_3 with 854 mg (3.76 mmol) of 2-hydroxymethyl-6-mesitylpyridine to produce 862 mg (2.97 mmol, 79%) of **4**.

Synthesis of 2-chloromethyl-6-mesitylpyridine hydrochloride (5). This compound was prepared by modification of a literature procedure[15] using 5.22 g (23.0 mmol) of 2-hydroxymethyl-6-mesitylpyridine instead of 2-hydroxymethyl-6-phenylpyridine to yield 5.98 g (21.2 mmol, 92%) of **5**. ^{1}H NMR (300 MHz, $CDCl_3$): δ 2.07 (s, 6H, mes-CH_3), 2.34 (s, 3H, mes-CH_3), 5.35 (s, 2H, CH_2), 7.04 (s, 2H, mes-C*H*), 7.75 (d, *J* = 7.8 Hz, 1H, py-C*H*), 8.03 (d, *J* = 7.8 Hz, 1H, py-C*H*), 8.50 (t, *J* = 7.8 Hz, 1H, py-C*H*); ^{13}C NMR (100 MHz, $CDCl_3$): δ 20.7, 21.5, 39.9, 125.3, 127.9, 128.2, 129.2, 136.3, 141.27, 145.49, 153.19, 154.94. HRFABMS ($[M-Cl]^+$) *m/z* calcd for $C_{15}H_{17}NCl$ 246.1050, found 246.1049.

Synthesis of 2-aminomethyl-6-mesitylpyridine hydrochloride (6-HCl). This compound was prepared by modification of a literature procedure[15] using 1.75 g (6.20 mmol) of 2-chloromethyl-6-mesitylpyridine hydrochloride instead of 2-chloromethyl-6-phenylpyridine hydrochloride to afford 397 mg (1.51 mmol, 24%) of **6-HCl**. The free base **6** was obtained by extraction using sat. aq. $NaHCO_3$ from water and diethyl ether and used without further purification. ^{1}H NMR (300 MHz, D_2O): δ 2.03 (s, 6H, mes-CH_3), 2.32 (s, 3H, mes-CH_3), 4.59 (s, 2H, CH_2), 7.10 (s, 2H, mes-C*H*), 7.85 (d, *J* = 8.1 Hz, 1H, py-C*H*), 8.01 (d, *J* = 8.1 Hz, 1H, py-C*H*), 8.55 (t, *J* = 8.0 Hz, 1H, py-C*H*); ^{13}C NMR (75 MHz, D_2O): δ 19.2, 20.5, 40.7, 124.8, 128.7, 128.9, 130.0, 136.8, 141.4, 146.2, 148.5, 156.1. HRFABMS (MH^+) *m/z* calcd for $C_{15}H_{19}N_2$ 227.1548, found 227.1550.

Synthesis of Tris(6-mesityl-2-pyridylmethyl)amine, TPA^{3Mes} (7). 2-aminomethyl-6-mesitylpyridine (834 mg, 3.69 mmol) was stirred with 2-chloromethyl-6-mesitylpyridine hydrochloride (2.1 g, 7.44 mmol), cesium carbonate (7.1 g, 21.8 mmol), and sodium iodide (1.9 g, 12.7 mmol) in 15 mL acetonitrile at room temperature for three days. The reaction mixture was filtered by gravity filtration to remove salts and rinsed with 25 mL dichloromethane. The filtrate was evaporated to dryness and purified on basic alumina (20% ethyl acetate in hexanes) to produce **7** as a white solid (921 mg, 1.43

mmol, 39%). ^{1}H NMR (300 MHz, $CDCl_3$): δ 2.00 (s, 18H, mes-C*H*$_3$), 2.31 (s, 9H, mes-C*H*$_3$), 3.98 (s, 6H, C*H*$_2$), 6.92 (s, 6H, mes-C*H*), 7.09 (d, *J* = 7.5 Hz, 3H, py-C*H*), 7.59 (d, *J* = 7.5 Hz, 3H, py-C*H*), 7.73 (t, *J* = 7.5 Hz, 3H, py-C*H*); ^{13}C NMR (100 MHz, $CDCl_3$): δ 20.4, 21.3, 60.4, 120.8, 123.1, 128.5, 135.9, 137.8, 137.5, 137.9, 159.4, 159.9. HRFABMS (MH^+) *m/z* calcd for $C_{45}H_{49}N_4$ 645.3957, found 645.3958.

Synthesis of [TPA^{3Mes}FeCl]PF$_6$ (8). To a stirred, colorless slurry of TPA^{3Mes} (127 mg, 0.197 mmol) in acetonitrile was added $FeCl_2$ (25.1 mg, 0.198 mmol) as a slurry in acetonitrile. Within minutes the reaction mixture became yellow with precipitation of a yellow solid. After stirring for 2 hr, $TlPF_6$ (70 mg, 0.20 mmol) was added with immediate precipitation of TlCl. After stirring overnight, the reaction mixture was filtered through celite, washed with acetonitrile, and the yellow filtrate was evaporated to dryness. Precipitation from CH_2Cl_2/pentane, filtering and washing with pentane and diethyl ether produced **8** as a yellow solid (126 mg, 0.143 mmol, 73%). Single crystals suitable for X-ray structure determination were grown from butyronitrile/pentane. ^{1}H NMR (300 MHz, CD_3CN): δ -12.85, -7.82, 1.35, 5.68, 6.46, 6.97, 9.52, 47.88, 61.83, 198.23. Magnetic susceptibility (CD_3CN): μ_{eff} = 4.95 μ_{BM}.[18] HRFABMS (M^+) *m/z* calcd for $C_{45}H_{48}N_4ClFe$ 735.2917, found 735.2918.

Synthesis of [TPA^{3Mes}FeNC$_4$H$_7$](PF$_6$)$_2$(C$_4$H$_7$N)$_2$ (9). To a stirred, colorless slurry of TPA^{3Mes} (121 mg, 0.188 mmol) in acetonitrile was added $FeCl_2$ (24.0 mg, 0.189 mmol) as a slurry in acetonitrile. Within minutes the reaction mixture became yellow with precipitation of a yellow solid. After stirring for 2 hr, $TlPF_6$ (131 mg, 0.375 mmol) was added with immediate precipitation of TlCl. After stirring overnight, the reaction mixture was filtered through celite, washed with acetonitrile, and the colorless filtrate was evaporated to dryness. The product was precipitated from butyronitrile/pentane, filtered, and washed with pentane to produce **9** as a white solid (152 mg, 0.144 mmol, 76%). Single crystals suitable for X-ray structure determination were grown from butyronitrile/pentane. ^{1}H NMR (300 MHz, CD_3CN): δ -12.85, -7.83, 1.36, 6.46, 6.96, 9.52, 32.26, 47.87, 61.85, 198.83. Magnetic susceptibility (CD_3CN): μ_{eff} = 5.13 μ_{BM}.[18] HRESIMS (M^{2+}) *m/z* calcd for $C_{45}H_{48}N_4Fe$ 350.1609, found 350.1605. Anal. Calcd for $C_{57}H_{69}F_{12}FeN_7P_2$: C, 57.15; H, 5.81; N, 8.18. Found: C, 57.0; H, 5.70; N, 8.0.

Synthesis of 2-formyl-6-phenylpyridine (10). This compound was prepared by modification of a literature procedure[15] using 2.97 g (16.0 mmol) of **1**, 2.326 g (19.0 mmol) of phenylboronic acid, 3.4 g (32.0 mmol) Na_2CO_3, and 600 mg (0.052 mmol) of $Pd(PPh_3)_4$ to provide **10** as a yellow oil after purification (2.565 g, 14.0 mmol, 88 %).

Synthesis of 2-hydroxymethyl-6-phenylpyridine (11). This compound was synthesized by modification of a literature procedure[15] using 6.575 (35.9 mmol) of **10** and 4.1 g (108 mmol) of $NaBH_4$ to yield **11** (6.349 g, 34.3 mmol, 95 %).

Synthesis of 2-chloromethyl-6-phenylpyridine hydrochloride (12). This compound was prepared by modification of a literature procedure[15] using 2.337 g (12.6 mmol) of **11** in 14 mL $SOCl_2$ to afford **12** (2.649 g, 11.0 mmol, 88 %).

Synthesis of 2-aminomethyl-6-phenylpyridine hydrochloride (13). This compound was prepared by modification of a literature procedure[15] using 1.62 g (6.75 mmol) of **12**, 1.38 g (7.45 mmol) potassium phthalimide, and 810 mg (7.64 mmol) of Na_2CO_3 to provide **13**.

Synthesis of TPA^{3Ph} (14). 13 (306.9 mg, 1.39 mmol), **12** (860.5 mg, 3.58 mmol), Cs_2CO_3 (4.737 g, 14.5 mmol), and NaI (772.5 mg, 5.15 mmol) were stirred under N_2 in

acetonitrile for one week. The reaction was judged complete by TLC (Al_2O_3; 30 % EtOAc in hexanes), filtered and rinsed with acetone and dichloromethane and concentrated under vacuum to a pale yellow powder. The powder was recrystallized from hot CH_3CN to provide **14** as a white solid. ^{1}H NMR and ESI MS characterization data matched that of the previously reported **14**.

Synthesis of [(TPA^{3Ph})Fe(CH$_3$CN)](OTf)$_2$ (15). To a stirring acetonitrile slurry of **14** (39 mg, 0.075 mmol) was added solid $Fe(OTf)_2(CH_3CN)_2$ (32.6 mg, 0.075 mmol). After 30 minutes, the reactants had dissolved to form a colorless solution. The solution was stirred a further 1.5 hours and concentrated under vacuum to yield a white powder. Recrystallization of the powder from CH_3CN/ether provided colorless block-shaped crystals, which were suitable for Xray crystallographic analysis. The crystals were rinsed with ether and dried under vacuum to provide **15** as a colorless powder (64.1 mg, 0.064 mmol, 86 %). ^{1}H NMR (300 MHz, CD_3CN): δ 74.3, 71.23, 53.77, 27.73, 8.05, 3.49, -15.33. ESI MS *m/z* calculated for (**15**-OTf): 723.1335, found 723.1346. CHN calculated for $C_{44}H_{39}F_6FeN_7O_6S_2$ (**15**$(CH_3CN)_2$): C, 53.07; H, 3.95; N, 9.85. Found: C, 53.49; H, 3.89; N, 9.52.

Synthesis of [(TPA^{2PhOPh})Fe(OTf)]OTf (16). To a stirring acetonitrile solution of **15** (31.6 mg, 0.032 mmol) was added iodosylbenzene (11.7 mg, 0.053 mmol). Within seconds, the color of the reaction had changed to a dark blue/green. After ca 15 minutes, the reaction mixture was concentrated under vacuum to a green/blue oil. This oil was recrystallized from DME/pentane to provide thin plate-like crystals of **16**, which were washed with pentane and dried (20.3 mg, 0.021 mmol, 65 %). The crystals obtained from DME/pentane were suitable for Xray diffraction analysis. ESI MS *m/z* calculated for (**16**-OTf): 738.1206, found 738.1207. CHN calculated for $C_{38}H_{29}F_6FeN_4O_7S_2$ (**16**): C, 51.4; H, 3.3; N, 6.3. Found: C, 51.7; H, 3.4; N, 6.0.

General Methods for X-Ray Crystallography. Xray crystallographic data was collected using fine-focused Mo-Kα radiation on a Bruker 3-circle Smart-Apex or Siemens Smart 1000 diffractometer with an Apex 1 or Smart 1000 CCD detector, respectively. Samples on Smart-Apex were cooled to 100 K using an Oxford Cryostream 700 low temperature device (or to ca 130 K on the Smart 1000 using a home-built device). Structures were solved using either direct methods or the Patterson method in conjunction with standard difference Fourier techniques and refined by full-matrix least-squares procedures.[19] A semi-empirical absorption correction (SADABS) was applied to the diffraction data for all structures. All non-hydrogen atoms were refined anisotropically, and hydrogen atoms were treated as idealized contributions and refined isotropically. All software used for diffraction data processing and crystal-structure solution and refinement are contained in the APEX2 program suite (Bruker AXS, Madison, WI).[20]

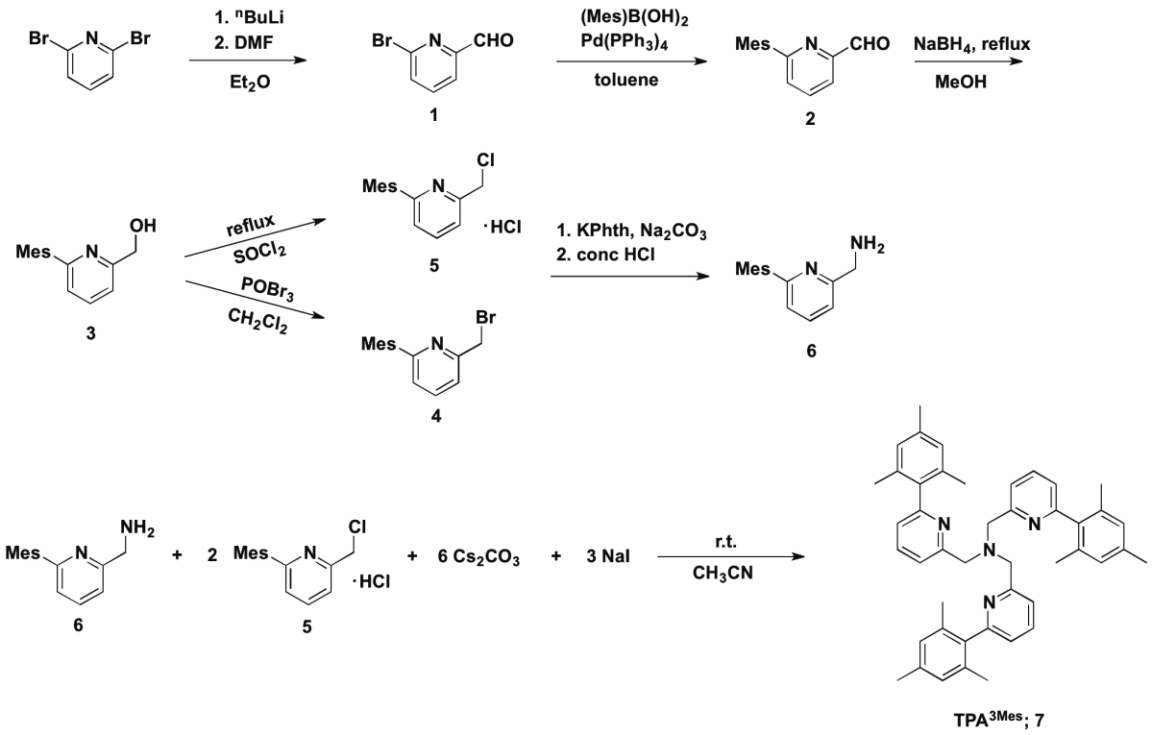

Scheme C.10. Synthesis of the new ligand, TPA^{3Mes}.

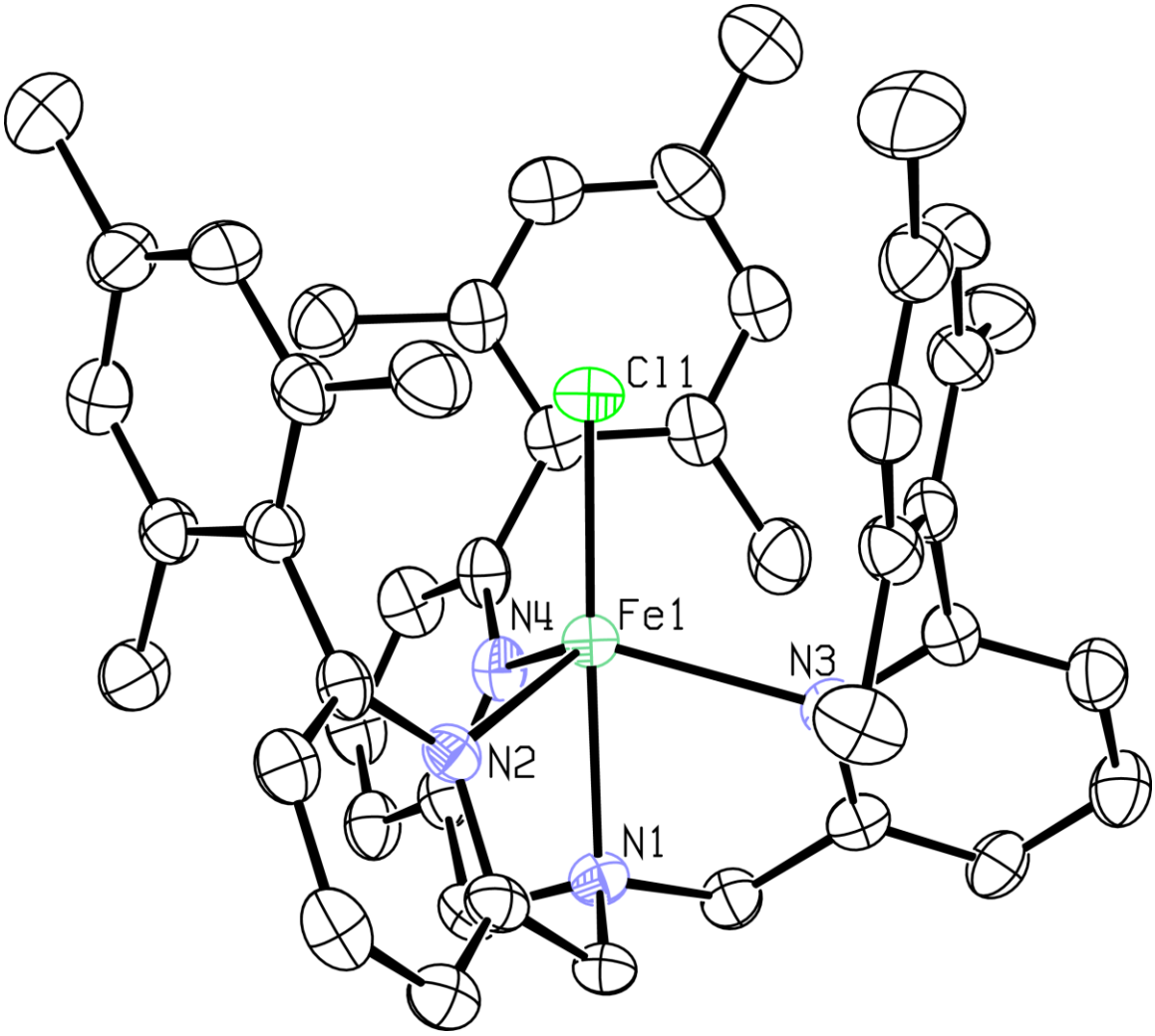

Figure C.1. Molecular structure of the cationic portion of **8** as determined by Xray diffraction. The ellipsoids are shown at 50 % probability. Hydrogen atoms, the triflate counter anion, and solvents of crystallization are not displayed for clarity.

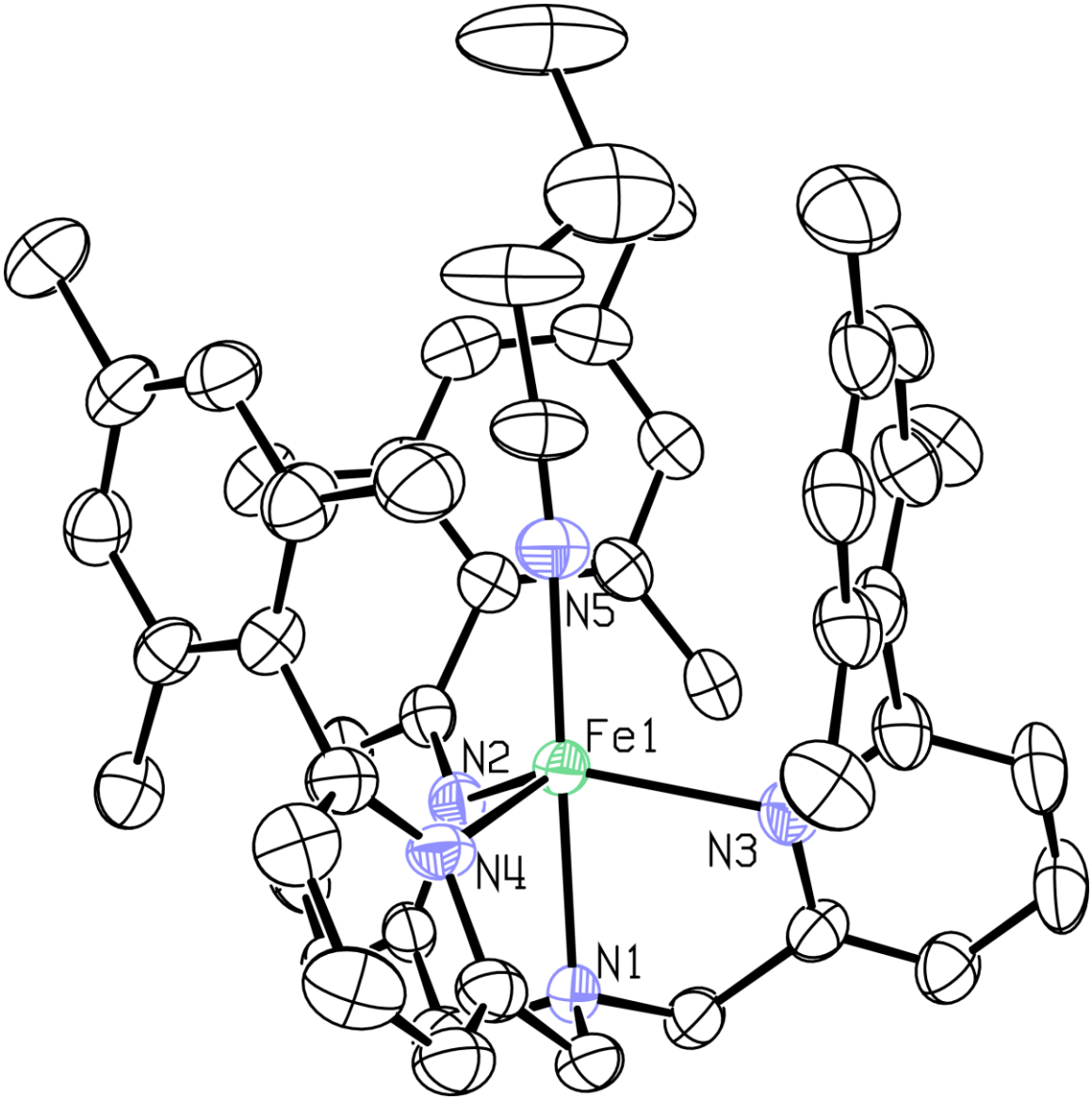

Figure C.11. The molecular structure of the dicationic portion of **9** determined by Xray diffraction analysis. The ellipsoids are shown at 50 % probability. All hydrogen atoms, triflate counterions, and solvents of crystallization are not shown for clarity.

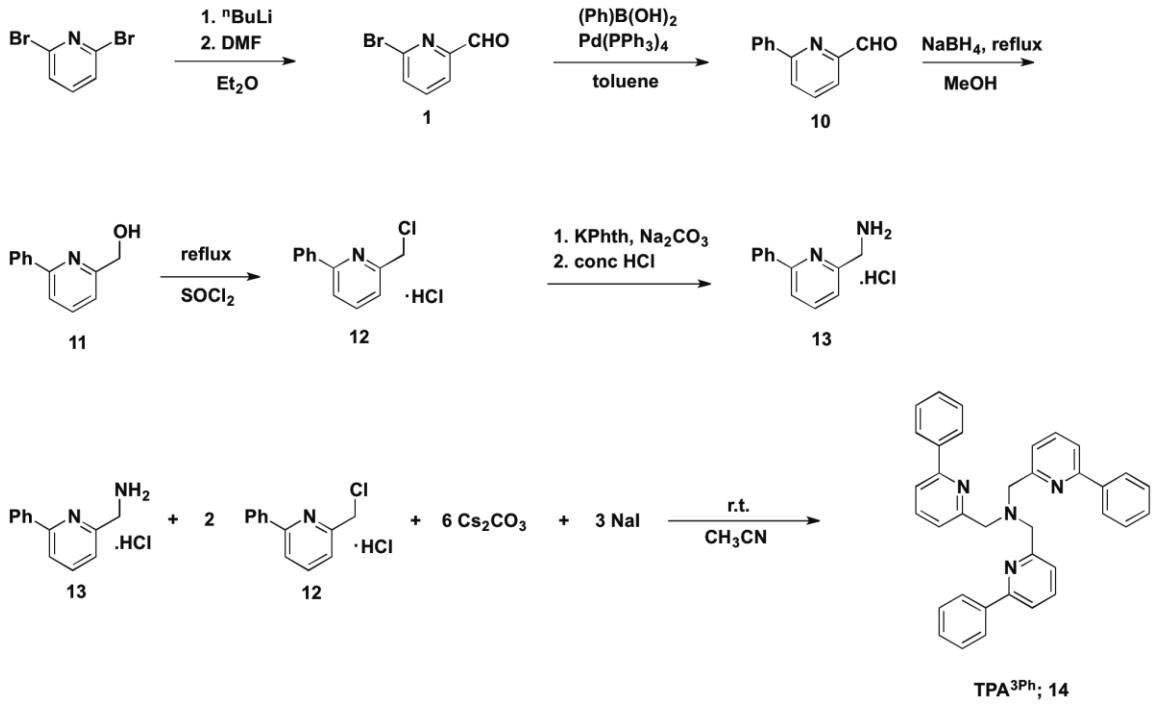

Scheme C.2. Synthesis of TPA^{3Ph}.

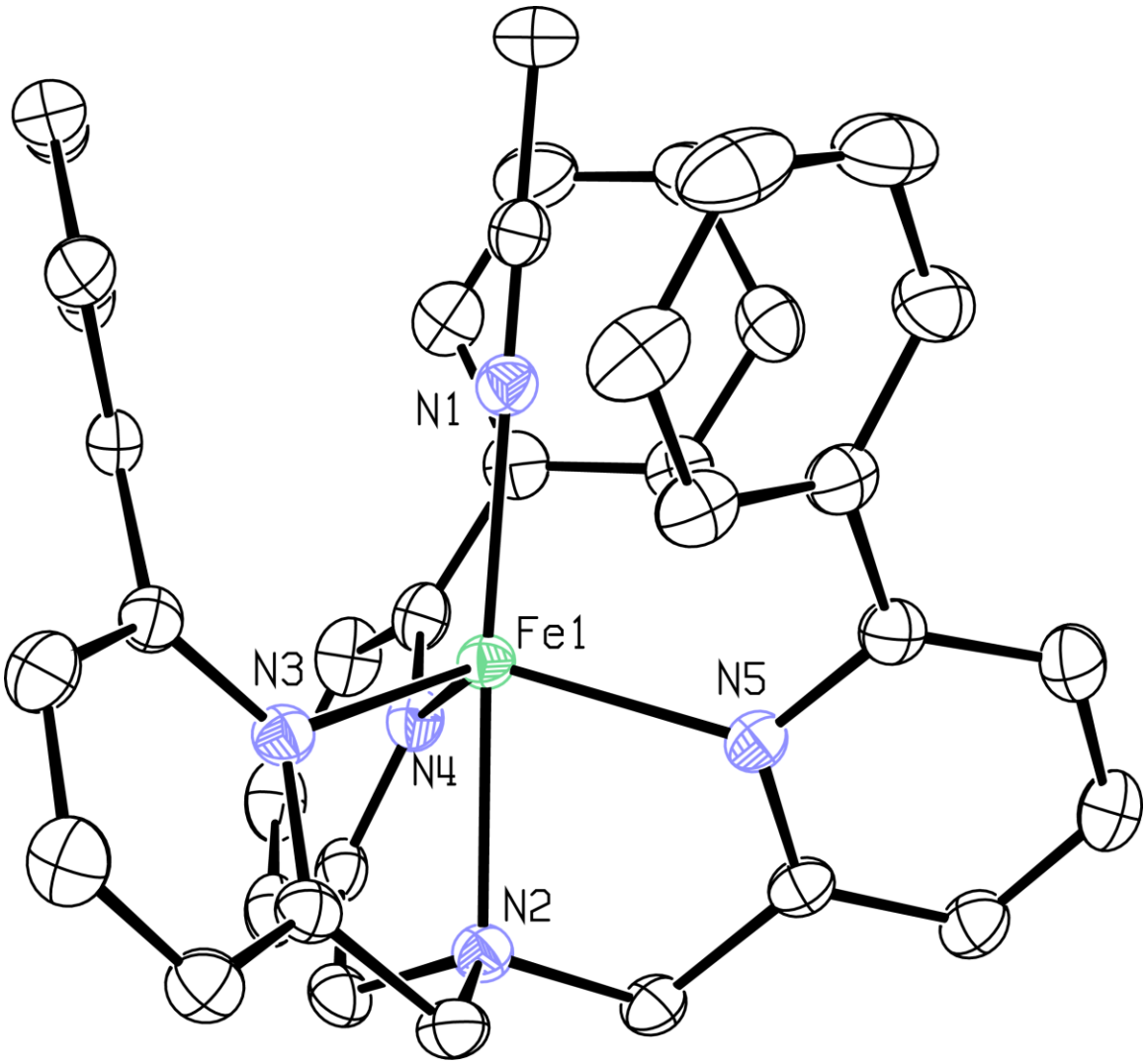

Figure C.12. The molecular structure of **15** from Xray crystallographic analysis. Ellipsoids are shown at 50 % probability. Hydrogen atoms, triflate counterions, and solvents of crystallization are removed for clarity.

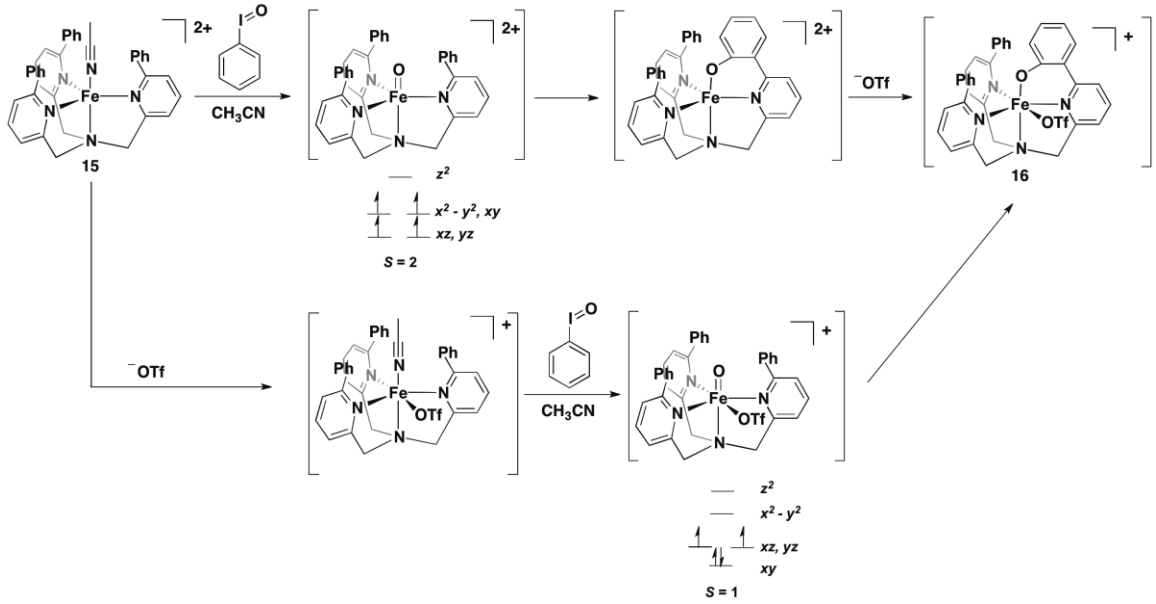

Scheme C.3. Two alternative pathways for the formation of **16** via two distinct iron(IV)-oxo complexes.

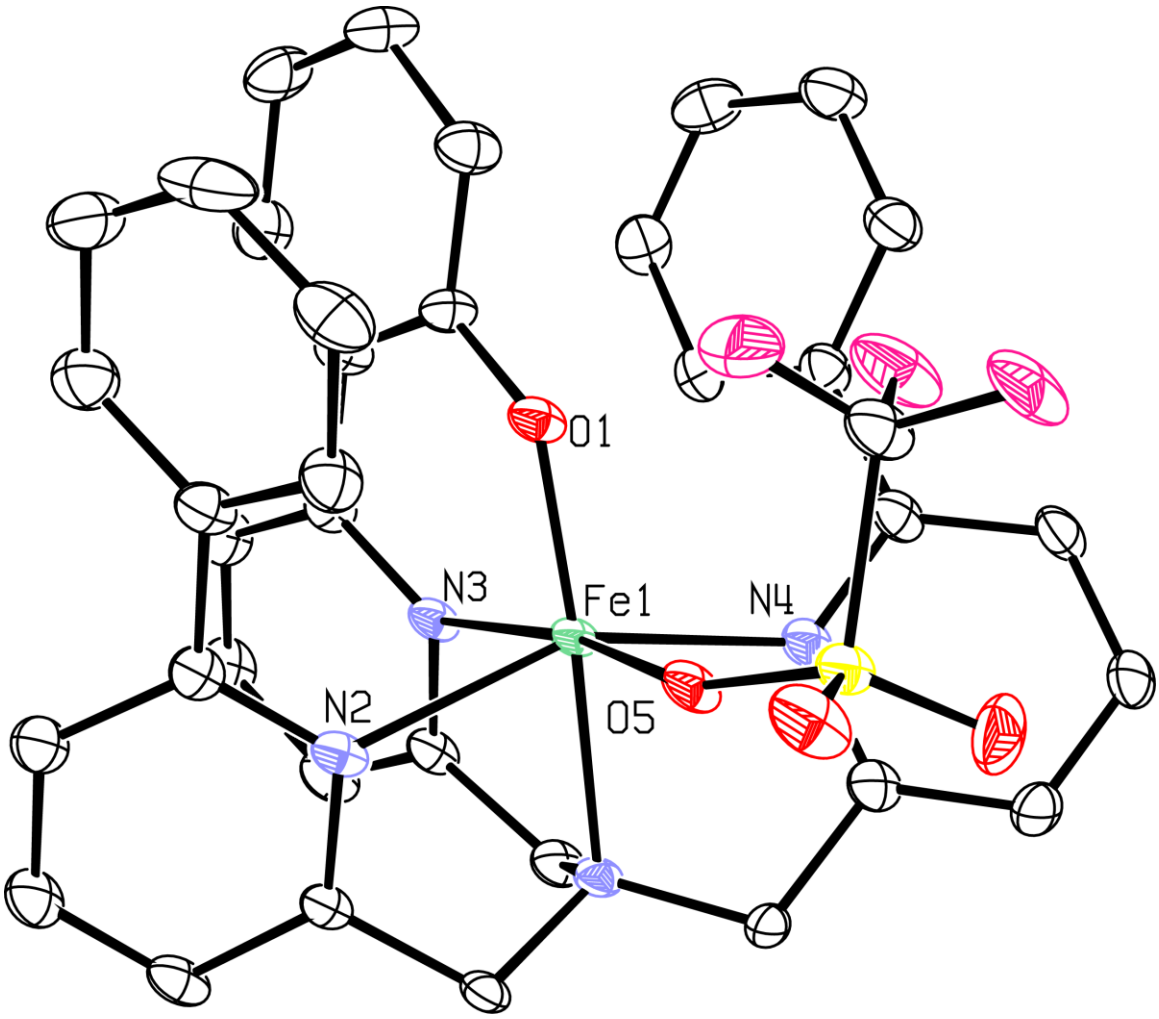

Figure C.4. The molecular structure of **16** determined by Xray diffraction. The probability ellipsoids are shown at 50 % and hydrogen atoms, the triflate counterion, and solvents of crystallization are removed for clarity.

Table C.1. Crystallographic Details for **8** and **9**.		
	8	**9**
Empirical Formula	$C_{51}H_{58.5}ClF_6FeN_{5.5}P$	$C_{57}H_{69}Cl_2F_{12}FeN_7P_2$
Formula Weight	984.8	1197.98
T (K)	141	
λ (Å)	0.71073	0.71073
Crystal System	Orthorhombic	Monoclinic
Space Group	*P2(1)/2(1)/2(1)*	*Pc*
a (Å)	11.0657(11)	11.2285(16)
b (Å)	19.0106(19)	14.252(2)
c (Å)	46.786(5)	18.313(3)
α (º)	90.00	90.00
β (º)	90.00	99.904(2)
γ (º)	90.00	90.00
V	9842.1(17)	2886.8(7)
Z	8	2
ρ_{calc} (g/cm^3)	1.329	1.204
μ (mm^{-1})	0.46	0.39
reflctns collected	44153	14310
T_{min}/T_{max}	0.94	0.92
data/restr/params	16549/ ?/1180	7074/2/712
$2\theta_{max}$ (º)	49.4	49.4
R, R_w (%; I>4σ)	4.4, 11.2	4.9, 13.8
GOF	0.87	1.006
mean shift/error		0.018

Table C.2. Crystallographic Details for **15** and **16**.		
	15	**16**
Empirical Formula	$C_{40}H_{33}F_6FeN_5O_6S_2$	$C_{38}H_{29}F_6FeN_4O_7S_2$
Formula Weight	913.68	887.62
T (K)	147	100
λ (Å)	0.71073	1.54178
Crystal System	Monoclinic	Triclinic
Space Group	*P2(1)/n*	*P-1*
a (Å)	13.8852(18)	11.4710(6)
b (Å)	13.8525(17)	13.4247(7)
c (Å)	23.171(3)	14.9580(8)
α (º)	90.00	95.285(3)
β (º)	94.548(2)	108.252(3)
γ (º)	90.00	102.021(3)
V	4442.8(10)	2108.67(19)
Z	4	2
ρ_{calc} (g/cm^3)	1.366	1.398
μ (mm^{-1})	0.507	4.475
reflctns collected	89092	16365
T_{min}/T_{max}	0.87	0.69
data/restr/params	8113/0/607	7174/0/577
$2\theta_{max}$ (º)	50.6	136.4
R, R_w (%; I>4σ)	2.7, 7.4	7.6, 21.1
GOF	0.994	1.408
mean shift/error	0.003	0.000

References

(1) Bigi, J. P.; Harman, W. H.; Lassalle-Kaiser, B.; Robles, D. M.; Stich, T. A.; Yano, J.; Britt, R. D.; Chang, C. J. *Journal of the American Chemical Society* **2012**, *134*, 1536-1542.

(2) England, J.; Guo, Y.; Farquhar, E. R.; Young Jr, V. G.; Münck, E.; Que Jr, L. *Journal of the American Chemical Society* **2010**, *132*, 8635-8644.

(3) England, J.; Guo, Y.; Van Heuvelen, K. M.; Cranswick, M. A.; Rohde, G. T.; Bominaar, E. L.; Münck, E.; Que, L. *Journal of the American Chemical Society* **2011**, *133*, 11880-11883.

(4) England, J.; Martinho, M.; Farquhar, E. R.; Frisch, J. R.; Bominaar, E. L.; Münck, E.; Que, L. *Angewandte Chemie International Edition* **2009**, *48*, 3622-3626.

(5) Lacy, D. C.; Gupta, R.; Stone, K. L.; Greaves, J.; Ziller, J. W.; Hendrich, M. P.; Borovik, A. S. *Journal of the American Chemical Society* **2010**, *132*, 12188-12190.

(6) Gupta, R.; Lacy, D. C.; Bominaar, E. L.; Borovik, A. S.; Hendrich, M. P. *Journal of the American Chemical Society* **2012**, *134*, 9775-9784.

(7) Harman, W. H.; Chang, C. J. *Journal of the American Chemical Society* **2007**, *129*, 15128-15129.

(8) Lim, M. H.; Rohde, J.-U.; Stubna, A.; Bukowski, M. R.; Costas, M.; Ho, R. Y. N.; Münck, E.; Nam, W.; Que, L. *Proceedings of the National Academy of Sciences* **2003**, *100*, 3665-3670.

(9) Pestovsky, O.; Stoian, S.; Bominaar, E. L.; Shan, X.; Münck, E.; Que, L.; Bakac, A. *Angewandte Chemie International Edition* **2005**, *44*, 6871-6874.

(10) Que, L. *Accounts of Chemical Research* **2007**, *40*, 493-500.

(11) Jensen, M. P.; Lange, S. J.; Mehn, M. P.; Que, E. L.; Que, L. *Journal of the American Chemical Society* **2003**, *125*, 2113-2128.

(12) Jensen, M. P.; Mehn, M. P.; Que, L. *Angewandte Chemie International Edition* **2003**, *42*, 4357-4360.

(13) Mukherjee, A.; Martinho, M.; Bominaar, E. L.; Münck, E.; Que, L. *Angewandte Chemie International Edition* **2009**, *48*, 1780-1783.

(14) Yamashita, M.; Furutachi, H.; Tosha, T.; Fujinami, S.; Saito, W.; Maeda, Y.; Takahashi, K.; Tanaka, K.; Kitagawa, T.; Suzuki, M. *Journal of the American Chemical Society* **2007**, *129*, 2-3.

(15) Chuang, C.-l.; Lim, K.; Chen, Q.; Zubieta, J.; Canary, J. W. *Inorganic Chemistry* **1995**, *34*, 2562-2568.

(16) Parks, J. E.; Wagner, B. E.; Holm, R. H. *Inorganic Chemistry* **1971**, *10*, 2472-2478.

(17) Wang, C.-Y.; Liu, Y.-H.; Peng, S.-M.; Liu, S.-T. *Journal of Organometallic Chemistry* **2006**, *691*, 4012-4020.

(18) Evans, D. F. *Journal of the Chemical Society (Resumed)* **1959**, 2003-2005.

(19) Sheldrick, G. *Acta Crystallographica Section A* **1990**, *46*, 467-473.

(20) Sheldrick, G. *Acta Crystallographica Section A* **2008**, *64*, 112-122.

Appendix D
Synthesis and Structural Characterization of $(TPA^{3Mes})Co^{II}$ and $(TPA^{3Mes})Mn^{II}$ and Electrocatalytic Proton Reduction by $(TPA^{3Mes})Co^{II}$

Introduction

In the context of our ongoing work on $(TPA^{3Mes})Fe^{II}$ (Appendix C), we are interested in the chemistry of the analogous cobalt(II) and manganese(II) complexes. In particular, the ability of the cobalt(II) to serve as an electrocatalyst for proton reduction is of interest in relation to our work on cobalt polypyridyl electrocatalysts, which have shown high activity for the reduction of protons in the presence of water.[1,2] The manganese(II) complex could potentially serve as a platform for studying manganese(IV)-oxo chemistry as non-porphyrinoid manganese(IV)-oxo complexes are still relatively rare.[3-5] Manganese(IV)-oxo complexes are of interest as environmentally benign oxidants or mimics of nature's water-oxidizing complex, the oxygen-evolving complex of Photosystem II.[6-8]

Results and Discussion

The dicationic cobalt(II) complex $[(TPA^{3Mes})Co(NCCH_3)](PF_6)_2$ (**1**) is synthesized by reaction of TPA^{3Mes} with $CoCl_2$ in acetonitrile followed by halide abstraction with two equivalents of $TlPF_6$. The bright green complex is high-spin (μ_{eff} = 4.1 μ_{BM} compared to the spin-only value of 3.9) as determined by Evans' method[9] and crystallizes as a trigonal bipyramidal complex similar to the iron(II) complex of TPA^{3Mes} (Figure D.1, Table D.1).

The cyclic voltammogram (CV) of **1** reveals a reversible reduction at ca -1.44 V vs ferrocene/ferrocenium. This reduction is likely due to the Co(II)/Co(I) reduction, in analogy to similar cobalt(II) complexes studied by our group.[1,2] Significantly, this reductive wave loses reversibility and shows a spike in current in the presence of TFA (Figure D.2). In addition, a controlled potential electrolysis experiment provides a turn over frequency of 3.5 at an overpotential of 670 mV (Figure D.3). We attribute this generation of current to the electrocatalytic production of dihydrogen. Interestingly, the current increase is strikingly similar for the trigonal bipyramidal **1** to that observed for $(PY4)Co^{II}$, an octahedral complex of the tetradentate PY4 ligand: 200 µA vs 300 µA at identical concentrations of catalyst and TFA.[1] Whether the two complexes form similar species under electrocatalytic conditions, however, is unknown at this time. It is thus of note that octahedral cobalt(II) complexes of the pentadentate, polypyridyl PY5 ligand also serve as pre-catalysts for the electrocatalytic production of hydrogen.[2] Determining the optimal number of coordinated pyridines and overall coordination geometry for electrocatalysis with cobalt polypyridyl complexes will be the subject of future studies.

The manganese(II) complex of TPA^{3Mes}, $[(TPA^{3Mes})Mn(NCCH_3)](PF_6)_2$ (**2**), is prepared similarly to the cobalt(II) complex. The molecular structure of **2** as determined by Xray diffraction analysis is shown in Figure D.4 (crystal data shown in Table D.1). **2** adopts a trigonal bipyramidal coordination geometry in the solid-state and is high-spin as determined by the method of Evans.[9] The oxidative chemistry of **2** will be investigated in due course.

Concluding Remarks

In conclusion, the preparations of the Co(II) and Mn(II) complexes of TPA^{3Mes} are presented as well as their structural characterization. Both complexes adopt trigonal bipyramidal structures similar to the Fe(II) structure (Appendix C). In addition, the Co(II)

complex **1** serves as an electrocatalyst for the reduction of protons. The electrocatalysis was investigated by cyclic voltammetry and controlled potential electrolysis.

Experimental Section

General Methods. Unless noted otherwise, all manipulations were carried out at room temperature under a dinitrogen atmosphere in a VAC Atmospheres Co. glovebox or using high-vacuum Schlenk techniques. Methylene chloride, diethyl ether, tetrahydrofuran, and pentane were dried over activated 4 Å molecular sieves, passed through a column of activated alumina, and sparged with nitrogen prior to use. Acetonitrile, acetonitrile-d_3, and butyronitrile were refluxed over CaH_2, distilled, and sparged with nitrogen. All other reagents and solvents were purchased from commercial sources and used without further purification. Electrochemistry experiments were conducted with a glassy carbon working electrode, a platinum auxiliary electrode, and a silver wire as a floating reference electrode. Ferrocene or cobaltocene was added as an internal standard. A BASi Epsilon potentiostat was used to control the cell potential. NMR spectra were recorded on Bruker spectrometers operating at 300 or 400 MHz as noted. Chemical shifts are reported in ppm relative to residual protiated solvent; coupling constants are reported in Hz. Mass spectra and elemental analyses were determined at the University of California, Berkeley Mass Spectrometry and Microanalytical facility.

Synthesis of [(TPA^{3Mes})Co(NCCH$_3$)](PF$_6$)$_2$ (1). TPA^{3Mes} (52.6 mg, 0.0816 mmol) and $CoCl_2$ (10.6 mg, 0.0816 mmol) were stirred in CH_3CN to form a turquoise mixture. After one hour, $TlPF_6$ (57.0 mg, 0.0163 mmol) was added as a solid with the immediate formation of TlCl. After one hour, the TlCl was removed via filtration through celite to provide a green filtrate. The green residue was concentrated *in vacuo* and recrystallized from propionitrile/pentane to provide green, xray quality crystals of **1**. ESI MS: *m/z* for [**1**-$(PF_6)_2$]$^{2+}$ calcd 351.6600, found 351.6603. Magnetic susceptibility[9] (CD_3CN): μ_{eff} = 4.1 μ_{BM}.

Synthesis of [(TPA^{3Mes})Mn(NCCH$_3$)](PF$_6$)$_2$ (2). TPA^{3Mes} (109.3 mg, 0.169 mmol) and $MnCl_2$ (21.5 mg, 0.171 mmol) were stirred in CH_3CN overnight to form a pink slurry. $TlPF_6$ (119.4 mg, 0.342 mmol) was then added with the immediate precipitation of TlCl. After stirring for three hours, the mixture was filtered through celite to remove the TlCl and the filtrate was concentrated under vacuum. Recrystallization from DCE/THF provided colorless crystals of **2**, which were suitable for Xray diffraction analysis. ^{1}H NMR (300 MHz, CD_3CN): 6.51 (b). ESI MS: *m/z* for [**2**-OTf]$^+$ calcd 848.2780, found 848.2767. Magnetic susceptibility[9] (CD_3CN): μ_{eff} = 6.03 μ_{BM}.

General Methods for X-Ray Crystallography. Xray crystallographic data was collected using fine-focused Mo-Kα radiation on a Bruker 3-circle Smart-Apex or Siemens Smart 1000 diffractometer with an Apex 1 or Smart 1000 CCD detector, respectively. Samples on Smart-Apex were cooled to 100 K using an Oxford Cryostream 700 low temperature device (or to ca 130 K on the Smart 1000 using a home-built device). Structures were solved using either direct methods or the Patterson method in conjunction with standard difference Fourier techniques and refined by full-matrix least-squares procedures.[10] A semi-empirical absorption correction (SADABS) was applied to the diffraction data for all structures. All non-hydrogen atoms were refined anisotropically, and hydrogen atoms were treated as idealized contributions and refined isotropically. All software used for

diffraction data processing and crystal-structure solution and refinement are contained in the APEX2 program suite (Bruker AXS, Madison, WI).[11]

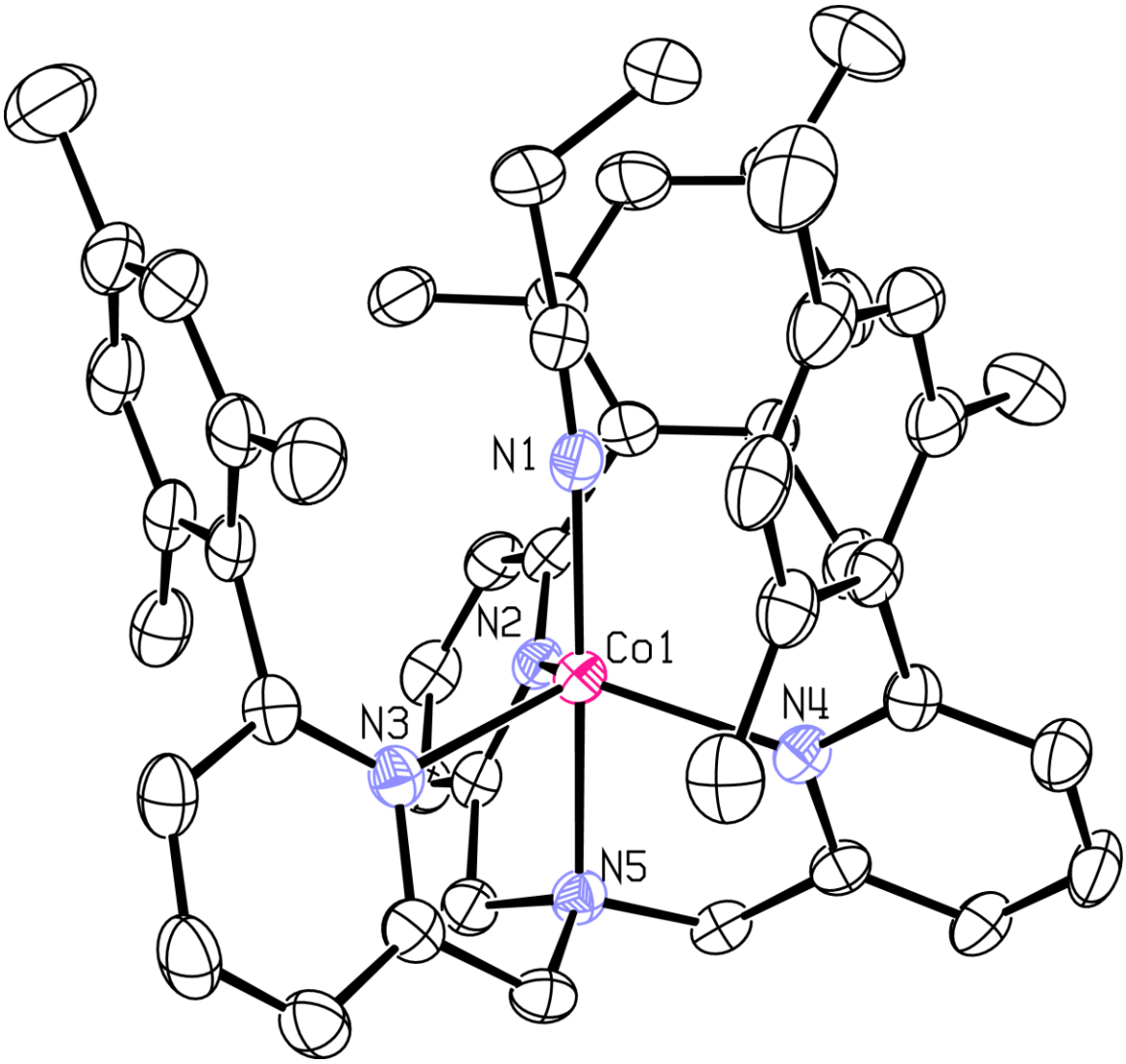

Figure D.13. Molecular structure of the dicationic portion of **1** determind by Xray crystallographic analysis. Ellipsoids are shown at 50 % probability. All hydrogen atoms, hexafluorophosphate counterions and solvents of crystallization are removed for clarity.

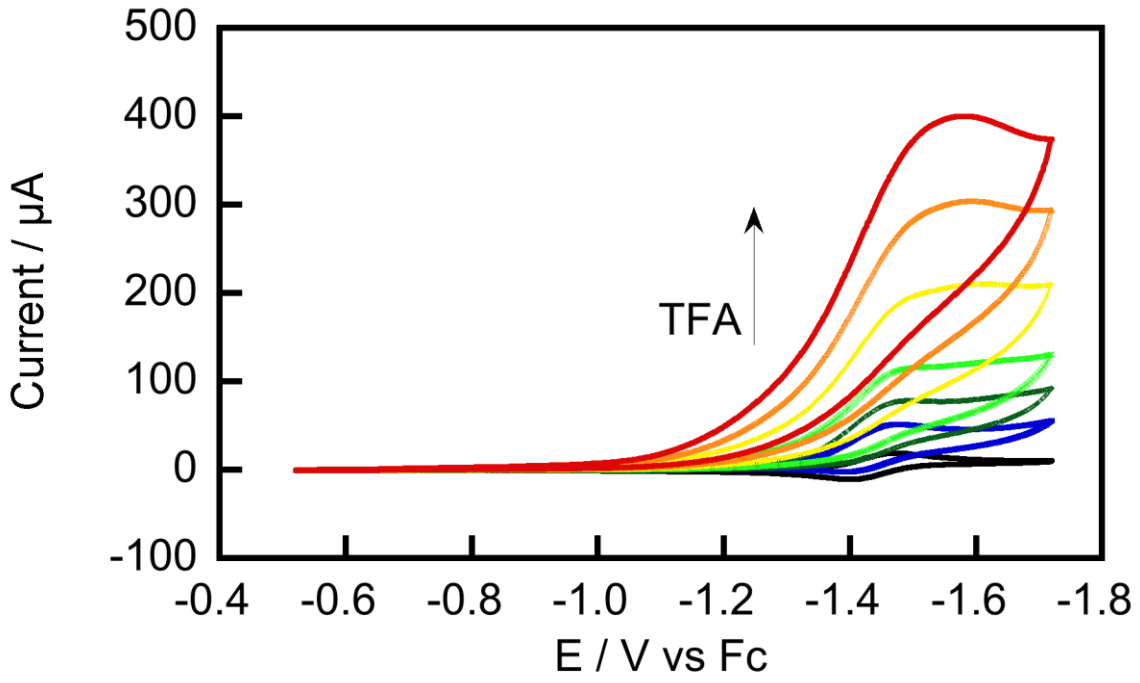

Figure D.14. Cyclic voltammogram of **1** in 0.1 M $^{n}Bu_4NPF_6$ in CH_3CN with increasing amounts of TFA. Scan rate: 100 mV/sec; working electrode: glassy carbon.

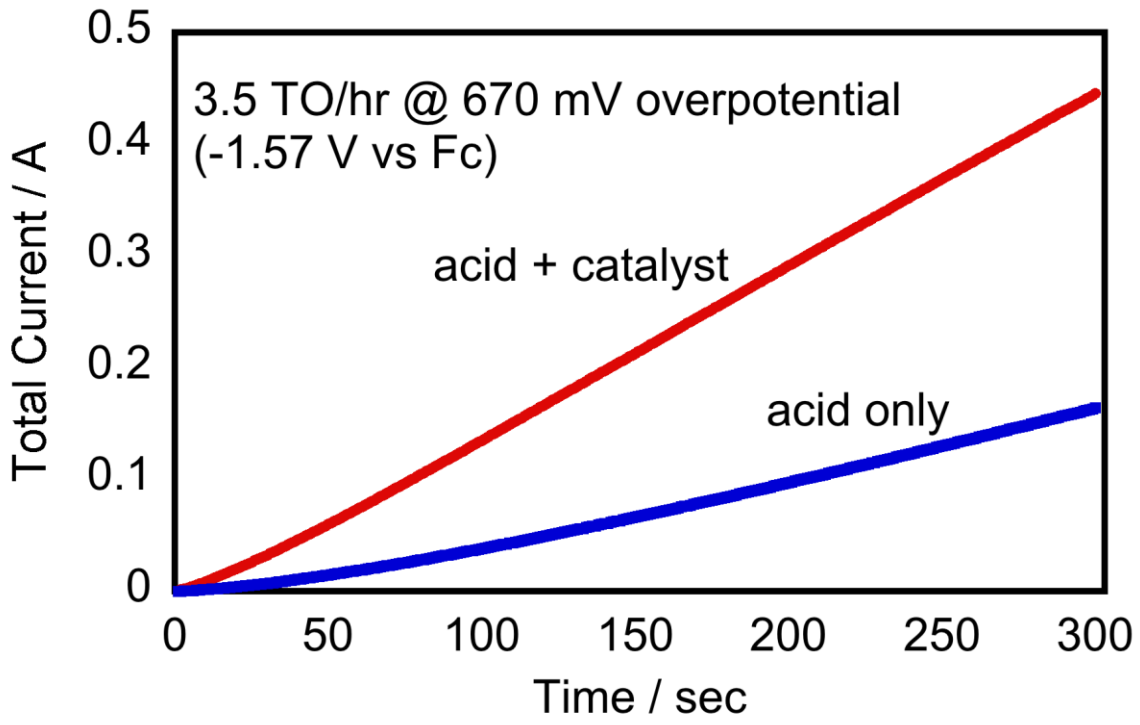

Figure D.15. Controlled potential electrolysis of 1.0 mM **1** in 0.1 M $^{n}Bu_4NPF_6$ in acetonitrile in the presence of 60 equivalents TFA (red trace). The background reaction in the absence of **1** is shown as the blue trace. Working electrode: glassy carbon.

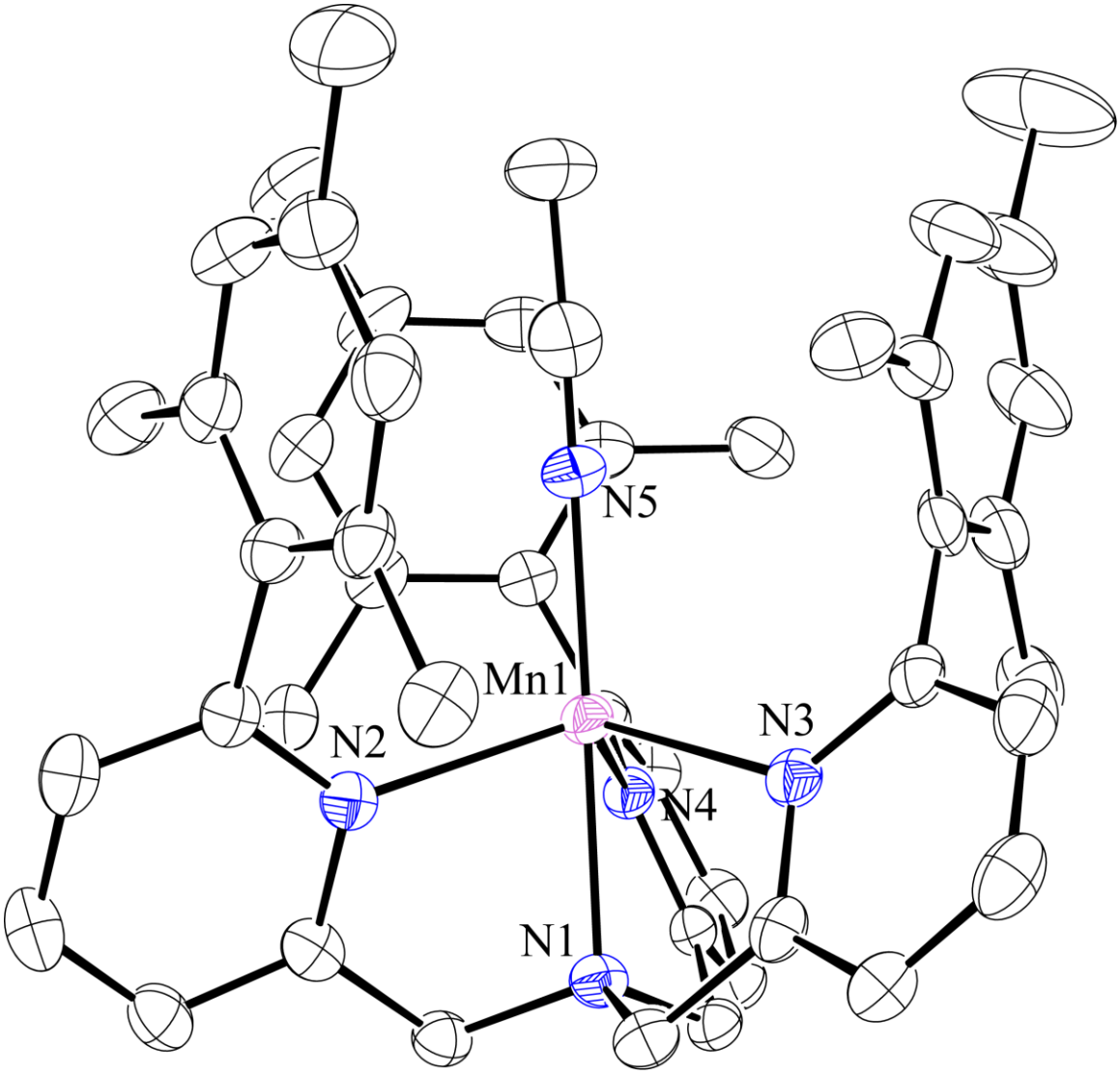

Figure D.4. The Xray structure of the dicationic portion of **2** shown with ellipsoids at 50 % probability. Hydrogen atoms, hexafluorophosphate counterions, and solvents of crystallization are not shown for clarity.

Table D.1. Crystallographic Details for **1** and **2**.		
	1	**2**
Empirical Formula	$C_{51}H_{58}CoF_{12}N_6P_2$	$C_{50}H_{57}Cl_2F_{12}MnN_5P_2$
Formula Weight	1103.90	1143.79
T (K)	100	100
λ (Å)	0.71073	0.71073
Crystal System	Monoclinic	Monoclinic
Space Group	*P2(1)/n*	*P2(1)/n*
a (Å)	11.412(2)	11.421(2)
b (Å)	18.703(4)	18.566(4)
c (Å)	24.681(5)	24.799(5)
α (º)	90.00	90.00
β (º)	99.840(2)	99.381(2)
γ (º)	90.00	90.00
V	5190.3(17)	5188.1(17)
Z	4	4
ρ_{calc} (g/cm^3)	1.413	1.464
μ (mm^{-1})	0.477	0.503
reflctns collected	24197	24234
T_{min}/T_{max}		0.92
data/restr/params	9859/0/649	9421/0/650
$2\theta_{max}$ (º)	52.8	50.8
R, R_w (%; I>4σ)	5.9, 16.8	6.4, 20.1
GOF	1.014	1.044
mean shift/error	0.001	0.04

References

(1) Bigi, J. P.; Hanna, T. E.; Harman, W. H.; Chang, A.; Chang, C. J. *Chemical Communications* **2010**, *46*, 958-960.

(2) Sun, Y.; Bigi, J. P.; Piro, N. A.; Tang, M. L.; Long, J. R.; Chang, C. J. *Journal of the American Chemical Society* **2011**, *133*, 9212-9215.

(3) Wu, X.; Seo, M. S.; Davis, K. M.; Lee, Y.-M.; Chen, J.; Cho, K.-B.; Pushkar, Y. N.; Nam, W. *Journal of the American Chemical Society* **2011**, *133*, 20088-20091.

(4) Parsell, T. H.; Behan, R. K.; Green, M. T.; Hendrich, M. P.; Borovik, A. S. *Journal of the American Chemical Society* **2006**, *128*, 8728-8729.

(5) Lassalle-Kaiser, B.; Hureau, C.; Pantazis, D. A.; Pushkar, Y.; Guillot, R.; Yachandra, V. K.; Yano, J.; Neese, F.; Anxolabehere-Mallart, E. *Energy & Environmental Science* **2012**, *3*, 924-938.

(6) Ferreira, K. N.; Iverson, T. M.; Maghlaoui, K.; Barber, J.; Iwata, S. *Science* **2004**, *303*, 1831-1838.

(7) Umena, Y.; Kawakami, K.; Shen, J.-R.; Kamiya, N. *Nature* **2011**, *473*, 55-60.

(8) Kanady, J. S.; Tsui, E. Y.; Day, M. W.; Agapie, T. *Science* **2011**, *333*, 733-736.

(9) Evans, D. F. *Journal of the Chemical Society (Resumed)* **1959**, 2003-2005.

(10) Sheldrick, G. *Acta Crystallographica Section A* **1990**, *46*, 467-473.

(11) Sheldrick, G. *Acta Crystallographica Section A* **2008**, *64*, 112-122.

Appendix E
Synthesis of Triazacyclododecane Derivatives Toward the Development of a Selective Fe^{2+} Probe

Introduction

Selective probes for studying transition metal homeostasis in living cells are an area of intense current research. Probes selective for copper(I),[1-5] zinc(II)[6] and even cobalt(II)[7] have been reported, but turn-on probes selective for iron have been less common, despite iron's central role in biology.[8-12] Our research group is interested in reaction-based probes as a method of engendering probe selectivity and have focused our efforts on hydrogen peroxide,[13] hydrogen sulfide[14] and cobalt(I).[7] Inspired by a report on using C-O cleavage to detect copper(I),[1] our group recently described a Co(II) probe that was used in the lung carcinoma cell line A549.[7] We next set out to design a probe for iron(II) using a similar strategy: i.e., an iron-mediated, oxidative C-O cleavage to release a fluorescent reporter or precursor molecule. Importantly, the requirement of using O_2 as the terminal oxidant highlighted the need for selectivity, as Cu(I) complexes are well known to mediate similar reactivity as iron via O_2 activation.[15]

Our probe design strategy is summarized in Scheme E.1. To select for Fe(II) over Cu(I) we are focusing our work on derivatives of the macrocyclic triazacyclododecane (tacdd) which release a benzothiazole reporter for a luciferase assay upon iron-mediated C-O cleavage.[16] Significantly, a report from Tolman and coworkers described how tacdd ligates Cu(I) in a trigonal planar geometry, which leads to little reactivity with O_2, while smaller triaza macrocycles form tetrahedral, O_2 sensitive Cu(I) complexes.[17] In contrast, Busch and coworkers reported a tacdd derivative (with two pendant picolyl groups) which stabilized an iron-based oxidant potentially capable of mediating the desired C-O cleavage.[18] Furthermore, an iron(IV)-oxo complex of the tetra-aza macrocycle tetramethylcylcam was successfully prepared using dioxygen under a variety of conditions.[19-21]

Results and Discussion

The preparation of our initial target with a picolyl group and two methyl groups appended to the tacdd framework is outlined in Scheme E.2. This ligand was targeted to serve as a model of the desired benzothiazole-appended tacdd for coordination chemistry studies (*vide infra*). The methine templated macrocycle **1** is prepared by alkylation of 1,5,7-triazabicyclo[4.4.0]dec-5-ene with 1,3-propaneditosylate in the presence of $NaBH_4$, KOH, and KBr.[22] Methylation with iodomethane provides the amidinium salt **2**, which is reduced with $NaBH_4$ to provide the free macrocycle **3**.[23] The picolyl-substituted macrocycle ($tacdd^{Me2Py}$, **4**) is then prepared via reductive amination with 2-pyridinecarboxaldehyde or alkylation with 2-chloromethylpyridine hydrochloride.

The Cu(I) complex of **4** is prepared in a straightforward manner by reacting $[Cu(NCCH_3)_4]PF_6$ with **4** in CH_3CN to provide $[(tacdd^{Me2Py})Cu]PF_6$ (**5**). The yellow, diamagnetic complex displays a complicated ^1H NMR suggesting multiple isomers are present in CD_3CN solution. However, yellow single crystals can be obtained and reveal a four-coordinate, trigonal monopyramidal complex in the solid state with two of the amine nitrogens and the pyridine forming the equatorial plane and the last nitrogen providing axial coordination (Figure E.1, Table E.1). Importantly, **5** does not react with O_2 in either CH_3CN or CH_3CN/H_2O solutions, suggesting the tacdd platform is a viable candidate for selecting against Cu(I) reactivity with O_2. Unfortunately, no Fe(II) complexes of **4** could be isolated as crystals suitable for Xray crystallographic analysis.

The desired benzothiazole-appended tacdd analog was then prepared (Scheme E.3). First, 2,6-bis(chloromethyl)pyridine is reacted with 2-cyano-6-hydroxybenzothiazole at 50 ºC in THF to provide the benzothiazole-appended chloromethylpyridine **6**. Second, alkylation of **3** with **6** provides the desired macrocycle with the picolyl reporter group, tacdd^{Me2PyBt} (**7**). Note that reaction of **3** with the bromomethyl analog of **6** leads to over-alkylation. **7** was then tested for reactivity with the biologically relevant metal ions Na(I), K(I), Mg(II), Ca(II) Mn(II), Fe(II), Fe(III), Co(II), Ni(II), Cu(II), Cu(I), and Zn(II) using our group's luciferase assay. Unfortunately, no reactivity (no luminescence) is observed. This result, coupled with our inability to isolate an Fe(II) complex of **4**, suggests **7** is a poor ligand for iron. We thus turned our attention toward an analog of **4** with a second picolyl substituent, namely tacdd^{MePy2}.

To this end, **1** is alkylated with 2-chloromethylpyridine to yield the picolyl-substituted amidinium salt **8**, which is reduced with $NaBH_4$ to afford the macrocyclic amine **9** (Scheme E.4). Unfortunately, alkylating **9** with 2-chloromethylpyridine results in overalkylation (only 8 % of the desired product **10** was isolated). Furthermore, preparation of the benzothiazole version of **8** is hampered by low yields arising from decomposition during purification with alumina. In addition, reduction of the resultant amidinium also reduces the cyano group. The cyano group is also converted to the ethyl ester and carboxylic acid under the reduction conditions. Future work will investigate alternative preparations of the targeted macrocycle.

Concluding Remarks

In summary, preliminary work toward a tacdd-based metal sensor is described. The new macrocyclic ligand tacdd^{Me2Py} was prepared and its Cu(I) complex structurally characterized. Although the Cu(I) complex **5** does not react with O_2 as hoped, the benzothiazole-appended macrocycle tacdd^{Me2PyBt} is not a successful probe for any other biologically-relevant metal ion. The ease of incorporating multiple distinct groups onto tacdd, however, highlights the promise of this platform for future work.

Experimental Section

General Methods. Unless noted otherwise, all manipulations were carried out at room temperature under a dinitrogen atmosphere in a VAC Atmospheres Co. glovebox or using high-vacuum Schlenk techniques. Acetonitrile, diethyl ether, THF, toluene and pentane were dried on a Vacuum Atmospheres Solvent purification system and stored over 3 Å molecular sieves. Dichloroethane, chloroform, and acetonitrile-d_3 were refluxed over CaH_2, distilled, sparged with nitrogen and stored over 3 Å molecular sieves prior to use. Molecular sieves, alumina, and celite were activated by heating at 200ºC under dynamic vacuum for at least 24 hours. All other reagents and solvents were purchased from commercial sources and used without further purification. NMR spectra were recorded on Bruker spectrometers operating at 300 or 400 MHz as noted. Chemical shifts are reported in ppm relative to residual protiated solvent; coupling constants are reported in Hz. Mass spectra were determined at the University of California, Berkeley Mass Spectrometry facility.

Bioluminescence Assays. Samples for bioluminescent measurements were placed in white, opaque 96-well plates, which were purchased from Corning Inc. The two controls were prepared similarly to the following protocol either without probe or with probe but

without metal. Samples for bioluminescence assays were prepared in three steps in pH 7.4 Tris buffer. First, 1.25 µL of a 500 µM probe solution was combined with 1.25 µL of a 10 mM metal solution, 60 µL of 50 mM pH 7.4 Tris buffer and 62.5 µL of 10 mM glutathione stock solution. The metal reaction was allowed to occur for one hour at room temperature. Second, 2.5 µL of a 10 mM EDTA solution, 1.25 µL of a 100 mM DTT solution and 1.25 µL of a 2 mM D-cysteine solution were added and allowed to react for 15 minutes with each probe/metal reaction at room temperature. Last, 100 µL of the reacted probe solution was combined with 100 µL of a 100 µg/mL luciferase solution that contained 2 mM ATP, 10 mM $MgCl_2$, and 0.1 mM $ZnCl_2$ (in 50 mM pH 7.4 Tris buffer). Luminescence was recorded using a Molecular Devices SpectraMax M2 plate reader for one hour at 37 ºC. ATP was purchased from MP Biomedicals, and luciferase was purchased from Promega. Catalase was purchased from Sigma-Aldrich.

Synthesis of orthoamide 1. This compound was prepared by modification of a literature preparation[22,24,25] using 5.0 g (35.9 mmol) 1,5,7-triazabicyclo[4.4.0]dec-5-ene, 16.7 g (43.4 mmol) 1,3-propaneditosylate, 1.68 g (44.4 mmol) $NaBH_4$, 6.25 g (111 mmol) KOH, and 6.25 g (52.5 mmol) KBr to afford 4.60 g (25.4 mmol, 71 %) of **1** as a colorless oil that solidified upon standing.

Synthesis of amidinium 2. This compound was synthesized by modification of a literature preparation.[23] **1** (938 mg, 5.17 mmol) was stirred in 40 mL $CHCl_3$ under N_2. Iodomethane (0.8 mL, 12.9 mmol) was added via syringe and the solution was stirred at room temperature for two days under N_2. The solvent was removed *in vacuo* to yield **2** as a colorless solid (1.515 g, 4.69 mmol, 91 %).

Synthesis of 1,5-dimethyl-1,5,9-triazacyclododecane (3). This compound was synthesized using a modification of a literature preparation.[23] A mixture of **2** (3.23g, 10 mmol) and $NaBH_4$ (3.87 g, 102 mmol) was heated to reflux in 200 mL absolute ethanol under N_2 overnight. Upon cooling the mixture was quenched with 1 M aq. HCl, neutralized with 1 M aq. NaOH and extracted into dichloromethane. The organic extracts were combined, dried over Na_2SO_4, filtered and concentrated under vacuum to provide **3** as a colorless oil (1.966 g, 9.9 mmol, 99 %).

Synthesis of tacdd^{Me2Py} (4). *Reductive amination.* A dichloroethane solution of **3** (520 mg, 2.6 mmol) and DIPEA (0.48 mL, 2.8 mmol) was stirred under N_2 for 15 minutes at room temperature. 2-pyridinecarboxaldehyde (240 µL, 2.5 mmol) and sodium tri(acetoxy)borohydride (1.1 g, 5.2 mmol) were then added and the mixture was stirred overnight. The reaction mixture was then filtered, rinsed with dichloromethane, and the filtrate concentrated under vacuum to yield **4** as a yellow oil which was purified by flash chromatography (Al_2O_3, 15 % MeOH in EtOAc; 246.6 mg, 0.849 mmol, 33 %). *Alkylation*. **3** (184.7 mg, 0.927 mmol), 2-chloromethylpyridine hydrochloride (160 mg, 0.975 mmol), and Cs_2CO_3 (668 mg, 2.05 mmol) were stirred in THF under N_2 overnight. The reaction mixture was then filtered to remove Cs_2CO_3 and rinsed with dichloromethane. The filtrate was concentrated *in vacuo* on a rotary evaporator to provide **4**. ^{1}H NMR (300 MHz, $CDCl_3$): δ 8.46 (d, 4.2 Hz, 1H), 7.6 (td, 1.8 Hz, 7.7 Hz, 1H), 7.46 (d, 7.8 Hz, 1H), 7.09 (m, 1H), 3.63 (s, 2H), 2.50 (t, 6.2 Hz, 4H), 2.41 (m, 8H), 2.15 (s, 6H), 1.57 (m, 6H).

Synthesis of [(tacdd^{Me2Py})Cu]PF_6 (5). To a stirring CH_3CN solution of **4** (55.1 mg, 0.19 mmol) was added solid $[Cu(NCCH_3)_4]PF_6$ (70.7 mg, 0.19 mmol). The yellow/green mixture was stirred overnight, filtered through celite and the filtrate

concentrated under vacuum. The residue was crystallized by diffusing ether into a concentrated solution of the product in CH_3CN/THF to yield yellow plate-like crystals of **5** which were suitable for Xray diffraction analysis. **5** has two chemically equivalent, though crystallographically distinct molecules in the asymmetric unit (Table E.1).

Synthesis of benzothiazole 6. A mixture of 2,6-bis(chloromethyl)pyridine (503 mg, 2.86 mmol), 2-cyano-6-hydroxybenzothiazole (273 mg, 1.5 mmol), and Cs_2Co_3 (500 mg, 1.5 mmol) was stirred in ca 10 mL THF under N_2 at 50 ºC overnight. The reaction mixture was then filtered, concentrated under vacuum and purified on SiO_2 (dry loading) using a gradient of 10 % - 30 % EtOAc in hexanes to elute (222 mg, 0.70 mmol, 47 %). The second compound to elute from the column was **6**. ^{1}H NMR (400 MHz, $CDCl_3$): δ 8.10 (d, 9.2 Hz, 1H), 7.78 (t, 7.8 Hz, 1H), 7.46 (m, 3H), 7.34 (dd, 2.4 Hz, 9.2 Hz, 1H), 5.30 (s, 2H), 4.70 (s, 2H).

Synthesis of tacdd^{Me2PyBt} (7). A mixture of **3** (52 mg, 0.26 mmol), **6** (82 mg, 0.26 mmol), and Cs_2CO_3 (160 mg, 0.49 mmol) was stirred in THF under N_2 overnight. The reaction mixture was filtered, concentrated under vacuum and purified on Al_2O_3 (wet loading; 5 % MeOH in EtOAc) to yield **7** (42.4 mg, 0.088 mmol, 34 %). ^{1}H NMR (300 Hz, $CDCl_3$): δ 8.10 (d, 9.2 Hz, 1H), 7.68 (t, 7.8 Hz, 1H), 7.47 (d, 7.8 Hz, 1H), 7.43 (d, 2.4 Hz, 1H), 7.34 (m, 2H), 5.26 (s, 2H), 3.69 (s, 2H), 2.55 (t, 6.0 Hz, 4H), 2.44 (m, 8H) 2.18 (s, 6H), 1.60 (m, 6H).

Synthesis of amidinium salt 8. A mixture of **1** (290 mg, 1.6 mmol), 2-chloromethylpyridine hydrochloride (262 mg, 1.6 mmol), NaI (500 mg, 3.3 mmol), and Cs_2CO_3 (1.04 g, 3.2 mmol) was heated to 80 ºC under N_2 in CH_3CN (15 mL) for three hours. The mixture was then filtered and concentrated under vacuum to a red oil. The product was purified on Al_2O_3 (dry loading; 15 % MeOH in EtOAc) to afford **8** as a red oil (559.9 mg, 1.4 mmol, 87 %). ^{1}H NMR (400 Hz, $CDCl_3$): δ 9.60 (s, 1H), 8.55 (d, 4.0 Hz, 1H), 7.668 (t, 7.6 Hz, 1H), 7.23 (m, 2H), 4.39 (t, 13.2 Hz, 2H), 3.66 (s, 2H), 3.47 (m, 6H), 3.22 (d, 14.4 Hz, 2H), 3.11 (d, 12.0 Hz, 2H), 3.00 (d, 11.2 Hz, 2H), 1.75 (m, 2H), 1.40 (d, 14.8 Hz, 2H).

Synthesis of 1-methyl-5-(2-picolyl)-1,5,9-triaazacyclododecane (9). This compound was prepared by heating a mixture of **8** (70.9 mg, 0.177 mmol) and $NaBH_4$ (67 mg, 1.77 mmol) in absolute ethanol to reflux under N_2 for three hours. After cooling, the reaction mixture was quenched with 30 % aq HCl, neutralized with NaOH and extracted into dichloromethane. The organics were then combined, dried over Na_2SO_4, and concentrated on a rotary evaporator to a colorless oil of **9** (39.2 mg, 0.142 mmol, 80 %). ^{1}H NMR (400 Hz, $CDCl_3$): δ 8.52 (d, 4.8 Hz, 1H), 7.69 (td, 1.6 Hz, 7.8 Hz), 7.56 (d, 3.6 Hz, 1H), 7.15 (m, 1H), 3.62 (s, 2H), 2.78 (m, 2H), 2.65 (m, 2H), 2.57 (m, 2H), 2.48 (m, 4H), 2.43 (m, 2H), 2.16 (s, 3H), 1.68 (m, 6H).

Synthesis of tacdd^{MePy2} (10). A mixture of **9** (150 mg, 0.543 mmol), 2-chloromethylpyridine hydrochloride (89 mg, 0.543 mmol), and Cs_2CO_3 (354 mg, 1.09 mmol) was stirred in THF under N_2 overnight. The mixture was filtered and purified on Al_2O_3 (15 % MeOH in EtOAc) to provide **10** (16.5 mg, 0.0449 mmol, 8 %). The desired compound was the second product to elute from the column. The last product to elute appeared to be a complex mixture, but LC/MS suggested the major component was an over-alkylated compound (see Scheme E.4). ^{1}H NMR (300 Hz, $CDCl_3$): δ 8.48 (d, 4.2 Hz, 2H), 7.62 (td, 1.8 Hz, 7.8 Hz, 2H), 7.46 (d, 7.8 Hz, 2H), 7.11 (m, 2H), 3.65 (s, 4H), 2.70 (m, 2H), 2.55 (m, 6H), 2.42 (t, 6.0 Hz, 4H), 2.16 (s, 3H), 1.63 (m, 6H).

General Methods for X-Ray Crystallography. Xray crystallographic data for **5** was collected using Cu-Kα radiation from a rotating anode on an Enraf-Nonius Kappa Geometry with DX goniostat with an Apex II CCD detector. Samples were cooled to 100 K using an Oxford Cryostream 700 low temperature device. Structures were solved using either direct methods or the Patterson method in conjunction with standard difference Fourier techniques and refined by full-matrix least-squares procedures.[26] A semi-empirical absorption correction (SADABS) was applied to the diffraction data for all structures. All non-hydrogen atoms were refined anisotropically, and hydrogen atoms were treated as idealized contributions and refined isotropically. All software used for diffraction data processing and crystal-structure solution and refinement are contained in the APEX2 program suite (Bruker AXS, Madison, WI).[27]

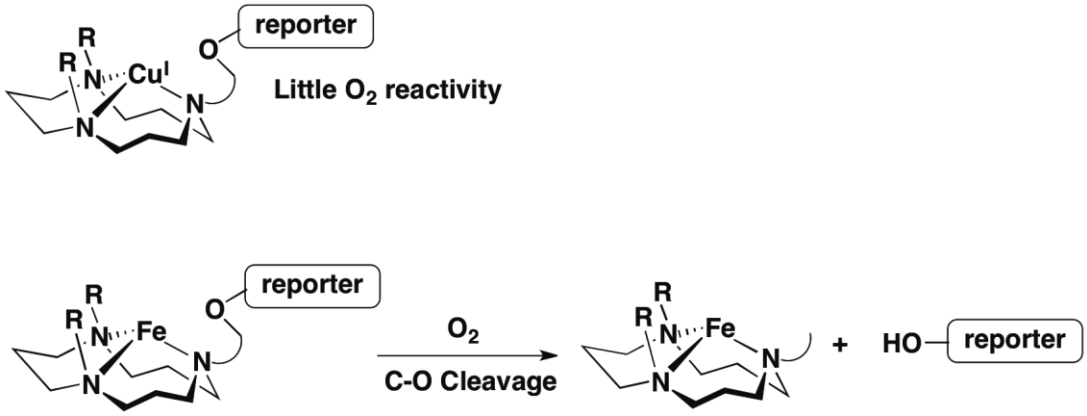

Scheme E.16. Design strategy for a reaction-based, iron-selective molecular probe.

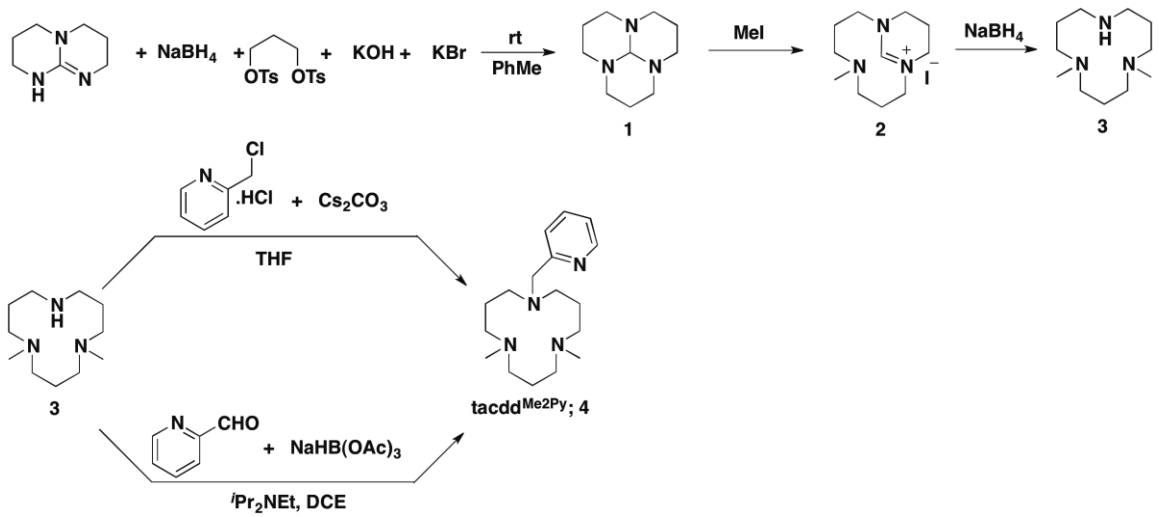

Scheme E.17. The synthesis of tacdd^{Me2Py}.

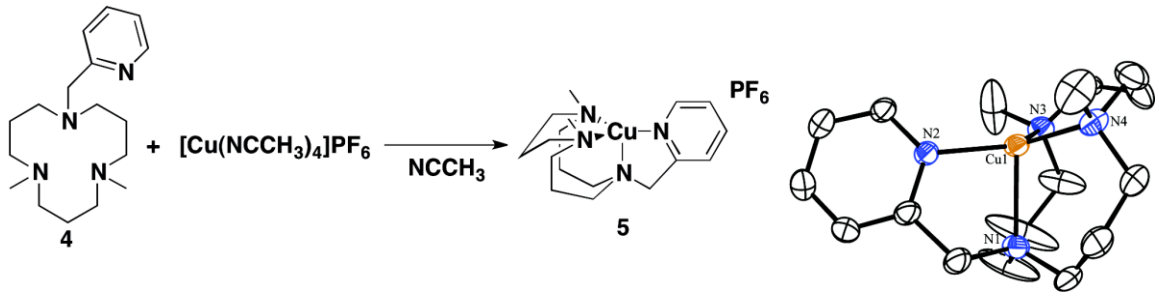

Figure E.1. Synthesis of the Cu(I) complex of tacdd^{Me2Py} and the molecular structure of its cationic portion (50 % ellipsoids, hydrogens and hexafluorophosphate anion removed for clarity).

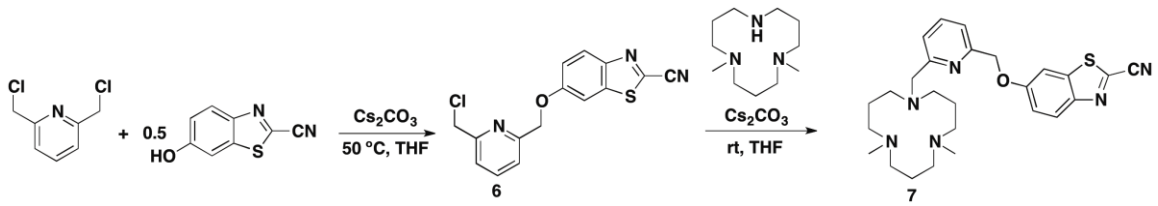

Scheme E.18. Synthesis of benzothiazole appended tacdd.

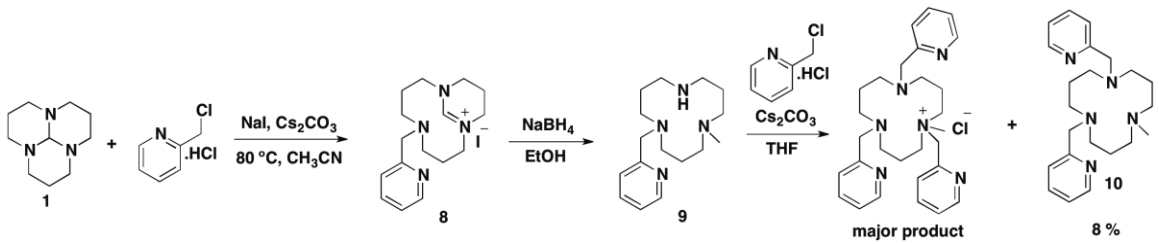

Scheme E.19. Progress toward the synthesis of tacdd^{MePy2}.

Table E.1. Crystallographic Details for **5**.	
	5
Empirical Formula	$C_{34}H_{60}N_8Cu_2F_{12}P_2$
Formula Weight	997.92
T (K)	100
λ (Å)	1.54178
Crystal System	Monoclinic
Space Group	*P2(1)/n*
a (Å)	8.9299(6)
b (Å)	14.3946(11)
c (Å)	32.963(3)
α (º)	90
β (º)	94.301(4)
γ (º)	90
V	4225.3(5)
Z	8
ρ_{calc} (g/cm^3)	3.137
μ (mm^{-1})	5.52
reflctns collected	24324
T_{min}/T_{max}	0.80
data/restr/params	7451/0/523
$2\theta_{max}$ (º)	137.04
R, R_w (%; I>4σ)	6.6, 17.0
GOF	1.016
mean shift/error	0.01

References

(1) Taki, M.; Iyoshi, S.; Ojida, A.; Hamachi, I.; Yamamoto, Y. *Journal of the American Chemical Society* **2010**, *132*, 5938-5939.
(2) Que, E. L.; New, E. J.; Chang, C. J. *Chemical Science* **2012**, *3*, 1829-1834.
(3) Dodani, S. C.; Leary, S. C.; Cobine, P. A.; Winge, D. R.; Chang, C. J. *Journal of the American Chemical Society* **2011**, *133*, 8606-8616.
(4) Zeng, L.; Miller, E. W.; Pralle, A.; Isacoff, E. Y.; Chang, C. J. *Journal of the American Chemical Society* **2005**, *128*, 10-11.
(5) Domaille, D. W.; Zeng, L.; Chang, C. J. *Journal of the American Chemical Society* **2010**, *132*, 1194-1195.
(6) Nolan, E. M.; Lippard, S. J. *Accounts of Chemical Research* **2008**, *42*, 193-203.
(7) Au-Yeung, H. Y.; New, E. J.; Chang, C. J. *Chemical Communications* **2012**, *48*, 5268-5270.
(8) Que, E. L.; Domaille, D. W.; Chang, C. J. *Chemical Reviews* **2008**, *108*, 1517-1549.
(9) Wang, R.; Yu, F.; Liu, P.; Chen, L. *Chemical Communications* **2012**, *48*, 5310-5312.
(10) Chen, J.-L.; Zhuo, S.-J.; Wu, Y.-Q.; Fang, F.; Li, L.; Zhu, C.-Q. *Spectrochimica Acta Part A: Molecular and Biomolecular Spectroscopy* **2006**, *63*, 438-443.
(11) Bricks, J. L.; Kovalchuk, A.; Trieflinger, C.; Nofz, M.; Buschel, M.; Tolmachev, A. I.; Daub, J. r.; Rurack, K. *Journal of the American Chemical Society* **2005**, *127*, 13522-13529.
(12) Xiang, Y.; Tong, A. *Organic Letters* **2006**, *8*, 1549-1552.
(13) Lippert, A. R.; Van de Bittner, G. C.; Chang, C. J. *Accounts of Chemical Research* **2011**, *44*, 793-804.
(14) Lippert, A. R.; New, E. J.; Chang, C. J. *Journal of the American Chemical Society* **2011**, *133*, 10078-10080.
(15) Mirica, L. M.; Ottenwaelder, X.; Stack, T. D. P. *Chemical Reviews* **2004**, *104*, 1013-1046.
(16) Van de Bittner, G. C.; Dubikovskaya, E. A.; Bertozzi, C. R.; Chang, C. J. *Proceedings of the National Academy of Sciences* **2010**.
(17) Lam, B. M. T.; Halfen, J. A.; Young, V. G.; Hagadorn, J. R.; Holland, P. L.; Lledos, A.; Cucurull-Sanchez, L.; Novoa, J. J.; Alvarez, S.; Tolman, W. B. *Inorganic Chemistry* **2000**, *39*, 4059-4072.
(18) Zhang, X.; Zhang, D.; H. Busch, D.; van Eldik, R. *Journal of the Chemical Society, Dalton Transactions* **1999**, 2751-2758.
(19) Kim, S. O.; Sastri, C. V.; Seo, M. S.; Kim, J.; Nam, W. *Journal of the American Chemical Society* **2005**, *127*, 4178-4179.
(20) Lee, Y.-M.; Hong, S.; Morimoto, Y.; Shin, W.; Fukuzumi, S.; Nam, W. *Journal of the American Chemical Society* **2010**, *132*, 10668-10670.
(21) Hong, S.; Lee, Y.-M.; Shin, W.; Fukuzumi, S.; Nam, W. *Journal of the American Chemical Society* **2009**, *131*, 13910-13911.
(22) Du Ho Kim, R.; Wilson, M.; Haseltine, J. *Synthetic Communications* **1994**, *24*, 3109-3114.
(23) Alder, R. W.; Mowlam, R. W.; Vachon, D. J.; Weisman, G. R. *Journal of the Chemical Society, Chemical Communications* **1992**, 507-508.

(24) Long, N. J.; Parker, D. G.; Speyer, P. R.; White, A. J. P.; Williams, D. J. *Journal of the Chemical Society, Dalton Transactions* **2002**, 2142-2150.
(25) Atkins, T. J. *Journal of the American Chemical Society* **1980**, *102*, 6364-6365.
(26) Sheldrick, G. *Acta Crystallographica Section A* **1990**, *46*, 467-473.
(27) Sheldrick, G. *Acta Crystallographica Section A* **2008**, *64*, 112-122.

Appendix F
Mössbauer Protocols

1. Sample Preparation

Sample rod. It is extremely important not to bend the sample rod. Even an approximately 0.5 º bend will result in the sample rod contacting the inner wall of the sample chamber which will ruin the Mössbauer measurement by preventing vibrational isolation from the room's vibrations. In addition, do not twist the sample rod column relative to the crown of the sample rod as that can break the copper wires that run along the sample rod and are responsible for controlling the temperature of the sample rod. If the sample rod is damaged in these or any other ways, it must be returned to See Co for repair using the heavy duty crate next to the instrument.

Solid samples. Solid samples are prepared by combination of the Fe-containing compound with roughly ½ (by weight) of boron nitride. The rule of thumb is that the sample should contain ca 1 mg of Fe/cm^2. The two solids are then mixed by mechanical grinding to ensure a random dispersion of iron-57 nuclei in the sample. The mixture is then transferred to a plastic washer (purchased from Ace Hardware) attached to a piece of tape. The washer is covered with a second piece of tape (or by wrapping the original piece of tape over the exposed side of the washer) and attached securely to the end of the sample rod by wrapping a piece of tape a few times tightly around the sample and the sample rod. The washer should be aligned with the metal circle that sits at the end of the sample rod to ensure proper alignment of the gamma ray beam, the sample and the detector (note that alignment also depends, and more significantly so, on the height of the floating table; *vide infra*). It is extremely important that the sample be well attached to the sample rod to prevent loss of the sample in the sample chamber, which would add iron-containing components to every subsequent spectrum which would have to be subtracted from each subsequent spectrum.

Frozen solution samples. Solution samples are prepared by dissolving the Fe-containing compound in a solvent and transferring the solution to the teflon sample holder (fabricated in the machine shop). The solution is transferred to the smaller half of the sample holder and closed with the larger half of the sample holder (the 'cap'). The 'cap' should fit snugly on the bottom half. The sample is then frozen by submersion in liquid nitrogen and quickly attached to the sample rod holder by tape (the sample holder should fit snugly in the end of the sample rod). The end of the sample rod is then submerged in liquid nitrogen (sufficiently deep to cover the sample) prior to loading into the pre-cooled instrument. The sample chamber should be pre-cooled to ca. 100 K prior to sample loading to ensure the frozen solution sample remains frozen.

2. Sample Loading

Sample loading is essentially the same for both solid and solution samples. First, the lid is removed from the top of the sample chamber under a steady flow of helium. Second, the sample rod is inserted under the flow of helium and secured with the screws on the top of the sample chamber. Last, the sample chamber is evacuated briefly to ensure no oxygen enters the sample chamber. The main difference is that for solution samples the sample chamber must be pre-cooled to ensure the sample doesn't thaw during loading. For this reason, solution samples (or cold solid samples) should also be loaded as quickly as possible and the sample chamber should be left under a small pressure (ca -29 in Hg) of helium. For rt samples, the samples can be measured under vacuum or under He pressure.

3. Cooling

Prior to cooling, the vacuum shroud of the cryostat must be evacuated (using the turbomolecular pump) to ca $4/3 \times 10^{-3}$ mbar. The sample chamber should also be under vacuum (using the mechanical pump) during the initial phase of cooling (to ca 100 K). Check that the cooling water for the compressor is running (ca 3.5 L/min) and turn the compressor on by flipping the 'drive' switch on the front of the compressor unit (do not flip the switch that has the warning to not flip). The temperature for channel 2 (the cold head) on the temperature controller should then decrease gradually to ca 5K over the next couple of hours. Note that the cold head can be cooled to other temperatures by application of the heater for channel 2.

Once the desired temperature is reached, the sample rod is inserted under a steady flow of helium (if the sample rod is not already inserted prior to cooling). A small pressure of He (ca -20 in Hg) is then introduced, which should cool channel 1 until it nearly matches the cold head temperature. Alternatively, a small pressure of He (ca -20 in Hg) can be introduced to the sample chamber to cool the sample chamber prior to insertion of the sample rod. This latter protocol is necessary when a frozen solution sample is inserted. The pre-cooled sample chamber should ensure the frozen solution sample does not thaw and leak in to the sample chamber.

Note that the temperatures of channel 1 (the end of the sample rod) and channel 2 (the cold head) will never be quite the same. Furthermore, the temperature will gradually increase from the cold head up to the top of the sample chamber even when the He gas is enabling thermal contact between the cold head and the sample chamber.

4. Data Collection

The detector collects data continuously, as the source is constantly decaying and emitting gamma rays that are being detected by the counter. This data (in counts) is saved by the software every ca 10 minutes on a file that is overwritten unless it is given a different name in the 'data shortcut' folder. It is thus important to save and rename the data after finishing a sample , or changing temperatures, or changing velocity scales, etc. To begin a data collection, first open the W202 application and set the two windows to bracket the two gamma rays that correspond to the Mossbauer effect (the 14.4 keV gamma and the 2 keV 'escape' peak). Note the count levels for the two peaks (esp over time as the source decays). Second, open the W302 application and clear the data to start a new data collection. If the velocity scale needs to be changed do so, but remember that this will clear the data as well and will also necessitate a new calibration. A calibration should be performed every time the velocity scale is changed and every couple of weeks even if the velocity scaled has not been changed. The calibration is conducted at room temperature on a 27 μm alpha-iron foil with the compressor off. The calibration data is analyzed using the older Wmoss software package on Windows 98. Lastly, open the velocity transducer monitor to see whether the error signal looks good (i.e., 'fits' in the window at a scale of 37 mV).

5. Alignment

To maintain good vibration isolation, the cryostat and the floating table (to which the sample rod is connected) must be properly aligned. The alignment can be partially

judged by the three levels (two on the floating table and one for judging how straight the cryostat is). If the alignment is not good, the spectra will be broadened by vibrational contact between the room and the sample. The vibrational isolation is ultimately judged by the linewidth at half maximum of the inner doublet of the iron spectrum at room temperature with the compressor off as well as on. The linewidth at half maximum should be at or below 0.25 mm/sec. The alignment is most often corrected by correction of the height and alignment of the floating table. This is because the air pads on which the table floats leak and do so differently for each pad. To correct the height/alignment of the table add air to the air pads with the bicycle pump. This can be tedious, but is necessary for data collection. The height of the table should be raised such that there is 202 cm between the top of the table and the three-way valve when the sample chamber not under vacuum. Use the piece of measuring stick with the line marked off for the proper distance to help you. The alignment of the cryostat should not have to be corrected unless the cryostat has to be moved, although it should be checked in case something happens I don't foresee.

6. Source Installation

EH&S must be contacted prior to any work on the lead enclosure, including source removal/replacement. The following procedure was written by Tom at See Co:
VT400 Velocity Transducer :

A. *Installation and Removal of Ritverc Gamma Source in a Type 5 Holder*

Installation or removal of the gamma source on the SEE Co Model VT400 Velocity transducer requires removal of the primary source shield. In keeping with the As Low as Reasonably Achievable (ALARA) principle, the time the source is unshielded should be kept to a minimum and the distance from the source to the user should be maximized. With planning the source can be unshielded for less than 15 seconds. The time with the user's fingers are near the source can be as little as two seconds. Leak tests should be done on a regular schedule, e.g. biannually, to ensure the integrity of the sealed source.

Required items for source installation:
1. VT400 with source shield removed,
2. Gamma source stored in Pb pig,
3. Forceps with tips that fit into M4 female threaded hole.
4. 7/16 inch Hex Nut driver or similar tool,
5. Screwdriver (or Allen wrench) for 6-32 screws on VT400 source shield.

B. *Installation Procedure*

1. Place the VT400 in the vertical position on workbench and remove the source shield.
2. Keeping the source at arms length, remove the source from the Pb pig using the forceps. Grip the source by placing one tip of the forceps into the threaded hole in the source holder body. Be careful. Dropping the source will increase your exposure time and possibly damage the source.
3. Insert the source into the 7/16 nut driver.
4. Using the nut driver screw the source onto the VT400 motor drive shaft. Turn clockwise until the source slips in the driver.

5. Ensure the source is snug by quickly gripping the bottom of the source with your thumb and forefinger and giving the source a quick clockwise twist. Gripping the source at the bottom keeps the body of the Titanium holder between your finger and the active foil on the face of the source.
6. Place the source shield over the source and align the holes in the source shield base with the treaded 6-32 holes in the VT400 body.
7. Place the lid of the Pb pig over the source shield opening.
8. Secure the shield to the VT400 motor with the three 6-32 screws.
9. Place the VT400 in position, connect the control cable, and put any secondary shielding in place.
The entire installation procedure requires less than one minute. Survey the area around the spectrometer with a calibrated meter to confirm dose rates are acceptable.

C. *Source Removal Procedure*
1. All required items should be at hand.
2. Turn off the spectrometer electronics and remove the cable from the VT400.
3. Place the VT400 in the vertical position on the workbench and place the lid of the Pb pig over the shield aperture.
4. Remove the three 6-32 screws.
5. Keeping the VT400 and source at arms length, remove the source shield.
6. Place the 7/16 nut driver over the source and unscrew the source. If the source slips when the nut driver is turned try tilting the nut driver slightly.
7. Using the forceps remove the source from the nut driver and place the source in the Pb pig. Grip the source by placing one tip of the forceps into the threaded hole in the source holder body. Be careful. Dropping the source will increase your exposure time and possibly damage the source.
8. Place the lid on the Pb pig.
9. Store in secure place.
Survey the area to confirm no active material has leaked from source.

7. Troubleshooting

1. The most common problem is a large error signal (and the resulting broad data) due to poor vibrational isolation. This is fixed by improving the alignment of the table relative to the cryostat.
2. If the actual temperature reading for channel 1 on the temperature controller reads ??? then the sample rod copper wires have probably been broken. The sample rod would have to be sent back to See Co for repair. Prior to this the leads should be tested for the proper resistance. The cable connecting the sample rod to the temperature controller should be similarly tested. Here's Tom's message for testing the temperature cable:
    a. You will need an ohm-meter to test the temperature sensor on the sample insert. The sensor is a Lakeshore Model DT670 silicon diode. The connections to the 10 pin connector are specified in the Janis manual for the cryostat. The pins on the ten pin connector on the sample insert are label with letters, A - K (I think "I" is omitted). The diode temperature sensor is connected via four wires: Pin A and Pin B are connected to the

"+" side of the diode Pin C and Pin D are connected to the "-" side of the diode. The sensor lead wires are small and each has a resistance of approx. 5 to 10 ohms. If you measure with your ohm meter from A to B you should get 10 to 20 ohms. Same for C to D, 10 to 20 ohms. Resistance from any of A, B, C or D to sample rod or Heater should be several mega ohms at least. (*__Be careful not to touch the metal probes with your fingers when you make this measurement__.*) The resistance from A to C should be different from C to A because of the one way conductance of the diode. The Heater is connected to the last two pins, H and K (?). The heater resistance is 50 ohms, approx. The resistance between the heater and any of the diode connections and to the sample insert rod should be at least several mega ohms. Let me know the results. The most common problem is a broken wire between the ten pin connector and the diode. Inspect the full length of the wires carefully. Pay close attention to the connections on the back of the 10 pin connector. Excessive rotation of the sample rod will break the wires at that point.

3. If something happens with the motor, such as the shaft slipping (this happened once), the motor will have to be returned to See Co. The problem could also be the motor cable or the connection at the motor (ca 300 ohms between pins 2 and 4 on the cable and leads A and B on the motor; ca 20 ohms between pins 7 and 8 on the cable and leads C and D on the motor). Before shipping the motor to See Co, you must remove the source and store in the hazardous material facility, which means you must contact EH&S. If the lead enclosure is changed in any way, such as accessing the motor, EH&S must be contacted.
4. The appearance of condensation on the cryostat during heating or cooling implies a poor vacuum in the vacuum shroud. Check to make sure the turbo pump was used to evacuate the shroud. The worse case scenario is a leak in the cryostat (e.g., the mylar windows) that would require the cryostat be returned to Janis.

8. Contacts

Thomas Kent, president of See Co, tkent@seeco.us,

Tel: 1-952-426-3678

Fax: 1-612-395-5558

Address: SEE Co. 5255 Edina Industrial Blvd. Edina, MN 55439 USA

----The sample rod, 202, 303, and Wmoss software are designed by Tom. We bought everything from him as a package deal though.

Compressor repairs: Aya Skica, askica@shicryogenics.com

Cryostat repairs: Dan Logan, dlogan@janis.com

Turbopump repairs: Andrea Tzannos, Andrea.TZANNOS@adixen-usa.com

EH&S: Kathleen Dinnel-Jones, dinneljones@berkeley.edu